Deformation Behaviour of a Zr-Cu-based Bulk Metallic Glass

By

Vahid Nekouie

A Doctoral Thesis submitted in partial fulfilment of the requirements for the award of Doctor of Philosophy of Loughborough University

Wolfson School of Mechanical, Electrical and Manufacturing Engineering

June 2016

Project supervisors **Dr. Anish Roy**

Prof. Vadim Silberschmidt

Abstract

While inelastic mechanical behaviour of crystalline materials is well-understood in terms of lattice defects, bulk metallic glasses (BMGs) pose significant challenges in this respect due to their disordered structure. They can be produced by rapid cooling from the liquid state (among other technique) and, thus can be frozen as vitreous solids. Due to the absence of a long-range order in atomic structure and a lack of defects such as dislocations, BMGs generally show unique mechanical properties such as high strength and elastic limit, as well as good fracture toughness and corrosion resistance. Typically, inorganic glasses are brittle at room temperature, showing a smooth fracture surface as a results of mode-I brittle fracture. At small scale, it was well documented that inelastic deformation of bulk metallic glasses is localised in thin shear bands. So, in order to understand deformation mechanisms of BMGs comprehensively, it is necessary to investigate formation of shear bands and related deformation process.

In this thesis, a history of development of BMGs is presented, followed by a review of fundamental mechanisms of their deformation. A Zr–Cu-based BMG is characterised across several length scales (nano-, micro- and macro-scale) and various loading conditions (homogeneous and inhomogeneous loading states). At the macro-scale level, three-point bending was used to determine mechanical properties including the Poisson`s ratio (0.35) and the elastic modulus (E, 86 GPa). In this study, observations of fracture surfaces of the BMG exposed to three-point bending revealed features different from those observed in crystalline materials. Additionally, high-precision dynamical mechanical relaxation

measurements were performed with a DMA system at room and elevated temperatures. A decrease in the storage modulus indicated the glass-transition temperature (T_g), which confirmed the amorphous structure of the BMG that was initially investigated using X-ray diffraction (XRD). This study demonstrated that the dynamic properties of the material were not sensitive to the strain rate at room and elevated temperature.

Nano-indentation studies with a spherical indenter were carried out to characterise shear-band localisation on a surface of the BMG. Its initial deformation was also investigated with this method. The indentation cycle reflected elastic deformation with a yielding load of approx. 4 mN. Loading–unloading cycles were carried out at higher load magnitudes with the aim of observing shear steps on the material's surface and to investigate an indentation size effect. For designed cycling indentation, hardening phenomena were observed in nano-indentations. Additionally, micro-indentation experiments were conducted using a spherical indenter with maximum load of 15 N. While shear-band slips were observed on the surface at around 100 mN in the nano-indentation test, this phenomenon in spherical micro-indentation was found at loads in excess of 10 N. Unfortunately, due to the nature of the experiment conducted, it was impossible to observe the nucleation and initial propagation of shear bands, as they occurred inside the material volume.

Hence, an advanced technique was proposed to characterise a plasticity mechanism through the initiation and the evolution of localised shear bands beneath the indentation – wedge indentation- under incremental and single-cycle loading conditions. It was found that a semi-circular region of shear bands was formed beneath the indentation zone at 1 kN. With increasing load, secondary

shear bands developed inside the plastic region. This technique is particularly useful for development of appropriate constitutive models that characterise plastic behaviour of amorphous materials in a small-length scale.

For a more details study, micro-pillars with diameters of 10 μm and 230 nm were fabricated using a focus ion beam (FIB) technique to assess their apparent yield strength. Preliminary results indicated that a number of shear bands increased with the sample size. In the range of the sample dimensions (200nm-10 μm) micro-compression tests showed that yield strength was dependent on the sample size. Additionally, the thesis describes detailed micro-pillar compression tests carried out on the BMG in different structural sates (as-cast and fracture surface). The results clearly demonstrate yield strength in the deformed BMG was two times lower than that of undeformed regions.

Additionally, surface-decoration technique was employed to track formation and propagation of shear bands in the sample as a result of incremental loading. It was shown that shear bands formed in the localised deformation zone with a discrete character of their movement. Individual shear bands in the studied BMG were characterised to obtain better understanding of the effect of non-crystalline defects on shear-band-induced plasticity. The results clearly demonstrated that mechanical properties (including hardness and the Young`s modulus) in the deformed BMG were lower than those of undeformed regions. No compositional or structural changes were found in shear-band areas of the studied BMG. Digital image correlation (DIC) was employed to measure local strains during wedge-indentation experiments. Based on the DIC analysis, a numerical model was developed representing the material response of the studied amorphous

alloy. A good agreement between the obtained modelling results and the experimental data was shown.

Acknowledgements

I would like to acknowledge Dr. Anish Roy and Prof. Vadim V. Silberschmidt for their valuable support, guidance and encouragement throughout the period of this project. I sincerely thank them for guiding me in the right direction. Their encouragement, motivation, patience and help in presentation skills had an invaluable effect on the completion of this work. In particular, my sincere gratitude to my both supervisors for their understanding, persistence and dedication during the critical time of my study, and most importantly, their wisdom, meticulous guidance, constructive suggestions and remarks provided a real inspiration for the successful completion of this work.

I am indebted to all the people from Loughborough Materials Characterisation Centre (LMCC) in particular Mr. Scott Doak for their guidance and co-operation concerning various characterisation facilities. Many thanks to all the staff and students at Wolfson School of Mechanical, Electrical and Manufacturing Engineering and other departments for their help and support. Special thanks to all the members of the Mechanics of Advanced Materials (MOAM) group for helping me with my experiments.

I also would like to acknowledge my dear parents and my lovely wife, Shaghayegh, for their continuous support and motivation, which helped me to stay focussed.

Publications

1. Journal Papers

- **V. Nekouie**, U. Kuhn, A. Roy and V.V. Silberschmidt. Quasi-static and dynamic deformation of Zr-based bulk metallic glass, Journal of Physics: Conference Series, 451-55, 2013.
- **V. Nekouie**, G. Abeygunawardane-arachchige, U. Kuhn, A. Roy, and V.V. Silberschmidt, Indentation-induced deformation localisation in Zr-based metallic glass, Journal of alloys and compounds, 93-97, 2014,.
- **V. Nekouie**, A. Roy, and V.V. Silberschmidt. Indentation study of mechanical behaviour of Zr-Cu-based metallic glass, Conference Series, 291-299, 2015.
- **V. Nekouie**, A. Roy, and V.V. Silberschmidt. Shear bands in Zr-Cu-based metallic glass: New insight, 2016 (Accepted).
- **V. Nekouie**, A. Roy, and V.V. Silberschmidt, Microcompression studies of a Zr-Cu-based metallic glass: Effect of Size and structural state on the deformation mode and the strength, 2016 (Submitted).

2. Book Chapters

- V. Nekouie, A. Roy, and V.V. Silberschmidt, Applied Nanoindentation, Nanoindentation of Bulk Metallic Glass, Willey, 2015.
- V. Nekouie, G. Abeygunawardane-arachchige, A. Roy, and V.V. Silberschmidt, Bulk Metallic Glasses: Mechanical Properties and Performance, - In: Mechanics of Advanced Materials: Analysis and Properties. V.V. Silberschmidt, V.P. Matveenko (eds.), Springer International Publishing, 2015, DOI: 10.1007/978-3-319-17118-0_5.

Presentations at Conferences:

1. **V. Nekouie**, 14th European Nano-mechanical User Group meeting, 15-16 November, 2015, Sweden.

2. **V. Nekouie**, A.Roy, V.V. Silberschmidt, " Shear bands in Cu-Zr-based metallic glass: New insight" 10th International Conference on Advances in Experimental Mechanics (BSSM 2015), 1-3 September, 2013, Heriot-Watt University, Edinburgh, UK.

3. **V. Nekouie**, A.Roy, V.V. Silberschmidt," Indentation studies of mechanical behaviour of Zr-Cu-based metallic glass" Proceedings of XLIII International Summer School Conference (APM 2015), 22-27 July, St. Petersburg, Russia.

4. **V. Nekouie**, A.Roy, V.V. Silberschmidt, " Study of mechanical deformation of Zr-Cu-based metallic glass" 8th International Symposium on Mechanics of Materials and Structures, 31May- 3June, 2015, Augustow, Poland.

5. **V. Nekouie**, A.Roy, V.V. Silberschmidt, " Wedge indentation studies in Zr-Cu-based bulk metallic glass" 12th International Conference on the Mechanical Behaviour of Materials (ICM 2015), 10-14 May, 2015, Karlsruhe, Germany.

6. **V. Nekouie**, G. Abeygunawardane-arachchige, A.Roy, V.V. Silberschmidt, " Study of mechanical deformation of Zr-Cu-based bulk metallic glass: Experiment and numerical simulation" 11th World Congress on Computational Mechanics (WCCM XI), 20-25 July, 2014, Barcelona, Spain.

7. **V. Nekouie**, G. Abeygunawardane-arachchige, A.Roy, V.V. Silberschmidt, "Elastic-plastic properties of BMG: indentation and numerical studies" Advances in Micromechanics of Materials (MICROMEC 2014), 8-11 July, 2014, Rzeszow, Poland.
8. **V. Nekouie**, G. Abeygunawardane-arachchige, A.Roy, V.V. Silberschmidt, " Deformation characteristics of Zr-Cu-based bulk metallic glass: Experimental and numerical studies" Third International Conference in

Advanced Manufacturing for Multifunctional Miniaturised Devices (ICAM3D-2014), 27-28 August, 2014, Ibaraki, Japan.

9. **V. Nekouie**, A. Roy, V.V. Silberschmidt, “Mechanical behaviour of materials in indentation” 13th European Nano-mechanical User Group meeting, 8 Dec, 2013, Oxford, UK.
10. **V. Nekouie**, G. Abeygunawardane-arachchige, A.Roy, V.V. Silberschmidt, “ Quasi-static and dynamic deformation behaviour of Zr-Cu-based metallic glass” International Symposium on Dynamic Deformation and Fracture of Advanced Materials (D2FAM 2013), 9-11 September, 2013,Loughborough University, UK.
11. **V. Nekouie**, G. Abeygunawardane-arachchige, A.Roy, V.V. Silberschmidt, “ Mechanical behaviour of Zr-Cu-based metallic glass in indentation” 20th International Symposium on Metastable, Amorphous and Nano-structured Materials (ISMANAM2013), June 30-July 5, 2013 Torino, Italy.

Table of Contents

List of Figures

List of Tables

Symbols

μ	Coefficient of friction
t	Pseudo-effective stress
θ	Friction angle
d	Effective cohesion parameter
p	Hydrostatic pressure
r	Third invariant of the deviatoric stress
K	Ratio of the yield stress in tri-axial tension to that in tri-axial compression
q	Von Mises equivalent stress
g	Flow potential
ψ	Dilatation angle in the *p-t* plane
f	Drucker Prager yield criterion
ε_{xy}	Shear stress
LE11	Axial logarithmic strain
E	Elastic modulus
E_d	Elastic modulus in the damaged area
H	Hardness
H_d	Damaged hardness
ν	Poisson's ratio
D	Damage parameter
d_0	Initial diameter of the cylindrical pillar
d_1	Final diameter of the cylindrical pillar
φ	Tapered angle
P_f	Fracture possibility

σ_0	Scaling parameter
σ_u	Stress at which there is a zero failure probability
m	Weibull module
V	Volume of tested sample
d	diameter of the compression sample
σ_f	Failure strength
S	clusters/superclusters with stiff phase
M	A solvent matrix with lower stiffness
G	Global elastic moduli of metallic glasses
V_m^M	Molar volumes of the matrix
V_m^S	molar volumes of clusters/superclusters
G^M	Elastic modulus of matrix
G^S	Elastic modulus of clusters/superclusters
f^M	fractions of matrix phases
f^S	fractions of clusters/superclusters phases
B	Bulk modulus
τ	Shear stress
T_0	Temperature at which the free volume disappears
α	Coefficient of thermal expansion
υ_m	Mean atomic volume at zero pressure
β	Mean compressibility
υ_p	Mean atomic volume for the pressure increment ΔP
ΔP	Pressure increment
η	Geometrical factor
υ_f	Average free volume per atom

v^*	Critical volume
Δf	Fraction of sample volume
Ω	Atomic volume
ΔG^m	Activation energy
k	Boltzmann constant
J	Debye frequency
$\dot{\gamma}$	Strain rate
α_0	Constant incorporating the fraction of material being able to undergo shear transformation
υ_0	Natural frequency of the STZs
Ω_0	Volume of an individual STZ
γ_0	Strain rate of an individual STZ
ΔF_0	(Helmholtz) free energy for STZ activation
$\mu(T)$	Temperature-dependent shear modulus
τ_0	Ideal shear strength of the STZ
h	Indentation depth
H_0	Hardness in the limit of the infinite
H	Hardness
C_f	Concentration of flow defects
T_g	Glass transition temperature
d	Spacing between the atomic layers
n	Any integer
λ	Wavelength of the incident
δ	Phase difference between the maximum stress and strain
E'	Storage modulus
E''	Loss modulus

$\mathrm{h_p}$	Plastic depth
$\mathrm{R_r}$	Loading impression of radius
$\mathrm{R_i}$	Rigid indenter radius
$\mathrm{h_e}$	Elastic depth
$\mathrm{h_t}$	Total depth
P_{max}	Maximum load
$h_r.$	Residual depth
E_r	Reduced modulus
E_i	Indenter modulus
ν_i	Poisson's ratio of the indenter
h_a	Depth of the contact area
a	Radius of the circle of contact
S	Stiffness
ε	Shape function
C_f	Instrument compliance
δ	Height of the tip that contact with the sample
P_I	load at the first pop-in
k	Thermal conductivity
C_p	Specific heat capacity
h	Shear band thickness
$\dot{\gamma}_b$	Shear strain rate
Δh	Average displacement burst
$A_{total\ in\ contact}$	Total area in contact
$A_{flank\ side}$	Flank side area

Abbreviation

2D	Two-dimensional
3D	Three-dimensional
AFM	Atomic force microscopy
BCC	Body-centred cubic
BMG	Bulk metallic glass
BF	Bright-field
DMA	Dynamic mechanical analysis
DAF	Diamond area function
D-P	Drucker Prager
DIC	Digital image correlation
EDM	Electrical discharge machining
EDS	Energy dispersive spectroscopy
GND	Geometrically necessary dislocations
HCP	Hexagonal close-packed
HFW	Horizontal field width
FCC	Face-centred cubic
FEA	Finite element analysis
FEB	Focused electron beam
FEG-SEM	Field-emission-Gun SEM
FIB	Focussed ion beam
ISE	Indentation size effect
JH	Johnson and Holmquist
JHB	Johnson-Holmquist-Beissel
LMIS	Liquid-metal ion source

LMCC	Loughborough Material Characterisation Centre
MD	Molecular dynamics
MG	Metallic glass
PAS	Positron annihilation spectroscopy
SAED	Selected area electron diffraction
SEM	Scanning electron microscopy
SBIA	Shear-band`s inclination angle
STZ	Shear transformation zone
TEM	Transmission electron microscopy
XRD	X-ray diffraction
RRP	Revolute–revolute–prismatic

1 Introduction

1.1 Motivation

Bulk metallic glasses (BMGs) are relatively new materials that are increasingly being used for various applications thanks to their unique and remarkable properties. These properties make BMGs ideal candidates for various applications such as MEMS (micro-electromechanical systems), miniaturised biomedical devices and implants as well as micro-robotics devices. In the last few decades, research have led to the discovery and development of new BMGs in a variety of multi-component alloy systems with easy verification during conventional solidification resulting in thickness values of several centimetres and weights up to several kilograms [1,2]. BMGs also received much scientific and technological attention thanks to their prominent mechanical properties such as a high ratio of elastic limit to the Young's modulus and higher fracture toughness, when compared to their crystalline counterparts of similar compositions. On average, specific strength of metallic glasses is more than twice than that of their crystalline counterparts. Metallic glasses also absorb less energy in stress-induced deformation compared with crystalline materials [3]. This is typically attributed to the absence of a long-range order in their atomic structure and a lack of defects such as dislocations, which control ductility in traditional metallic materials. Figure 1-1(a) compares mechanical properties of different types of materials, showing that metallic glasses display a combination of strength of crystalline materials with elasticity of polymers. Figure 1-1(b) presents failure strength, σ_f, against the Young's modulus, E, for all types of metallic glasses, such Zr-, Mg-, Fe- and Co- based metallic glass, and several

commercial metals. As shown in this figure, the highest fracture strengths can be found in Fe- and Co-based BMGs, where values above 5 GPa were reported.

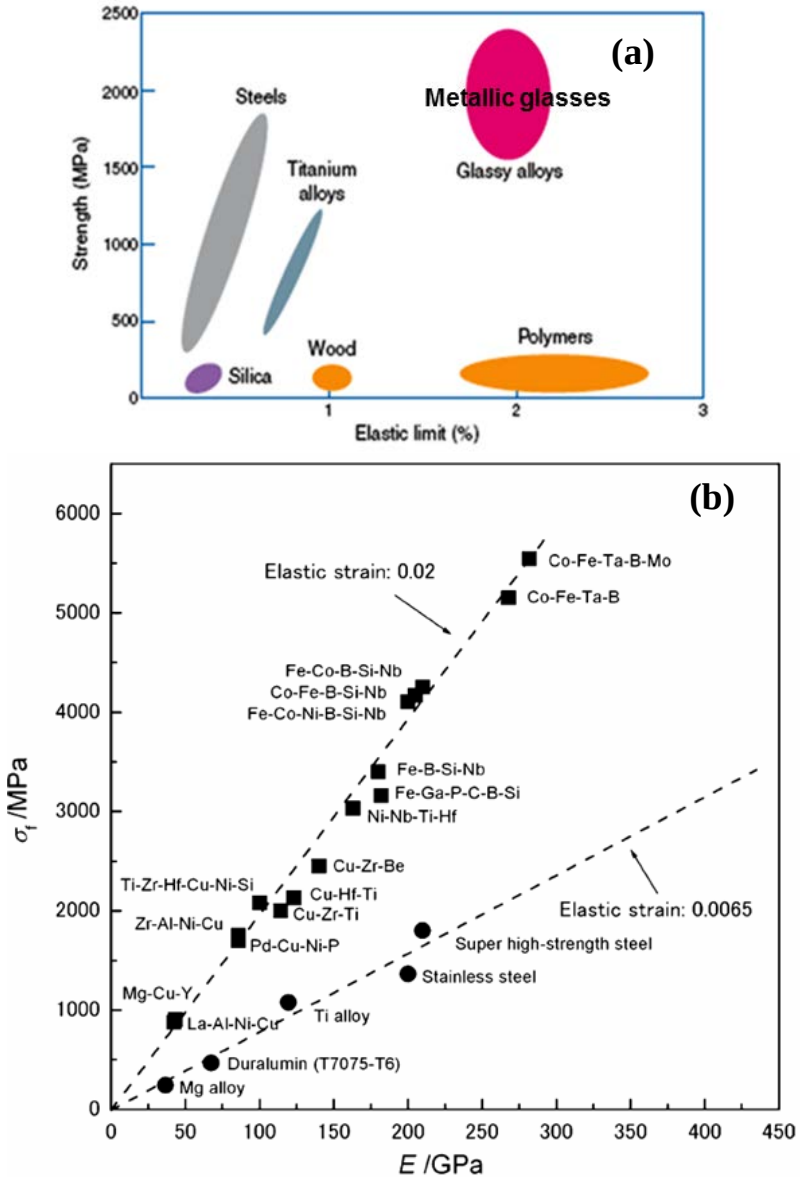

Figure 1-1 (a) Comparison of characteristics of metallic glasses and counterpart materials. (b) Relationship between fracture strength and Young's modulus for variety of metallic glasses. The data for several commercialised crystalline alloys are indicated for comparison [4]

Typically, inorganic glasses are brittle at room temperature, exhibiting a smooth fracture surface as a result of mode-I brittle fracture. BMGs have nearly no plasticity in macro-scale under tensile and compressive deformations, and their mechanical behaviour is very sensitive to internal and surface flaws such as microcracks and voids. The cause of this limited macroscopic plasticity in BMGs compared to the conventional metals is the absence of grain structure and an extreme localisation of plastic flow into narrow shear bands that initiate strain-softening. As shown in Figure 1-2 (a), metallic glasses fail on the plane of maximum shear stress under tension loading, which is at 45° to the tension axis. The resulting fracture surfaces have two distinct regions - smooth and veined. For BMGs, at temperatures significantly lower than their glass transition (Tg), observed plastic deformation is spatially and temporally inhomogeneous and carried by highly localised, narrow shear bands [2].

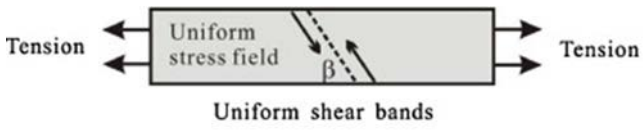

(a)

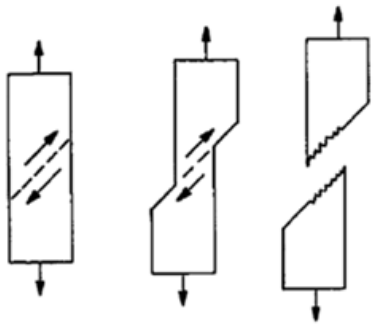

(b)

Figure 1-2 (a) Shear band formation in metallic glass samples in uniaxial tension. (b) Fracture process of BMGs specimen in tension with formation of smooth and veined regions [2].

Significant efforts were made to develop glassy metals, capable to distribute shear bands uniformly or to hinder their propagation in order to enhance their deformability. Some recent experiments on sub-micron and nano-sized metallic-glass specimens showed that the process of shear localisation became more stable and less catastrophic, compared to that in large-size samples [5].

The study was focused to study deformation of behaviour of Zr-Cu based BMGs. These BMGs have attracted attention due to extremely high-yield strength (close to theoretical value), high hardness and elastic modulus make them a good candidate for BMG structural applications. On the contrary to other type of BMGs, they showed large compressive plastic strain and strain hardening-type phenomena due to chemical heterogeneities and Cu [3].

Zr-Cu-MGs with relatively high thermal stability and low critical cooling rates resulted in considerable improvements in specimen`s sizes from µm to mm (Any MGs with sizes in excess of 1mm is called BMGs). Zr-Cu-based BMGs have outstanding glass forming ability (GFA) compared to other type of BMGs such that rapid solidification is unnecessary and BMGs thus have become obtainable with conventional copper-mold casting. In addition, there is no noticeable room temperature aging for Zr-Cu-based BMGs, thus these BMGs can be use at room temperature for long time.

1.2 Historical background

Based on the periodicity of an identical unit in the structure, materials can be classified as crystalline and non-crystalline. Metals, alloys and some ceramic materials are the examples of crystalline materials. The arrangements of atoms,

ions or molecules making up the solid define its physical structure. In crystalline solid, its atoms are arranged in a pattern repeating itself in three dimensions and, hence, form a solid with a crystal structure [6]. So, it is often convenient to subdivide these structures into small repeating entities called *unit cells* while describing them. It is this representative unit cell that possesses most of the properties the structure shows under loading conditions, as it is considered the smallest unit of the arrangement of atoms. Most elemental metals (about 90%) crystallise upon solidification into three densely packed crystal structures: body-centred cubic (bcc), face-centred cubic (fcc) and hexagonal close-packed (hcp) (Figure 1-3). Crystallographic slip is the governing mechanism of plastic deformation in metals and alloys and it happens by means of the motion of dislocations. Dislocation motion is analogous to the distortion process of pack of cards in case when it is pushed from one end. The dislocations may be introduced in materials during plastic deformation, during solidification and as a result of thermal stresses owing to rapid cooling [7]. Mechanical properties of these materials are mostly governed by the nature, density of the dislocation and their movement.

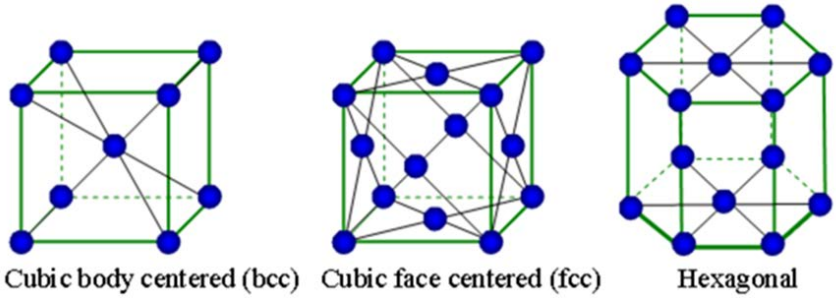

Figure 1-3 Different crystalline structures of metals: (a) cubic body centred (bcc); (b) cubic face centred (fcc); (c) hexagonal close-packed (hcp) [6].

Non-crystalline solids were conventionally called 'amorphous' solids, with glass and polymer being significant representatives. Natural glass existed from the early times of the earth and man-made (non-metallic) glasses were fabricated in Egypt and Eastern Mesopotamia from 3500 BC. In contrast, amorphous metals or metallic glasses were first reported only around 1960s. These glasses were processed using solid-state amorphisation [8] via hydrogen absorption [9,10], mechanical alloying [11], or heat treatment enabling anomalous diffusion in crystalline bi-layers [12]. In 1960, Klement and co-workers fabricated a metallic glass (Au-Si alloy) by rapid quenching from 1300ºC to room temperature with a high cooling rate of $10^6\ \mathrm{K\,s^{-1}}$ [13]. From the late 1980s, metallic glasses were manufactured in a variety of multi-component alloys with cooling rates less than $100\ \mathrm{K\,s^{-1}}$ and thickness of several centimetres. The first commercial metallic glass, $Zr_{41.2}Cu_{12.5}Ni_{10}Ti_{13.8}Be_{22.5}$ alloy named Vitreloy 1, was produced by Johnson and Peker in 1992 with a critical cooling rate of $1\ \mathrm{K\,s^{-1}}$. Over the last 40 years, critical casting thickness was increased by more than three orders of magnitude, and high quantity of amorphous components was formed, as shown in Figure 1-4. Inoue and co-workers [14] suggested three empirical rules for stabilising a supercooled metallic liquid. Firstly, the multi-component system should include three or more elements as the presence of several elements causes a significant extension of the supercooled liquid region before crystallisation. Secondly, there should be a considerable difference (greater than ~12%) in the atomic sizes of the main constituent elements. The atomic size differences result in a highly dense random packed structure in amorphous phases. Finally, the elements should have negative heats of mixing with each other; these increases the energy barrier at the solid-liquid interface and

accelerate atomic diffusivity. Hence, the supercooled liquid temperature is extended due to slowing local atomic rearrangements and a low crystal nucleation rate. A variety of BMGs such as Fe-based, Cu-based etc. were synthesized employing these rules.

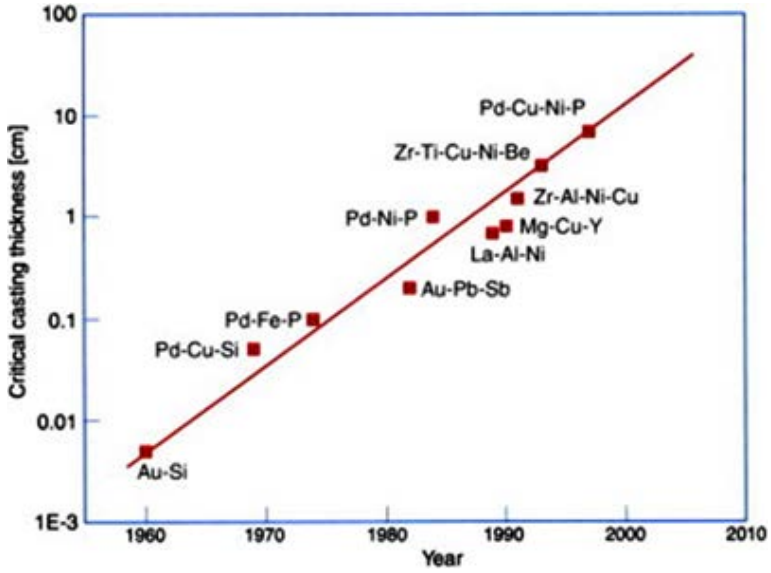

Figure 1-4 Increase in critical casting thickness for various glass-forming alloys over 50 years [15].

Elastic properties of metallic glasses can be derived from the properties of constituent metallic element and the other dependent on the particular glassy configuration prepared using a modified rule of mixture as suggested by Liu and Ma [16,17]; as the elastic properties of metallic glass cannot be predicted with the conventional rule of mixture in individual alloy systems. Widely various properties have been stated for metallic glasses of different alloy compositions, or the metallic glasses of the same composition but with different processing history. This approach originated from the motion of disordered atomic structures in metallic glasses and their intrinsic local heterogeneities. The internal structure of metallic glasses was initially reported as dense random packing of hard

spheres. Research over the years has found that while atomic packing is indeed dense, it cannot be random. Unlike the well-defined long-range order in crystalline metals, the atoms inside metallic glasses are in a range of distinctly local atomic configuration at the level of nearest neighbour coordination. In general, metallic glasses can be considered as having short- and medium- range orders in the matrix with excess of solvent atoms. Systems with short-range orders can be modelled as solute-centred clusters, while those medium-range orders are always characterized as interconnected clusters. Liu and co-workers [16] proposed that metallic glasses can be treated as hybrids composed of dual phases of clusters/superclusters and solvent matrix.

As shown in Figure 1-5, a stiff phase (S) represents the clusters/superclusters and (M) shows a solvent matrix with lower stiffness. In Figure 1-5(b), BMG is considered as a homogenous material, in which the local stress is distributed uniformly among different constitute atoms. As shown in Figure 1-5(d), the two phases are supposed to sustain equal stress under an applied elastic loading; however, their strain responses may differ. As a result, the global elastic moduli of metallic glasses (G) can be calculated according to the modified rule of mixture under iso-stress conditions [16]:

$$\frac{1}{G} = \frac{V_m^M f^M}{G^M V_m} + \frac{V_m^S f^S}{G^S V_m} \qquad 1\text{-}1$$

where V_m^M and V_m^S are the molar volumes of the matrix and clustres/superclusters, respectively, G^M and G^S are their elastic moduli and f^M and f^S are the fractions of the two phases, where they are considered to follow the relation $f^M + f^S = 1$.

Unlike the conventional rule of mixture, the hybrid model with dual phases provides a relation to validate the calculated value of the elastic modulus with its experimental value. The model helps to predict and design the elasticity of metallic glasses much more precisely based on their alloy compositions. In addition, this model is capable of describing the softening phenomena in BMGs, when the global modulus G decreases due to increasing base metal contents.

The Poisson`s ratio ($\upsilon$) of BMGs is closely related to some factors such as its toughness and glass-forming ability. The Poisson`s ratio (υ) inversely scales with the ratio of shear modulus to bulk modulus (B) correlating with the degree of plasticity or brittleness. Metallic glasses with a Poison`s ratio of higher than 0.31-0.32 shows high fracture toughness [18]. Yujie and co-worker [19] proposed a general relation between υ of BMGs and fracture energy for two types of Zr-based metallic, $Zr_{41}Ti_{14}Cu_{12.5}Ni_{10}Be_{22.5}$ (Vitreloy 1) and $(Cu_{50}Zr_{50})_{95}Al_5$. These metallic glasses showed significant toughness and less likely to develop into cracks due to the υ value was higher than a critical value of 0.31-0.32. Higher (υ) is an also result in more uniform plastic deformation without significant heating inside shear bands during operation. Hence, these effects extend before failure, which is similar to the effect of (υ) for polycrystalline metals. The measured toughness value was considered as an intrinsic property of metallic glasses; however, they could be affected by extrinsic factors, such as the presence of brittle oxide inclusions [20]. The choice of composition can significantly influence the pattern of shear banding and, consequently, mechanical properties of the metallic glasses. It is obvious that the shear-band spacing and shear offset are important factors in shear-band pattern and they were typically decreased with a higher

value of ν of BMGs. This prediction was verified in a limited number of experiments.

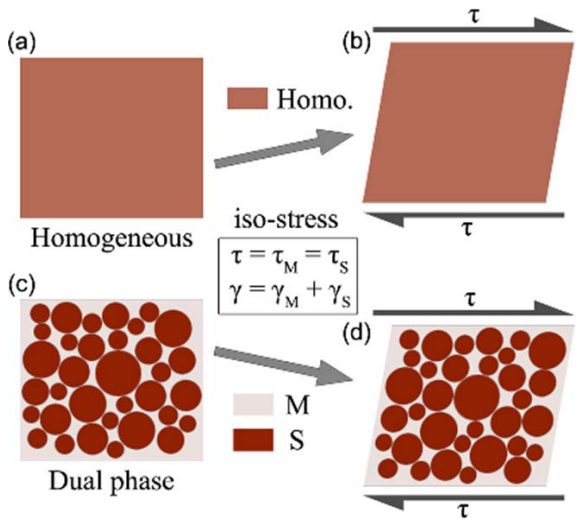

Figure 1-5 Schematics of ideally homogeneous BMG (a) and their strain responses to applied elastic shear stress $\boldsymbol{\tau}$ (b), and, dual- phases BMG (c) as well as their strain responses to applied elastic shear stress $\boldsymbol{\tau}$ (d). The compliant solvent matrix **M** and stiff clusters/superclusters **S** are supposed to sustain equal stress **s**, but display different strain $\boldsymbol{\gamma}$, which conforms to the iso-stress condition [16].

1.3 Application potential

The lack of room-temperature plasticity in BMGs noticeably restricts their industrial and structural applications, where reliability is essential. However, their unique properties attract a lot of attention and make them suitable for many potential applications, where specific functionalities are required and/or components are small. Metallic glasses demonstrate soft magnetic properties (i.e. high permeability and low coercivity). These magnetic properties of metallic glasses can be improved by inducing nanocrystallisation and adjustment of the grain size, which lead to the first large-scale application of Fe-based ribbons as

low-loss magnetic cores in transformers, magnetic readheads or as components in electronic article surveillance systems. BMGs have also found applications in sports equipment, such as golf club heads, baseball bats or parts of tennis rackets due to their unique impact properties compared to conventional metals [21]. BMGs are also capable of storing high densities of elastic energy, which led to utilisation of their efficient energy transfer characteristics this spheres for shot-peening purposes are ideal. A high elastic strain limit of BMGs resulted in their use for Coriolis mass flowmeters, pressure sensors and strain gauges with properties superior to conventional crystalline parts. Metallic glasses are also suitable for medical applications, such as implants and surgical instruments, due to biocompatibility and self-sharpening effect of BMGs. Generally good hardness and peculiar tribological properties of metallic glasses make them attractive as coating materials. And, indeed, there have been efforts to fabricate amorphous coatings, for example by low-temperature spraying or radio-frequency magnetron sputtering.

As mentioned previously, micro-materials have created an increasing demand for miniature parts. Semiconductor fabrication technologies are limited to silicon and related materials, which are not mechanically suitable for many requested applications. Lithography, electroplating and moulding techniques have been used to manufacture precision metal microparts [22], but complexity and resulting costs of these technologies limit their commercial viability. In addition, they are strong, highly elastic and exhibit enhanced plasticity at small scales. They can also be fabricated thermoplastically, similar to plastics at low temperature. Recently, BMG processing methods have been developed to create precise and various geometries on different length scales, which helps to

fabricate complex BMG microstructures in an accurate manner with materials showing unique properties [23]. Figure 1-6 compares the surface finishing of metallic glasses and steel moulds used in microinjection moulding (µIM) for mass production of polymer containing micro- and nano-features with a size of 100 nm. The smooth surface finish on the metallic glass can be clearly seen due to its lack of crystalline structures.

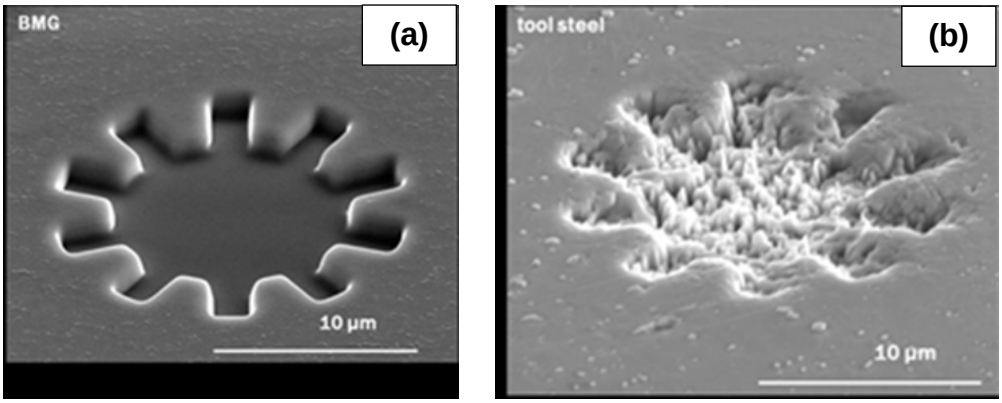

Figure 1-6 Comparison between surface finishing of metallic glasses (a) and steel moulds (b) [24].

More critical than limited plasticity at room temperature, which to some extent hampers their structural application, the production costs of BMGs are generally much higher than those of conventional crystalline alloys. This is due to their fabrication method often involving high-purity elements and expensive vacuum-processing techniques. Thus, the most prominent future applications of BMGs might be microcomponents made in large quantities with very specific functionality.

1.4 Aim and objectives

The aim of this research is to undertake extensive experimental studies of a Zr-Cu-based metallic glass to obtain understanding of its elastic and inelastic deformation behaviour under various loading conditions from a macroscale to a nanoscale. As localised shear-band formation is responsible for an inelastic deformation mode, this study focused on characterisation of shear bands as well as their initiation, formation and evolution.

Objectives:

In order to achieve the aim of this study, several objectives were identified:

- Effect of size and structural states on deformation characteristics of the BMG under imposed homogeneous loading states using microcompression techniques.
- Characterising surface shear-band localisation surface of the BMG using nano/micro indentation and Field Emission Gun Scanning Electron Microscopy (FEG/SEM).
- A study of deformation characteristics of the BMG under imposed inhomogeneous loading states using an experimental technique named *wedge- indentation* to investigate deformation behaviour in the material`s volume including initiation, formation and evolution of shear bands.
- Characterisation of shear bands in the BMG using combination of experimental techniques including nano-indentation and characterisation techniques including X-ray Diffraction (XRD), FIB/SEM and Transmission

electron microscopy (TEM) to investigate initiation, formation and evolution of shear bands.

1.5 Research methodology

A schematic of the overall layout of this thesis including its research methodology is given in Figure 1-7. The thesis covers seven main areas: introduction, literature review, experimentations, conclusions and future work. Apart from sections dedicated to introduction, conclusions and future work, each area is presented in more than one chapter. With above mentioned aims and objectives, the experimental programme is comprised of two main parts: an analysis of deformation behaviour of BMGs and shear-band characterisation. To explore the deformation behaviour, several experiments were carried out to characterise various behaviours of BMGs at different length scales (nano, micro and macro) and various loading conditions (homogeneous and inhomogeneous loading states. Therefore, the experimentation section is divided into parts dealing with nano, micro- and macro-scale experiments. In the part covering the macro-scale level, three-point bending and dynamic mechanical analysis (DMA) were performed to determine mechanical properties at room and elevated temperatures. Next, indentation tests including those at both nano- and micro-scales were conducted to characterise the resulting elastic-plastic deformation under imposed inhomogeneous loading conditions. Loading-unloading tests were conducted in the nano-indentation experiments, with an incrementally increased load to study indentation size effect (ISE) in the Zr-Cu-based metallic glass. Scanning Electron Microscopy (SEM) was used to assess shear-band

evolution in the BMG material with the aim of observing shear steps on the material surface.

In nano- and micro-indentation experiments, by their very nature, shear bands in the BMG can be observed only after they intersected a free surface of the sample. Hence, wedge-indentation test was developed and designed in-house to overcome limitations of nano-indentation to observe the evolution of shear bands of BMGs beneath the indenter, also allowing for simplified analytical and numerical modelling schemes. The primary motivation of wedge indentation studies was to characterise the initiation of shear bands in the materials and correlate this to the initiation of plastic deformation in indentation. The wedge-indentation technique was also used to study evolution of various sets of shear bands at the volume of the studied materials. Additionally, this thesis summarises an investigation on different techniques to prepare micropillars of the BMG and the results of microcompression tests on as-cast and deformed regions of the specimen to evaluate their deformation behaviour. The possibility of size-dependent strength in micro-pillars of BMG was investigated under imposed homogeneous loading states.

Shear-banding is one of the primary mechanisms of plastic deformation in BMGs. Hence, in order to investigate the nature of plastic deformation in the studied BMG, shear bands were directly characterised using various experimental techniques including surface decoration, microstructural analysis (SEM, EDS, TEM) and nano-indentation. The surface-decoration method was employed to track formation and propagation of multiple shear bands in wedge-indentation experiments. The nano-indentation technique was carried out on fracture

surfaces and individual shear bands to study a dilatation mechanism and properties of shear bands, respectively. In the latter, quantitative strain analysis of plastic deformation of the BMG under wedge indentation was implemented using a digital image correlation (DIC) technique and the obtained results were compared with finite-element simulations.

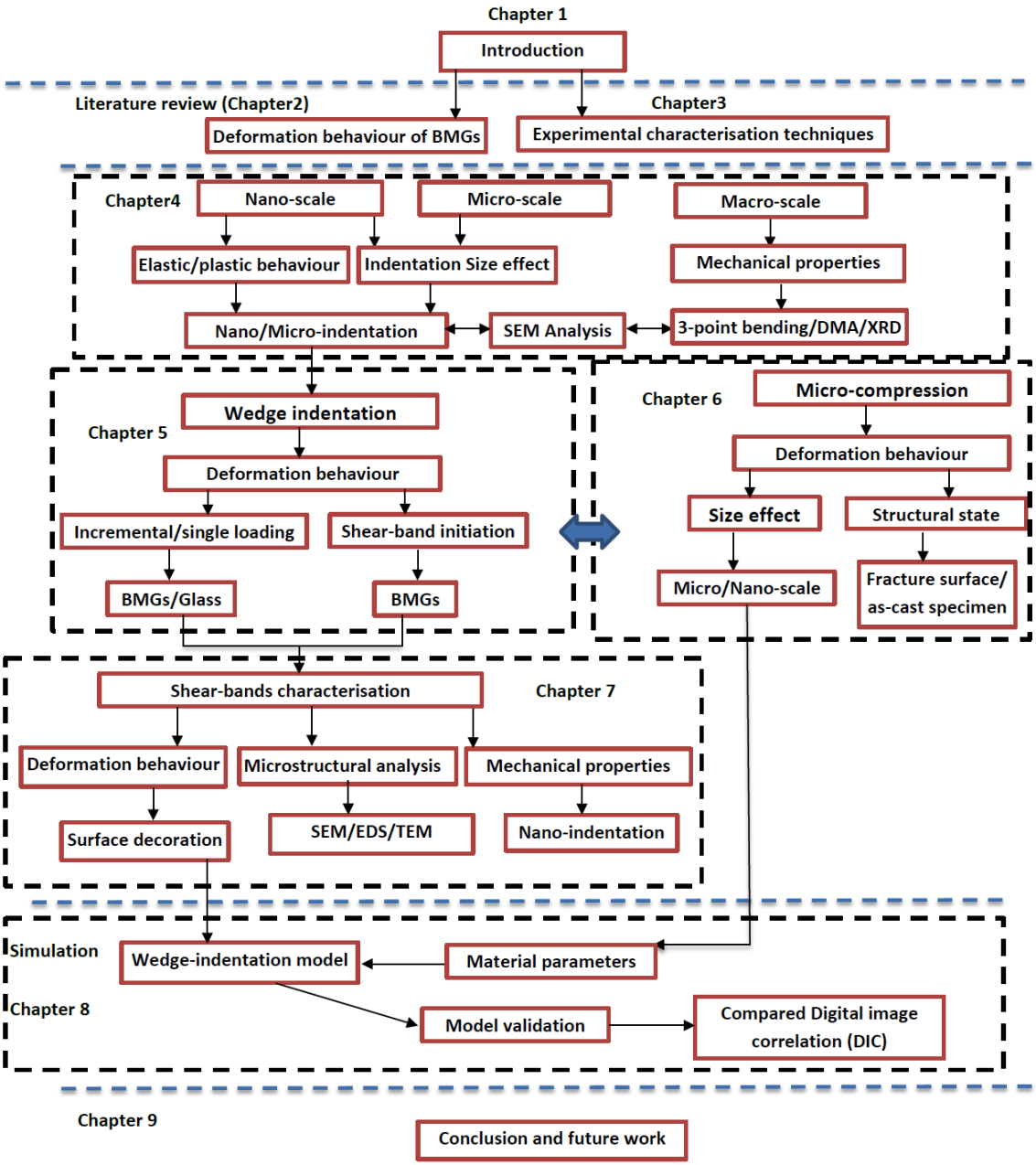

Figure 1-7 Overall thesis layout and research methodology.

1.6 Thesis structure

The thesis is divided into 9 chapters; a brief description of the remaining chapters of this thesis is given below:

- **Chapter 2 Deformation behaviour of BMGs**

A review of the main deformation mechanisms of metallic glasses is provided, highlighting theories proposed for inhomogeneous plastic flow and explaining an effect of temperature and strain rate on plastic flow. This is followed by discussion of a length-scale dependency of mechanical behaviour of BMGs under various loading conditions. Additionally, characterisation of shear bands and indentation techniques for evaluating mechanical properties and plastic deformation of metallic glasses is summarized in this chapter. Finally, current understanding of the constitutive models of deformation is presented together with modelling challenges.

- **Chapter 3 Experimental characterisation techniques**

Experimental and characterisation techniques employed in this work are explained in this chapter including X-ray diffraction (XRD), electron microscopy, focussed ion beam (FIB), dynamic mechanical analysis (DMA), Laser interferometry and nano-indentation. The calibrations required for nano-indentation are presented in this chapter.

- **Chapter 4 Basic characterisation of BMG**

Macroscale characterisation is presented in order to determine the Young's modulus used in the modelling part. In addition, nano- and micro-indentation

tests conducted on the Zr-Cu-based metallic glass to study plastic deformation, shear-band evolution, hardening or softening phenomenon and an indentation size effect (ISE) are discussed in this chapter.

- **Chapter 5 Experiments under imposed inhomogeneous loading: Wedge indentation**

A robust experimental technique named *wedge indentation* is developed for characterisation of deformation behaviour through evolution of localised shear bands in the volume of materials. This technique is used to implement single and incremental loading conditions to investigate systematically initiation, formation and evolution of shear bands. In addition, application of 2D full-field optical displacement measurements for quantitative validation of finite-element (FE) simulations in the BMG. The DIC method is used to study local plastic deformation in the Zr-Cu-based metallic glass under conditions of wedge indentation and compared with 2D FE simulation results.

- **Chapter 6 Uniaxial compression experiments**

This chapter summarises an investigation of different techniques used to prepare micropillars of the Zr-Cu-based metallic glass. The possibility of size dependent strength in the BMG was investigated on micro-pillars. Micro-compression tests were also conducted on as–cast and deformed specimens to understand directly the effect of multiple shear bands on elastic-plastic deformation of the BMG.

- **Chapter 7 Characterisation of shear bands**

A surface-decoration technique was adapted to investigate formation and evolution of shear bands in wedge indentation experiments at sub-micron length

scales. Shear bands were microstructurally characterised using XRD and TEM. Mechanical properties of individual shear bands in the Zr-Cu-based metallic glass were investigated using an indentation technique in order to obtain a better understanding of the effect of non-crystalline defects on shear-band plasticity.

- **Chapter 8 Conclusions and future work**

The outcomes and conclusions drawn from this research are presented in this chapter. Suggestions and recommendations for the possible future research are also introduced.

2 Deformation behaviour of BMGs

2.1 Microscopic Process relevant to deformation behaviour of metallic glass

As mentioned above, the lack of long-range order in metallic glasses makes their plastic deformation fundamentally different from that of crystalline solids, where deformation can generally be explained based on the underlying dislocation dynamics. While at low temperatures crystal dislocations allow changes in the atomic structure at low level of energy and stress, atomic rearrangements in amorphous metals are a relatively high-energy/stress process. A number of mechanistic theories have been proposed to describe the plastic flow and deformation behaviour of metallic glasses.

Some early approached employed dislocation theory to describe plastic deformation [25]. In them, shear was as result of a glide of a discrete microscopic dislocation line with local differences in the magnitude and direction of a Burgers vector. Resistance to glide originates from a work of dilatation normal to the glide plane. The energy required for dilatation and, consequently, allowing motion of the dislocation should exceed a barrier determined using similar thermally-activated equations derived as in STZs and the free-volume theory. It should be considered that the dislocation theory cannot be used to determine mechanical properties of metallic glasses in the manner common to crystalline solids. While hardness of crystalline materials increases as the result of an increase in the defect density, metallic glasses does not show any strain hardening, even at high shear band densities because of the increasing free-volume content or entropy. This shows that the dislocation model is not

appropriate to describe plastic deformation in metallic glasses. Plastic deformation in MGs was also described using idea of free volume and shear transformation zone (STZ) proposed in the Argon and Spaepen`s model, which were based on the atomic motion [26,27] .

2.1.1 Free volume

A free volume is referred to the atomic volume in excess of the ideal densely packed, but still disordered, structure. The initial free volume in a glass is fixed at the glass transition temperature, when the atomic configuration is frozen as the liquid solidifies. The free volume in glassy materials was first proposed by Cohen and Turnbull [28], developed later by Spaepen [27] to be used for BMGs. As mentioned previously, metallic glasses are produced by rapidly quenching of a metallic melt at certain rates to prevent crystallisation. The total volume of such a metallic glass liquid is divided into two parts: atoms of various sizes and so called “holes”, or “voids”. The “free volume” concept is related to “holes” or “voids”, which is the key to a diffusive arrangement of atoms. The possibility for an atom to jump into an adjacent hole (free volume) depends on the atom and the hole sizes. Free volume is considered to be pressure dependent in BMGs and the following equations can be used to describe an average free volume per atom subjected to hydrostatic pressure [27]:

$$v_f = \alpha v_m (T - T_0) - \beta v_p \Delta P \qquad 2\text{-}1$$

where T_0 is temperature at which the free volume disappears; α is the coefficient of thermal expansion at zero pressure; v_m is the mean atomic volume at zero pressure, β is the mean compressibility, which is a function of the Poisson`s ratio

and atomic volume [27]. v_p is the mean atomic volume for the pressure increment ΔP .

The free volume may be related to one atom, which can jump from one site to another with a coincident collapse of the original cage of the neighbouring atoms. Secondly, free volume may be related to more than one atom, and the motion of the atoms together will lead to shear flow [29]. In bulk metallic glasses such as Vitreloy 1, the shear flow can be associated with the motion of more than one atom. In addition, the free volume can be varied by external shear stress. Shear localisation and shear failure plays a key role in general deformation of metallic glasses. The concept of free volume was applied to model a non-linear thermo-mechanical behaviour of other amorphous solids such as polymers [30]. Spaepen developed a free-volume model for the metallic glasses based on the free volume theory proposed by Cohen and Turnbull [28]. According to Cohen and Turnbull, the probability p of the existence of an atom with a free volume between v and $v + dv$ is:

$$\mathrm{p}(\upsilon)\mathrm{d}\upsilon = \frac{\eta}{\upsilon_\mathrm{f}} \exp\left(-\frac{\eta\upsilon^*}{\upsilon_\mathrm{f}}\right)\mathrm{d}\upsilon \qquad 2\text{-}2$$

where η is the geometrical factor between 1 and 0.5, v_f is the average free volume per atom and v^* is the critical volume. The shear flow rate is the result of a competition between the thermal activation barrier and the shear stress driven potential [27] :

$$\dot{\gamma} = 2\Delta f J \exp\left(-\frac{\lambda v^*}{v_f}\right) \sinh\left(\frac{\tau\Omega}{2kT}\right) \exp\left(\frac{\Delta G^m}{kT}\right), \qquad 2\text{-}3$$

Where Δf is the fraction of sample volume, Ω is the atomic volume, k is the Boltzmann constant, T is the temperature, ΔG^m is the activation energy, J is the Debye frequency (frequency of atomic vibration), and τ is the applied shear stress. Thus, steady-state deformation in metallic glasses is a competition between the creation of free volume by external shear stress that squeeze an atom into avoid smaller than itself, and its annihilation by diffusion jumps of atoms towards its metastable equilibrium as shown schematically in Figure 2-1. The excess free volume is made when an atom with effective hard sphere volume v^* is squeezed into a neighbouring hole with a smaller volume v by applied stress τ. The applied stress provides enough energy to overcome the energy barrier ΔG^m for the motion. This lead to shear softening because of dilatation and decrease viscosity in the shear band as shear-band can sustain a large amount of shear induced excess free volume.

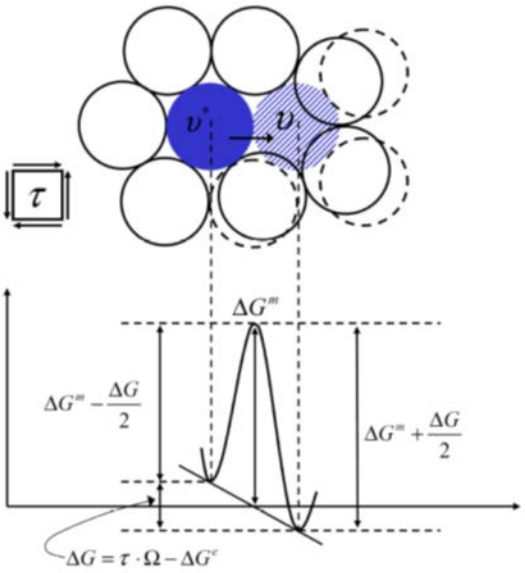

Figure 2-1 Schematic of the free volume flow stress [27].The application of a shear stress τ biases the energy barrier by an amount $\Delta G=\tau\Omega-\Delta G^m$, where Ω is the atomic volume and ΔG^m is the energy required to fit an atom with volume u^* in a smaller hole of volume u.

This free-volume model demonstrates a simple and clear description for the strain softening and, hence, heterogeneous deformation of metallic glasses at low temperatures, and has been broadly used to describe qualitatively different mechanical properties. However, this model did not make clear the motion and rearrangement of constitute atoms within shear-bands during plastic flow as a single atomic jump is not able to accommodate shear strain. Furthermore, the deformation mechanism of metallic glasses characterized with computer simulations, creep tests and nano-indentation measurements include multiple atoms rather than a single-atom motion [31-33].

2.1.2 Shear transformation zone

Argon and co-workers [26] proposed a model to describe the plastic deformation of metallic glasses employing flow units that were much larger than an atomic size flow units, which is related to atomistic simulations and sheared bubble raft experiments. As shown in Figure 2-2, according to this model shear transformation takes place by reorganization of a local cluster of randomly closed-packed atoms referred to as “shear transformation zones” (STZs), which are thermally activated around high free volume regions under inelastic transition [34-36]. Similar to the Spaepen’s model, local shear transformations can result in local dilatation and, hence, strain softening.

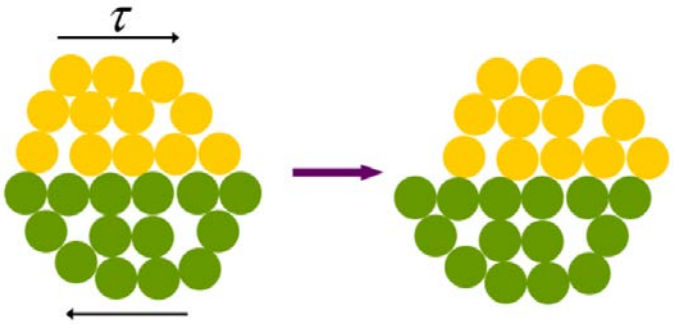

Figure 2-2 : Schematic of deformation mechanism of STZ [26]

With shear stress τ, the strain rate obtained from a superposition of many individual STZ operations is then given as:

$$\dot{\gamma} = \alpha_0 \nu_0 \gamma_0 . \exp\left(-\frac{\Delta F_0}{kT}\right) \sinh\left(\frac{\tau \gamma_0 \Omega_0}{kT}\right), \qquad 2\text{-}4$$

where α_0 is the constant incorporating the fraction of material being able to undergo shear transformation, υ_0 is the natural frequency (attempt rate) of the STZs, Ω_0 and γ_0 are the volume and shear strains of an individual STZ and ΔF_0 is the (Helmholtz) free energy for STZ activation and is considered as:

$$\Delta F_0 = \left[\frac{7-5\nu}{30(1-\nu)} + \frac{2(1+\nu)}{9(1-\nu)}\beta^2 + \frac{1}{2\gamma_0}\frac{\tau_0}{\mu(T)}\right]\mu(T)\gamma_0^2\Omega_0, \qquad 2\text{-}5$$

where $\mu(T)$ and ν are the temperature-dependent shear modulus and Poisson`s ratio of the glass, respectively, and τ_0 is the ideal shear strength of the STZ, i.e., the thermal stress needed to activate the shear transformation. Parameter β is the numerical constant that explains the volumetric dilatation of the STZ related to its shear distortion, and is about unity for an amorphous metal. γ_0 is usually taken to be of order of ~ 0.1. Ω_0 is generally believed to encompass between

around ~ 100 atoms based on simulations and a variety of indirect experiments measurements [8,26]. This suggests that STZs can be considered as a deformation unit in MGs and the size and energy of them may vary for each type of glass with various compositions. There is a difference between the free volume and STZs models, though they share many common features. Firstly, both mechanisms demonstrate characteristics of forward jumps or STZ operations compete with backward one. Secondly, they are associated with mechanical dilation, and, finally both mechanisms are thermally activated, and exhibit similar energy scales.

2.1.3 Deformation map

At macro level, the deformation mechanism of metallic glasses based on the free volume and STZs theory can occur homogenously or inhomogenously depending on the values of strain rate, temperature and applied stress. Thus, the deformation map of metallic glasses was developed based on that for crystalline materials proposed by Ashby and Frost [37]. Such maps were used to explain different modes and mechanisms of plastic deformation of the crystalline materials as a function of shear stress, temperature and structure. The steady-state constitutive flow law explains each deformation using equation of the type

$$\dot{\gamma} = f(\tau, T, \text{structure}), \qquad 2\text{-}6$$

where $\dot{\gamma}$ is the strain rate and “structure” presents all the relevant structural parameters of the material. The steady-state condition indicates that the external parameters such as stress and temperature are used to determine the structural parameters, which are constant during the course of the flow. Spaepen [31]

suggested a deformation map showing a transition from a homogeneous behaviour to an inhomogeneous as a function of temperature and strain rate (see Figure 2-3). Based on this deformation map, homogeneous deformation happens at low stresses, which a strong function of strain rate, and high temperatures, as indicated by the strain rate contours. Moreover, inhomogeneous deformation takes place at high stress levels and low temperatures and it is insensitive to the strain rate. This deformation map can be used for melt-spun metallic glass ribbons as MGs show wide range supercooled liquid regions.

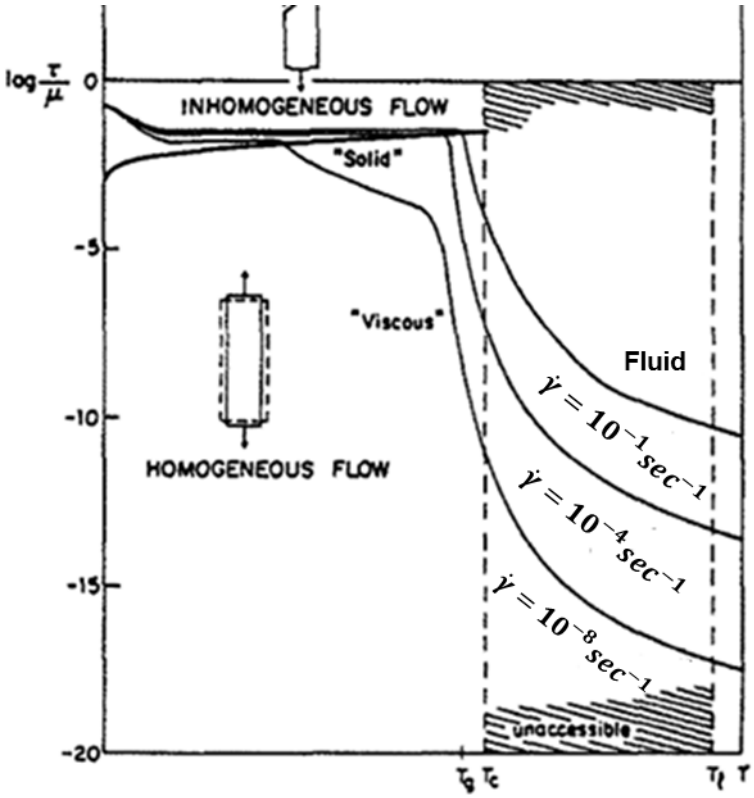

Figure 2-3 Schematic deformation map for metallic glass with various deformation modes [31].

Schuh and co-workers [38] modified the deformation-mechanism map to incorporate other observations. They indicated deformation modes with two complementary deformation maps using the concept of STZ. Figure 2-4 (a) represents normalised stress as a function of temperature similar to that proposed by Spaepen [31]. Figure 2-4 (b) is in a coordinates of shear strain rate and temperature and follows the analysis suggested by Megusar *et al.* [39]. The most important aspect is that the deformation map presents a boundary, at which a transition occurs from the homogeneous mode at high temperature and low stresses and strain rates to the inhomogeneous mode of deformation at low temperature and higher levels of stress and strain rate. As shown in Figure 2-4, Schuh and co-workers modified the deformation map with inclusion of strain rate contours instead of putting a single dividing line to show this transition. In the map, the homogeneous regime is divided into “elastic”, “Newtonian”, and “non-Newtonian” sub regions. The transition from Newtonian to non-Newtonian occurs at $10^{-5}s^{-1}$; the non-Newtonian flow is observed at strain rates below this value. However, it is important to mention that at high enough shear rates, the non-Newtonian flow as well as shear localisation can happen at high temperatures even in the supercooled region. The pressure dependence is also shown in Figure 2-4(a) as iso-pressure contours for a single value of shear stress. The pressure effect on inhomogeneous behaviour can be more clearly observed in Figure 2-4(b) with iso-pressure contours for various applied shear stresses. This figure presents the effect of shear strain rate on shear banding and serrated flow patterns as the high strain rate and lower temperature result in shear bands of smaller offset that are more finely spaced. The deformation map developed by Schuh *et al.* [38] does not consider the evolution of glass structure during the

deformation and cannot be used to explain the fracture behaviour. However, this map can be employed to compare the mechanical response of different metallic glasses at the same absolute temperature (e.g. room temperature) but at different homologous temperatures.

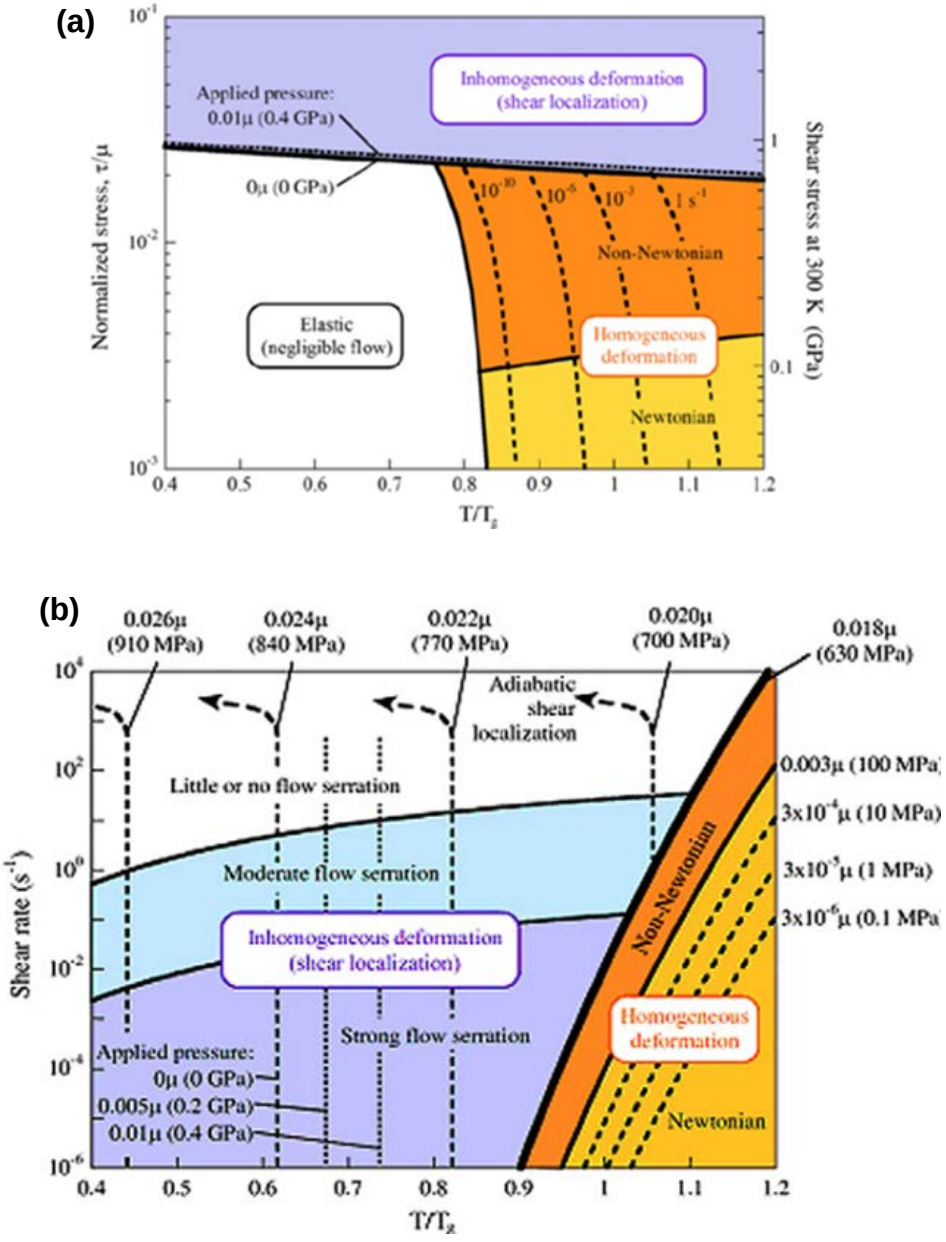

Figure 2-4 Map showing deformation mode as function of strain rate and temperature (a) normalized stress versus normalized temperature (b) strain rate versus normalized temperature plane[38].

2.2 Indentation studies of metallic glasses

During 1970s and 1980s, it was difficult to measure the mechanical properties of metallic glasses due to limitation of small specimen sizes produced. Thus, standard microhardness measurement was a common technique to assess mechanical strength of thin ribbons of metallic glass. In recent years, depth-sensing indentation experiments have been used to characterise mechanical properties across various length scales. Nanoindentation experiments play a major role in analysis and elucidation of the mechanisms of plastic flow in metallic glasses as this technique can be used to gain insight into the nuances of deformation their behaviour. The underlying reason for ubiquitous use of the indentation technique is its relative experimental simplicity. Experiments can be performed several times on a single specimen including the possibility to probe different volumes of materials via an appropriate choice of load and tip geometry [40].

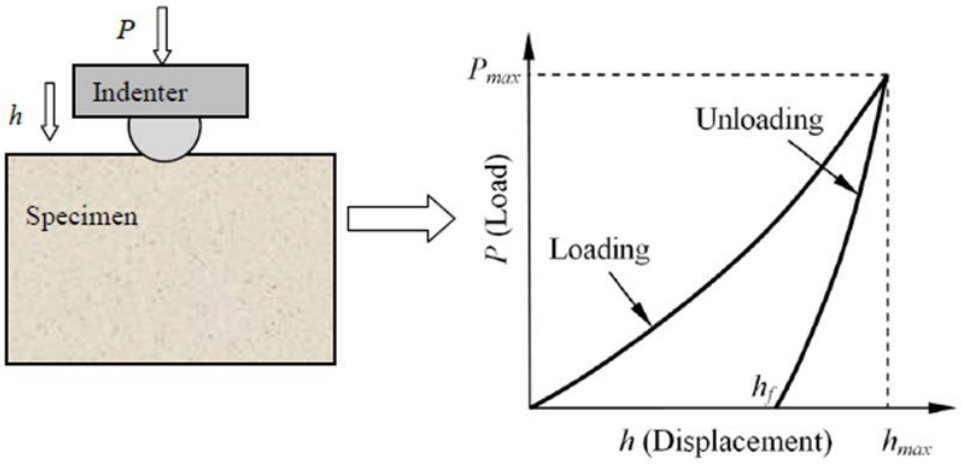

Figure 2-5 Schematic of indentation of bulk materials [41].

In indentation experiments, an applied load and a penetration depth into the studied material are simultaneously recorded, and a load-penetration depth curve is produced (see Figure 2-5). This curve contains a wealth of information related to the deformation behaviour of materials and can be used to determine mechanical properties such as hardness and elastic modulus [42]. Indenters are classified based on their shape and geometry. These are conical, spherical, Berkovich (consisting of 3 planer sides), Cube corner indenter (consisting of 3 planer sides with mutually perpendicular faces arranged in a geometry like the corner of a cube) and Vickers indenter (consisting of four planer sides). Figure 2-6 shows these different types of indenter used in experiments and analyses. Spherical indenters (Figure 2-6 (a)), have been widely used for brittle materials where a small deformation is preferable. In spherical indentation, the contact stresses are initially small and produce only elastic deformation; later, a transition from elastic to plastic deformation occurs, allowing assessment of yielding and work-hardening of the indented material. Sharp indenters such as Vickers and Berkovich are preferred for indentation at nano-scale, as minimising the effect of friction. In contrast to them, cube-corner indenters have relatively small face angles, useful in producing small, well-defined cracks around imprints in brittle materials. These cracks can be used to estimate fracture toughness at a very small scale. For the cube-corner indenters, the projected area of contact is the same as that for the Berkovich indenter.

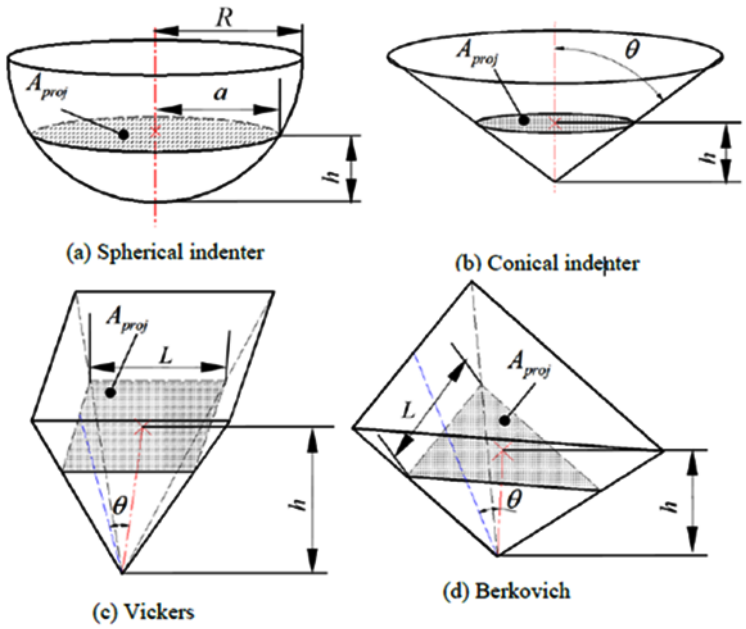

Figure 2-6 Geometries of indenters used in instrumented indentation [43].

Due to their specific mechanical behaviour, the initiation of localised plastic deformation in MGs is captured in nanoindentation be analysis of pop-in events. The pop-in behaviour depends on the type of metallic glass and its free-volume content as well as the specifics of experimental procedures such as the indenter's tip shape and applied loading rates. Generally, the size of pop-ins increases with the depth of indentation based on the strain accommodated by the indenter [33,44]. For instance, the cube-corner indenter produces larger pop-in events than the Berkovich tip thanks to its lower included angle and higher generated stress [45].

As shown in Figure 2-7, the pop-in behaviour differs with composition of MGs. For instance, Pd-based glasses show sharp and well defined pop-ins, whereas Zr-based metallic glasses demonstrate ripples rather than displacement bursts. This variation from glass to glass is expected because of their varied chemical nature and different states of short- or medium-range ordering. A large number

of studies showed that the pop-in behaviour was changed in MG with the same composition when varying the deformation rate [38,44]. As illustrated in Figure 2-7(b), low indentation rates show more displacement burst compared to high indentation rates, due to the activation of single shear as a result of plastic deformation [46] .

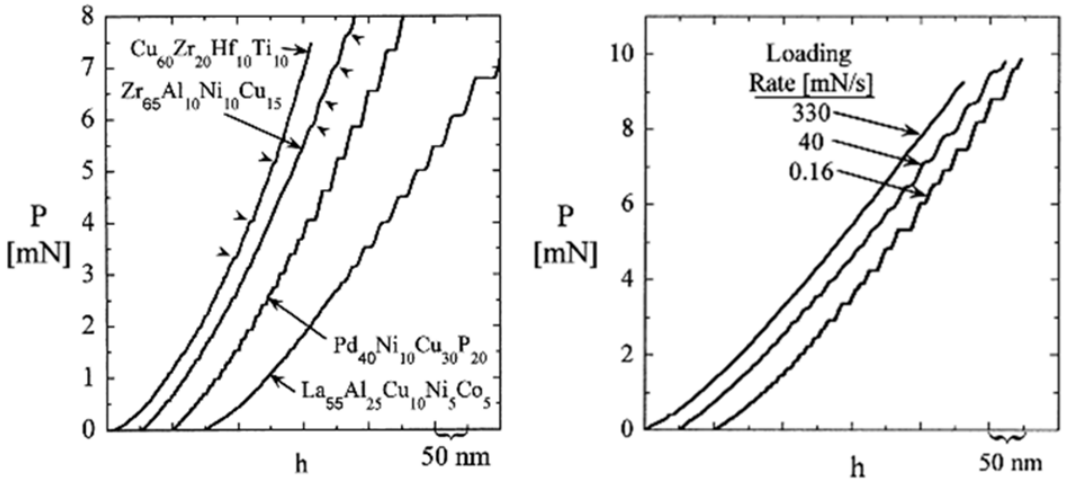

(a) (b)

Figure 2-7 (a) Example of indentation P-h curves for different MGs, showing discrete pop-ins, or flow serration. (b) Example of rate-dependence of serrated flow beneath nanoindenter in Pd-based metallic glass [46]**.**

In other studies, an intrinsic change in plasticity of MGs was reported at high homologous temperatures (T/T_g), as the degree of flow serration was significantly reduced. Furthermore, there was an evidence of creep during unloading or constant-load hold with an increasing penetration depth when metallic glasses were indented at high homologous temperatures [47,48].

More recently, a flattened indenter's tip was used to perform micro-compression tests on micro-pillars patterned with Focused Ion Beam (FIB). Micro-compression of metallic glasses helps to run uniaxial testing with high resolution without

imposing strain gradients to study the effect of individual shear banding [49-51]. Still, a size-dependent behaviour was reported by many researchers in micro-compression studies in MG micropillars with a reported correlation between a size and mechanical properties such as maximum plastic strain before failure and yield. The length scale dependent behaviour will discussed in details in section 2.3.

2.2.1 Pile-up and sink-in

Two main modes of deformations are observed in indentation. The loaded material is displaced with compression along the radial direction, imparting further displacement perpendicular to the indent surface. These combined movements force the material around the indenter either to pile up (upwards) or sink-in (downwards) [52]. Both phenomena are schematically illustrated in Figure 2-8. The extent of these changes depends on the E/σ_Y and strain–hardening properties of the materials [53]. Alcala *et al*. [54] investigated the piling-up and sinking-in using Vickers and spherical indentation tests. The study demonstrated that sinking-in predominated in materials with a strain-hardening modulus larger than 0.2. Circular patterns around the indent representing layers of overlapped displaced materials are not considered as cracks. The non-strain hardening features of metallic glasses were further proved by an upward flow of the material (i.e. pile up) along the indenter's face. Metallic glasses seem to deform in an elastic-perfectly plastic manner (Figure 2-9).

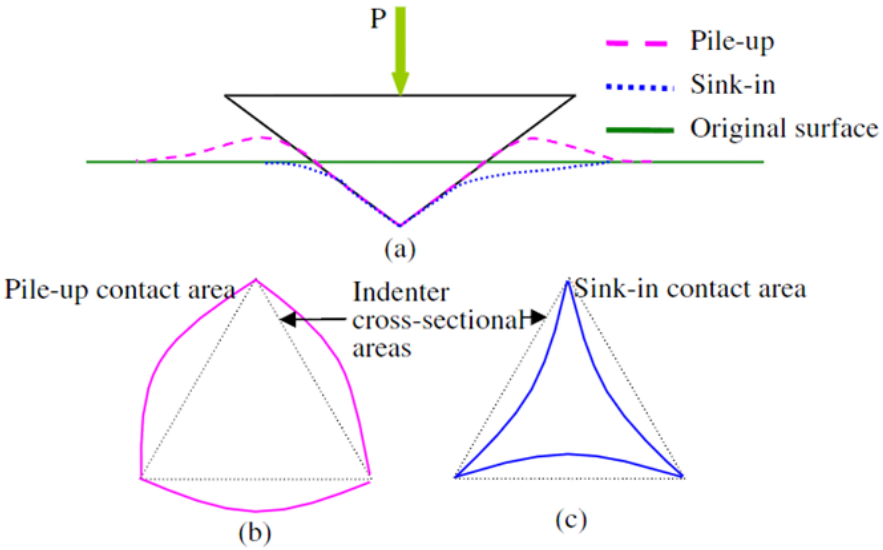

Figure 2-8 Schematic of pile-up and sink-in effects in indentation(a), pile-up contact area (b) and sink-in contact area (c) [54].

The piling-up and sinking-in phenomena are of interest, since they affect the accurate determination of contact areas and, thus, the assessment of hardness and the elastic modulus. For instance, sink-in patterns reduce the contact area, while pile-up patterns increase it, and neglecting them can result in significant errors, when extracting properties from the experimental data. Fischer-Cripps [43] argued that the errors could be as high as 60%. An Oliver and Pharr approach takes into account the sink-in effect but not the pile-up effect; thus, Martin and Troyon [55] pointed out that it can grossly underestimate the true contact area. To determine the actual contact area, different techniques have been suggested. Atomic force microscopy (AFM) was recently employed to determine the actual contact area for Berkovich indenter tips, assuming simplified pile-up geometry. However, this procedure considered a residual imprint, i.e. an accurate continuous measurement of the elastic recovery was not possible. To overcome this limitation, numerical techniques such as a finite-

element (FE) method can provide a helpful alternative in development of accurate models for indented materials.

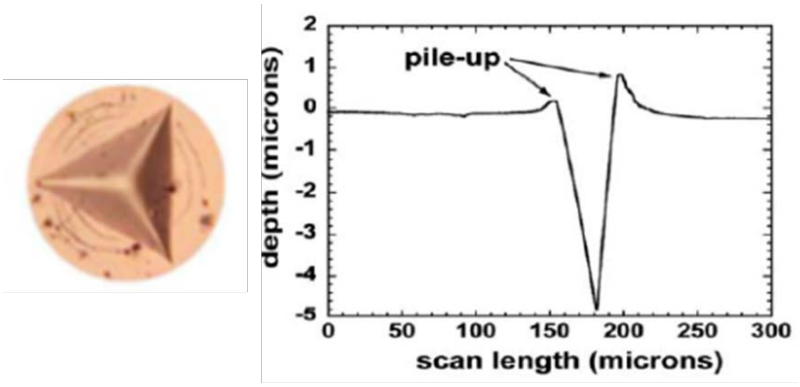

Figure 2-9 (a) Pile-up around indenter in MG. (b) Pile-up profile around indenter [54]**.**

So, in indentation tests on metallic glasses, the pile-up height should be measured, and added to the measured indentation depth to calculate a representative contact area using the standard Oliver-Pharr scheme. This method is usually employed to measure hardness and to characterise the indentation size effect (ISE). Another important factor is the effect of residual stress on morphology of pile-up in indentation as reported in the literature for different types of materials, using both experiments and finite element modelling [56,57]. The results showed that the amount of free volume in the materials and the stress state beneath the indenter change the pile-up morphology and formation: a large amount of free volume can induce stable and homogeneous flow in nanoindentation at low temperature [58]. As shown in Figure 2-10, there is a confined plastic zone due to compressive stress, leading to extensive pile-up formation. In a tensile state, there was no indication of pile-up formation. It was

observed in tests that activation of shear bands on the shear plane underneath the indenter was increased under tension and decreased under compression.

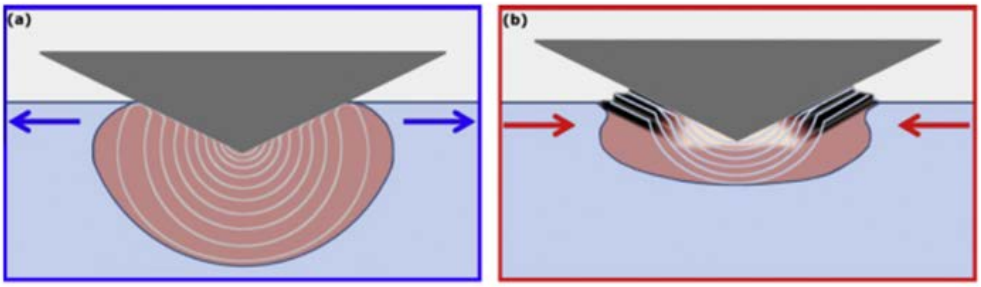

Figure 2-10 Effect of tensile (a) and compressive (b) residual stress on plastic-zone size, pile-up behaviour and shear-band activity [58].

2.2.2 Indentation size effect (ISE)

Homogeneous and isotropic materials are expected to possess unique values of hardness and modulus. However, experimental results show a variation in hardness and modulus with indentation depth. It is now well known that size plays a significant role in the overall mechanical response of material. The apparent variation in the perceived material properties such as hardness and elastic modulus with the depth of indentation h and indenter radius R is known as indentation size effect (ISE) [59].

A number of studies argued that ISE depended on the level of strain and the magnitude of strain gradient in the loaded material. The characteristic features of plastic deformation in conventional metals are formation, motion and storage of dislocations. The level of indentation hardness of such materials is observed to increase with a decrease in the indentation depth owing to the nucleation of dislocations in the plastic zone. In conventional metals, the most popular strain-

gradient-based ISE mechanism was proposed by Nix and Gao [60], who assumed a density of dislocation together with a Taylor`s dislocation strengthening model employing a concept of geometrically necessary dislocations (GNDs). The depth dependence on hardness can be obtained from this model in the following form:

$$\frac{H}{H_0} = \sqrt{1 + \frac{h^*}{h}}\,, \qquad 2.7$$

where H is the hardness for the given indentation depth h, H_0 is the hardness in the limit of the infinite depth and h^* is the characteristic length depending on the indenter's shape, shear modulus and H_0. Experimental results for cold-worked polycrystalline copper and single-crystal silver showed that ISE is more pronounced in metals with a low value of intrinsic hardness. Hence, little and significant ISEs are expected for soft and hard crystalline materials, respectively. Since the Nix-Gao model is based on dislocation strengthening, it is expected that ISE does not occur in materials with a non-crystalline (amorphous) structure because of the absence of dislocations and strain hardening. However, some researchers reported ISE-like behaviours in Zr-Cu, Pd- and Fe-based metallic glasses [61,62]. There are different hypothesises described ISE mechanisms in MGs. Firstly, Lam and Chong [63] and, more recently, Yang [33] used the Nix-Gao model to describe ISE in MGs based on the strain-gradient plasticity. The concept of non-crystalline flow defects including shear clusters or excess free volume were used instead of dislocations. An increase in these defects at low indentation depths is mainly responsible for ISE in MGs, as the increase in dislocations is in metals in the Nix-Gao model. Hence, it is claimed that plasticity

in metallic glasses is induced by a strain gradient, which should be accommodated by these defects. However, this model has drawbacks as an increase in a free volume would lead to softening rather than hardening in MGs [64,65] that the model cannot characterise.

Secondly, ISE can be explained based on a strain-softening behaviour [1] and dependency of hardness on in indentation-imposed strain as proposed by Van Steenberge *et al*. [62]. Vincent *et al*. [66] conducted micro-hardness tests on Zr-Cu based metallic glass at four different loads of 1, 2, 3 and 5 N and nano-indentation experiments with a maximum load 80 mN. The hardness values from nanoindentation were higher than those reported from micro-indentation. In addition, a decrease in hardness with increase in the load level was observed. This phenomenon can be described based on [59], where metallic glasses showed strain softening in plastic deformation rather than strain hardening due to shear localisation. In shallow indentations, a plastic zone is quite small to have sufficient STZs and, hence, shear bands operate at limited locations resulting in an increase in hardness. For large penetration depths, a continuous process of accumulation of excess free volume during deformation can induce strain softening, and this softening is the source of ISE. Hence, a relationship between hardness and a strain rate based on the classical metallic flow equations developed by Spaepon [31] and Argon [26] was introduced:

$$H(\approx 3\sqrt{3}\,\tau) \propto \sinh^{-1}\left(\alpha\dot{\gamma}/C_f\right), \qquad 2.8$$

, where τ is the shear stress, α is a constant, $\dot{\gamma}$ is the shear strain rate and C_f is the concentration of flow defects. According to this equation, the strain rate reduces in indentation tests under a constant loading rate, and the high indentation strain rate at low indentation depth can induce an increase in hardness.

However, both stress and strain should not vary significantly in penetration of a sharp indenter according to the classical contact mechanics. Jang and co-workers systematically studied ISE in a Zr-Cu-based BMG through nanoindentation with Berkovich indenters with different angles from 35º to 70º. As shown in Figure 2-11, the variation of hardness changed with indentation depth. The sharper indenters produced smaller contact radius and, thus a localised highly-stressed or plastic zone, which led to lower activities of STZs. Lower activation of STZs resulted in higher hardness values, as confirmed in Figure 2-11. The authors showed that the mentioned hypothesis cannot be used to explain the angle effect on hardness as the use of sharp indenters resulted in higher hardness value.

The phenomenon of ISE can also be explained by occurrence of STZs [38]. In this hypothesis, the STZ population controls the indentation size or the volume of indentation-induced elastic/plastic deformation. In low-depth indentation, a highly stressed volume beneath the indenter is too small to generate a sufficient number of STZs; thus, the shear bands are forced to operate in a confined zone, leading to higher hardness values for lower loads. In contrast, in high-depth indentation, a large volume of plastic zone is formed resulting in activating a large population of STZs and shear bands. The STZ hypothesis can be used to

describe the angle effect on hardness, as higher hardness is expected for sharp indenters.

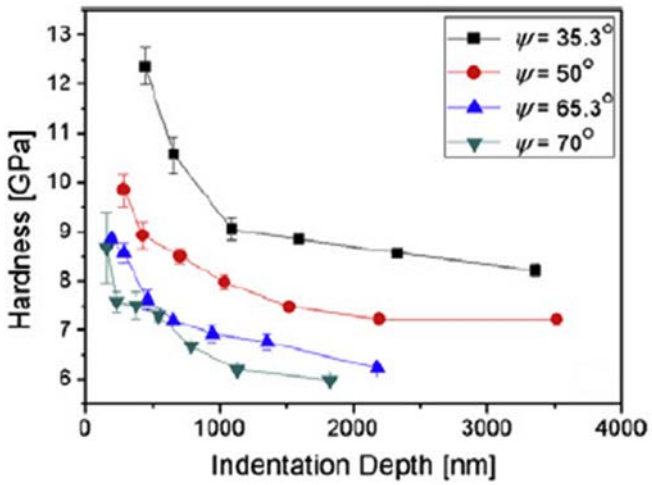

Figure 2-11 Analysis of hardness data according to Nix-Gao model: plots of hardness *vs*. penetration depth [66].

Choi and co-workers [59] studied the existence of ISE in Zr-Cu-based BMGs by employing spherical nanoindentation experiments with varying tip radii (R) of 2.91, 5.75 and 31.5 µm. The load, at which a first pop-in event occurred in Zr-based MGs, was measured for three tip radii and in two different structural states: as-cast and structurally relaxed. The experimental results showed the existence of ISE, with shear yield stress increasing with a decrease in the tip radius. Figure 2-12 shows variations in the average values of τ_{max} with R for both as-cast and annealed specimens, where τ_{max} increases with reducing R for both states. Larger volumes of metallic glass were affected as R grew, increasing the possibility of finding weaker regions in the bulk materials; as a result, lower stress was needed to initiate plasticity. Additionally, structural relaxation decreased availability of potential sites for STZ operation with annihilation of free

volume in the metallic glass; thus, the annealed specimen exhibited τ_{max} higher at the first pop-in.

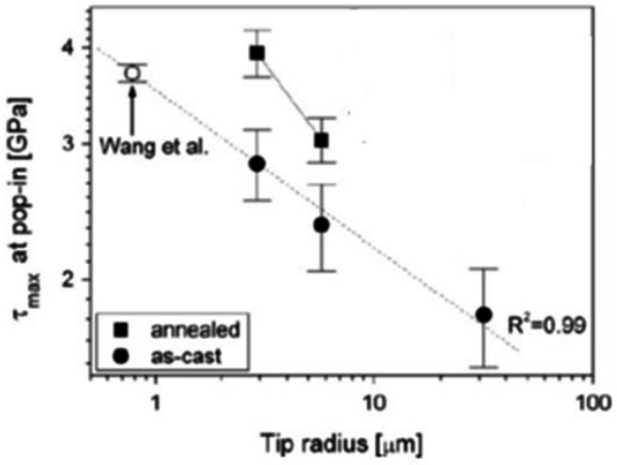

Figure 2-12 Variation in maximum shear stress at first pop-in with tip radius for as-cast and annealed Zr-based metallic glass [59]

Greer and co-worker [67] studied four types of metallic glasses including two-Pd based and two Zr-based MGs using nanoindentation with a spherical indenter tip radius of 10 μm and collected experimental data from the literature detailing indentation with such tips (180 nm < R < 31.5 μm) to investigate the relation between the indenter's tip radius and indentation pressure at yield. Clear signs of ISE were found as normalised yield pressure increased at the elastic limit when smaller tip radii were used: it was around three times higher than that in the macroscopic regime using the Hertzain equation to calculate yield pressure and stress. The increases in yield pressure and yield strain were independent of glass composition. The experiments demonstrated that yield pressure reached maximum when the tip radius decreased to 10 nm and below due to fewer structural defects. Greer and co-workers showed that the magnitude of the indentation size effect was inversely correlated with yield strain.

Still, existence of ISE is debated. Haung *et al.* [68] studied two types of Ti-based metallic glasses - ribbon-shaped and in a bulk form - to investigate the ISE effect. Ti-based ribbon specimens demonstrated that of lower hardness compared to bulk ones because of a higher amount of free volume. Hardness was observed to decrease, in both ribbon and bulk MGs, with increasing in the indentation depth. However, the perceived ISE disappears when the pile-up effect is accounted for with the Oliver-Pharr analysis.

2.2.3 Wedge-Indentation

A wedge-indentation experiment was designed to overcome limitation of nano- and micro-indentation to observe the initiation and propagation of shear bands under the indenter surface [125]. This technique has been used for variouse type of materials such as biomaterials (bone), conventional metals and polymers. In nano- and micro-indentation experiments, by their very nature, shear bands in the BMG can be observed only after they intersected the free surface of the sample.

In 1989, Donovan [126,127] used serial sectioning and etching in order to investigate plastic flow and fracture of Pd-based metallic glass loaded with traditional spherical and Vickers indenters at the load of 10 kg. In the sectioning method, the deformed specimens were etched in solution of three parts HCl, one part of HNO_3 and two parts H_2O and sectioned through the indentation in two orientations: “horizontal” sections parallel to the original surface of the specimens and “vertical” sections perpendicular to the original surface. In the study, it was explained that the plastic zone (shear bands) had a core region immediately beneath the contact zone, where the shear bands typically terminated before

they reached the free surface. The cracks seen in the etched section were related to the regions of high tensile strain with excess of free volume [127]. Ramamurty and co-workers [23,128,129] proposed a technique named `*Bonded interface*` to investigate shear-band propagation on a plane along the indentation axis in BMGs. In this technique, a pre-cut specimen is loaded along the direction in the plane of the cut with two halves of the specimen bonded along this interface by frictional forces. This technique was employed for brittle materials such as ceramics and oxide glasses in order to study the deformation mechanism underneath the indenter [112,130]. Zhang and co-workers [131] employed the bonded-interface technique on Vitreloy 106 in order to study the effect of increasing the load on shear-band propagation. At small indentation loads, plastic deformation was primarily accommodated by semi-circular shear bands surrounding the indentation. At higher loads, secondary and tertiary shear bands were formed inside the plastic zone. The same technique was used to observe the primary shear bands (PSBs) and secondary shear bands (SSBs) caused by the indentation in Zr-Cu-based metallic glasses [132]. As presented in Figure 5-1, PSBs with a high density were formed near the tip of the indenter and SSBs emanated radially from the tip. The SSBs intersected with the PSBs, but rarely approached the top surface of the indent. Based on the above observation, it was reasonable to claim that a hemispherical region of shear bands with different patterns was formed beneath the indent.

The bonded-interface technique was also employed at high temperatures on a Zr-Cu-based BMG to study plastic deformation characteristics in a subsurface deformation zone under a Vickers indenter and to find the reason for increased pressure-sensitivity of plastic flow with temperature [45]. Unlike the constant-

deformation zone, the shear-band spacing in the deformation zone increased with temperature as larger shear bands were formed due to the movement of a large number of STZs. The bonded-interface technique has an inherent problem with traction-free surfaces created when the specimen was split. As noted by Ramamurty et al. [128], an adhesive layer joining the sections together may relieve the elastic constraint for plastic flow, which would otherwise be present in bulk indentations. This may alter the size or shapes of the deformed zone and even the indentation mechanism itself [131]. This was noted by Mulhern [133], who found that the relaxation could affect the size of the deformed zone and the slope of the strain gradient but would not affect the contours of equal strain significantly. In contrast to the bonded-interface method, the wedge indentation would not require the material to be split open for observation of shear bands at the volume of the material. In this respect, the wedge-indentation test has an advantage over the bonded-interface technique, since it requires no adhesive and completely eliminates limitation due to the presence of interface [134]. In addition, wedge indentation can be used to apply incremental loading on any type of material to study the evolution of deformation mechanisms in materials by increasing the load.

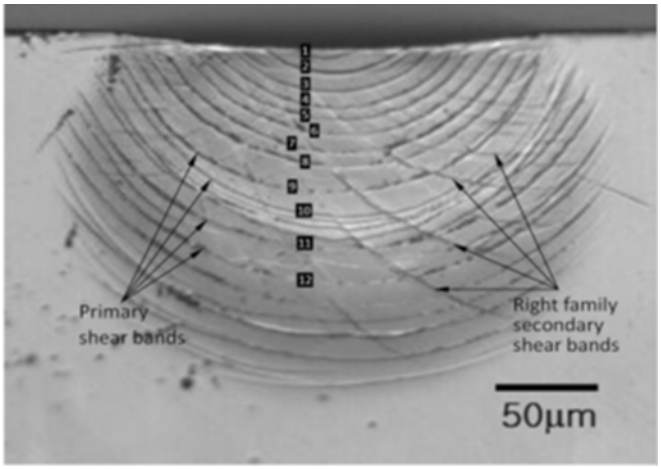

Figure 2-13 Primary and secondary shear bands created during indentation of $Zr_{52.5}$ $Cu_{7.9}$ $Ni_{14.6}$ $Al_{10}Ti_5$ BMG [131].

2.3 Length-scale effect

Modern advanced manufacturing processes often need to control component`s dimensions and material`s microstructure down to a nanometre level. In addition, recent advances such as focused ion beam (FIB), which is a technique for specimen preparation, or nanoindentation allowed materials characterisation at micron and sub-micron length scales. These developments help to achieve or design new material systems for these scales as an alternative to traditional strengthening techniques (Figure 2-13) and it is necessary to investigate mechanical properties and deformation mechanisms of MGs to understand their length-dependency and its effect on structural integrity.

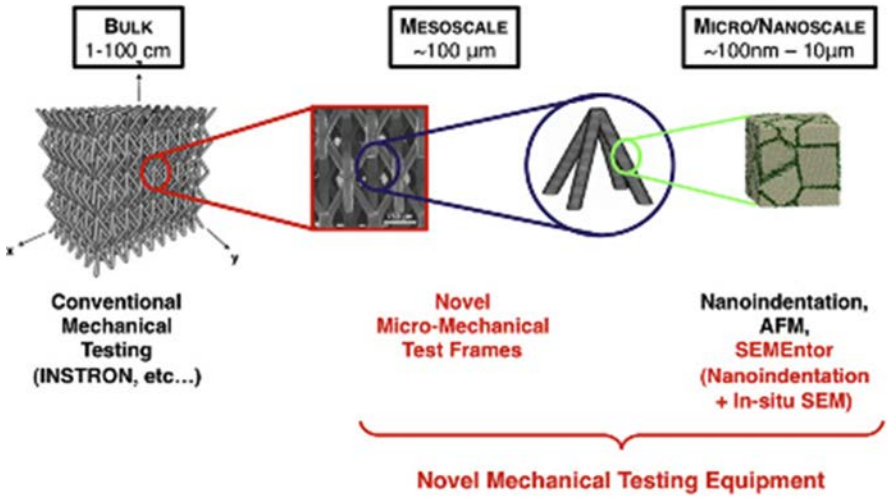

Figure 2-14: Micro-truss structure at various length scales as concept of “architectured material” [2].

Various research groups produced contradicting conclusions on the length-scale effect, based on different experiments performed on various BMG systems. The magnitude of yield stress measured for a large number of Cu- and Zr-based micropillars are plotted in Figure 2-14 as a function of the effective pillar diameter [3]. Apparently, the yield stress is independent of pillar diameter over the studied size scale due to a lack of dislocation sliding. In addition, it was claimed that MG strength is controlled by interatomic bonding, and there is a rarely linear relationship with the elastic modulus. However, it was shown that there was a considerable size effect leading to increase yield stress of micrometre sized specimens of Mg-based and Zr-based metallic glasses. Other groups carried out micro-compression experiments on metallic glass micropillars and reported a correlation between a reduced size and several mechanical properties including maximum plastic strain before failure, yield strength and deformation mode; however, most of them were inconsistent as can be seen in Table 2-1, an imperfect geometry, including tapering and top curvature of cylindrical pillars, is the main reason for the lack of agreement in micro-compression tests [2]. Moreover, when the sample size is reduced to nanometre scale, surface diffusion may contribute to plastic deformation and yielding, resulting in a decrease in strength. Schuster and co-workers [49] also confirmed that there was no size-dependent strength and deformation mode in compression of a Pd-based metallic glass. However, this finding is in contrast to other studies showing dramatic size effects in increasing the yield stress of micrometer sized Mg-based and Zr-based metallic glasses [3].

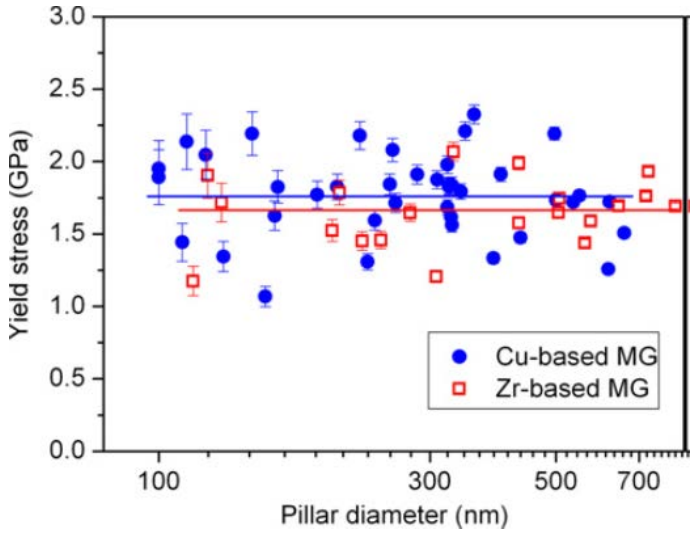

Figure 2-15 Yield stress versus pillar diameter for Cu- and Zr- based metallic glasses with trend line indicated [3].

As reported by Shimizu [3] that the critical lengths to nucleate and develop shear bands is 100 nm. If the specimen length is smaller than the critical length, shear bands are localised in the form of necking during plastic deformation of MG samples are in tension. Greer and co-workers showed that Zr-based MG nano-pillars with 100 nm diameter could attain ceramic-like strength (2.25 GPa) and metal like ductility (25%) simultaneously for non-tapered, free stranding nano-tension specimens for their in-situ uniaxial tension [23]. Shear banding developed and distributed deformation was observed in the form of non-localised flow followed by necking. However, it was found that the yield strength of metallic glass nanopillars showed size independency up to 500 nm diameters with changing deformation modes.

Table 2-1 Literature on size effect of strength in metallic glasses [3].

Reference	BMGs	Strength size dependence
Lee et al. (2007)	Mg-based metallic glass	Dramatic increase
Lai et al. (2008)	Zr-based metallic glass	Dramatic increase
Volkert et al. (2008)	Pd-based metallic glass	Slight reduction
Schuster et al. (2008)	Pd-based metallic glass	Slight reduction
Dubach et al. (2009)	Zr-based metallic glass	No change
Jang and Greer (2010)	Zr-based metallic glass	Small increase
Bhrathula et al. (2010)	Zr-based metallic glass	Yes
Dehosson et al. (2009)	Zr-Cu-based metallic glass	No change

As results a phenomenological model of two competing processes was proposed to explain the unique size-dependency including highly localised and homogeneous deformation mechanisms, related to the micro pillar diameter and the level of applied stress. These characteristics of plasticity impart distinct features to the mechanical behaviour of BMGs, such as flow softening, pressure sensitivity and ductile-to-brittle transition [69]. Thus, studying the influence of plasticity at microscopic length scales becomes essential for the development of robust modelling frameworks for BMGs.

2.4 Shear bands characterisation

Shear bands with a characteristic thickness of the order of 10-20 nm are responsible for deformation of MGs at low temperature and/or high stress. Most of the early work on shear bands in MGs involved inferences about their structure and behaviour from macroscopic observations. It was shown that deformation occurred preferentially at the pre-existing shear bands [70,71]. It was also found that shear bands were subjected to preferential etching [72], indicating a structural change in the deformed material such as increased free-volume content and/or chemical reordering. Both effects were omitted by annealing MGs below T_g plastic can also be improved deformation by repeating rolling-annealing cycles [73].

Shear bands induce softening in metallic glasses, and they are usually believed to be a contributor to plastic flow by reducing viscosity. Shear banding is a universal feature that can be also found in various materials such as polymers, fine-grained alloys and granular media. Shear induced dilatation is metallic glasses is very similar to that in soils, in which the shear deformation of randomly packed structures occurs in excess of free volume and leads to the formation of voids within the shear bands [74]. A direct consequence of this dilatation can be observed when a person walks on a wet beach: the water disappears underneath the foot because of the shear induced dilatation of the sand grains [31]. In addition, X-ray diffraction (XRD) of specimens exposed to indentation also provide indirect evidence of dilatation in MGs. Structural relaxation experiments near to T_g presented indirectly an increase in the free volume with an increasing degree of inhomogeneous deformation, consistent with the

dilatation measurements described above [75]. Investigation with Positron annihilation spectroscopy (PAS) also indicated that plastic deformation in MGs induced dilatation in the structure as the deformation resulted in an increase in positron lifetimes, consistent with a greater degree of open volume in the structure [76]. Suh and co-workers [77] observed two various types of free volume including shallow and deep positron traps. They illustrated that the deep traps could be removed by annealing and, thus, these traps might be related to potential STZs of particularly low activation energy. It is also possible to obtain insights into local chemical environment around the free volume using PAS measurements. For instance, it was shown that free volume sites consisted of Zr and Cu in a Cu-Zr-Ti metallic glass, while in Zr-Ti-Al-Ni-Cu metallic glass; the open volume sites included Ti and Zr atoms at expense of Cu and Ni.

The direct structural characterisation of shear bands around deformed regions was carried out to understand the nature of shear banding [78]. More recently, deformation-induced nanocrystallisation was observed in a number of BMGs with large plastic deformation [79-81]. These changes occurred in shear bands not only induced by bending or compression of metallic glass [79,82], but resulted from their nanoindentation or microhardness testing [83,84], ball milling or cold rolling [85,86]. Many researchers employed transmission electron microscopy (TEM) observation, which provide nanoscale resolution to exhibit more details on the structural evolution of the localised shearing which cannot be detected with optical microscopy and SEM, showing the presence of nanocrystals inside the shear bands. TEM were also employed to observe coalescence and spontaneous formation of nanometer-scale during deformation. It is also agreed that these in situ nanocrystals would lead to arrest or self-lock of shear bands

and, therefore, prevent runaway failure along the shear band. As shown in Figure 2-15, there is a nanosized band along the shearing direction. The bands include a large number of nanocrystalls that shows a bright spots in the dark-field image. The nanocrystals with a size of 5 nm are only visible within the shear bands and cannot be found in the regions out of the shear bands, which shows that the deformation process is related to localised shear deformation. The index of the ring pattern indicates that deformation-induced nanocrystals have a simple face-centred cubic (FCC) structure.

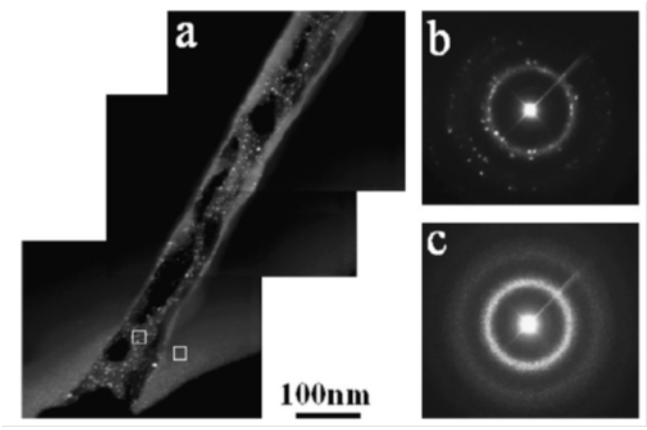

Figure 2-16 TEM micrograph and SAED patterns of shear in deformed Ni-based metallic glass: (a) dark-field TEM image of 100 nm wide shear band with a high density of nanocrystals:(b) and (c) nanodiffraction patterns taken from regions within shear bands and out of shear bands, respectively [87].

There are a number of suggestions for the mechanisms of deformation-induced nanocrystallisation in metallic glasses. One possibility is the localised heating of shear bands: it was suggested that significant adiabatic heating inside shear bands contributed to a viscosity decrease in them [88]. However, several experiments indicate that this mechanism was solely responsible for crystallisation in shear bands for BMGs with good glass-forming ability and a

wide super-liquid region. There are other factors such as an ultrahigh shear strain rate and an excess free volume produced by deformation along the shear bands that may cause in-situ crystallisation [89,90]. However, crystallisation was observed in some metallic glasses but not in others. Schuh and co-workers proved that there is no obvious long-range order in the area beneath Berkovich indenter for a Zr-based metallic glass. In addition, Greer and co-worker postulated when the crystals observed in shear bands region, at least sometimes, can be artifacts of a TEM specimen preparation technique [2] as some of the of the observed crystallisation in the deformed area was because of the thin sample. This hypothesis was confirmed by Wilde and Rosner [91], who found no crystallisation in shear bands for $Al_{88}Y_7Fe_5$ glass at ambient temperature. They claimed that compositional changes were observed within the shear bands and the observed variations in the resulting densities in various parts of one shear bands, were associated with propagation of each individual shear band. They found a mixture of amorphous or medium-range ordered domains within shear bands due to local variations in chemical composition and densities in shear bands. Certainly, the local structures are directly affected by both the free volume and local chemical composition. Thus, the question, whether there is any propensity for crystallisation is still open. In addition, the above discussion highlights the importance of local imaging methods for the characterisation of shear bands and their major role in deformation of BMGs that reported in the literature.

2.5 Modelling of deformation in BMGs

Degradation of elastic properties is related to accumulation of damage in brittle materials and primarily caused by evolution of micro cracks. Degradation of mechanical properties is a unique feature of brittle material behaviour. Both mode and stability of crack growth in brittle materials strongly depend on the sign and magnitude of applied stress. Weakening of effective elastic properties of a solid by a distribution of micro cracks and other defects was accounted in several analytical models by Nemat-Naseer *et al.* [92]. Various models were proposed for brittle fracture of materials [93] by Glucklich *et al.* [94] , Brace and Bombolaski *et al.* [95], Brandtzaeg *et al.* [96] namely; energy model, stress model, sliding crack model and lattice model, respectively. In all these approaches the material was assumed to be linear elastic and the analyses were limited to static or quasi-static conditions. Continuum damage mechanics models have were also used to study brittle materials with some critical drawbacks (see [93]), while micromechanical damage models are often computationally inefficient and impractical.

For metallic glasses, regardless of the experimental evidences of shear band initiation, the origin of shear band remains ambiguous. Theoretical investigations were conducted for shear -band initiation and evolution by Steif *et al*. [97], Huang *et al.* [98] and Jiang and Dai [99]. Ruan *et al.* [100] suggested a new model incorporating atomic structural change and free-volume generation but it lacks experimental validation. In this, the material was assumed to be viscoelastic to derive high- temperature stress–strain relationships and extension to low temperature scheme is a significant challenge.

Most acclaimed modelling strategies for BMG, mentioned in previous sections, such as free- volume theory of Argon and Spaepen and the STZ-based deformation mechanism are formulated for the atomistic domain and could not be employed in the continuum approach. For instance, as mentioned by Argon *et al.* [26] that the theory was based on free-volume regions typically conceived to be 5 atoms diameters across and Ghosh and Cheng [101] proposed a free volume-based constitutive model that accounts for transition from inhomogeneous to homogeneous deformation and non-Newtonian to Newtonian viscosity. The simulation results exhibit hydrostatic pressure dependence but for a certain range of temperature and strain rates. However, it does not clarify the size effect exhibited by metallic glasses. Molecular dynamics (MD) based simulations also provide deeper understanding of deformation mechanisms of metallic glasses, but for the nano scale. For instance Chu *et al*. [102]. employed the MD scheme to conduct nano-indentation simulations of Cu47Zr47Al6 metallic glass and Wang *et al.* [93] used it to simulate nano-indentation of $(Cu_{50}Zr_{50})_{100-x}$ Al_x thin film to study the effect of different Al content on material properties. Shi *et al.* [103] also adopted MD to perform 2D and 3D simulations of nano-indentation of metallic glasses [104]. However, MD analysis is limited to high deformation rates (>107s-1) and requires a considerable computational time. So, the use of continuum based constitutive models can support a study of the size effect exhibited by metallic glasses ([105]).

Finite-element analysis also contributed to the analysis of mechanical behaviour of BMG by Gao [106] and Chen *et al.* [107] and several contributors. Based on their studies, deformation of BMG was simulated at room temperature employing the free-volume method and considered only the effect of free volume on

deformation. Later, Yang *et al*. (2006) induced the evolution temperature into the study, while some researchers considered the effect of hydrostatic stress as well. Still, these works focused only on some facts of mechanical behaviour of BMGs and under certain deformation conditions. As mentioned by Thamburaja et al. [105]; these models were limited to relatively low strain rates and neglected the material failure of more advanced scheme with contributions of free volume, temperature, and hydrostatic stress was considered by Li *et al.* [108] as it also incorporated a failure criterion based on a critical free-volume concentration. However, as mentioned earlier, a single simulation still struggles to represent the entire pattern of deformation and failure in BMG [108].

2.6 Summary

In the first part of this chapter, the fundamental mechanisms of deformation and fracture of metallic glasses were reviewed. These include the effect of low and high strain rates, temperature and pressure on the deformation mechanisms. In the second part, introductory information about the main aspect of indentation experiments was reviewed. A Critical review about the main aspects of indentation size effects, pile-up and sink-in and the length-scale dependency of metallic glasses was studied to understand their deformation mechanism and mechanical properties at small scale, which are essential for the development of robust modelling frameworks for BMGs.

As shear bands play decisive role in controlling plasticity and failure at room temperature, an overview of shear bands characterisation was summarised, regarding key materials-science issues of shear bands in metallic glasses. A few of them is now solved and there are some key issues that remain puzzling such

as crystallisation inside the shear bands during plastic deformation and local imaging methods for shear bands characterisations. Their resolution would definitely result in better understanding and control of shear bands, possibly leading to improved mechanical properties for metallic glasses.

Continuum-based approaches to study the deformation behaviour of metallic glasses are essential for the macro scale engineering applications. Since metallic glass shows pressure- dependency, many studies were carried out to elucidate the mechanical deformation of the BMG with available continuum approaches that are pressure-dependent. It was shown that most common pressure-dependent continuum models in the literature did not agree with the macro scale behaviour of the BMG and the molecular dynamics approaches with the free volume theory is not adequate for the macro scale problems.

3 Characterisation techniques

3.1 X-ray diffraction (XRD)

An X-ray diffraction method is a rapid analytical technique primary used for phase indentation of crystalline materials. It can provide information about a degree of crystallinity, lattice parameters (the average spacing between layers or rows of atoms) and crystal structure of an unknown material. Samples with lower thicknesses, like thin films, require a longer time for the signals to be counted, otherwise the substrate effect dominates. Bragg [109] identified that if the atoms are arranged in a particular order inside the material then inter-planner spacing between them can be considered as grating for X-rays, since their wavelength is comparable to the spacing, and diffraction phenomenon could be observed. According to the Bragg`s law,

$$n\lambda = 2dsin\theta, \qquad 3\text{-}1$$

where d is the spacing between the atomic layers in a crystal, λ is the wavelength of the incident X-ray beam, n is any integer and θ is the angle between the plane and the source of X-rays. In crystalline materials, strong diffraction peaks can be seen at the particular angles, if Bragg's law is satisfied. Although, atoms inside amorphous and glassy solids do not have long-range periodicity, their diffraction patterns detect one or two broad maxima, which confirm their disordered structure. It shows that there are not enough planes to produce a destructive interface, so a broadened peak is observed. For example, Fe-based glassy metals show broad maxima in the range of $2\theta = 40° - 50°$ and for Ti-based glassy metals, the maximum is in the range between 30º-50º.

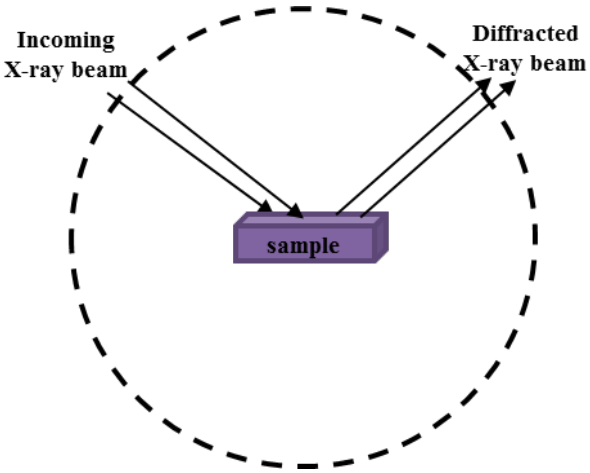

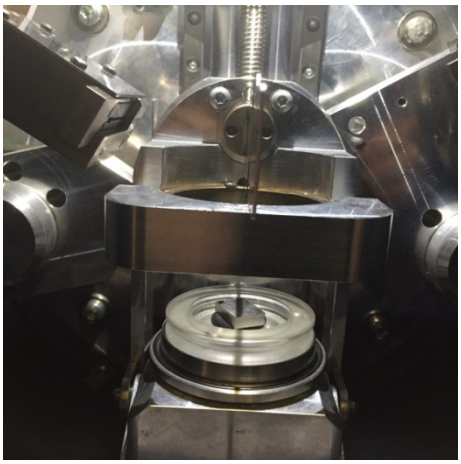

Figure 3-1 Bruker D-8 Diffractometer used for XRD analysis.

The amorphous nature of the supplied beam samples was initially investigated employing X-ray diffraction (XRD), (Bruker D-8 Diffractometer, Bruker AXS GmbH, Karlsruhe, Germany), Figure 3-1, using Cu-kα as a source of radiation with wave length of 1.5406 Å. The amorphous nature of the supplied beam samples of metallic glass (MG) was initially investigated using X-ray diffraction. All the sample were analysed at a step size of 0.02° increment in 2θ with a step time of 1 s. XRD patterns were recorded for 2θ in the range of 20 ° to 90˚ . Specimens were cut from the supplied beam samples with a low-speed diamond

disc under constant water irrigation to minimise the undesired mineral formation on the surface of the specimen.

3.2 Electron microscopy and ion beam technique

Electron microscopy is a scientific technique to examine objects on a very fine scale by using the energy electrons. A wave nature of accelerated electrons is responsible for a diffraction phenomenon, which can be applied to study the surface morphology as well as the internal structure of the materials depending on their thickness. Such energetic electrons can be excited by using high voltages applied to filaments or field emission guns and focused by electromagnetic lenses to spot sizes of several nanometres to enlarge the image by several thousand times, while bombardment of heavy ions on the surface of materials can be used to form different types of shape or produce deep holes into materials. This technique helps to look at the nanometer scale for understanding the material at the very fundamental level.

3.2.1 Scanning electron microscopy (SEM)/ Focused ion beam (FIB)

Scanning electron microscopy (SEM) is a useful technique, which can provide very useful information about surface morphology, fracture mechanisms and a shape and a size of grains, and size of the particle of the sample at nanoscale. Field-Emission-Gun SEM (FEG-SEM) provides better brightness compared to a thermionic-emission-gun SEM, because of the higher beam current in a small diameter of the beam. This device offers a significant signal-to-noise ratio when compared with conventional SEM. In this study, SEM (Leo 1530VP Cambridge SEM, LEO Elektronnenskopie GMbH, Oberkochen, Germany) and FEG-SEM (Leo 1530VP FEGSEM, LEO Elektronnenskopie GMbH, Oberkochen, Germany)

(as shown Figure 3-2 (a) and (b) respectively) were used at different magnifications to investigate shear-band initiation and evolution. An in-lens detector was used to record the images at 5 kV accelerating voltage and a working distance of ~ 5 mm. Sample preparation for FEG-SEM and SEM required a high-surface quality, which was challenging to obtain for BMGs samples. Polishing was carried out based on the procedure described in Section 3.6.1 until the samples appeared sufficiently clear to be analysed in FEG-SEM. It is worth mentioning that for the polishing process, the samples were embedded in a non-conductive resin; however, FEG-SEM demands a conductive sample. Thus, a thin layer of conductive metal, silver paste was used to prevent charge- accumulation effects and shield the specimen from potential damage by direct exposure to electron beam. In the absence of this conductive layer, a high-energy beam of electrons would rapidly charge up on the surface of the specimens to the point that no observation would be possible.

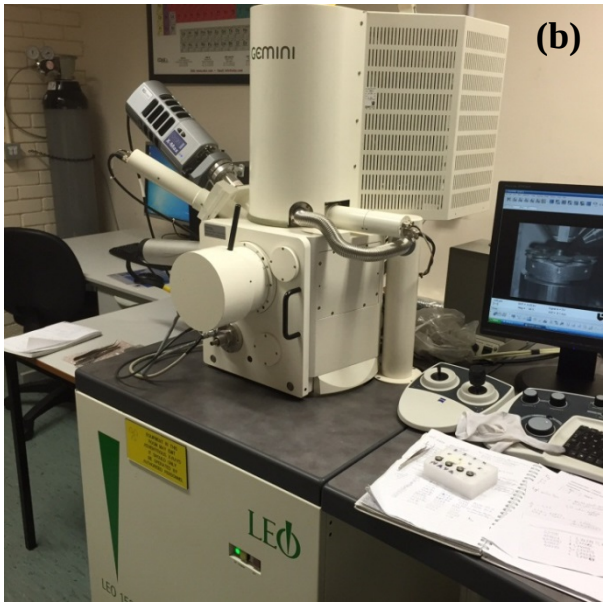

Figure 3-2 (a) Cambridge SEM and (b) Leo 1530VP FEGSEM.

Focused Ion Beam (FIB) is a technique employed for particle deposition and removal of materials from the specimens. It could be used as a milling machine to prepare three- dimensional shapes at nanoscale in a short time. FIB uses heavy ions to image the sample in the chamber instead of a focused beam of electrons as used in SEM. A dual-beam system, including a SEM and FIB, offers capabilities to image the surface using electrons from SEM with FIB used for material removal. Heavy ions such as delivered by a Ga-based liquid-metal ion source (LMIS), are used for milling thanks to a low melting temperature (30ºC) and low vapour pressure. When applying a high positive voltage to the liquid metal, it takes a conical shape and its apex continues to grow till evaporation of the metal takes place. Micro-scaled pillars for microcompression tests and TEM samples that are thin foils with 100 nm thickness, of studied BMGs were fabricated using the dual FIB system. A schematic diagram of the dual-beam SEM/FIB is presented in Figure 3-3 along with photograph of the instrument used for this work.

3.2.2 Transmission electron microscopy

A transmission electron microscope (TEM) is composed of a vertical column, which consists of an electron gun (thermionic or field emission), electromagnetic lenses, few apertures and a sample holder. TEM is a microscopy technique, where an electron beam interacts with an ultra-thin specimen when electrons accelerate, due to a high potential difference, in a fine and very small tube. The interaction can cause transmittance, diffraction or absorption. An image is formed, which is magnified 50-100 times, from the focused transmitted electron onto an objective lens. For further magnification a series of intermediate and projector lenses are used and projected on a fluorescent screen.

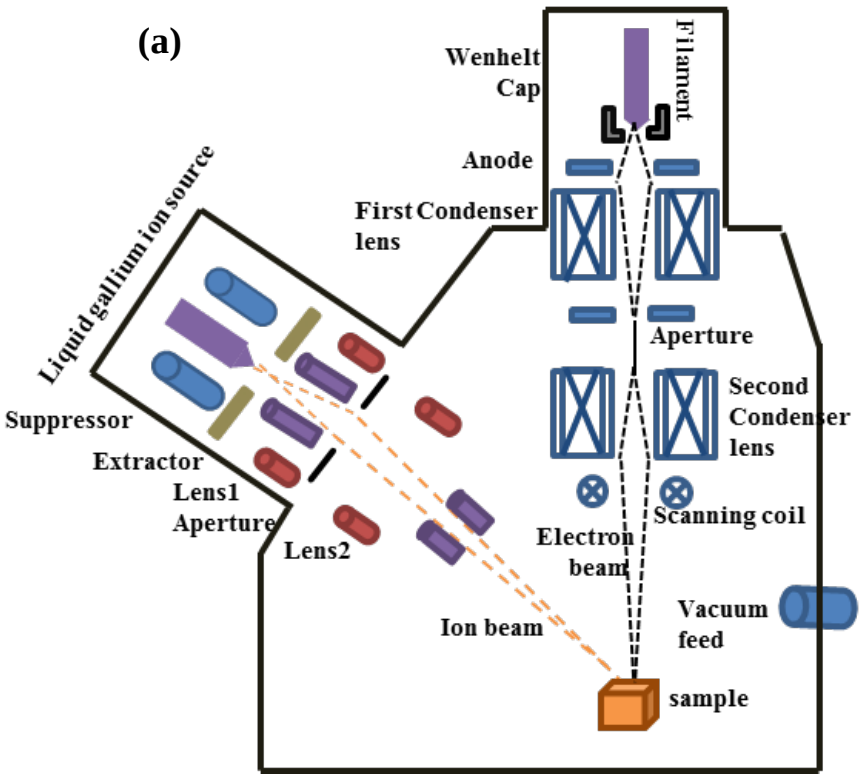

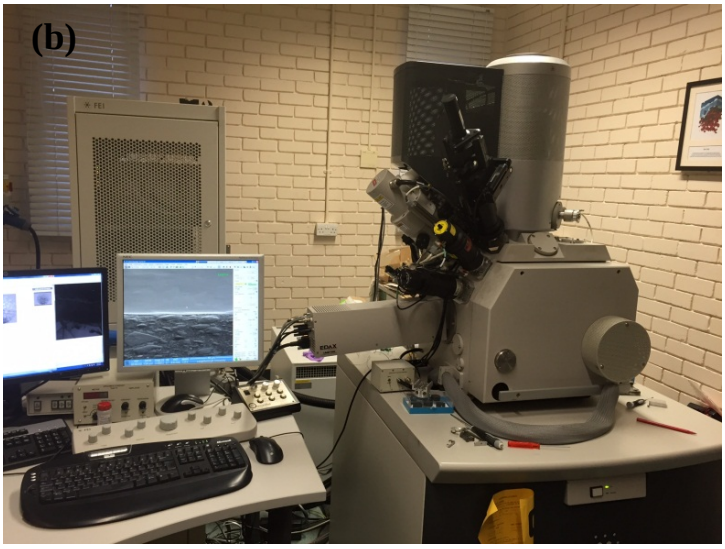

Figure 3-3 (a) Schematic diagram of dual-beam SEM/FIB system; (b) dual beam SEM/ FIB (Nova 600 Nanolab by FEI Company).

A schematic diagram of TEM with different components is presented in Figure 3-4. The microstructure of the BMG samples was determined using TEM (JOEL JEM 2000FX, JEOL Ltd. Tokyo, Japan) at 300 kV. An Energy dispersive spectroscopy (EDS) system, referred to as EDS or EDAX, is attached to the TEM; it is used to identify the elemental composition of materials. The EDS technique is non-destructive and specimens of interest can be examined *in situ*. The data generated by EDS analysis include spectra showing peaks corresponding to the elements making up the true composition of the sample analysed. EDS was employed to determine the composition of the studied as-cast and deformed BMG.

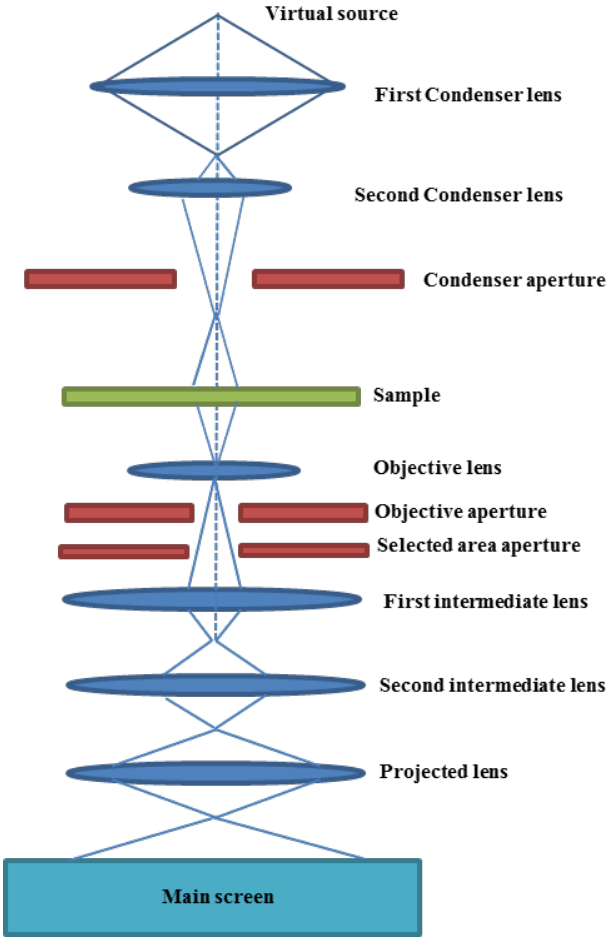

Figure 3-4 Schematic diagram of TEM.

The selected area electron diffraction (SAED) was performed using TEM. The samples were subjected to a parallel beam of high-energy electrons. In this case, electrons were treated as waves, rather than particles. Because the wave length of high-energy electrons is a fraction of a nanometer, and the spacing between atoms in a solid is only slightly larger, the atoms act as a diffraction grating to the electrons. Some fractions of electrons were scattered at particular angles, determined by the crystal structure of the sample, while others passed through the sample without deflection. This resulted in ordered spots corresponding to the planes of crystal structure. Hence, this technique was used to confirm the amorphous structure of the Zr-Cu-based metallic glasses.

3.3 Dynamic mechanical analysis

Dynamic Mechanical Analysis (DMA) is used to measure mechanical and viscoelastic properties of materials as a function of temperature, time and frequency. In DMA, a sinusoidal mechanical stress is applied to a specimen, and the resulting sinusoidal strain is acquired via a transducer. Materials that can be analysed with this technique include thermoplastics, thermosets, composites, elastomers, ceramics and metals. Two types of module are calculated using a ratio of stress to strain storage and loss moduli. The storage modulus, E', represents the energy stored elastically and reversibly, and the loss modulus, E'', measures the energy dissipated as heat and irreversibly lost. The ratio of the loss modulus to the storage modulus can be explained in terms of the phase difference,δ, between the maximum stress and strain. This is the ratio of energy lost, (dissipated as heat) to the energy stored per cycle, and is referred to as the *relaxation* or *damping* factor:

$$Tan\delta = \frac{E''}{E'}. \qquad 3\text{-}2$$

The loss or storage moduli, measured as a function of temperature or frequency can yield to find valuable information such as glass transition temperature (Tg) and sub-Tg transitions [110]. Figure 3-5 (a), presents the typical storage and loss moduli of Vitreloy bulk metallic glass ($Zr_{46.75}Ti_{8.25}Cu_{7.5}Ni_{10}Be_{27.5}$) determined from 473 K to 750 K at frequency of 1 Hz. From 500 K to glass transition temperature (603 K), both moduli increased slowly and gradually, however, the storage modulus dropped significantly to reach zero value at higher temperature, showing a typical liquid characteristic. Figure 3-5 (b) shows the storage and loss

moduli as function of frequency at 653 K. As the frequency increased, an asymmetrical peak was also revealed in the loss-modulus graph, and the storage modulus increased from zero to a constant value. Hence, the measurement of dynamic mechanical properties is a powerful tool for monitoring the structural evolution during glass transition and crystallization of metallic glasses.

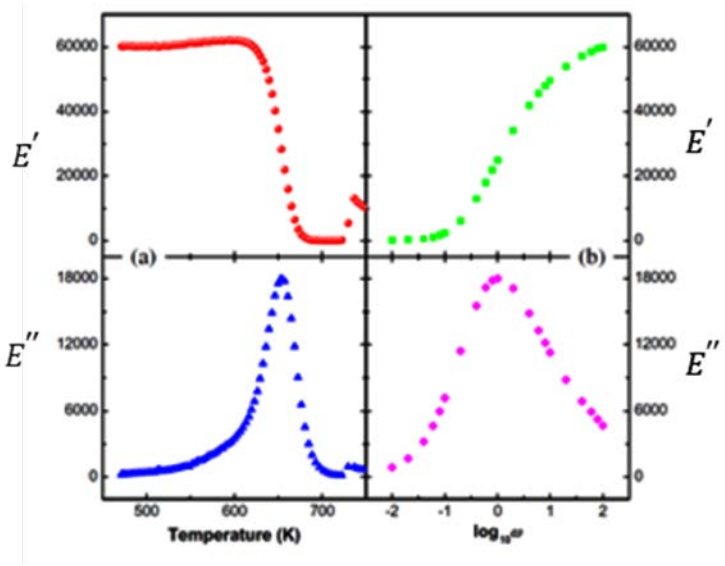

Figure 3-5 Storage and loss moduli of Vitreloy BMG determined in heating (a) and isothermal (b) processes (changing the frequency ω) [111].

A METLLER Toledo DMA/SDTA861e was used to investigate the effect of temperature and frequency on the mechanical properties of the Zr-Cu-based metallic glasses. Both displacement and force of specimens under dynamic loading can be measured using this equipment associated with comprehensive and well-proven STARe software. The force and frequency ranges can be between 1 mN to 40 N and 0.001 Hz to 10000 Hz, respectively.

Table 3-1 METLLER Toledo DMA/SDTA861e specification.

	Range	Technical resolution	Sensitivity
Temperature	-150-500ºC	0.003 K	0.5 K
Force	0.001-40 N	0.15 mN	1 mN
Displacement	±1.6 mm	0.6 nm	5 nm
Stiffness	$10\text{-}10^6$ N/m	-	0.2%
Tan delta	0.0001-100	0.00001	0.001
Frequency	0.001-1000 Hz	0.00001	0.0001

There are six different deformation modes, which can be used to analyse dynamic characteristics of the specimens including shear, three-point bending, dual and single cantilever as well as tension and compression modes. There are some requirements for the size of the samples for all these experiments to obtain reliable and accurate results. The three-point bending mode is the most appropriate method for hard sample of metals and alloys. This is due to the absence of clamping as the ends of the sample rest on two knife-edges and an oscillatory force is applied to the middle by a moving knife edge.

In this study, beam-shape specimens of 40 mm length, 6 mm width and 2 mm thickness were prepared, and these dimensions were kept constant for qualitative comparisons in storage modulus ($E^{`}$) and to reduce the edge effect. The samples were loaded in a 3-point bending mode with a frequency range of 0.2-1 Hz. The DMA spectra were recorded for a range of room temperature to

500˚C. The temperature was increased at 3˚C/min and readings were taken every 4 seconds to yield accurate tan δ and $E^{`}$ curves over the desired temperature range. Accuracy of measurement of the temperature and frequency-dependent modulus with the DMA were within 2%. From the measurement of the in-phase and out-of-phase responses of the sample, the storage and loss moduli were determined.

3.4 Laser interferometry

Zygo NewView 5000 is a non-contact instrument that uses white-light interferometry to acquire topography of a measuring surface. With the software MetroPro (produced by Lambda Photometrics), it allows for the acquisition of high-resolution 3D contour plots to characterise the surface structure of the test area. The instrument allows very accurate measurements of surface contours in a fraction of time needed for a contact instrument.

Table 3-2 Zygo NewView 5000 specification.

Objectives	5,10, 50X
Vertical resolution	0.1-20 nm
Lateral resolution	0.64-2.6 µm
Vertical scan rate	≤100 µm/s
Max roughness	100 µm

The excellent vertical resolution of the instrument allows for high-resolution characterisation and analysis of the measured surface. Measured 3D plots were

then elaborated in TalyMap Platinum software to obtain the needed measurements.

3.5 Nano-indentation

The NanoTest Platform III system (see Figure 3-6), manufactured by Micro Materials Wrexham, UK, was used for the depth-sensing Indentation (DSI) experiments. Figure 3-6 shows a schematic view of the NanoTest 600 unit used for the experiments. The sample stage can be manipulated using precise DC motors having a displacement resolution of 17.3 nm in the X, Y and Z directions. The NanoTest system is supplied with a high-resolution microscope and a microscope monitor, which helps to define the exact positions of the indents in a sample. The high-resolution microscope had the ability to magnify in the range of 4X, 10X, 20X and 40X. Before starting the test, the focal and measurement planes needed to be calibrated. The focal plane was the plane parallel to the Y-Z plane of the sample holder, in which the surface of the sample was in focus at the highest magnification. Whenever the sample was changed, it was brought to the focal plane before starting an indentation test. The measurement plane was the plane parallel to the Y-Z plane of the sample holder, in which the surface of the sample was approximately 50 µm away from the tip of the indenter. A schematic of Nano Test platform III indentation system is shown in Figure 3-6 .The Nano head consists of a pendulum with an indenter having a load range of 0.1–500 mN for nano-indentation, 1-20 N for micro-indentation and resolution of 0.1 µN. The pendulum can rotate on a frictionless pivot and is designed to be lightweight. The solid shaft of the pendulum is made of a ceramic, stiff enough to withstand the maximum load with negligible deflection. A coil is mounted at the

top of the pendulum and when the coil current is applied, it is attracted towards a permanent magnet, producing motion of the indenter towards the sample and into the sample surface. The parallel-plate capacitor measures the displacement of the indenter, as one of the plates is attached to ITS holder. Thus, when load was applied and as the indenter displaced into the sample, the capacitance changed and the displacement was measured by means of a capacitance bridge.

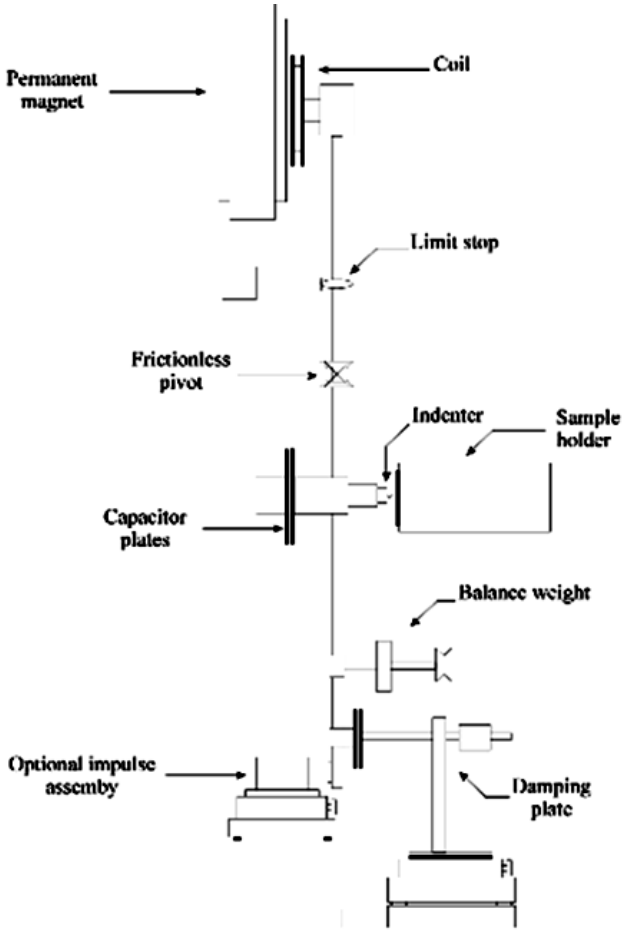

Figure 3-6 Schematic of Nanotest platform III indentation system

To minimise or reduce unwanted capacitance effects, the capacitance bridge unit is located close to the measuring capacitor. Below the capacitance plates, there is a counter-balance weight necessary to counter the mass of the coil and the indenter that is inserted into the diamond holder.

Table 3-3 Nanotest 600 specification.

Load resolution	≤100 nN
Force noise floor	100 nN
Maximum displacement resolution	0.05 nm
Thermal drift	≤0.004 nm/s
Maximum displacement	80 µm

3.5.1 Calibration

Nano-indentation systems require calibration and calibration standards to ensure that the instrument is working correctly. Three calibration measurements are required for all nano-indentation systems including frame compliance, indenter area function, and cross-hair or targeting alignment. It is expected that calibration standards show no pile-up or sink-in behaviour and very little creep. Standards should be economical and easily obtainable in an optically flat or highly polished condition. It is desirable that the standard materials show little or no ISE. Table 3-4 illustrates material properties of used calibration standard materials, when coupled with a diamond indenter [43].

Table 3-4 Material properties of commonly used calibration standard material when coupled with diamond indenter.

Material	Elastic Modulus, E	Poisson`s Ratio, v	Hardness	Reduced Modulus,E_r

Fused Silica	72 GPa	0.17	8.8 GPa	0.75 GPa
Tungsten	412 GPa	0.28	~ 6.6 GPa	0.75 GPa

- *Cross-hair calibration*

Cross-hair calibration [43] can be performed any time that indenter tips are exchanged in the system. This calibration process involves characterising precisely the movement of the sample stage in a way that the region of the sample at the microscope cross hair is re-positioned exactly in front of the indenter. When the cross-hair calibration is completed correctly, it is possible to position indentation at a chosen location to an accuracy of about 1 μm. Hence, the only requirement of calibration standard is that it readily holds a clear indentation impression. It is necessary that the standard calibration is very hard and stiff for the indenter area function calibration as loads at very low indentation depth are still large enough to be well within the force resolution of the indentation system. Thus, fused silica with superior on elastic isotropy is appropriate for this calibration.

- *Diamond Area Function (DAF)*

In indentation testing, the contact area at plastic depth (h_p) is found from geometry. The DAF [112] is an essential calibration to obtain accurate nanoindentation data. The area for each type of indenter can be measured from Table 3-5; however, the contact area is considered for the ideal indenter and this is impossible to achieve in practice. Crystal anisotropy of diamond indenters can

also affect the expected shape of the indent. Thus, it is necessary to apply a correction factor to the project area equations, shown in Table 3-5, in order to measure the actual contact area. The correction factor is the ratio of actual contact area to real contact area at the plastic depth (h_p).

Table 3-5 Projected area, intercept correction and geometry correction factor for various types of indenters.

Indenter type	Projected area	Semi angle (θ)	Effective cone angle α	Intercept factor	Geometry correction factor β
Sphere	$A \approx 2\pi R h_p$	N/A	N/A	0.75	1
Berkovich	$A = 3\sqrt{3} h_p^2 \tan^2 \theta$	65.3°	70.2996°	0.75	1.034
Vickers	$A = 4 h_p^2 \tan^2 \theta$	68°	70.32°	0.75	1.012
Knoop	$A = 2 h_p^2 \tan \theta_1 \tan \theta_2$	$\theta_1 = 86.25°$, $\theta_2 = 65°$	77.64°	0.75	1.012

To calculate the area function, a series of 100 indentations is performed at varying maximum loads on fused silica standard specimens using the Berkovich Indenter, as shown in Table 3-6:

Table 3-6 Indentation procedure of calculation of Diamond area function using Bekorvich indenter on fused silica standards specimens.

Minimum load (mN)	Maximum load (mN)	Initial load (mN)	Load time (s)	Dwell time (s)
0.5	1	0.005	10	5
0.5	0.5	0.005	10	5
1	5	0.01	10	5
5	10	0.01	10	5
10	25	0.01	10	5
25	50	0.02	10	5
50	100	0.02	10	5
150	200	0.02	10	5
200	200	0.02	10	5
500	500	0.02	10	5

Then, the actual contact area (A) is used to determine elastic properties of the specimens. A typical force-displacement curve, which was used to calculate the elastic moduli and hardness of metallic glasses, is shown in Figure 3-7.

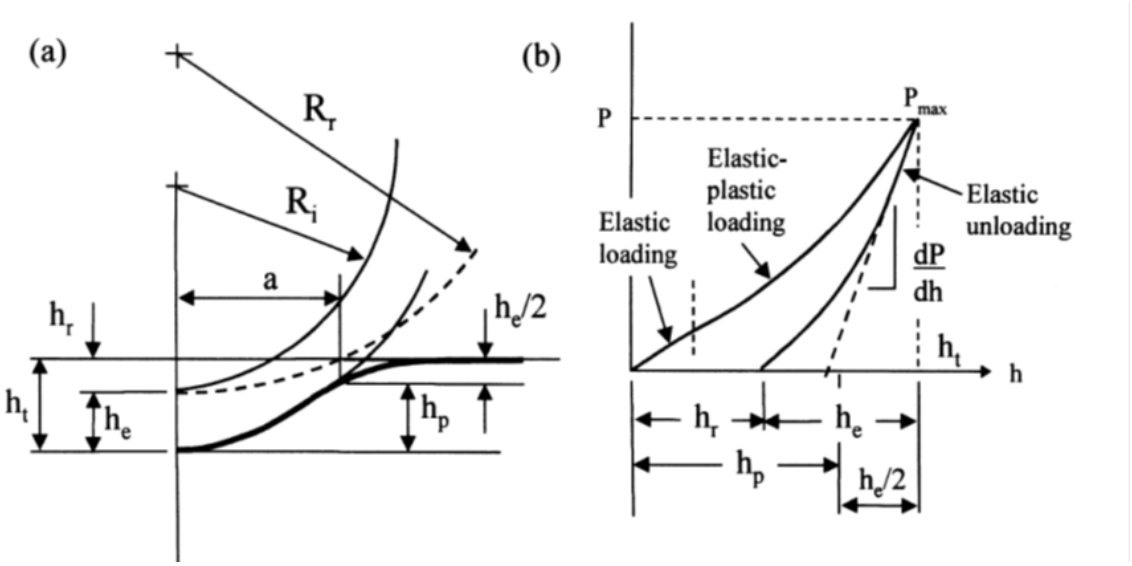

Figure 3-7 (a) Geometry of loading impression of radius $\mathbf{R_r}$ performed with a rigid with a rigid indenter radius $\boldsymbol{R_i}$. and (b) load vs displacement diagram for an elastic specimen loaded with spherical indenter showing both loading and unloading response [43].

When a flat specimen is loaded with a spherical indenter, there can be an initial elastic response at low loads followed by elastic-plastic deformation of the specimen`s material at higher loads [112]. As shown in Figure 3-7, the maxium penetration depth of a spherical indenter beneath the original specimen`s free surface is h_t at full load P_{max}. When the load is removed, assuming no reverse plasticity, the unloading is elastic and at the complete unloading, there is a residual impression of depth h_r. As can be seen in Figure 3-7, the elastic depth (h_e) is the unloading distance from h_t to h_r, $h_e = h_t - h_r$, according to the Hertz equation:

$$P = \frac{4}{3} E_r R^{1/2} h_e^{3/2}, \qquad 3\text{-}3$$

where R is the tip radius and E_r, is the reduced modulus, depending on deformation of the material and the diamond tip, determined from:

$$\frac{1}{E_r} = \frac{1-\nu^2}{E} + \frac{1-\nu_i^2}{E_i}, \qquad 3\text{-}4$$

where E and E_i are the moduli of the specimen and the indenter, respectively, ν is the Poisson's ratio of the specimens and ν_i is the Poisson's ratio of the indenter. Calculation of the elastic moduli with Eq.3-4 assumed a spherical diamond tip with the elastic modulus of 1.141 TPa and the Poisson's ratio of 0.07. A well-established method proposed by Oliver and Pharr [43] was used to calculate elastic properties of materials in the nano-indentation tests. In this method, the initial portion of the unloading curve ($^{dP}/_{dh}$) is used to determine the plastic depth (h_p). The derivative of ($^{dP}/_{dh}$) at the point of initial unloading h_t can be calculated,

$$S(h_t) = \frac{dP}{dh} = 2E_r R^{1/2} h_e^{1/2}. \qquad 3\text{-}5$$

$^{dP}/_{dh}$ can be used to determine the contact stiffness S indicating resistance of the material to elastic deformation. By substituting Eq. 3-5 to Eq. 3-3,

$$P = \frac{2}{3}\frac{dp}{dh} h_e. \qquad 3\text{-}6$$

Then

$$h_e = \frac{2}{3} P \frac{dh}{dP}. \quad 3\text{-}7$$

Based on the Hertz equations for a spherical indenter, the depth of the contact area h_a beneath the specimen`s free surface is half of the elastic displacement h_e:

$$h_a = \frac{h_e}{2}. \quad 3\text{-}8$$

Hence,

$$h_a = \left[\frac{3}{4}\right] \frac{P_t}{dP/dh}. \quad 3\text{-}9$$

From Eq.3-9, the radius of the circle of contact can be extracted from geometry:

$$a \approx \sqrt{2R_i h_p}. \quad 3\text{-}10$$

From Eq. 3-5, E_r can also be calculated from slope of the initial unloading:

$$E_r = \frac{dP}{dh}\frac{1}{2a} = \frac{dP}{dh}\frac{\sqrt{\pi}}{\sqrt{A}}\frac{1}{2}, \quad 3\text{-}11$$

, where $A = \pi a^2$ is the area of contact. These parameters were computed from the unloading part of the force-displacement curves with Nanoindenter III software, according to the well-established method [45].

The definition of hardness is the mean pressure under the indenter at maximum depth. In a spherical indenter-tip indentation process, the hardness can be calculated from the corresponding P-h curves [43]:

$$H = \frac{P}{2\pi R h_P} . \qquad 3\text{-}12$$

Plastic displacement (h_P) can be found from

$$h_P = h_i - \varepsilon \times \frac{P}{S} , \qquad 3\text{-}13$$

where h_i is the recorded indenter displacement, ε is the shape function (equal to 0.75 for a spherical indenter) and S is the stiffness, which is obtained from the unloading curve of the indentation test.

- *Frame compliance*

The depth measured during the indentation process includes the depth of penetration of the indenter into the specimens along with any displacement of the instrument due to its deflection [43]. The compliance of the instrument, C_f, is defined as the deflection of the system divided by the load. The instrument`s compliance includes the compliance its loading frame, indenter shaft and the specimens mount. When the sample compliance is small (high-modulus sample), the instrument`s compliance makes up an appreciable fraction of the total measured deformation, so small errors in the machine compliance can affect the accuracy of determination of the sample modulus. The compliance of the indenter material, $\frac{1}{S}$, is included in the reduced modulus E_r , where the stiffness of the contact S is given as a rearrangement of Eq. 3-14:

$$\frac{dh}{dp} = \frac{1}{S} + C_f. \qquad 3\text{-}14$$

Frame compliance calibration is required to determine the area function, and standard materials should have a low ratio of hardness to elastic modulus. Hence, a large and stiff contact can be easily obtained with a minimum error of indenter area function. Tungsten is ideal for this calibration as it behaves elastically isotropic under indentation. For the case of spherical indenter as $A = 2\pi R h_p$, the Eq.3-14 can be converted to

$$\frac{dh}{dp} = \left[\frac{1}{2E^* R_i^{\frac{1}{2}}}\right] \frac{1}{h_p^{\frac{1}{2}}} + C_f. \qquad 3\text{-}15$$

There are three methods to calculate C_f for the spherical indenter. The first technique is to plot $\frac{dp}{dh}$ against $h_p{}^{-1/2}$ obtained for an elastic unloading into elastic-plastic for a range of maximum indentation depth. The plot should be linear with the slope proportional to $\frac{1}{E_r}$ and an intercept, which gives the compliance of the instrument C_f directly. The second method establishes instrument`s compliance, which includes testing of a range of specimen materials with a spherical indenter with a relatively large radius using repeated loading at a single location. Such repeated loading minimizes surface effects such as roughness and other irregularities. A relatively large indenter (R) is used at reasonably high loads, where compliance effects are more readily observed and where indenter tip effects are minimized. Since the displacement of the

loading column is proportional to the load, the total displacement between two fixed points under a load P is

$$\delta = \left[\frac{3}{4E_r}\right]^{2/3} P^{2/3} R^{1/3} + C_f P. \qquad 3\text{-}16$$

The displacement, δ, and load, P, are calculated by the indentation instrument. For any two loads P_1 and P_2 resulting in deflection δ_1 and δ_2, the following relation holds:

$$C_f = \left[\frac{\delta_1 - \left(\frac{P_1}{P_2}\right)^{2/3} \delta_2}{P_1 - \left(\frac{P_1}{P_2}\right)^{2/3} P_2}\right]. \qquad 3\text{-}17$$

The third method is the current ISO standards for nanoindentation (ISO 14577), which was used for the compliance calibration in this project, and works well provided that the diamond area function (DAF) and depth calibration are known precisely. For this method, the Berkovich indenter and fused silica calibration standard is required. A series of indentations were conducted using the following parameters as presented in Table 3-7.

Table 3-7 Experimental procedure for frame compliance calculation using Berkovich indenter on standard fused silica specimens based on ISO 14577.

Minimum load	200 mN
Maximum load	200 mN
Loading time	20 s

Unloading time	20 s
Dwell time at maximum load	5 s
Thermal drift time	60 s
Spacing between indentations	30 µm

A series of automated calculations took place using Nanotest Platform III software to calculate the frame compliance of the system, and the calculated value was around 0.314 nm/mN.

3.5.2 Sample preparation

$Zr_{48}Cu_{36}Al_8Ag_8$ (at%) alloy was used in this study and specimens with a length of 2 cm and a width of 1 cm were used in the test. The specimens were difficult to prepare, as high surface hardness, high modulus, and tendency to smear of BMG require careful preparation of metallographic samples. Specimens were cut from the supplied beam samples with a low-speed diamond disc (1000 rpm) under constant water irrigation to minimise the undesired crystal formation on a surface of the specimen. In order to avoid subjecting work-piece sample to thermal stress, the specimens were initially mounted in epoxy resin. These resins when mixed with a hardener underwent setting with an exothermal reaction; the chemical-heat generation increased the temperature up to 60-70 ºC. The selected resin was Buehler Epoxicure, which was available in the materials lab, set in soft silicon moulds. The resin did not have good edge retention so during the polishing, edge effects were unacceptably high. The same resin mixed with conductive Ni particles was also used for early SEM

analyses. A resin with lower shrinkage and better edge retention was needed; it was therefore necessary to switch to hot mounting.

Figure 3-8 Embedding hot press

The resin of choice of this was Buehler Bakelite. This resin offered higher performance than the cold-set Expoxicure granting better edge retention and lower shrinkage. The samples were embedded on a Struers mounting press, with a mounting pressure of 20 kN at 180ºC (see Figure 3-8). The mounted sample were polished using a semi-automatic polishing machine (TegraPol-25, Struers Ltd.), shown in Figure 4-8 (a) with a rotating sample holder (TegraForce-5, Struers Ltd.) and an automatic feeding system for polishing media (TegraDoser-5, Struers Ltd.). As a typical polishing cycle, mounted samples were initially ground using a polishing disc with a grit size of 400 (35 µm), followed by 600 (25 µm), 1200 (15 µm), and finally 5000 (3 µm). Subsequently, polishing was continued by using a diamond paste consisting of particles of 1 µm in size. After finishing each polishing step and before starting the next one, the mounted samples were removed from the specimen holder, cleaned with deionised water and dried with a heat gun. When the final stage was completed, in order to get a clean surface without any contamination, all the samples were subjected to

ultrasound in deionised water for two minutes, sprayed with ethanol and dried using a heat gun. A white- light 3D interferometry Zygo profilometer was used to determine surface roughness. The system offers fast, non-contact, high-precision 3D metrology of surface features. The obtained results showed that samples were polished to a mirror-like finish with average roughness of around 5 nm.

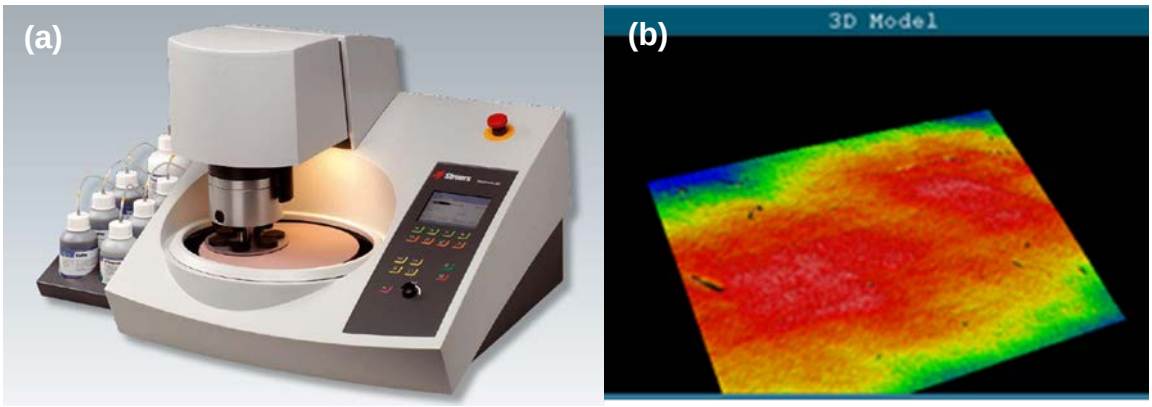

Figure 3-9 (a) TegraPol-25, Struers Ltd. used for sample preparation. (b) Zygo micrograph for polished BMG sample showing roughness of 2-3 nm.

3.6 Wedge-Indentation

For the wedge-indentation test, the supplied beam samples were cut into specimens with length of 40 mm and width of 3 mm. An electrical Discharge Machining (EDM) system, by GF AgieCharmilles, was used to achieve the desired shape and dimensions of specimens required for the study. EDM is capable of precise machining of tools, fixtures and dies from hardened metals, steel, titanium or ceramics. The steps for sample preparation:

1- Specimens were emerged in water in order to reduce the temperature and avoid splashing of debris.

2- The specimens were cut with brass wire of 0.25 mm diameter, which is used to cut hard metals for high-speed machining and cutting samples requiring superb surface precision. The motion of the metal wire was controlled by a computer with AC Cam Easy software.

Figure 3-10 Micrograph of EDM with brass wire employed to prepared wedge indentation specimens.

Afterwards, the samples were polished using manual polishing systems (Kemet 300 Series and Metaserv), as shown in Figure 3-11; a semi-automatic polishing machine could not be used because of the particular shape of the specimens. For the polishing process, a clamp made of steel was designed and manufactured in-house. Figure 3-12 illustrates the designed clamp and its dimensions used to polish the metallic glass samples. The mounted samples were manually grinded with increasing grit size up to 1200.

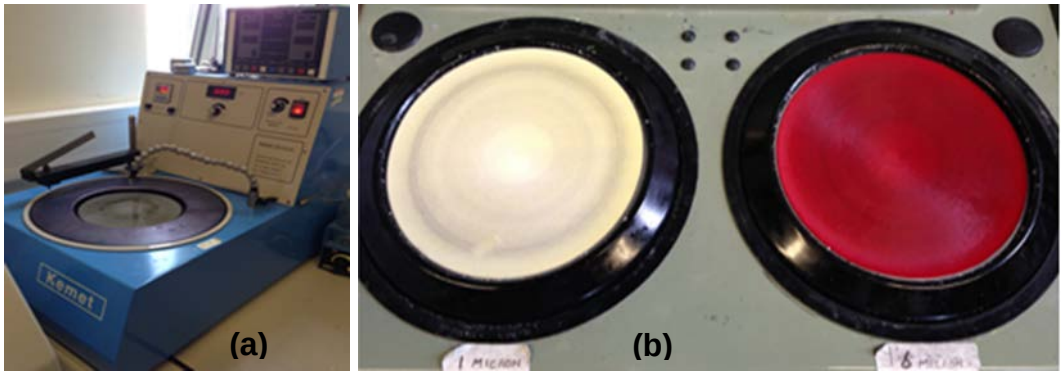

Figure 3-11 Kemet 300 Series (a) and Metaserv (b) polishing machines.

The manual polishing included two steps: first, on Buehler Texmet 1500, with 6 diamond pastes following by Buehler Microcloth with 1 μm diamond paste. The surface finish of the specimens was examined using an optical microscope. As shown in Figure 3-13 (b), some polishing artefacts were observed on the surface of the samples. Hence, it was suggested to modify the polishing procedure, and a use of 6 diamond paste as a polishing step was eliminated. As a result, samples were grinded with increasing grit size up to 5000 and then polished using only 1 μm diamond paste. Figure 3-13 (a) showed that the surface finish of the samples was significantly improved.

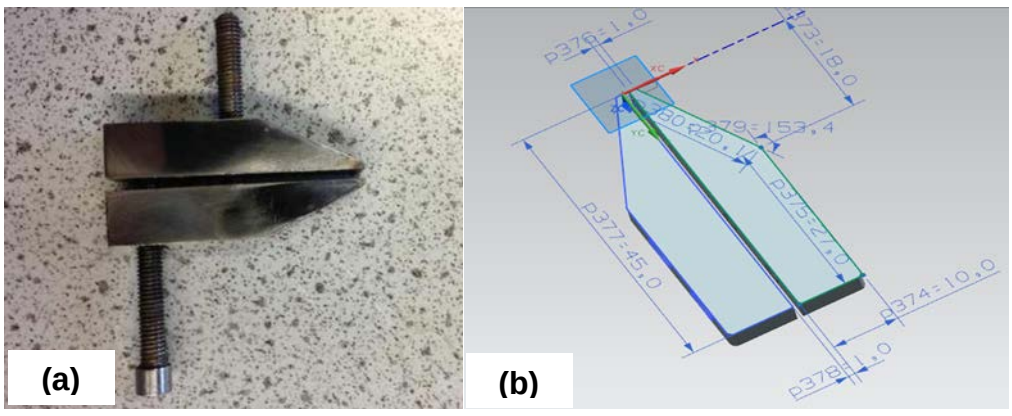

Figure 3-12 Polishing clamp and its dimensions.

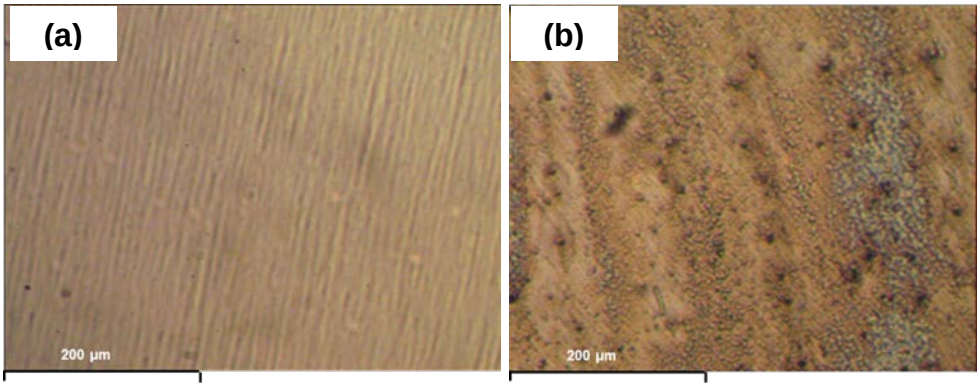

Figure 3-13 Comparison of two polished surfaces prepared using different polishing procedures: without (a) and with (b) using a diamond paste with particles of 6 µm.

After ensuring that the wedge indenter was flat enough, it was revealed during the indentation experiments that the sample surface was not flat enough due to the manual grinding and polishing procedure. As shown in Figure 3-14, uniform shear-band evolution was not observed on the sample`s top surface in the wedge-indentation experiments at loads less than 1 kN and the indenter did not touched completely the corners of the sample due to the sample is uneven surface. Therefore, an automatic surface grinder, OKAMOTO Grind-X ACC-450DXA, was employed for initial grinding procedure (Figure 3-14). The beam-shaped sample can be positioned in the holder of the surface grinder without any movement during the grinding procedure. The grinder used a rotating wheel to flatten the sample with the accuracy of 2 µm. The specimens were subsequently polished using 5000 grit size and 1 µm diamond paste in order to observe uniform shear bands on the top surface.

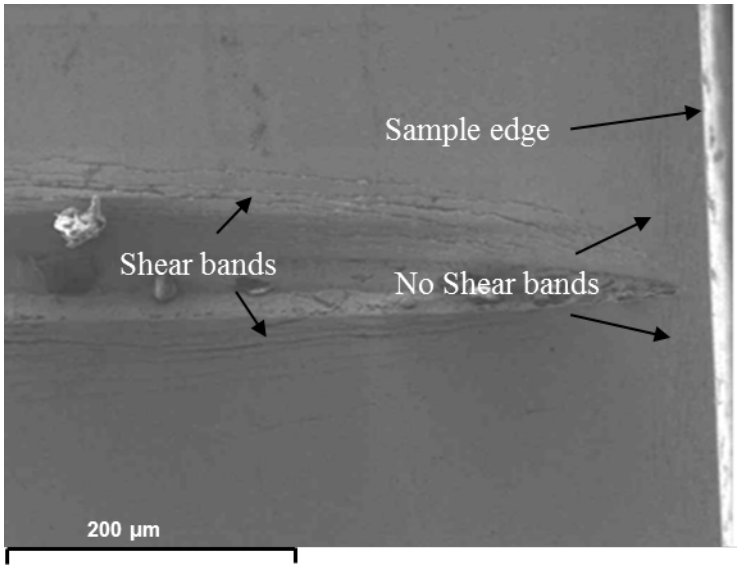

Figure 3-14 Shear band evolution during wedge indentation after manual grinding.

Figure 3-15 OKAMOTO Grind-X ACC-450DXA surface grinder.

4 Basic characterisation of a Zr-Cu-based metallic glass

4.1 Material specification

A Zr-Cu-based alloy with a nominal composition of $Zr_{48}Cu_{36}Al_8Ag_8$ (at%) was critically evaluated. The alloy was initially produced by arc-melting on a water-cooled copper mould under a high purity argon atmosphere at IFW Dresden, Institute for Complex Materials, Germany. The ingot was re-melted at least three times to obtain homogeneity. Furthermore, using the alloy ingot rectangular beam-shaped samples with a cross-section of 10 mm × 2 mm and a nominal length of 80 mm were prepared by suction casting into a copper mould.

4.1.1 X-ray diffraction

As shown in Figure 4-1 (a), the sample exhibited a broad diffuse peak without any detectable crystalline peaks on the XRD plot confirming its amorphous state. Similar results were observed for different parts (top, middle and bottom) of the specimens. However, as shown in Figure 4-1 (b), if the metallic glass is not completely amorphous, there are some sharp peaks showing crystalline phases in the sample. These peaks are related to metastable quasicrystalline phases formed in the metallic glasses as the composition of crystalline phases cannot be recognized by XRD. These phases only precipitate at the early stage of crystallisation in Zr-based metallic glasses at low volume fraction and the small particle size. In addition, the formation of quasicrystals phases is sensitive to the cooling rate during solidification of metallic glasses, the impurity contents and fabrication condition [113]. The position of peaks with higher intensity, like (100 000) and (110 000) in the spectrum, almost overlap with those of the

intermetallics, such as Zr_3Al_3 and Zr_2Cu, which may appear in multicomponents alloys.

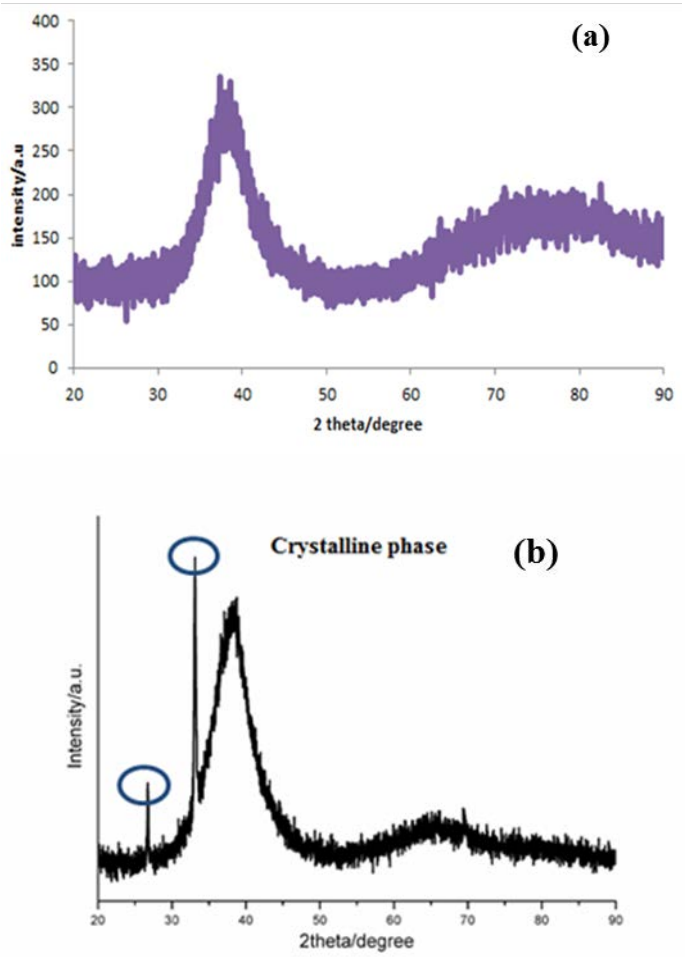

Figure 4-1 XRD patterns of (a) Zr-Cu-based metallic glass used in the project and (b) Zr-based metallic glass [113].

4.1.2 Electron diffraction pattern

The microstructure of the as-cast BMG was further characterised using TEM. The TEM results confirmed the amorphous nature of the alloy as the first halo ring of a Selected Area Electron Diffraction (SAED) pattern did not show any presence of nanocrystals. The pattern is only comprised of a set of diffuse amorphous halo rings and no distinct evidence of thin crystalline rings was found

anywhere across the whole specimens, which agrees well with XRD. The HRTEM micrograph further revealed the amorphous nature of the specimen and nano-sized crystallites with a periodic lattice contrast cannot be found. It shows a maze-like structure with a uniform contrast through the image and any ordered atomic packing cannot be found.

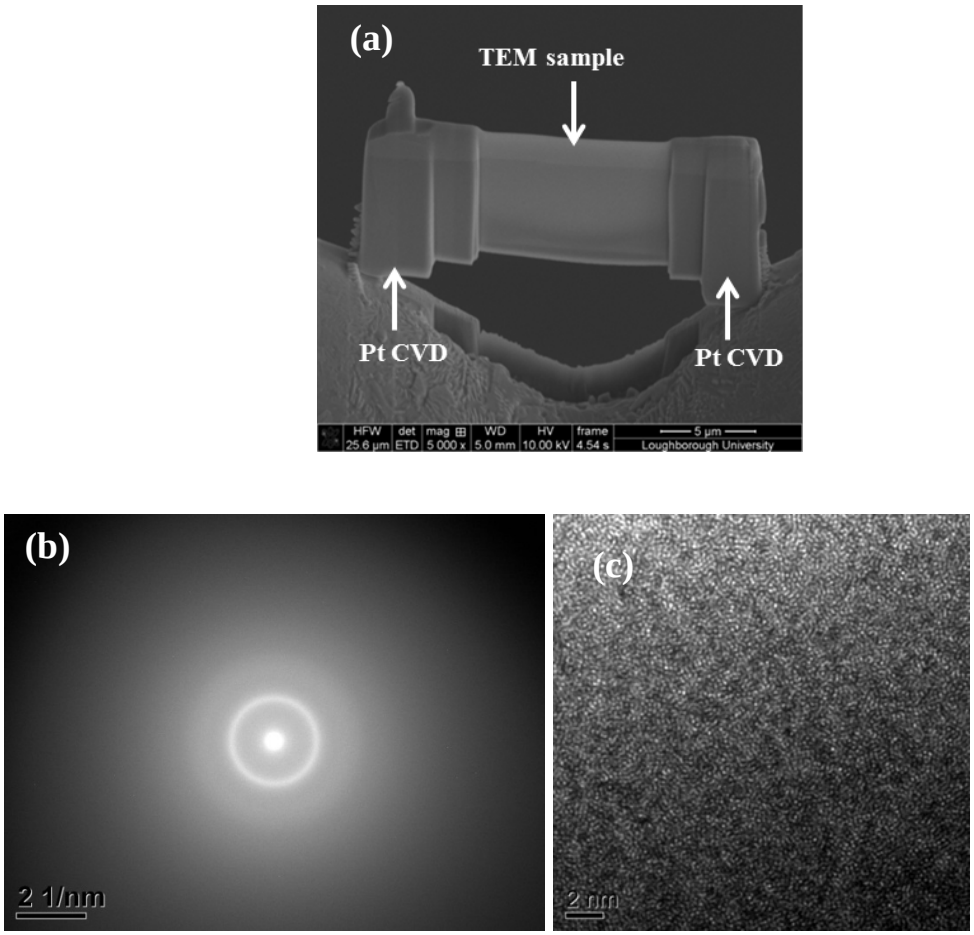

Figure 4-2 (a) TEM sample mounted to TEM grid and (b) the corresponding SAED pattern (c) HTTEM image of undeformed matrix

The composition of the locations, where the SAED were obtained from, was tested *in-situ* with EDS. The present measurement shows that the elemental concentrations were closed to the nominal values of 47.9 at.% Zr, 36.5 at.% Cu,

7.9 at.% Al and 7.7 at.% Ag . However, there is a limit as to what percentage in composition EDS can detect and the variation from measurement is within ± 1% .

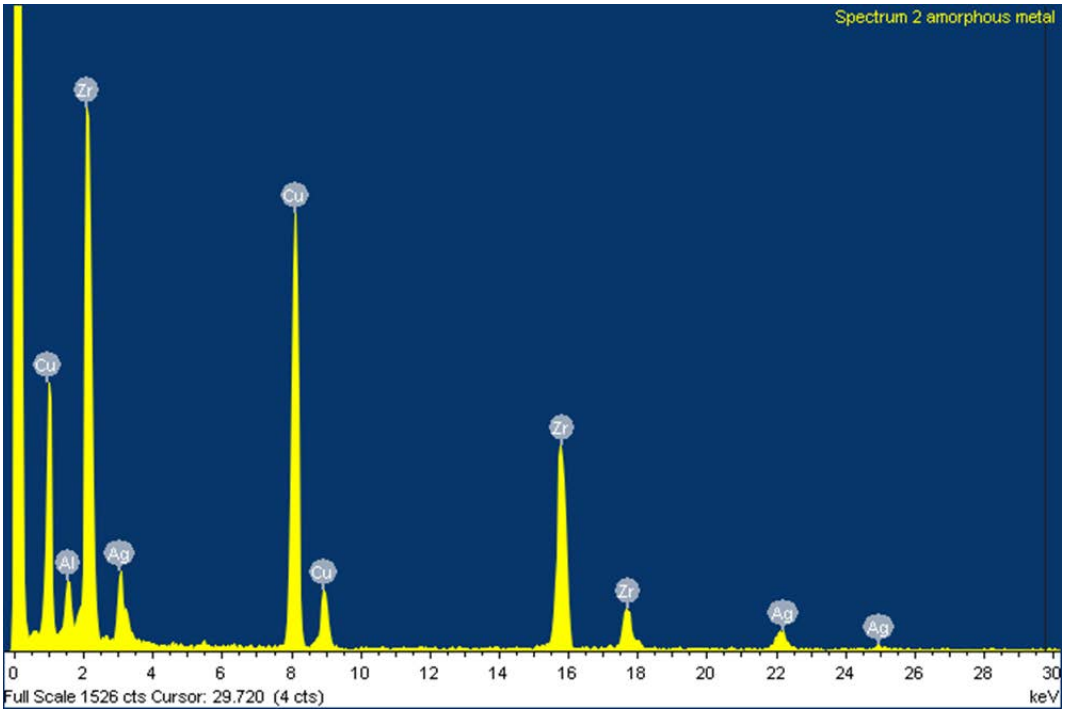

Figure 4-3 EDX graph obtained from TEM for Zr-Cu-based metallic glass.

4.1.3 Dynamic Mechanical Analysis

The glass-transition behaviour of the Zr-Cu-based BMGs was examined using DMA. Figure 4-4 exhibits the typical storage and loss moduli of the BMG determined in the range from 300°C to 450°C at heating rate of 3°C/min at the frequencies of 0.5, 1.0 and 2.00 Hz. The measured temperature scope contains its super liquid regions. During heating, the storage modulus decreases rapidly to zero within different temperature ranges at different loading frequencies. A decrease in the storage modulus and the accompanying maximum of the loss modulus indicate the glass-transition temperature (T_g). Hence, the glass transition of the MG is around 420°C based on the storage-modulus and loss-

modulus graphs, which confirmed the amorphous structure of the studies metallic glass. The maximum value of storage modulus and loss modulus are ~80 GPa and 3.57 GPa, respectively. It can be seen that dynamic characteristics of the metallic glass are effectively independent of the frequency at room temperature. This study indicates that the dynamic properties of the material are not sensitive to the strain rate at room temperature.

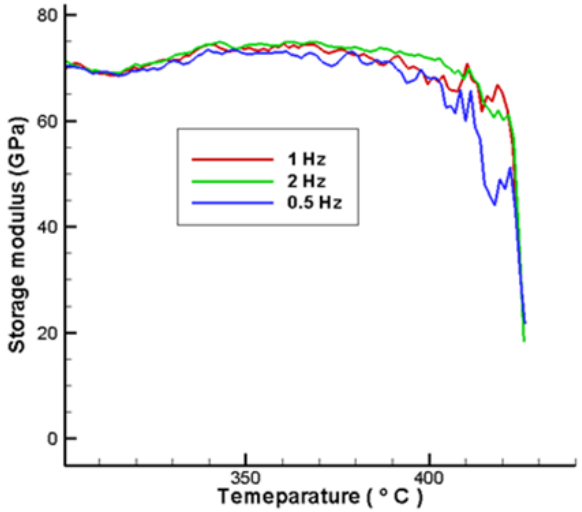

(a)

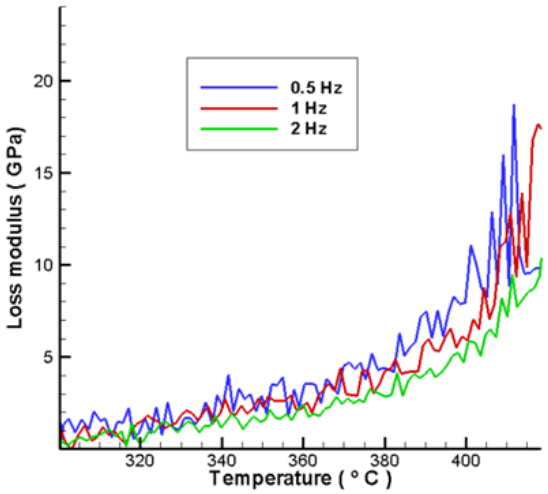

(b)

Figure 4-4 Temperature dependence of storage (a) and (b) loss moduli of $Zr_{48}Cu_{36}Al_8Ag_8$ determined with DMA at heating rate of 3°C/min.

4.1.4 Macroscale bending test

Macroscopic three-point bending test was carried out, with the sample subjected to both tensile and compressive stresses. Simplicity of the bending test in determining elastic modulus is worth considering in comparison to tensile tests, which often suffer from fixation, gripping and alignment problems. To perform the three-point bending test, beam samples with a length of 40 mm, width of 10 mm and thickness of 2 mm were prepared. The bending tests were conducted using a standard tensile/compression testing machine. A biaxial strain gauge, Figure 4-5, was attached to the specimen to measure strains along the axial and transverse directions during the loading process. The load was applied by the mechanical test system operating with a displacement rate of 0.5 mm/min. The macroscale bending tests consistently led to the elastic modulus (E) of 95 GPa with the Poisson's ratio (ν) of 0.35. The obtained elastic modulus was observed to be less than what is typically reported in literature ~110 GPa. The latter magnitude was measured using ultrasonic techniques; this may be the reason for the discrepancy between the magnitudes.

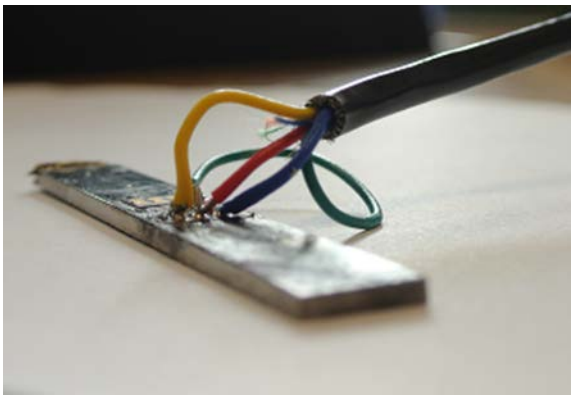

Figure 4-5 Specimen for three-point bending test with strain gauge attached.

As described previously, the elastic modulus can be derived from the properties of constituent metallic elements and the other dependent on the particular glassy configuration prepared using a modified rule of mixture as suggested by Liu and Ma [16,17]. As a result, the global elastic moduli of metallic glasses (G) can be calculated for iso-stress conditions:

$$\frac{1}{G} = \frac{V_m^M f^M}{G^M V_m} + \frac{V_m^S f^S}{G^S V_m}, \qquad 4\text{-}1$$

where V_m^M and V_m^S are the molar volumes of the matrix and clustres/superclusters, respectively, G^M and G^S are their elastic moduli and f^M and f^S are the fractions of the two phases (considering $f^M + f^S = 1$). The above equation can be converted, if the molar volume of MGs is considered as the average of those of the two phases weighted by their fraction following $\overline{V_m} = V_m^M f^M + V_m^S f^S$:

$$\frac{1}{G} = \frac{1}{G^M} - \frac{(G^S - G^M)V_m^S f^S}{G^M G^S} \cdot \frac{1}{V_m}. \qquad 4\text{-}2$$

The shear modulus of two phases can quantitatively be expressed using the calculated values of BMGs G_{cal} by the conventional "rule of mixture" under iso-stress condition, where $G^M = AG_{cal}$ and $G^S = BG_{cal}$ are for the solvent matrix and the clusters/superclusters, respectively, where $0 < A < 1$ and, generally, $B > 1$. Accordingly, the calculated shear modulus normalised by the experimental one $\frac{G_{cal}}{G}$ can be described as

$$\frac{G_{cal}}{G} = \frac{1}{A} - \frac{(B-A)V_m^S f^S}{AB} \cdot \frac{1}{V_m} \qquad 4\text{-}3$$

Weng and Jiang [114] showed that the elastic properties of BMGs can be closely related to their molar volume by universal power relations. Hence, the elastic moduli vary almost linearly with the molar volume, when plotted in logarithmic scale. The general trend can be described as $\bar{V}_m \propto G^m$ and $\bar{V}_m \propto K^{-n}$, where the constant exponents m and n are fitted as $m = 0.5184$ and $n = 0.4173$, respectively. By using the mentioned relationship, Eq.4-3 can be converted into

$$\frac{G_{cal}}{G} = a - bG^m, \qquad 4\text{-}4$$

Where $a = \frac{1}{A}$ and b scales with $\frac{(B-A)V_m^S f^S}{AB}$. In addition, the ratio between the calculated bulk modulus and the experimental one can be expressed as:

$$\frac{K_{cal}}{K} = c - dK^n, \qquad 4\text{-}5$$

Where c and d are the newly introduced parameters. Table 4-1 presents the fitted values of the parameters a, b, c, d and V_m^{bas} for Zr and Cu alloys. It can be observed that the characters of amorphous structures of MGs can be determined to a large extent by the nature of the corresponding base elements. In addition, the properties and behaviour of glassy materials can be characterised from the composite perspective. On the other hand, the present relationships provide the possibilities to predict accurately and design the elastic modulus of MGs from their composition.

Table 4-1 Fitted values for the parameters a, b, c, and d in Zr-Cu-based metallic glass and the molar volume of the corresponding based elements [16].

Metallic glass	a	b	c	d	$V_m^{bas}(cm^3mol^{-1})$
Zr ($f_{Be} < 15\ \%$)	3.1599	0.3435	2.8291	0.2809	14.02
Zr ($f_{Be} < 15\ \%$)	3.2553	0.3340	3.1328	0.3163	14.02
Cu	2.6686	0.2580	2.4942	0.2296	7.11

To calculate E, the conventional rule of mixture is used by considering the iso-stress assumption (Eq. 4-6) to calculate G_{cal} and K_{cal} and then substitute them into 4-4 and 4-5 to predict precisely the shear and bulk moduli of BMGs.

$$\frac{1}{P} = \sum \frac{V_m^i}{P^i V_m} \ (iso - stress) \qquad 4\text{-}6$$

In addition, the elastic constants for isotropic materials are related according to $E = 2G(1+\nu) = 3K(1-2\nu)$, where E and ν are the Young`s modulus and Poisson`s ratio, respectively. Hence, all the elastic properties can be determined as soon as $G$and K are quantified independently. In $Zr_{48}Cu_{36}Al_8Ag_8$ (at%), both Zr and Cu can be considered as the base elements according to the percentage of Zr and Cu in the metallic glass composition. The Young`s modulus was determined based on its constituent elements.The Young`s modulus of $Zr_{48}Cu_{36}Al_8Ag_8$ (at%) was calculated using the above equations; the modulus value was approximately 92 GPa. This measured value is comparable with the results obtained in the 3-point bending and DMA experiments. It was also found

that the compliant solvent matrix for the studied BMG was copper (Cu), as the diffraction equations (from Eq.4-4 and Eq. 4-5) cannot be solved for the Zr-based element.

The fracture-surface morphology on both tension and compression sides of specimens tested in three-point bending was studied. Figure 4-6 shows SEM images of the failure pattern and fracture-surface morphology of the Zr-Cu-based BMG. In compression mode, the fracture surface is typically smooth with periodic bands in the direction of fracture. Formation of a vein pattern indicates that fracture occurred in compression mode while river patterns are related to the fast tensile fracture mode. The differences in fracture surfaces are associated with the influence of the normal stress and the dominance of shear stress in tension and compression modes, respectively. A shear band zone can be found in both tension and compression sides as shown in Figure 4-6. Some branches of these structures can be found at the sites where the propagation direction deviates from the case of the maximum shear stress. This behaviour is distinctly different from the case of propagation of principle shear bands along slip plan, which was widely reported in the literature [64,115,116].

The process of shear bands formation makes the material softer thanks to dilataion of shear bands and temperature rise inside them [117]. Hence, shear bands play the weakening role in materials, showing lower strength and stiffness compared to the undeformed BMG matrix. Thus, it is important to characterise fracture surface using the indentation technique, which will be presented in Chapter 7.

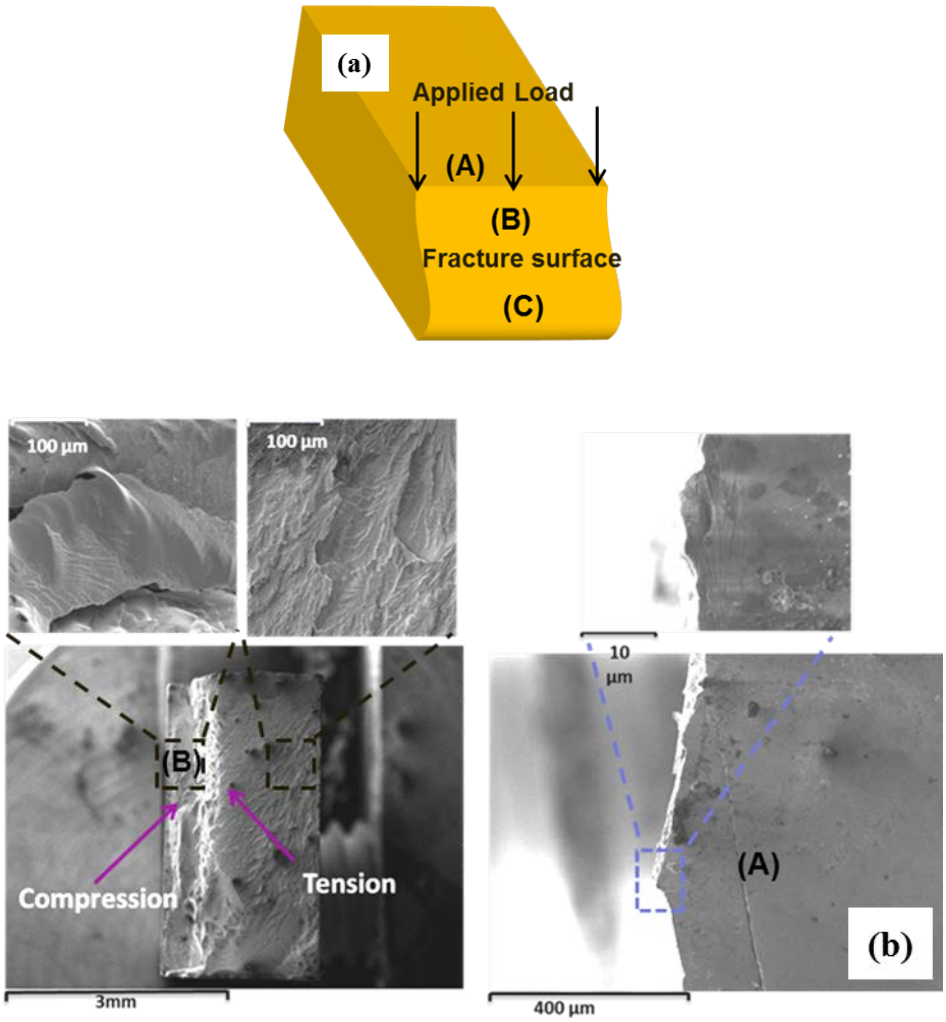

Figure 4-6 (a) Schematic of fracture surface observation of fracture surfaces of $Zr_{48}Cu_{36}Al_8Ag_8$ metallic glass under three-point bending loading mode (b) SEM observation of the fracture surface in compression and tension mode. High magnification images clearly show the presence of vein pattern on fracture surface and slip steps associated with shear bands.

4.2 Micro/nano scale characterisation of Zr-Cu-based metallic glass

4.2.1 Nanoindentation

4.2.1.1 Experimental Procedure

All the tests on BMG specimens for measuring the elastic modulus and hardness were performed at room temperature (23ºC). Both load- and displacement-controlled nanoindentation tests were performed. A holding (dwell) time was set 60s to allow negligible creep displacement. A thermal shift correction was used so that absolute values of a thermal drift rate were usually well below 0.05 nm/s. In this present study to capture the first pop-in, a spherical indenter was used with a radius of 5 µm with a conical shape with a spherical tip Figure 4-8 (b). Obviously, only the indenter's tip was used to penetrate the specimen surface in indentation tests.

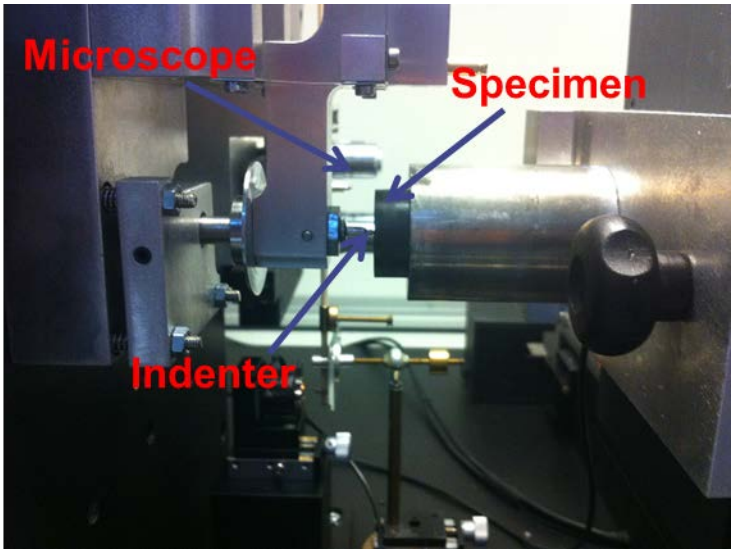

Figure 4-7 Experimental arrangement for indentation test of MG.

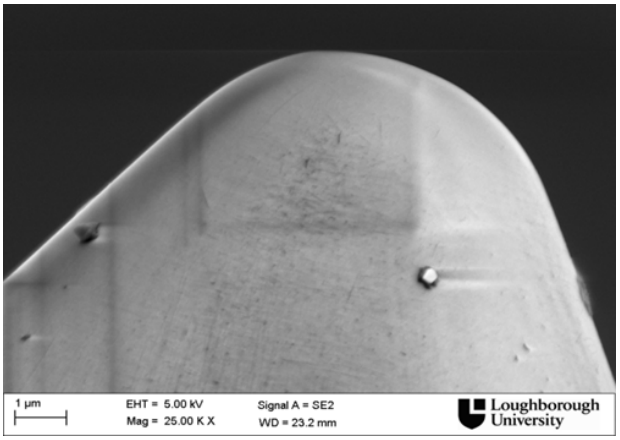

Figure 4-8 Tip of spherical indenter used for nanoindentation testing with nominal tip radius of 5 µm.

4.2.1.2 Results and Discussion

To investigate initial elastic deformation, a maximum load of 10 mN was applied with a loading rate of 0.1 mN/s to specimens in the nanoindentation test. The estimated yielding load was 3 mN for a typical Zr-based BMG for a 5 µm spherical tip following the work of Packard and co-workers [118]. Figure **4-9** showed the response of the BMG to nano-indentation loading, holding and unloading cycle with maximum loads of 2 mN and 3.5 mN, respectively. It can be seen that the loading and unloading responses are similar below 4 mN, with no obvious disparity between the two, implying pure elastic deformation.

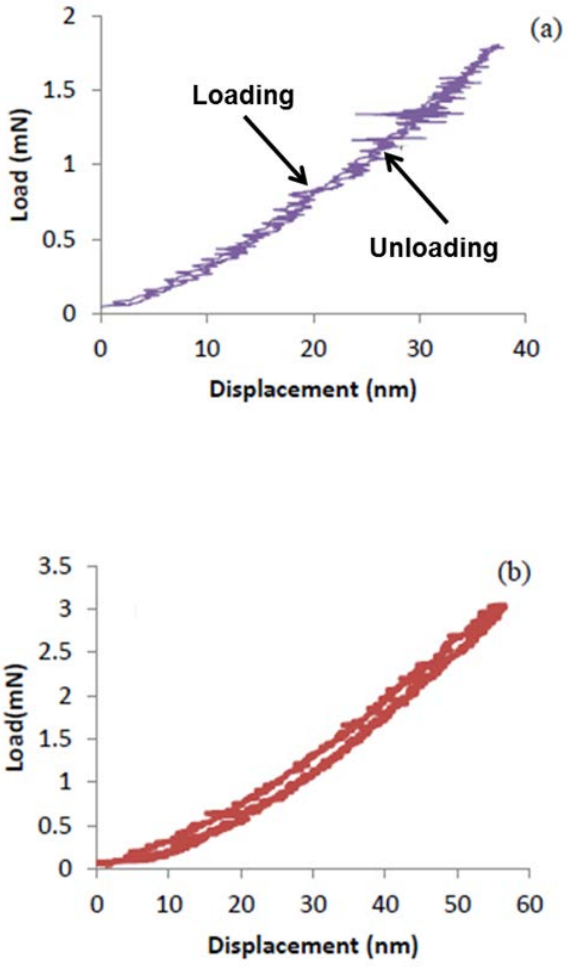

Figure 4-9 Typical load-displacement plot for Zr-based BMGs at loading rate of 0.1 mN/s: (a-b) purely elastic deformation.

A presented load-displacement plot for 16 mN (Figure 4-10) is a typical example for several tests, showing closely correlated pop-in events. A significant plastic event was observed at around 4 mN (see Figure 4-10), which was considered to be the first pop-in event. It is associated with an initiation and propagation of an individual shear band underneath the indenter tip. As can be seen in Figure 4-10, other pop-in events were found to occur at ~5 mN, ~7 mN and ~9 mN.

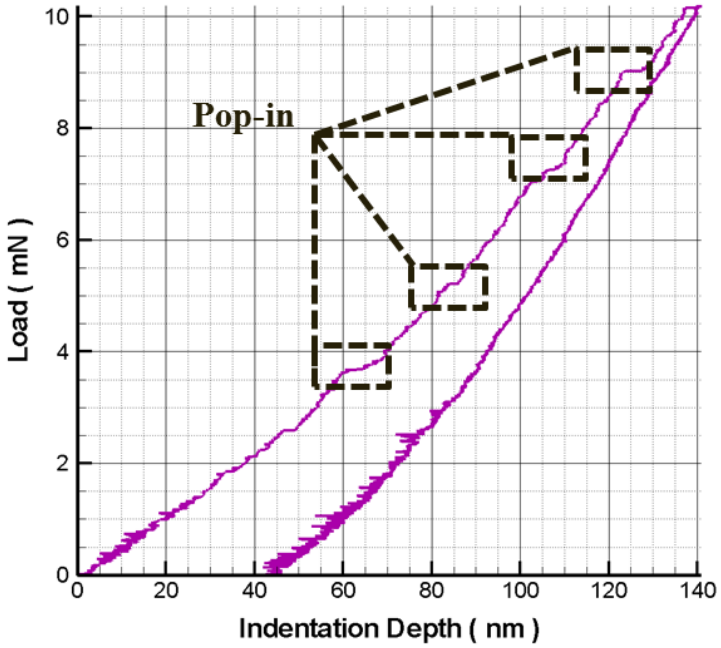

Figure 4-10 Typical load-displacement response of $Zr_{48}Cu_{36}Al_8Ag_8$ at loading rate 0.1 mN/s showing initial deformation.

In order to assess the evolution of shear bands in the BMG material, loading–unloading cycles were carried out at higher load magnitudes with the aim of observing shear steps on the material's surface. Such steps in spherical indentation of BMG were found at loads in excess of 100 mN. Features of shear bands at various loads in a range from 130 mN to 275 mN are shown in Figure 4-11 (a-d). The shear bands originated from the periphery of residual impression and moved outwards in direction of shear stresses on the free surface. The shear bands were not straight, but spiral in shape. This is because along the lines of shear bands, directions of the radial, hoop and, thus, shear stresses changed constantly in a spiral fashion [119]. It can be seen in Figure 4-11 (a-d) that these bands were not cracks but overlapping layers of an upwardly displaced material. Owing to a volume- conserving nature of plasticity,

deformation in elastic-perfectly plastic solids occurred in form of pile-ups of the material against the faces of the indenter. These pile-ups were seen as discrete steps due to the inhomogeneous nature of plastic deformation in MGs (see Figure 4-11 (f)).

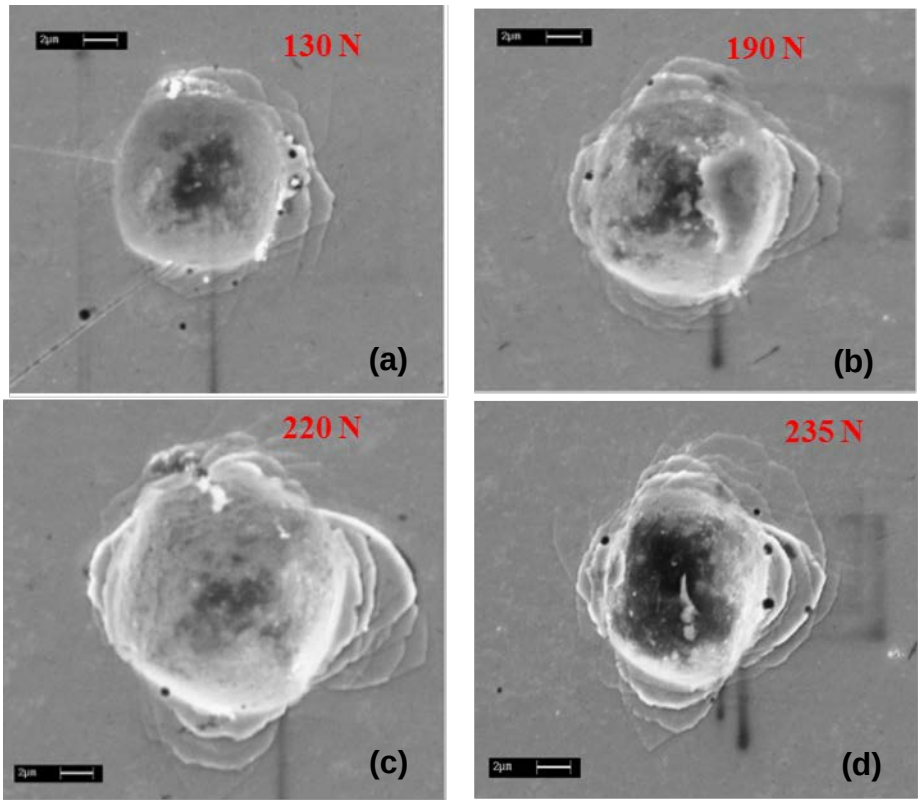

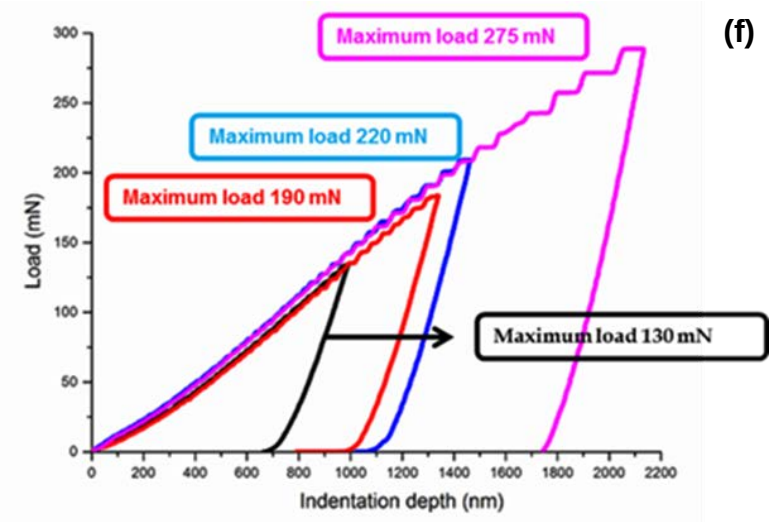

Figure 4-11 SEM images of evolution of shear-band patterns with incremental loading-unloading at loading rate of 2 mN/s: (a) 130 mN; (b) 190 mN; (c) 220 mN; (d) 235 mN. (f) Respective load-displacement curves.

Subsequent fractographic analysis also revealed the evolution of shear bands on the surface with increasing magnitudes of load/displacement (Figure 4-11). In other words, the number of shear bands increased dramatically with increasing load. Interestingly, the spacing between the semi-circular shear bands was not constant. As can be clearly seen in Figure 4-11((a-d)), there were concentrations of shear-bands at four corners of indentation imprints, with several intersecting shear bands. Incidentally, the elastic modulus obtained from the unloading part of the load–displacement curves indicates that E = 86 GPa in other tests is accurate.

The incremental loading-unloading experiments were also performed to investigate a hardening (or softening) effect on yield stress, hardness and an elastic modulus as this technique allows for measurements of these parameters at different indentation depths for the same location in the specimen. These experiments were performed using a spherical tip with 5 µm diameter in the load range from 7 mN to 27 mN with the same loading rate – 0.1 mN/s. Unloading was performed with the rate of 0.1 mN/s down to a prescribed limit of 20% of the load peak in the previous cycle. As shown in Figure 4-12, pop-in events took place in each reloading stage at higher levels than those in the previous cycle, demonstrating an increase in the first pop-in from ~4 mN to ~21 mN.

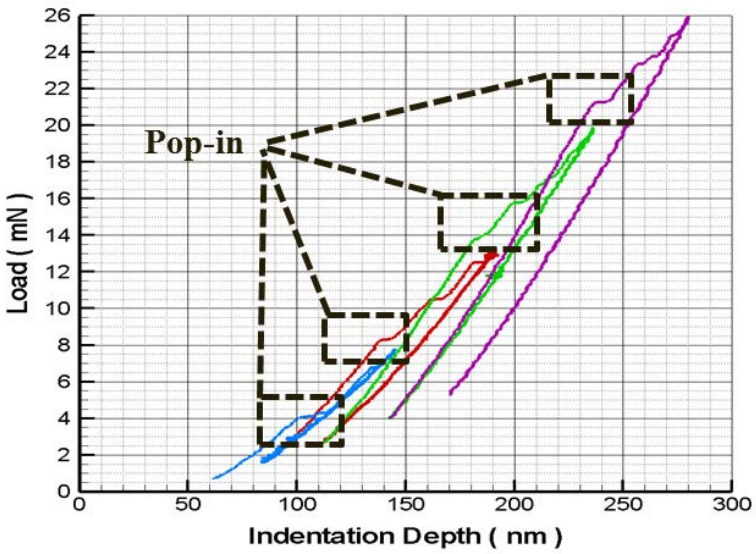

Figure 4-12 Indentation load-depth plots for $Zr_{48}Cu_{36}Al_8Ag_8$ under incremental loading-unloading nanoindentation at load rate of 0.1 mN/s.

As mentioned earlier, the pop-in events depend on composition and a free-volume content of MGs as well as on parameters of the experimental procedure such as a tip shape and applied loading rates. The maximum shear stress (τ_{max}) at the first-pop-in corresponds to the critical shear strength of the onset of plasticity in the indented material. In spherical indentation, τ_{max} occurs at a distance of approximately half the contact radius, directly below the rotational axis of the contact and can be calculated as [59]:

$$\tau_{\max} = 0.31\left(\frac{6{E_r}^2}{\pi^3 R^2} P_I\right)^{1/3}, \qquad 4\text{-}7$$

where P_I is the load at the first pop-in, R is the indenter radius and E_r is the reduced modulus, which was around 95 GPa. There was a significant rise – some 50%) – in the average value of $\tau_{\max}$ as the first pop-in load increased from ~4 mN to ~15 mN. Initially, the maximum shear stress was approximately 2 GPa

for in the former load, increasing to around 3.45 GPa at the latter one. This is the evidence of the hardening effect caused by multiple loading-unloading cycles; the reason for this phenomenon is explained below.

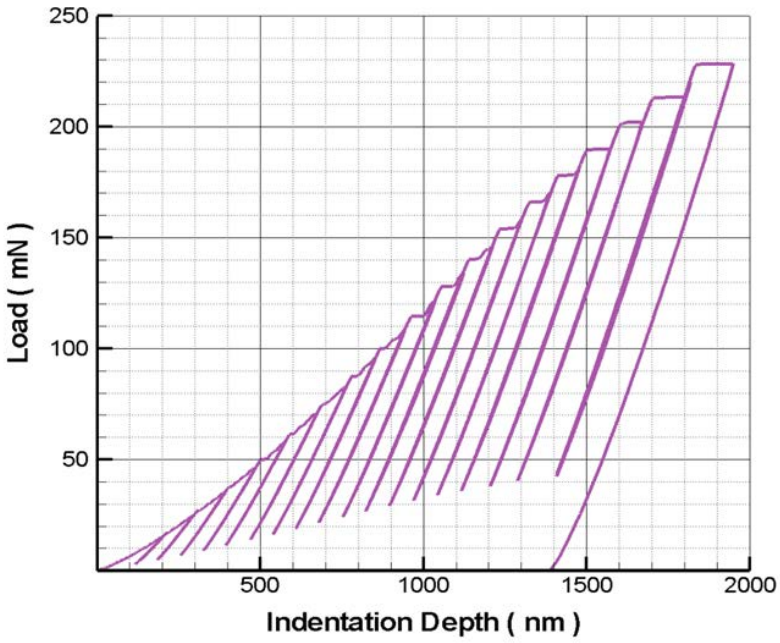

Figure 4-13 Indentation load-displacement curve for Zr-based MG for incremental loading-unloading at loading rate of 2 mN/s.

Subsequently, multiple unloading-reloading experiments were performed using a loading rate of 2 mN/s to investigate variations of hardness and the elastic modulus with depth in MG specimens. The maximum applied indentation depth ranged between 200 nm and 2000 nm and 20 partial unloads down to 20% of the peak load at each step were applied in these tests. As discussed previously, a large plastic zone was formed under the indenter tip in indentation [63,120]. This zone contained a high density of shear bands, which is ideal for investigation of deformation-induced hardening and softening effects [120]. Our results show the dependence of hardness on the penetration depth indicating a work-hardening

phenomenon in the studied metallic glass, especially at nano-scale (see Figure 4-13). It is clear (Figure 4-13) that the onset of yielding upon each reloading always took place at a higher load than in the previous cycle, apparently suggesting the hardening effect. In addition, the level of hardness increased from 3.7 GPa to 5.7 GPa with a sharp enhancement in the first 10 cycles and a slight rise in the subsequent 10 cycles. This can be described employing ideas of a free-volume evolution proposed originally by Spaepen [120]. According to this model, the change of free volume (which is a thermally activated process) is a competition between the free-volume accumulation in a stress-biased system and the free-volume annihilation by local rearrangements of atoms. During the unloading process, the latter is the dominant process thanks to a sudden reduction of the applied stress. This results in relaxation of the free volume, leading to an immediate arrest of propagating shear bands and a significant temperature decrease inside shear bands because of their arrest. As a result, hardness increased due to decreasing temperature magnitude and free volume [121]. At the next reloading step, previously generated shear bands remained arrested resulting in an increase in hardness. However, with the onset of initiation and propagation of multiple shear bands, the increased free volume in the propagating shear bands caused a reduction of hardness, known as the *recovery phenomenon*. The measured hardness was a combined response of propagating and arrested shear bands as well as the undeformed region in the material [44].

A strain rate is a more suitable parameter to describe inhomogeneous deformation according to the classic free-volume theory [122]. A constant loading

rate can be converted into a representative strain rate using the following equation [122]:

$$\dot{\varepsilon} = \frac{\dot{P}}{2P}, \qquad 4\text{-}8$$

Figure 4-16 presents a P-h curve obtained with the loading rate of 2 mN/s for a termination load of 16 mN, with the inset presenting the corresponding conversion from the loading rate to the strain rate. The discrete serrated flow can be observed for indentation depths in excess of 50 nm, where the strain rate is below 0.02 s^{-1}. In other words, lower strain rates promote more pronounced serrations, and high rates supress the serrated flow. Hence, the pop-in events for this metallic glass, demonstrated as the stepped P-h curve, showed significantly strong rate-sensitivity. The serration flow behaviour can be analysed using the notions of free volume and localised heating mode.

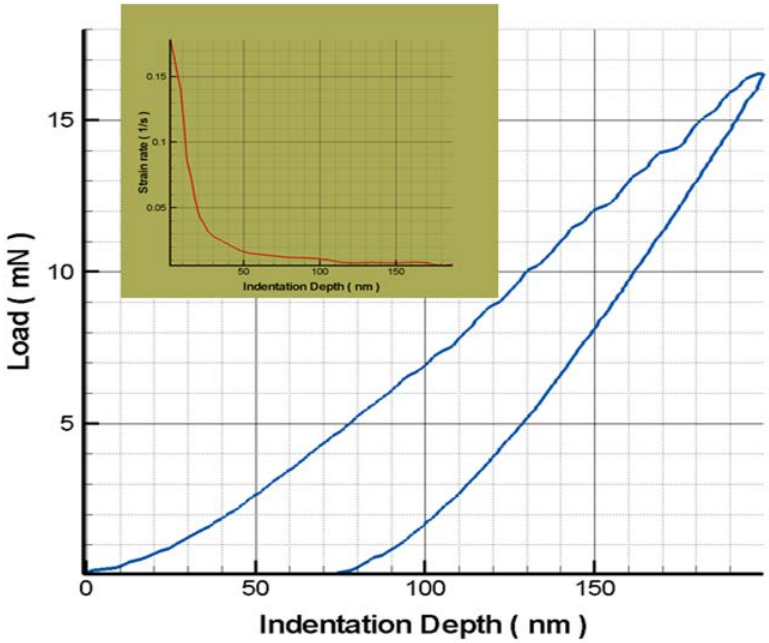

Figure 4-14 Representative P-h curve for loading rate of 2 mN/s demonstrating discrete serrated flow (The inset shows a conversion from the loading rate to the strain rate).

Several researchers showed that temperature rises (from 0.1 K to ~ 1000 K) occured inside shear bands. Such temperature rises resulted in appearance of droplets on fracture surfaces. Therefore, it is important to study the mechanism of shear-band softening to understand whether a temperature rise or/and free-volume increase was the underpinning mechanism. Both mechanisms cause a lower viscosity of metallic glasses resulting in shear-band propagation and formation. Eshelby and Pratt [123] proposed the following equation to predict a temperature rise inside a shear band:

$$\Delta T = \frac{\tau \dot{\gamma}_b h}{2\pi k} \sqrt{\frac{\pi k \Delta \gamma}{C_p \dot{\gamma}_b}}, \qquad 4\text{-}9$$

Here, shear yield stress τ is 925 MPa for the studied BMG, which is half of compression yield strength (1850 MPa), assuming an angle of 45º to the loading axis. The shear strain rate $\dot{\gamma}_b$ inside the shear band is estimated to be 10^3 $s^{-1}\{\{415\ \text{Neuhäuser, H}\ 1978\}\}$. The shear-band thickness h, thermal conductivity k and specific heat capacity C_p are ~ 10 nm, 20 w/(m K) and 0.33 J/(g K), respectively [38]. The average displacement burst Δh for each serration was 2 nm. Plastic deformation was considered to proceed in the plane of the shear band; the shear strain $\Delta\gamma = \Delta h/h$ can be calculated as 0.20. Hence, the temperature rise was around 0.04 K after substituting the above data into Eq.4-9, similar to experimental measurements of the local temperature rise under quasi-static loading [124]. It was shown that the temperature rise is negligible at low strain rates; therefore it could conclude that the onset of serration was controlled

by the free-volume creation and annihilation leading to formation of shear bands. Under high-strain-rate deformation the temperature rise might occur and affect shear-band propagation.

To study high strain rates, an impact regime of nanoindentation was implemented employing a pendulum-based impact test with the Nano Test system using a diamond spherical probe of radius R = 5 µm. The operating principles of the experimental set are outlined in [125]. This regime can be used for analysis of low cycle-fatigue, work hardening and dynamic hardness. In this experiment, the pendulum is moved away from the specimen by a known distance and then released to produce a single impact. Successive impacts can be performed at a single point until failure occurs. In most cases, an initial period is characterised by damage generation, with cracks developing and expanding, but in which no appreciable increase in penetration depth in observed. Figure 4-15 illustrates that there is an evidence of strain hardening as there is a significant increase in displacement (penetration depth) in the first 30 seconds, where the cracks coalesce, and a slight enhancement afterwards. Additionally, these results indicate that the Zr-Cu-based MG is an elastic-perfectly plastic material since the material demonstrates linear elasticity followed, as the load increases to the yield point, constant stress at strains increased.

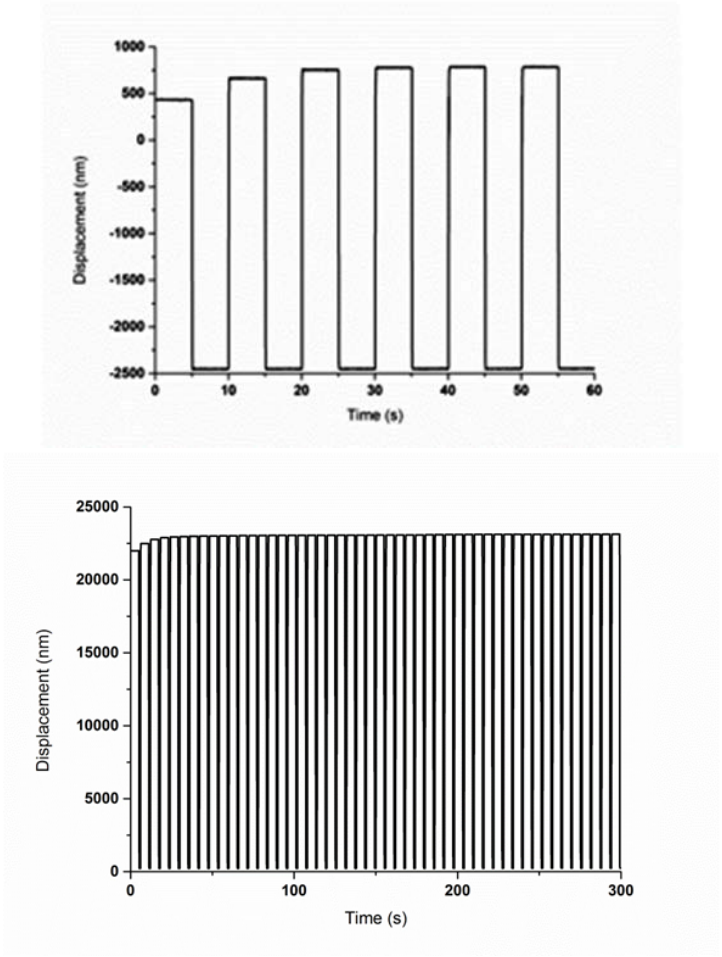

Figure 4-15 Typical displacement-time plot of impact results for Zr-based BMGs (a) for 60 s; (b) for 300 s.

4.3 Micro-indentation

Micro-indentation experiments were conducted using a spherical indenter with diameter 50 μm at loading rates of 2 mN/s with maximum load of 15 N. While shear-band slips on the surface were observed around 100 mN in nano-indentation test, this phenomenon in spherical micro-indentation was found at loads in excess of 10 N (Figure 4-16). Based on the Herztain elastic equation for a spherical indenter [43], mean pressure is inversely related to the contact radius and, hence, the radius affects the initial yield pressure, which is revealed on a

pressure-depth curve as pop-in events that occur at yield load and corresponding displacement. In addition, yielding of metallic glasses was initiated at locations of maximum shear stress (τ_{max}) in the volume. As proposed by Greer and co-workers [2], the normalised yield pressure increased with a decreasing indenter tip radius (see Figure 4-16). They found by using indenter tips with various radii that the plastic-flow mechanism was changed, with deformation controlled by heterogeneous nucleation of shear bands for small indenters changing to propagation of already nucleated shear bands at a larger scale. A clear size effect can be observed (Figure 4-16 (b)) as smaller radii give higher levels of normalised yield pressure.

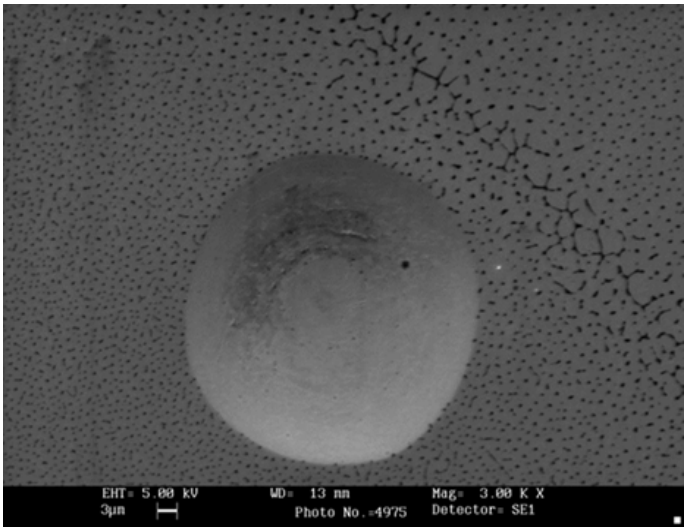

(a)

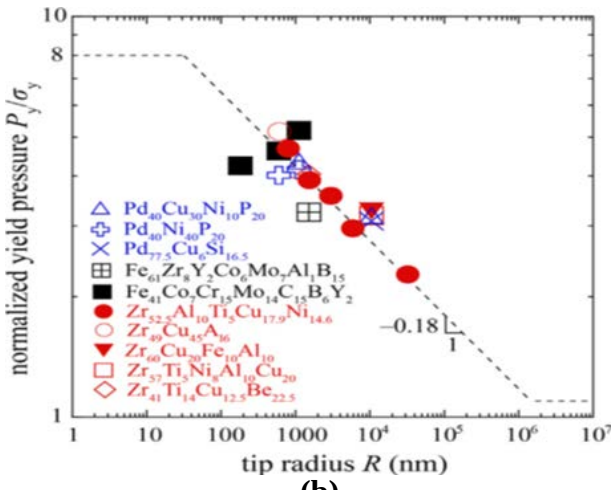

(b)

Figure 4-16 a) SEM images of micro-indents in $Zr_{48}Cu_{36}Al_8Ag_8$. There are no shear bands around the indent with 10 N load. b) Normalised yield pressure versus indenter tip radius for various metallic glasses [2].

These subsequent cycles of loading-unloading in indentation implemented with the aim of assessing the process of evolution of shear bands in the Zr-Cu based metallic glass are exhibited in Figure 4-17. The maximum indentation depth ranged from 6 μm to 18 μm, and three partial unloads down to 20% of the peak load at each step were applied in these cycles. As can be seen in Figure 4-17, a shear band moving from the top right corner (denoted A in Figure 4-17) crossed a shear band coming from the top left corner (denoted B); however, the subsequent nucleated shear bands were arrested by the same shear bands originating from the top left to top right corner. Instability of the shear bands were observed in the form of nucleation of several secondary shear bands from the primary ones during the course of deformation. A high density of shear bands was found.

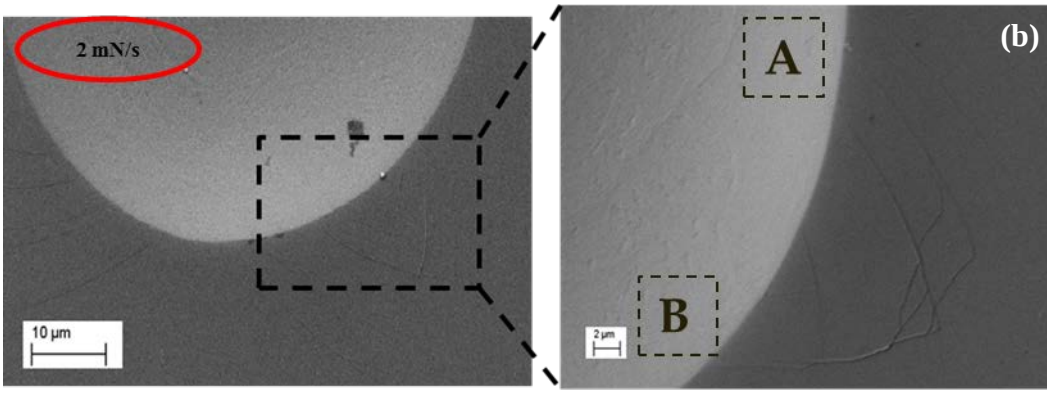

Figure 4-17 (a) Representative load-displacement curves; (b) SEM images of micro-indentation in $Zr_{48}Cu_{36}Al_8Ag_8$ with loading rates 2 mN/s for maximum load of 15 N.

4.4 Summery and conclusion

Experimental techniques employed in the current work are described in this chapter. The used nano-indentation system in this study and the required calibration standards including frame compliance, indenter area function, and cross-hair or targeting alignment were explained in details. In the present study, initial macroscale characterisation of $Zr_{48}\,Cu_{36}\,Al_8\,Ag_8$ was illustrated in order to determine mechanical properties such as the elastic modulus (E), the Poisson's ratio (ν) and glass-transition temperature (T_g). The value of the elastic modulus (E) was confirmed using the modified rule of mixture. In addition, the amorphous nature of the supplied beam samples of the MG was investigated using X-ray diffraction and TEM techniques, which did not show any presence of crystalline structure in the materials. The composition of the locations, where the TEM were obtained from, was tested in-situ with EDS. It was also shown that dynamic characteristics of the metallic glass are effectively independent of the frequency at room temperature. In this study, observation of fracture surface of the of the Zr-Cu-based BMG under three-point bending revealed failure that are different from those observed in crystalline materials.

Indentation techniques were extensively used initially to examine the elastic deformation of the studied BMG alloy, followed by a systematic analysis of initiation and evolution of shear-band localisation in the indented material. Increasing yield strength of the Zr-Cu-based metallic glass was investigated by recourse to spherical indentation experiments employing the incremental loading technique. The load at the first pop-in was converted into the maximum shear stress underneath the indenter with the help of Hertz`s spherical contact

mechanics. The temperature rise, calculated as 0.04 K for the low strain rate, was negligible to have an effect on the deformation mechanism.

5 Experiments under imposed inhomogeneous loading: Wedge indentation

5.1 Design and manufacture of wedge indenter

All parts for wedge indentation studies were designed and manufactured in-house (Figure 5-1 and Figure 5-2). The connection fixture, made from stainless steel, was directly bolted between the indenter and the Instron machine. As the indenter is easily replaceable in the case of mechanical failure, High Speed Steel (HSS) was used to manufacture it.

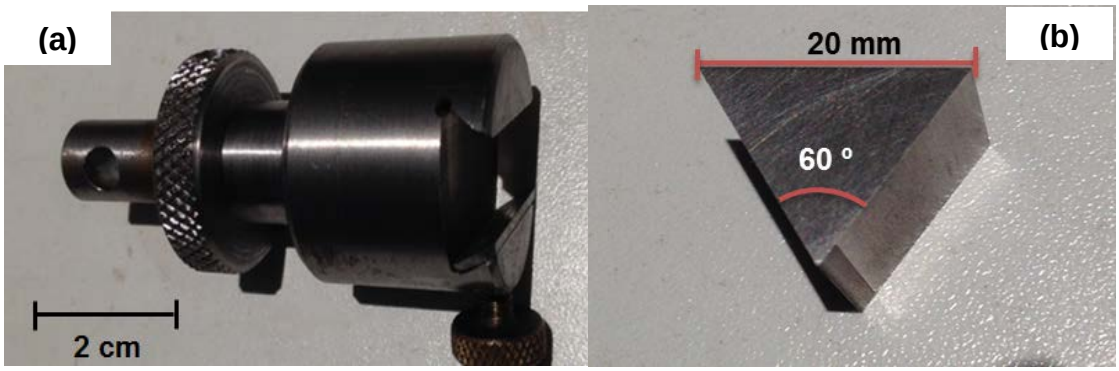

Figure 5-1 (a) Connection fixture (indenter holder) and (b) wedge indenter and its dimensions.

A fixture was designed and manufactured in-house with the capability of applying the load incrementally on the same point of a specimen. The fixture could not move on its own during operation; a spring was installed at one end to ensure the sample remains at the same position.

Figure 5-2 Fixture prototype.

The designed loading jig allowed for a sample-wedge self-adjustment of system with one degree of freedom to minimize misalignment. However, there is still misalignment in the system during the indentation experiment, which is consistent for all the experiments. Figure 5-3 shows the residual indentation imprint corresponding to 1 kN wedge indentation. The shear band patterns exhibit asymmetry due to the minor misalignment between the wedge indenter and the specimen.

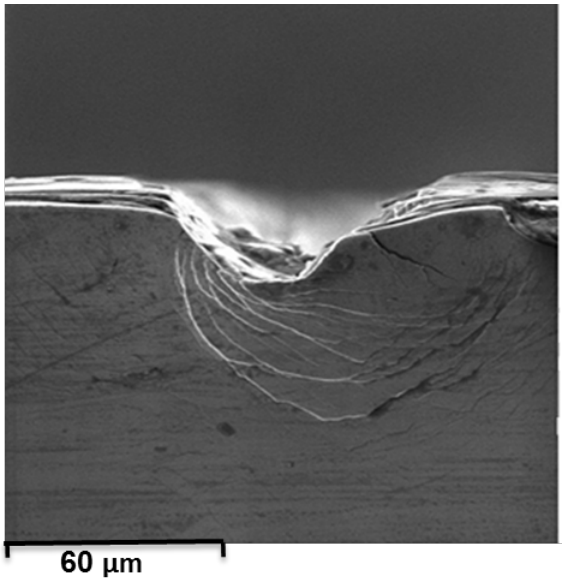

Figure 5-3 SEM image of residual indentation imprint after wedge-indentation experiment under 1 kN single loading condition showing asymmetrical shear-band pattern due to misalignment of system.

In the wedge-indentation experiments, load up to a maximum of 3 kN can be applied to the BMG samples. Therefore, the fixture and the wedge indenter which would remain undamaged under high loads were essential. Finite element analysis with the ABAQUS software was used to determine the displacement of the fixture, when subjected to a surface load and a line load; the former represents the load applied by the wedge and the latter represents a general load of 3 kN applied to the surface of the fixture. For the simulation, the fixture was fixed using fixed boundary conditions on the bottom face (Figure 5-4) as this face was expected to be stationary throughout the whole indentation process. The fixture made of stainless steel was considered to be an elastic isotropic material. All the mechanical properties of the steel (Table 5-1) were obtained from the supplier.

Table 5-1 : Mechanical properties of stainless steel.

Material	Density (ρ)	Young`s modulus(E)	Poisson's ratio (ν)
Steel	7.85 kg/m^3	210 GPa	0.3

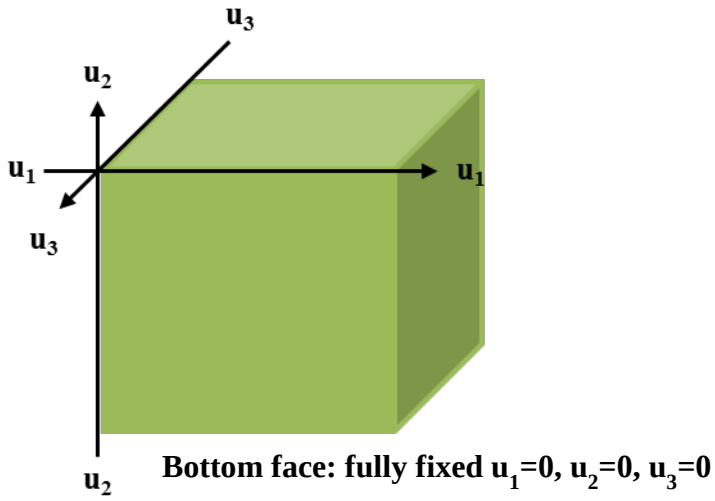

Figure 5-4 Boundary condition for FE simulation of wedge indentation fixture.

The colours represent the magnitude of the U2 (Y) direction; this orientation was selected because the load would be effectively applied along the Y direction in the experiments. For the line load of 3 kN, it can be seen that the fixture displaces with a maximum of -1.26×10^{-2} mm in the U2 direction (see Figure 5-5). For the four corner and centre loads, the maximum displacement in this direction is approximately -1.77×10^{-2} mm (see Figure 5-6). The models suggested that for loads of up to 3kN, the fixture was unlikely to deflect significantly to cause any damage; however, this deflection would modify a force-displacement graph in the wedge- indentation test results.

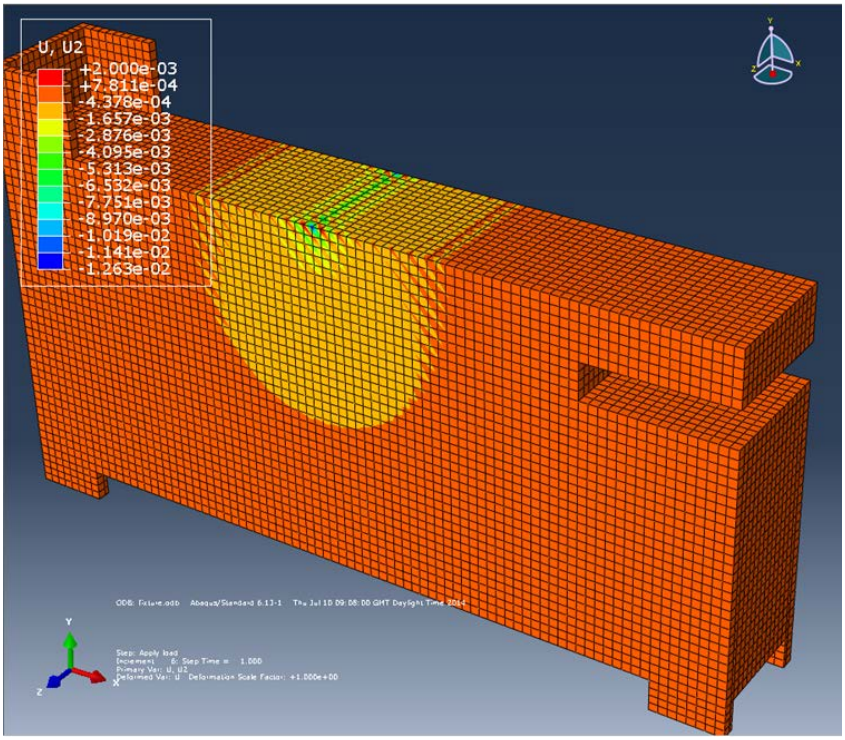

Figure 5-5 Displacement in mm distribution along loading direction for line load of 3 kN.

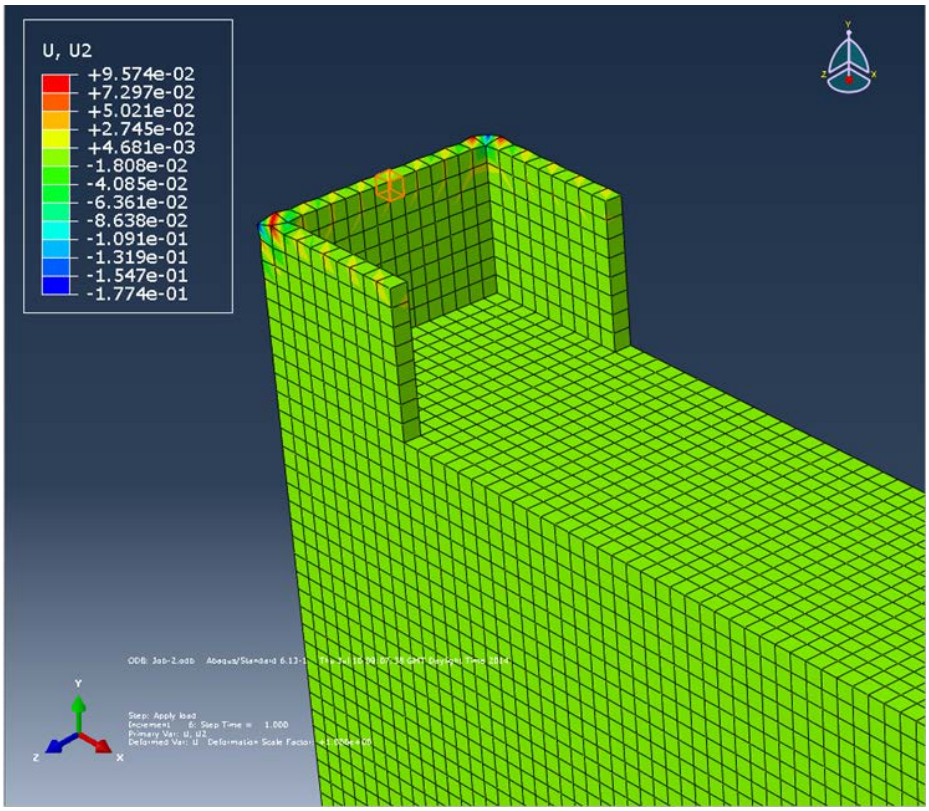

Figure 5-6 Displacement filed along loading direction for four corner loads.

Finite-element analysis with the ABAQUS software was also applied to determine the deformation of wedge indenter made from high speed steel (HSS) during wedge indentation experiment. The simulation results illustrated that there is no deformation on the indenter at the maximum applied of 4 kN.

5.2 Wedge-indenter characterization

Prior to carrying out the experiment, it was required to characterize the wedge indenter as its properties would be used in complex calculations in order to identify the level of yield stress corresponding to shear band initiation. The parameters include the indenter radius, r, the height of the cap, h, the hight of the flank in contact with the wedge indenter, a, in addition to the angle of the assembled wedge indenter (Figure 5-7). These values were required to calculate the contact surface of the indenter tip with a specimen (A_{total}) in the indentation experiments to estimate the applied force for shear-band initiation. These parameters were measured using Infinite Focus Alicona Ltd. (Figure 5-8), a non-destructive 3D measurement system with an optical technology based on focus variation. Three different positions including two corners and the middle of the indenter tip, as shown in Figure 5-9 (a), were used to measure the parameters mentioned above. These values were 60.50, 60.72º, 60.55º, respectively, and the mean value of these three angles was 60.60º.

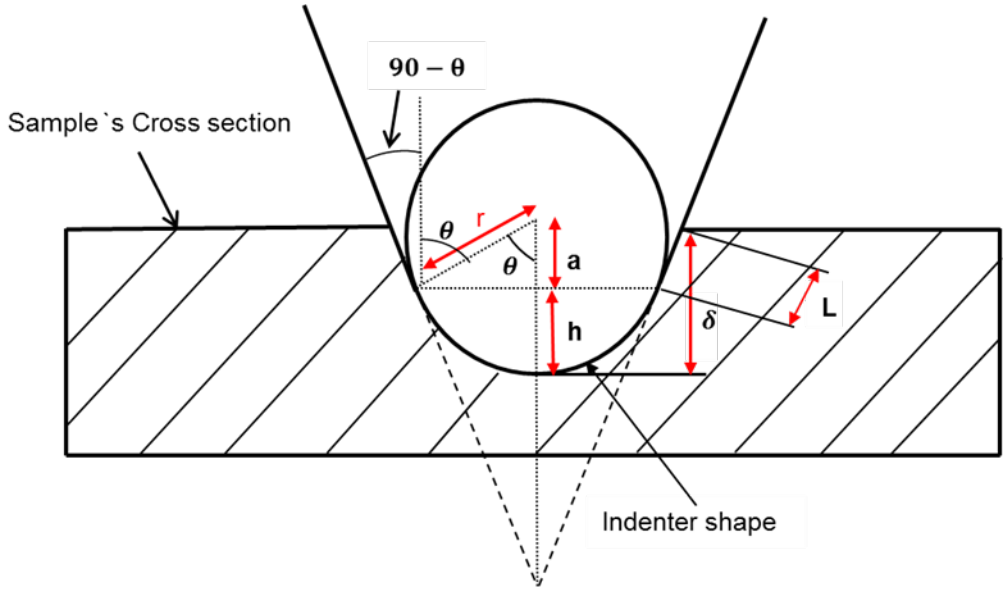

Figure 5-7 Schematic illustrating cross-section of wedge indenter. δ is the height of the tip in contact with the sample and L is the length of the flank side in contact with sample.

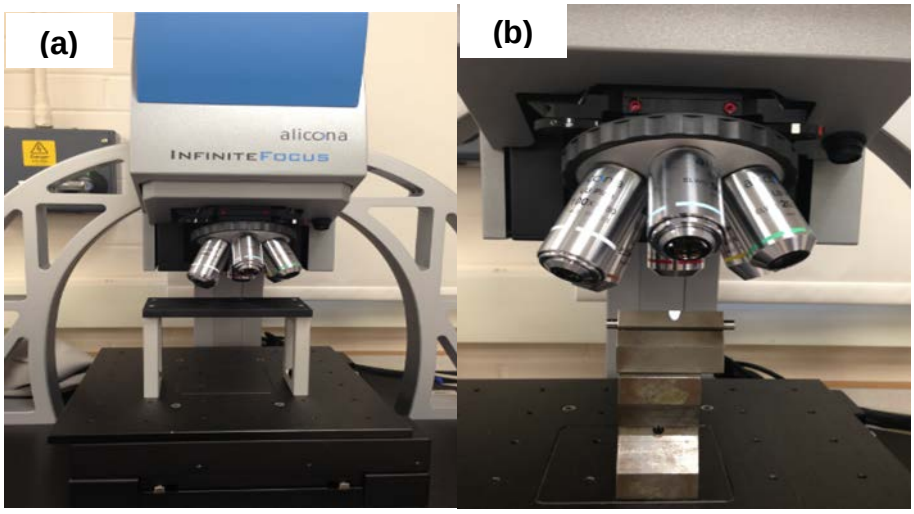

Figure 5-8 (a) Alicona Infinite Focus; (b) experimental setup used to charaterise manufactured wedge indenter.

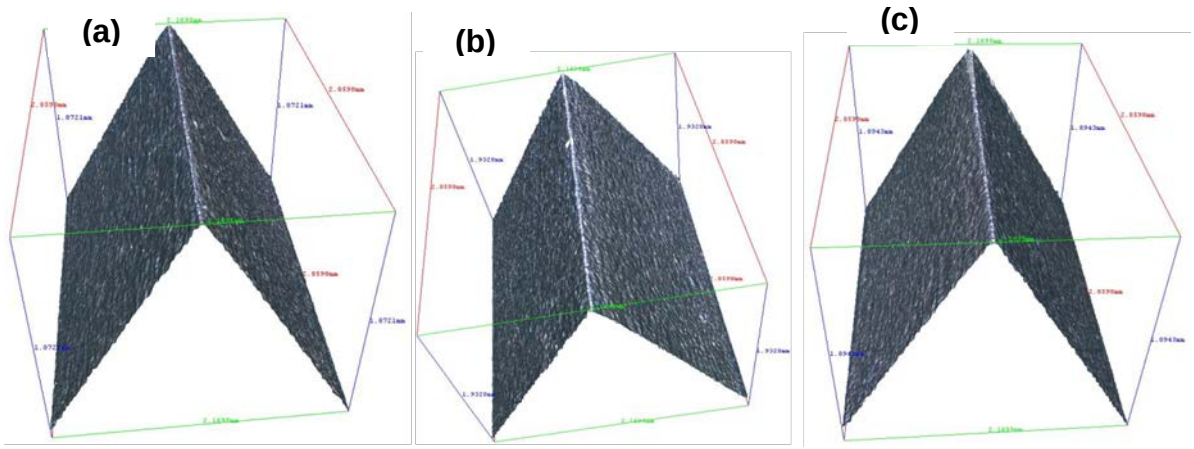

Figure 5-9 3D profiles of wedge indenter including its left corner (a), the middle of indenter (b) and (c) the right corner obtained with Alicona optical microscope.

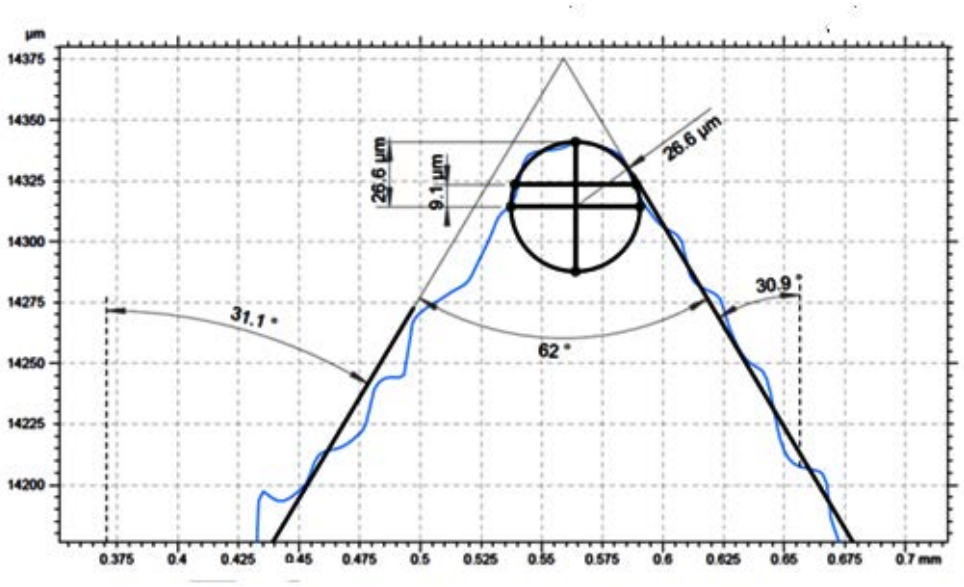

Figure 5-10 Diagram obtained with Alicona Infinite Focus showing indenter radius, $\boldsymbol{r}$, height of cap, $\boldsymbol{h}$, height of flank in contact with wedge indenter, $\boldsymbol{a}$, in addition to angle of assembled wedge indenter.

As presented in Figure 5-10, the indenter radius, r, the height of the cap, h, and the height of the flank in contact with the wedge indenter, a, were 26.6 µm, 9.1 µm and 17.5 µm, respectively. The average values of these parameters at the three mentioned positions were 24.47 µm, 8.4 µm and 15.87 µm. A stress value

for the first pop-in was required to be calculated to estimate the applied force in wedge indentation for initiation of first shear bands. As presented in Figure 4-10, the first pop-in occurred at applied force of 4 mN in nano-indentation experiments showing indentation depth of 0.060 µm. The contact area between the spherical indenter and each specimen was considered as spherical cap (Figure 5-11). An area of this spherical cap is $A_{cap} = 2\pi rh$, where r is the indenter radius and h is the indentation depth. Hence, the total area of the contact and required stress for the first pop-in are 1.88 µm^2 and 2.12×10^9 N/m^2, respectively.

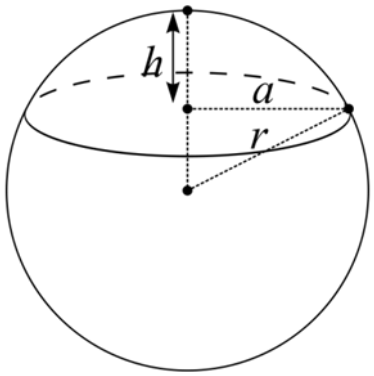

Figure 5-11 Schematic of spherical cap showing contact area between spherical indenter and BMG specimen.

It was also necessary to determine the contact area with the sample in the wedge-indentation experiments in order to predict an approximate force needed to initiate the formation of shear bands. The force applied could be calculated using the following equation:

$$F_{applied} = \sigma * A_{total\ in\ contact}\ , \qquad 5\text{-}1$$

where F is the applied force on the sample and $A_{total\ in\ contact}$ is the total area in contact with the surface of sample. As shown in Figure 5-14, the wedge indenter had two parts including an indenter tip and a cone side in which the total contact surface depends on the total height of the tip that contact with the sample (δ). If δ is larger than the height of the indenter tip (h), then the total surface contact can be calculated using:

$$A_{tot} = A_{arcside} + 2 * A_{flank}. \quad 5\text{-}2$$

Therefore, denoting the width of the sample as *w*, the area of the arc is:

$$A_{arc\ side} = length\ of\ an\ arc \times width\ of\ sample = 2\pi r \times \left(\frac{2\alpha}{360}\right) * w, \quad 5\text{-}3$$

where $\alpha = \theta = \arccos\left(\frac{r-h}{r}\right)$ and *h* and *a* can be obtained using the data from the Alicona test. As shown in Figure 5-14, the flank side area can be calculated using:

$$A_{flank\ side} = L \times w = \frac{\delta - h}{\cos(90 - \theta)} \times w \quad 5\text{-}4$$

Therefore the total area is

$$A_{total} = 2\left[\pi r\left(\frac{2\theta}{360} degrees\right) + \frac{\delta - h}{\cos(90 - \alpha)}\right] w. \quad 5\text{-}5$$

If the total height of the tip in contact with the sample is less than the height of the arc part, i.e. $\delta < h$, then the total area is:

$$A_{total} = A_{arc\ side} = 2\pi r\left(\frac{2\theta}{360}(degrees)\right) w \quad 5\text{-}6$$

5.3 Shear-band initiation

The aim of this experiment was to characterise initiation of the first plastic event in order to calculate the yield stress of the bulk metallic glass investigated in this study. It was found that the required load would be around 500 N using Eqs.5-1 and 5-6, where the values for the total contact area and required stress were 23.636 mm^2 and 2.12×10^9 N/m^2, respectively; hence, testing was carried out using the beam-shaped samples with the length of 40 mm, width 3 mm and thickness of 2 mm in a compression mode with a constant displacement rate of 0.05 mm/min using the wedge-indentation technique and the load value in the range from 200 N to 500 N. To avoid contact problems at low loads, the surfaces of the wedge indenter were ground using a surface grinder in an attempt to make the edge more uniform while maintaining the 60º angle.

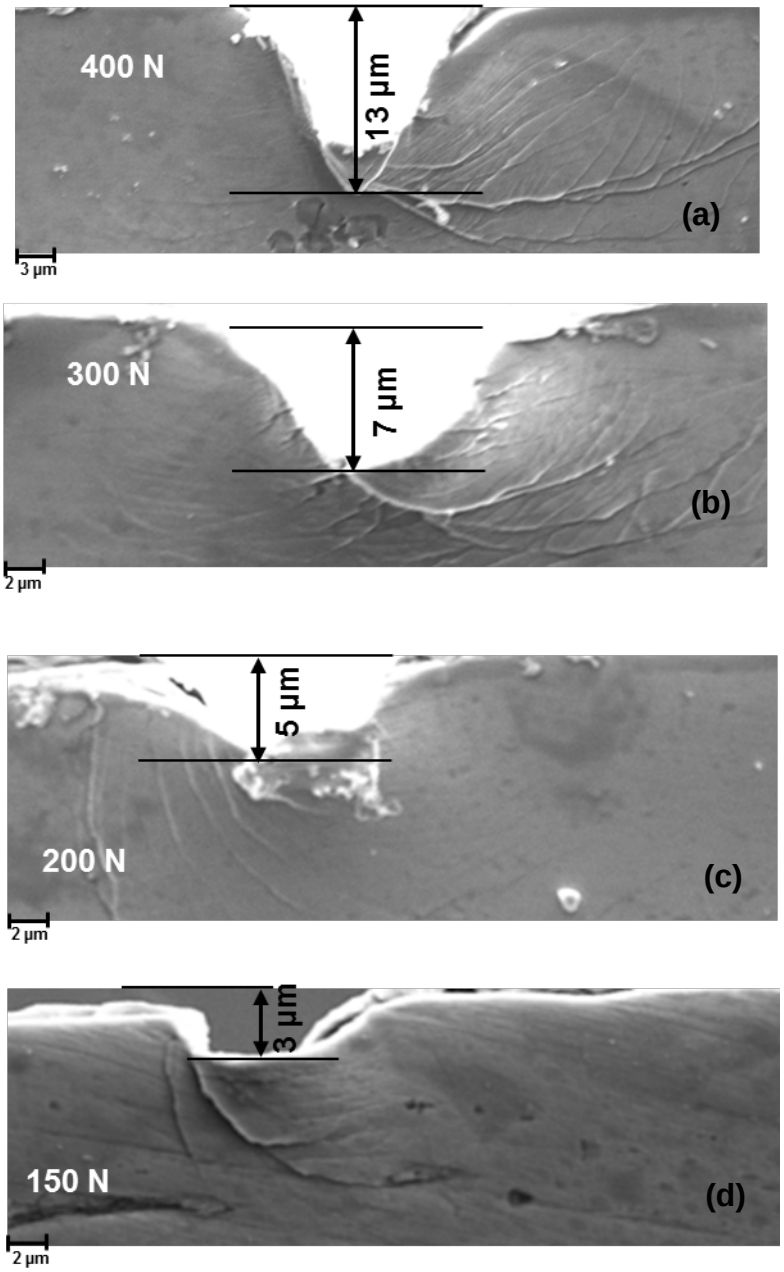

Figure 5-12 Evolution of shear-band pattern with load under wedge-indentation for different loads: (a) 400 N, (b) 300 N, (c) 200 N and (d) 150 N.

The new wedge had an edge radius of 8 µm and height of 5 µm. Evolution of deformation pattern on the front surface of the specimen is presented in Figure 5-12. The plastic depth increased from 5 µm to 13 µm by increasing the load from 200 N to 500 N, and serrated semi-circular slip-steps formed by shear

bands were observed. The results showed that the nucleation and initial propagation of shear bands occurred for loads less than 200 N. There was no shear-band formation at 100 N load. For 200 N, the indentation depth was 22.17 µm before unloading, as obtained from the F-D curve. The yield stress calculated with Eq. 4.6 was used to determine the contact area (a) as $\delta > h$.

$$A_{total} = 2.257 \times 10^{-7} m^2$$

$$\sigma = \frac{F_{applied}}{A_{total}} = \frac{200}{2.257 * 10^{-7}} = 0.886 GPa$$

At 100 N, the yield stress was ~ 0.7 GPa, therefore, it could be estimated that the required stress to initiate shear bands formation was in the range of 0.7-0.9 GPa.

5.4 Comparison between glass and metallic glass

A purpose of this experimental study was to compare characteristics of fracture in traditional soda lime silica glass and the studied Zr-Cu-based metallic glass, using the wedge- indentation technique at room temperature. The experiments were aimed at comparison of deformation mechanisms in these two materials at small scale as both have amorphous microstructure. A relationship between mechanical behaviour and fracture features can assist in elucidating the fracture mechanism. Wedge-indentation was applied to both glass and metallic glass bars with dimensions of 40 mm × 4 mm × 2 mm using loads 500 N, 1 kN, 1.3 kN and 2 kN to create a range of crack sizes. Fractography studies showed that fracture surfaces of materials failing in a brittle manner from surface cracks are characterised by a sequence of three distinct fractographic features including mirror, mist and hackle regions depending on the loading mode. For instance, no

mist region was observed on fracture surfaces failed in the mixed mode [64]. A side view of wedge indentation into the glass sample is presented in Figure 5-20; here, classical concentric cone cracks were observed. The contact radius at maximum pressure lied just within the outermost surface ring in this figure, confirming that cone fractures were formed in the region of weak tension outside a subsurface compression zone. In addition, no detectable deformation was observed beneath the contact circle; essentially, the material behaved as an ideally homogeneous solid. As shown in micrographs of subsurface damage at higher magnification in Figure 5-13(c), hackle markings on the fracture surfaces of soda glass appeared as lances. Observation of the fracture surfaces indicated that the propagating crack did not experience any energy- dissipation process such as plasticity or crack bridging, which could result in retarding the crack growth in a substantial manner. As shown in Figure 5-14, significant differences were found in appearance of the fracture surfaces of the brittle-glass and the metallic-glass specimens at microscale. In contrast to silicate glass, BMG was not brittle and its specimens demonstrated the ability to deform plastically, with many semi-circular shear bands created beneath the indenter. Shear bands bifurcated with increasing distance from the indenter tip, indicating branching mechanism contributing to energy dissipation, which led to plastic deformation at microscale.

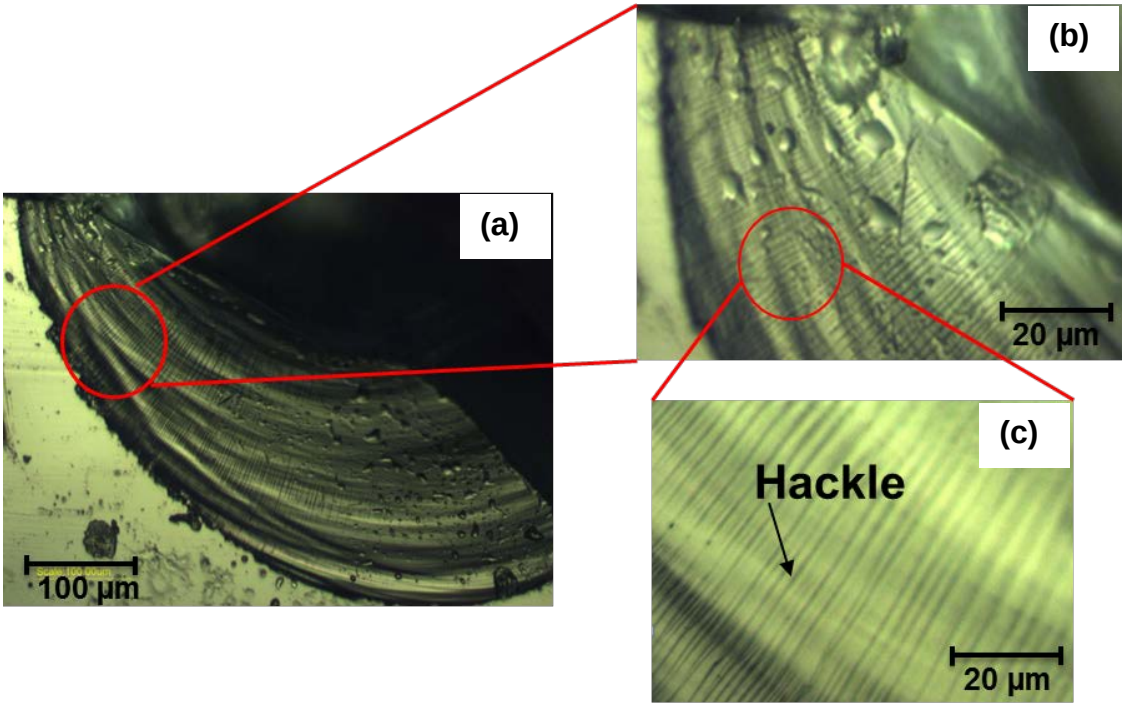

Figure 5-13 Optical micrographs of indented soda lime silica glass after applying 1.3 kN showing cone (a) hackle and (b and c) fractures.

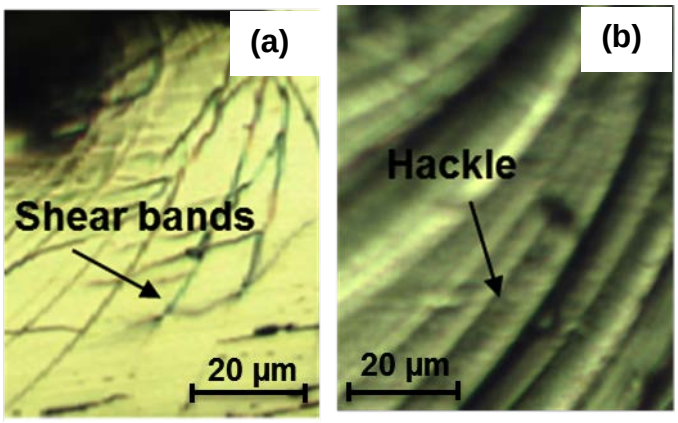

Figure 5-14 Optical micrographs of 1 kN wedge indentation. (a) As-cast $Zr_{48}Cu_{36}Al_8Ag_8$ metallic glass and (b) soda lime silica glass.

5.5 Incremental loading/unloading

This testing was carried out on the beam-shaped samples with the length of 40 mm, width of 4 mm and thickness of 2 mm with the wedge indenter in a

compression mode with a constant displacement rate of 0.05 mm/min. The applied load was from 1 kN to 3 kN in increments of 1 kN. Scanning Electron Microscope (SEM) was used to observe shear-band propagation at the top and front surfaces as shown in Figure 5-15 (b). The indentation tests reported here were conducted at room temperature. Figure 5-16 compares the indentation width measured on the top surface for incremental and single loading modes. As shown in Figure 5-15 ((a-b)), the measured indentation imprints for single and incremental loading of 2 kN and 1- 2 kN proved that the wedge indenter targeted the same location that was used at the applied load of 1 kN. Difference in the indentation widths for two modes of loading was less than 5%. A similar situation occurred for single and incremental loading of 3 kN and 1-2-3 kN. Contrary to micro- and nano-indentation, the described results demonstrated that wedge indentation was capable of providing an incremental study of the shear-band propagation.

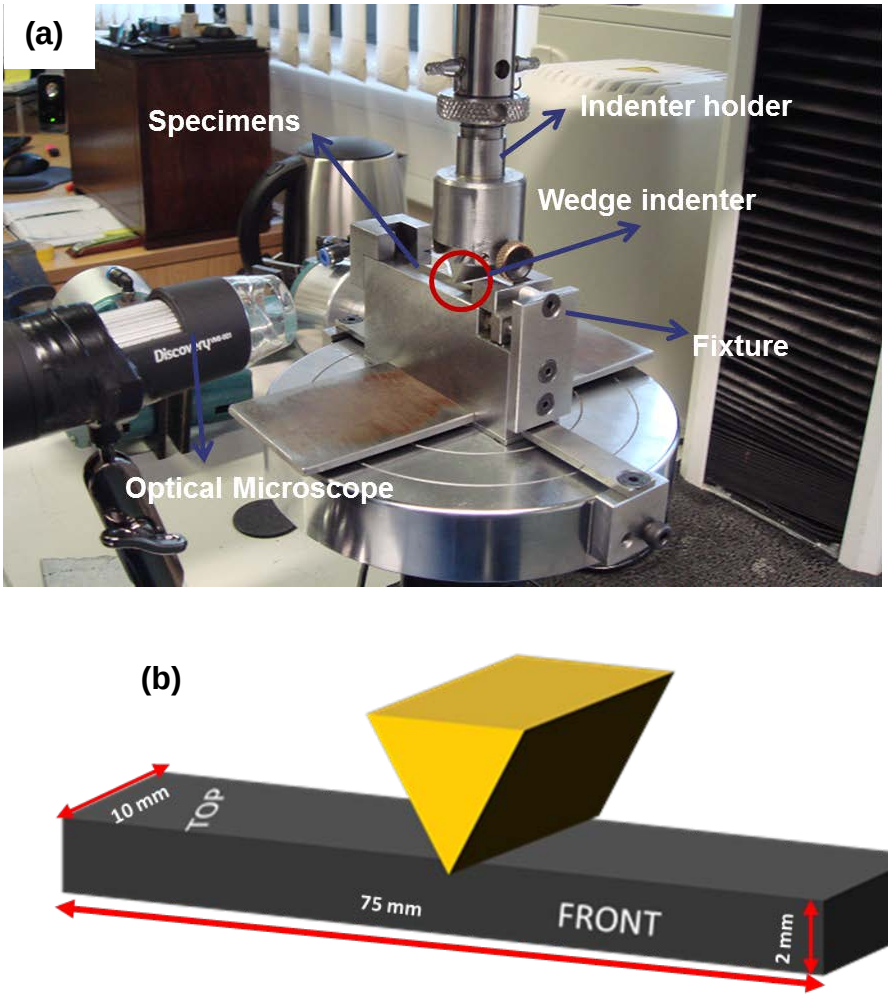

Figure 5-15 (a) Experimental set-up for wedge indentation and (b) schematic for shear-band observation.

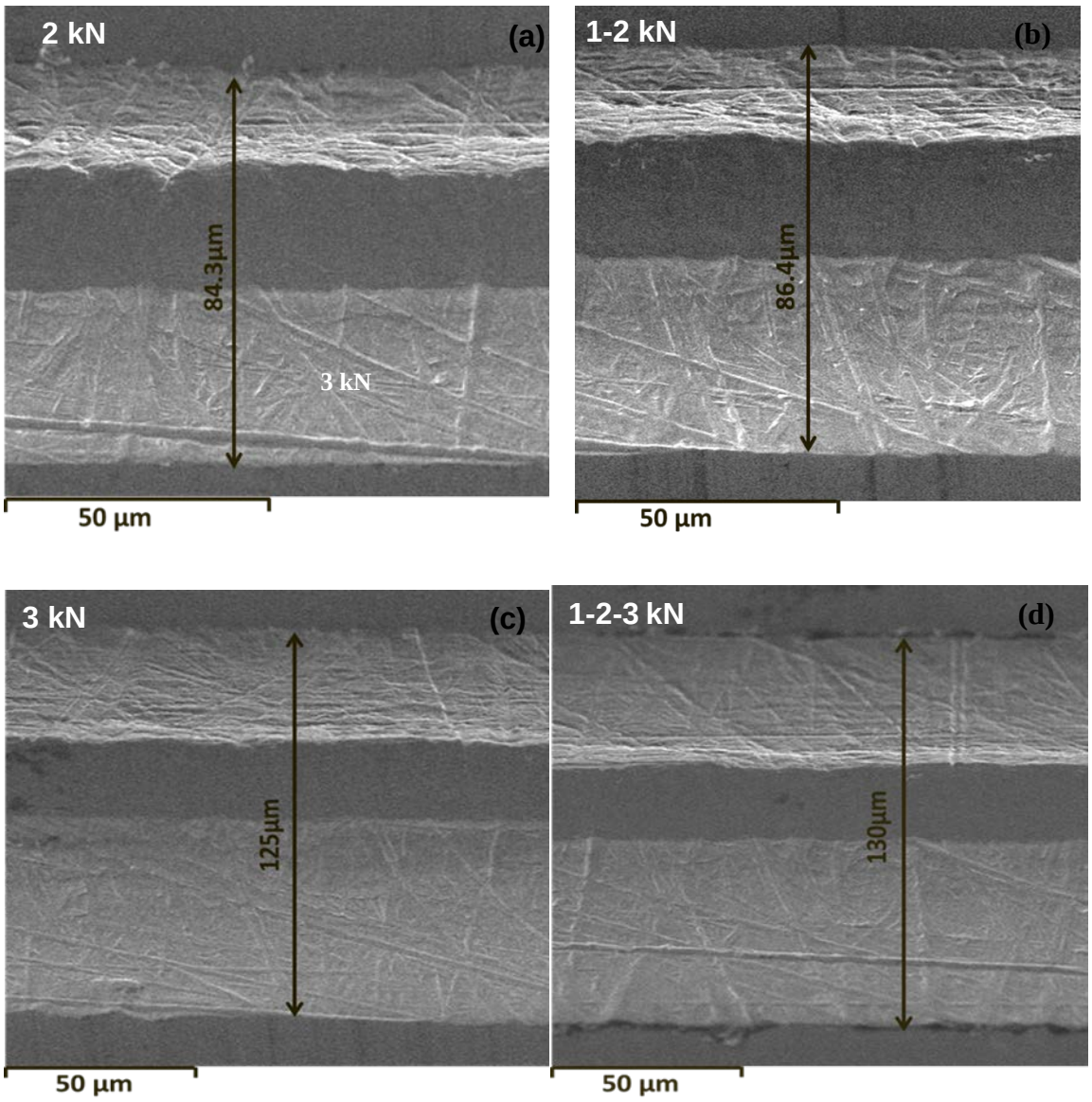

Figure 5-16 SEM images of indentation width on top surface for single loading (a and c) and incremental loading (b and d) load levels are shown in respective images.

SEM micrograph of front surface of a deformed region by a wedge indenter as results of incremental loading is given in Figure 5-17. In the deformed sample, the size of the plastic deformation zone with multiple shear bands increased with the maximum indentation depth, as expected. It can be noted (Figure 5-17) that the plastic depth increased from around 22 µm in the first increment (1 kN) to 130 µm in the third increment (3 kN). The generated shear bands (Figure 5-17(a-

c)) can be broadly categorized into two types including hemi-cylindrical (Primary shear bands) and secondary, radial shear bands. These results indicated some asymmetry due to misalignment of the wedge indenter. The hemi-cylindrical shear bands are a result of the out-of-plane plastic flow in BMGs [135], while the radial ones are related to plane-strain deformation indicating pressure sensitivity of BMGs to plastic deformation. At the first increment of loading, 1 kN, only hemi-cylindrical slip-steps due to shear-band operations appeared underneath the wedge indenter (Figure 5-17(a)). Additionally, some branches could be found in the areas where the propagation direction did not coincide with that of the maximum shear stress. This behaviour was completely different from the propagation of principle shear bands along a straight slip plane, which was widely reported in the literature, for example [116,136]. Figure 5-17(b) shows the shear-band patterns the BMG corresponding to the second incremental loading (1-2 kN). Here, secondary (radial) shear bands were formed in addition to hemi-cylindrical ones to accommodate the increasing level of plastic strain. These new shear bands have branched in various directions indicating the absence of preferential slip bands for their formation [131]. This additional dissipation of the accumulated elastic energy by branching of shear bands led to strain hardening of the BMG sample. A shear-band pattern after the third increment (1-2-3 kN) is shown in Figure 5-17(c). As in the case after the second increment, many new shear bands were formed. The evolution of deformation pattern on the top surface of the indented sample (Figure 5-18 (a-c)) provided as additional insight into shear-band formation. The shear planes intersected with the sample`s surface to form steps along straight lines parallel to the imprint`s axis. Contrary to the front surface, no shear bands were observed on the top surface at 1 kN

(Figure 5-18 (a)); the slip steps of the primary shear bands seemed to vanish, as they approached the indentation surface. In addition, the propagation of shear bands was along a hemi-cylindrical path until they reached the sample`s surface, further indicating that the nucleation of shear bands was easier than their evolution. Shear bands were initialized in “weak sites”, defined by the fluctuation of free volume or chemical heterogeneity. Such weak sites control the energy barrier for operation of shear bands. Thus, higher loads are required to activate new shear bands at the higher barrier energy for shear bands to maintain the continuous plastic deformation. The process of shear-band propagation on the surface (Figure 5-18 (a-c)) depends on the indenter shape, load and material`s microstructure as was discussed in details by Zhang et al. [131]. For better understanding of plastic deformation in the BMGs, individual shear bands were analysed using microstructural characterisation techniques such as TEM, nanoindentation and surface decoration as described in the next section.

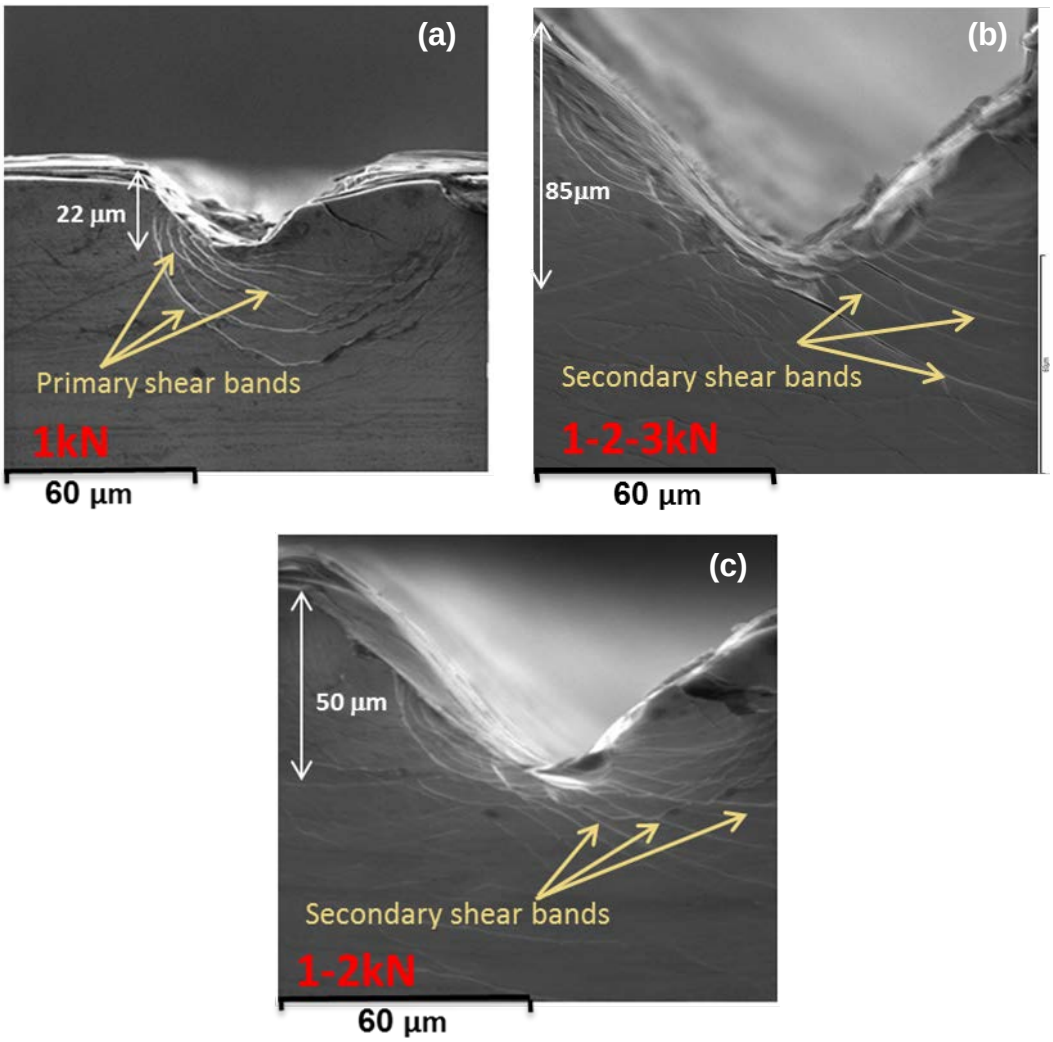

Figure 5-17 Evolution of shear-band pattern with load on front surface of BMG sample under wedge indentation: (a) 1 kN, (b) 1-2 kN and (c) 1-2-3 kN

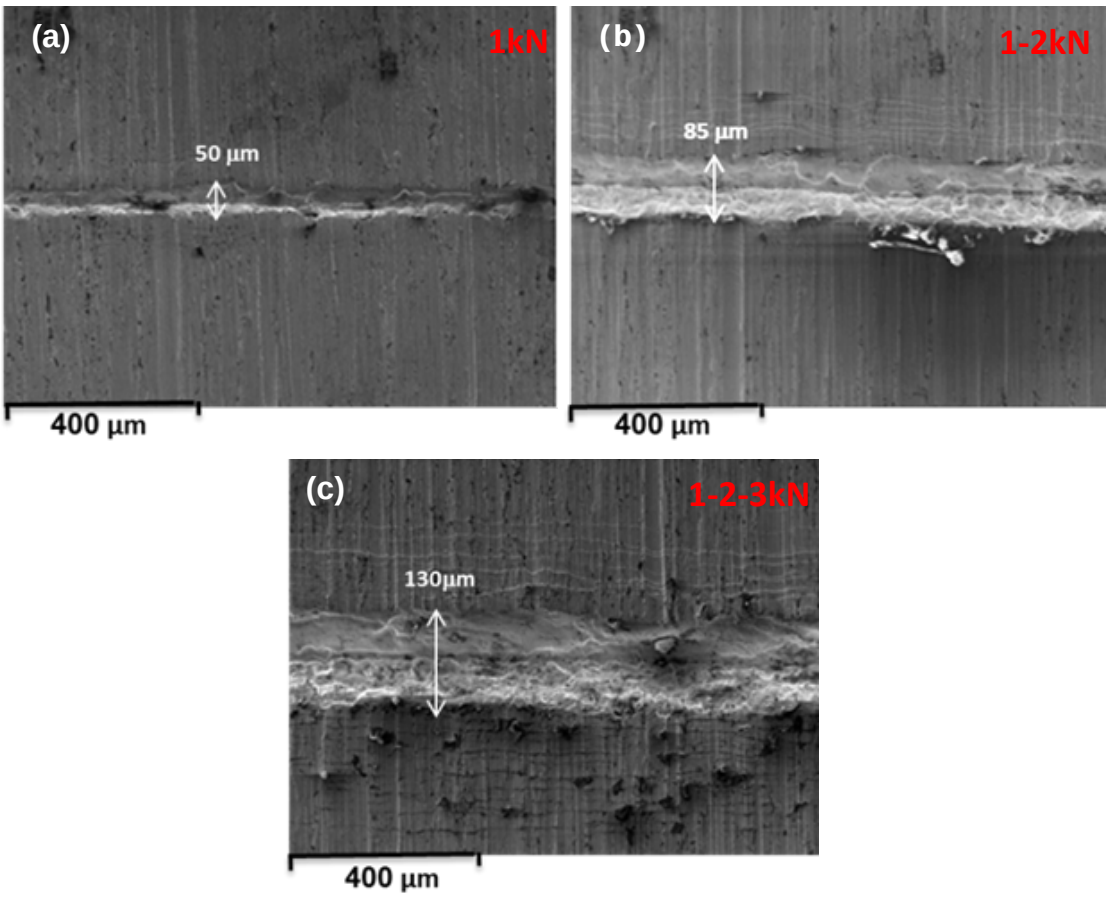

Figure 5-18 SEM images of evolution of shear bands with incremental loading on top surface under wedge indentation: (a) 1 kN, (b) 1-2 kN and (c) 1-2-3 kN.

5.6 Force-displacement curve

The graphs of indentation load (P) versus indentation depth (h) diagram for single and incremental loading regimes are shown in Figure 5-19. As can be seen in Figure 5-19 (a), single load including 1 kN, 2 kN and 3 kN were applied to the beam-shaped BMG specimens at three different independent locations. A smooth load-displacement curve, demonstrated a deviation from a linear-elastic deformation due to shear bands operations. Figure 5-19 (b) presents the incremental indentation test from 1 kN to 3 kN with the increment of 1 kN at the same location. As can be seen in this Figure 5-19 (b), the incremental loading

did not affect the overall mechanical response of the BMG, indicating that the evolution of deformation can be examined with the incremental indentation test. As shown in the inset Figure 5-19 (b), the residual imprints of the indenter for the first (1 kN) and second (1-2 kN) incremental loading were approximately 22 µm and 50 µm, respectively. As shown on the force-displacement curve (Figure 5-19 (b)), the initial displacements of the indenter in order to be reengaged with the specimen in the second (1-2 kN) and third (1-2-3 kN) incremental loading were also equal to 22 µm and 50 µm, respectively. Hence, it can be concluded that the incremental load-displacement curve is reasonable and repeatable, and the area underneath the P-h curve can be used to calculate the work done for the total deformation including elastic, plastic and damage deformations.

(a)

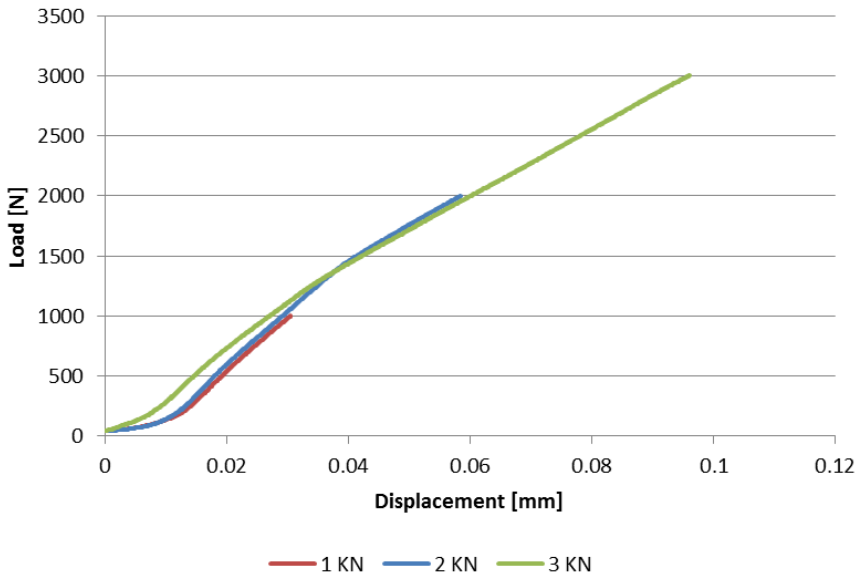

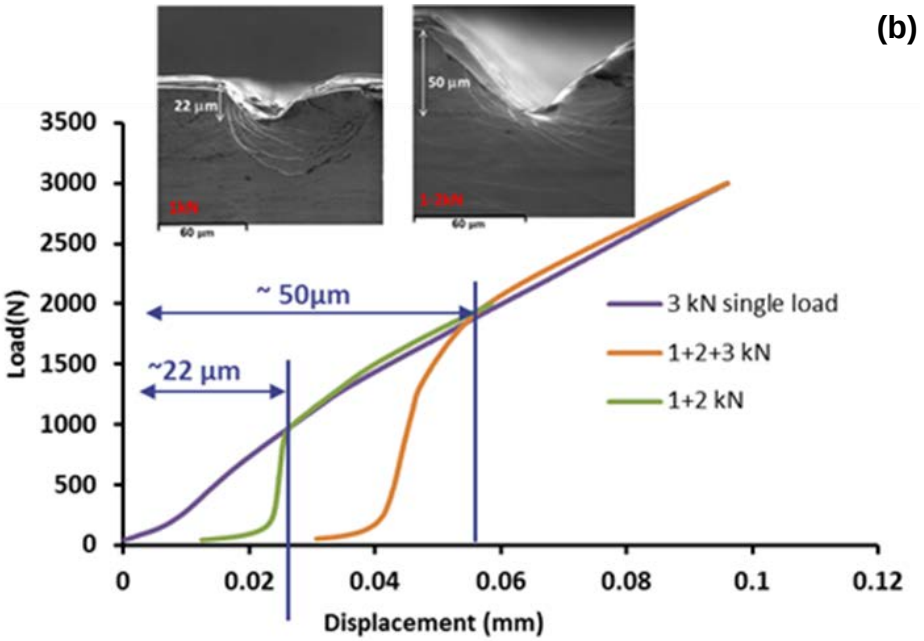

Figure 5-19 Experimentally measured P-h curves for single (a) and (b) incremental loading modes. The insets show the indentation plastic depth for 1 kN (left) and 1-2 kN (right).

5.7 Preliminary numerical modelling of BMGs

For a better understanding of deformation processes in BMGs and their localisation in the form of shear bands, especially in bulk materials, numerical simulation work can be performed. A number of studies have demonstrated that plastic deformation in BMGs is pressure dependent [159]. The deviation of the shear-band`s inclination angle (SBIA) from the classical 45° is due to the effect of shear stress and the normal stress component. Several well-established macro scale models of brittle materials already exist.

Johnson and Holmquist [160] proposed a constitutive relation for brittle materials known as JH-2. Details of this model could be found in Johnson Hulmquist et al. [160]. These models assume that the strength of materials such as ceramics

and glass are dependent on pressure, strain rate and damage. As described in the literature, these models are suitable for dynamic loading conditions. Johnson-Holmquist-Beissel (JHB) model is an extension of the JH-2 model and its primary distinctive feature is the ability to include the effect of pre-stress and phase changes [161]. Another well-established model for brittle materials is the Drucker – Prager criterion, which is widely used for frictional materials that exhibit pressure–dependent yield stress and materials with higher compressive yield strength, when compared to yield in tension. This model can be used in quasi-static conditions such as in quasi-static tension, compression or indentation experiments. In this this section, an application of 2D full-field optical displacement measurements for quantitative validation of finite-element (FE) simulations using Drucker Prager plasticity model is presented.

5.7.1 Drucker Prager Plasticity model

The Drucker Prager model (D-P), was chosen to represent the material response of the studied metallic glass. The important factors of each plasticity model are the yield surface, the flow rule and the hardening/ softening rule. The initial yield surface determines when the plastic deformation begins and the flow rule controls the direction of the plastic deformation. Softening or hardening rule outlines how the yield surface develops with the plastic deformation [162]. D-P yield function has been extensively used in recent years to study the deformation mechanism of pressure-dependent materials, such as concrete, polymers and foams. The simplicity of the model (including only two parameters) and capability of measuring shear strength as a function of hydrostatic pressure, makes it a popular choice for modelling of brittle materials. A model was developed based

on wedge indentation experiments. Due to the nature of the experiments, it was reasonable to assume 2D plane strain as the specimen`s height was very large compared to its thickness. Hence, the strains along the length are small compared to the strains along the width and along the thickness of the sample i.e. the x and y directions.

- *Boundary condition and contact*

Fixed boundary conditions (constrained displacements and rotations) were used to fix the bottom of the BMG sample on all sides, while the indenter was set to move into the work piece sample via displacement imposed on the reference point along the vertical direction of the indenter`s surface (see Figure 5-20). A surface to surface contact between the wedge and the top surface of the specimens was considered, as shown in Figure 5-20. The Coulomb's friction law with a coefficient of friction $\mu = 0.03$ was used to model the contact interaction between the indenter and the surface of the BMG sample. The value was chosen after carrying out some preliminary calibration tests.

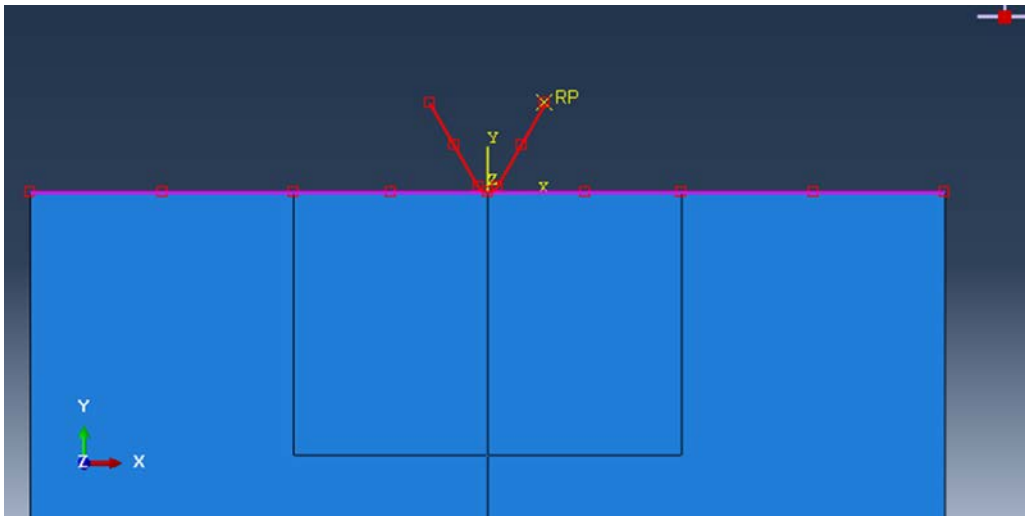

Figure 5-20 Surface to surface contact of wedge indenter and the specimen with displacement along the vertical direction.

- *Material Properties*

The mechanical behaviour of the studied BMG was assumed to closely represent the linear Drucker-Prager material model. The Drucker Prager yield criterion is defined as:

$$f = t - ptan\theta - d = 0, \qquad 5\text{-}7$$

where, the pseudo-effective stress (t), is defined as

$$t = 0.5q\left[1 + \frac{1}{k}\right] - \left(1 - \frac{1}{k}\right)\left(\frac{r}{q}\right)^3, \qquad 5\text{-}8$$

Here, θ is the friction angle of the material (the slope of the yield surface of the $p - t$ plane), d is the effective cohesion parameter, p is hydrostatic pressure, *r* is the third invariant of the deviatoric stress, *K* is the ratio of the yield stress in tri-axial tension to that in tri-axial compression and *q* is von Mises equivalent stress. In metal plasticity, d is equivalent to the current yield stress, ε_{eq}^{pl}, which is given by equation,

$$\varepsilon_{eq}^{pl} = \sqrt{\frac{2}{3}\varepsilon_{ij}^{pl}\varepsilon_{ij}^{pl}}; \qquad 5\text{-}9$$

The variable used by the linear Drucker-Prager yield function are shown in Figure 5-21:

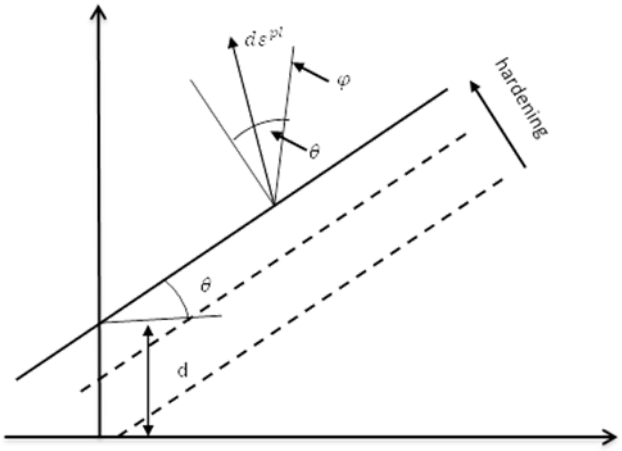

Figure 5-21 Finite Element model of wedge indentation with the expanded view of the indenter geometry and the mesh density of the material

For linear Drucker Prager model, the flow potential (g) is defined as:

$$g = t - p\tan\psi; \qquad 5\text{-}10$$

where `$\psi$`is the dilatation angle in the *p-t* plane. The original Druger-Prager formulation is recovered by setting $\psi = \theta$ and $r = 1$. Table 8-1 lists all the relevant parameters used in the model [162].

Table 5-2: Modelling parameters used in FEM simulations.

Drucker-Prager Parameters				
Angle of friction (θ)	Flow stress ratio	Dilation angle	**Hardening Characteristics**	
0.01	1	0.02		
Shear damage parameters			Yield stress (MPa)	Plastic strain
Fracture strain	**Shear stress ratio**	**Strain rate (s^{-1})**	1900	0
0.1	1	0.016	1900.4	0.015

- ***Damage Modelling***

Regarding the macroscopic behaviour of materials, it is important to discuss the mechanical effects due to material deterioration. The damage process brought by the internal defects leads it to final fracture so a proper understanding of the damage phenomena is important. Damage model proposed by Kachanov [167] and modified by Rabotnov [168] is used to represent damage of materials with distributed cavities in terms of internal state variables. Constitutive equations were then derived to describe the damage evolution and its behaviour (Murakami 1988).

A continuum - damage modelling approach offers the possibility to simulate mechanical behaviour of history - dependent materials which irreversibly degenerate under mechanical loads. The characterisation of damage relies on progressive stages - development, growth and coalescence of micro defects - leading to the formation and propagation of micro cracks and, eventually rupture. The increase of damage generally advances to local softening behaviour, such that the tangential stiffness becomes negative [167]. The influence of isotropic damage on elastic material's behaviour can be described in terms of a parameter called *damage* (*D)*. It is a monotonously increasing scalar quantity which lies in between $0 \leq D \leq 1$ and expresses the extent of material degradation.

Conforming to damage - mechanics approach, a constitutive relationship can be derived with pursuant to the Hooke's elasticity matrix H and the column of strain component ε as follows.

$$\sigma = (1 - D)H\varepsilon; \qquad 5\text{-}11$$

An undamaged state is characterised by D while the complete loss of stiffness is represented by $D = 1$ .In ABAQUS progressive damage and failure can be assigned to the material in conjunction with several plasticity models, including Drucker - Prage. This capability is sustained by more specifications including damage- initiation criteria and a damage - evolution criterion. Progressive damage models in ABAQUS allow a smooth degradation of material stiffness in both quasi - static and dynamic conditions.

For the fracture of metals, the damage - initiation criterion can be invoked by two criteria including ductile and shear. Once a distinct damage - initiation criterion is satisfied the material's stiffness is degraded according to the damage - evolution law. Two mechanisms could cause fracture of a metal: ductile fracture and shear fracture. Ductile fracture is primarily due to the nucleation, growth and coalescences of voids whereas shear fracture is due to shear - band localization. These options should be chosen accordingly with the knowledge of deformation mechanisms of the chosen material.

The shear nature of metallic glasses during their plastic deformation was initially established by Leamy et al [168] and there studies of the outer surface of bent samples demonstrated significant shear displacements with primary and secondary steps with no sign of tensile cracks. As shown in Figure 1-2 , the fracture surfaces consisted of two regions including a smooth sheared surface followed by localised necking resulting in characteristic pattern with vein pattern. Hence, the shear criterion should be chosen for the damage mechanism of

BMGs. The shear criterion can be invoked in both versions ABAQUS/Standard and Explicit - in affiliation with Drucker - Prager plasticity.

Shear Damage Criterion

Shear criterion in D-P model is used to predict the onset of damage due to shear band localisation. The ductile criterion needs the description of the equivalent plastic strain at the onset of damage, $\bar{\varepsilon}_D^{pl}$, as a function of shear stress ratio θ_D and effective strain rate $\dot{\varepsilon}_D^{pl}$. θ_D is defines as :

$$\vartheta_D = \frac{(q+K_D P)}{\tau_{max}}; \qquad 5\text{-}12$$

K_D is a material parameters and τ_{max} is the maximum shear stress. The following equation should be satisfied for damage initiation,

$$\omega_D = \sum \frac{\Delta\bar{\varepsilon}}{\varepsilon_D^{pl}(\theta_D, \dot{\bar{\varepsilon}}^{pl})} = 1; \qquad 5\text{-}13$$

Where ω_D is a state variable which increase with plastic deformation and proportional to the incremental change in equivalent plastic stress.

- *Mesh Topology*

The specimen under the wedge indentation should be discretised with sufficient refinement. Solid elements in ABAQUS can be used for linear analysis as well as complex nonlinear analysis including contact, plasticity and extensive deformations. The best element should be chosen for analysis based on the type of available solver in ABAQUS to provide accurate and reliable results. Although both triangular and tetrahedral elements can be used to discretise the specimen, these elements are stiff and an extremely refined mesh is required to obtain

accurate results to avoid volumetric locking in incompressible problems. In addition, first order tetrahedral elements C3D4 exhibit slow convergence with mesh refinement. Hexahedral and quadrilateral elements usually provide less accurate results, when they are initially distorted. Hourglassing is a phenomenon typically manifests as a patchwork of zig-zag or hourglass like element shapes, where individual elements are severely deformed, while the overall mesh section is undeformed. This occurs on hexahedral 3D solid reduced integration elements and on the respective tetrahedral 3D shell elements and 2D solid elements. Hourglass energy can be directly diagnosed by comparing energy contained in zero energy modes (hourglass energy) with the internal energy of the system. Hourglass energy should not exceed 5% of internal energy and can be controlled by refining the mesh. Based on the above consideration, a specimen with domain of 2mm ×2mm were discretised using 4-node bilinear element, reduced integration with hourglass control. A finer mesh was used to discretise the zone in proximity to the indenter in order to capture the stress variation accurately.

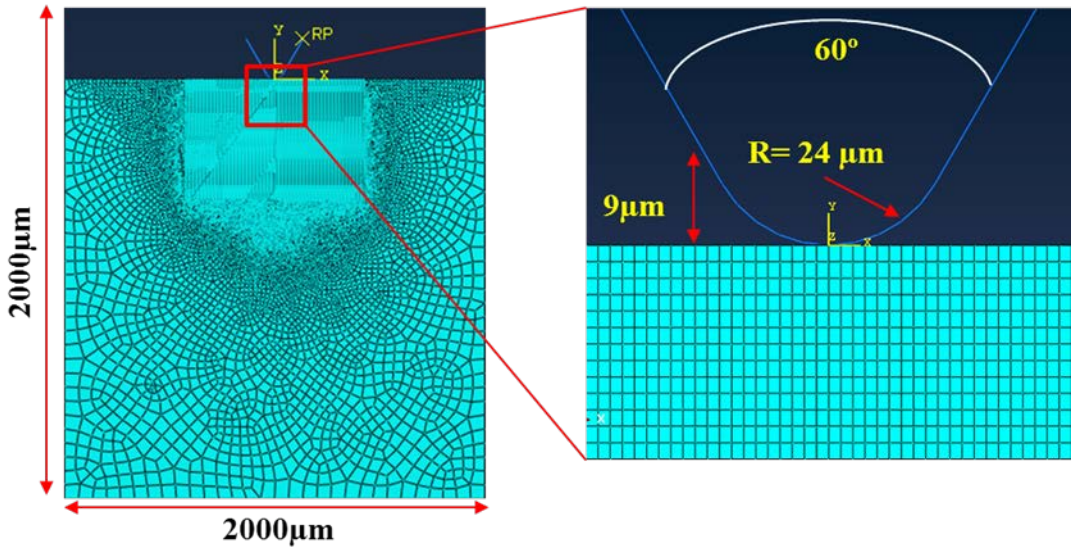

Figure 5-22 Finite Element model of wedge indentation with the expanded view of the indenter geometry and the mesh density of the material.

The finite element model developed here is shown in Figure 5-22. The mesh size was sufficiently fine to account for the local stress variation. The element size in the vicinity of the wedge indentation was 3.77 µm × 3.77 µm. As shown in Figure 5-22, the wedge tip radius (R) was 24 µm based on the measurement described in Chapter 5.

5.7.2 Digital image Correlation

The digital image correlation is an optical method applying a mathematical correlation analysis to study digital image data of specimens during mechanical testing [163]. This technique involves capturing consecutive images with a digital camera during the deformation to evaluate the change in surface characteristics and understand the behaviour of the specimens subjected to mechanical loading, which allows for a strain map of the entire specimen to be generated. This technique may be used to observe in-situ deformation experiments, or to measure residual stresses [164,165]. For precise DIC measurement deformed surface, three main features were required including the presence of a fine and high-contrast surface texture with distinctive features, use of large correlation patch sizes, and stability of the imaging conditions. With these three features, DIC can provide full-filled evaluations of the local surface displacement of 0.4 nm. There are two modes of DIC measurement including two-dimensional and three dimensional (3D) [166]. The 2D mode uses one camera and acquires images of flat surfaces, while 3D mode uses two cameras from images of which, a 3D image of bent surfaces is derived. The main focus of this section will be on 2D, since this mode has been used in current work.

In 2D analysis, the camera is directed to the test surface, which is loaded on the tensile machine and subsequently an appropriate load is applied. The deformation of the material occurs in-plane, therefore it is important that no out-of-plane motion occurs, which might be interpreted as pseudo image deformation by software. From the deformation results, it is possible to read three different strain fields, ε_{xx}, ε_{yy} and the shear strain ε_{xy}.

To achieve good testing conditions, there are three points requiring to be fulfilled:

- The test piece should have a flat surface.
- The surface should be at the right distance and angle with the objective/camera.
- Out-of-plane movements should be minimized by correct setup.

For the last two points, it is important to notice that vibration affects the image quality and that this vibration can come from the tensile machine and the camera frame [166]. 2D-DIC measurement was used to study local plastic measurement in the Zr-Cu-based BMG under condition of wedge indentation.

- *Experimental Procedure*

A wedge-indentation experiment was carried out on the beam-shaped samples in a compression mode with a constant displacement rate 0.05 mm/min using Tinius Olsen Tensile test machine and maximum applied load was 4kN for wedge indentation. The used specimens were 30 mm × 10 mm × 2 mm with a flat surface along the thickness for DIC measurements. To apply this method, specimen was required to be prepared by an application of a random dot pattern (Speckle pattern) on its surface. The speckle pattern is essential, as it permits

the software to be able to identify and calculate the accurate displacements. A sufficient speckle pattern must have a considerable quantity of black speckles with different shapes and sizes. In this study, the specimen`s surface was initially painted with a thin layer of white paint and then a black mist of paint was applied to create the black speckles (Figure 5-23).

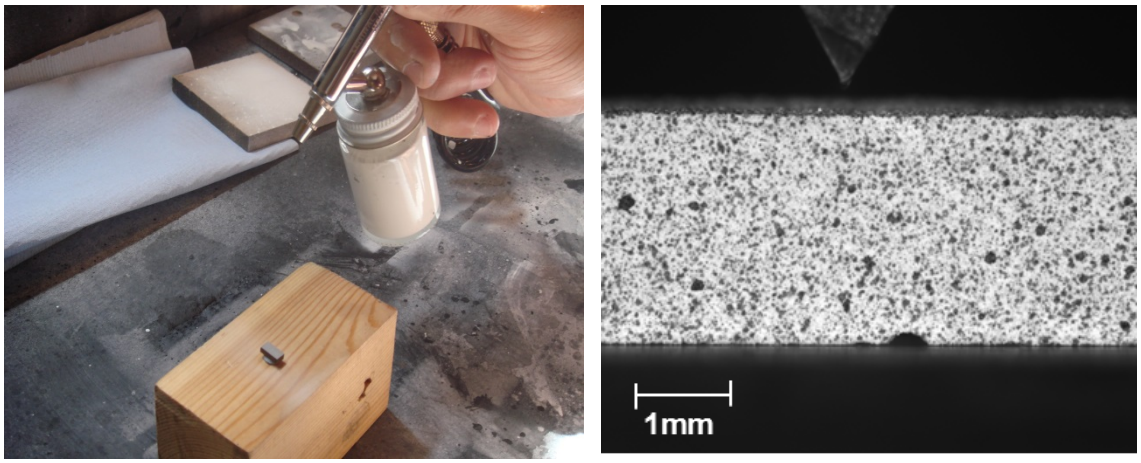

Figure 5-23 (a) Applying speckle pattern and (b) the speckle pattern taken with digital camera.

The equipment consists of computer software and digital camera (LIMESS system) with appropriate lens and resolution (See Figure 5-23). When the tensile test machine started, the upper part moved and the lower part was stationary. The loading direction can be seen in Figure 5-24. The micrographs were analysed using commercial image analysis software , DVIS 7.0 by LAVision to determine the in-plane displacement field, from which plastic strain values were calculated.

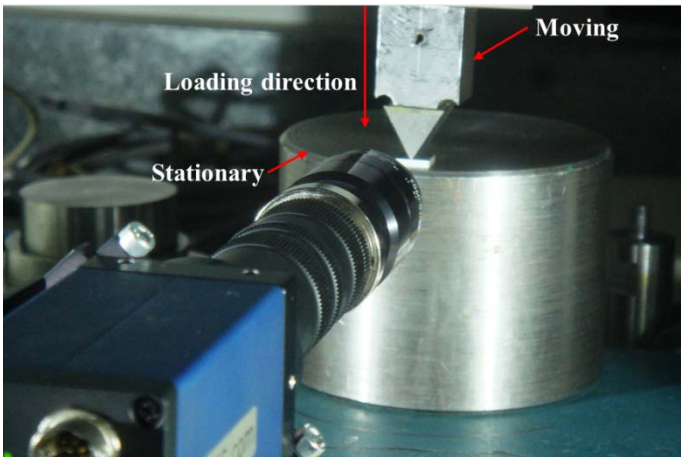

Figure 5-24 Loading direction of the test bar.

- *Local strain distribution*

As discussed previously, D-P model was employed to simulate the strain distribution under the wedge indenter under an imposed indenter displacement of 25 µm and 80 µm. The obtained results were compared to the DIC measurement in wedge indentation experiment. The axial logarithmic strain distribution (LE11) is shown in Figure 5-25 (a-b) for the DIC measurement and the FE model, respectively. As expected, a large plastic zone was formed under the indenter tip commensurate with [120] and [46]. The maximum Lagrangian strain (LE11) distribution in the model was compared to the strain distribution in the DIC measurement, which was around 0.0172. A reasonable match between the spatial depth (marked in Figure 5-25 (b)) and the depth, at which the shear bands formed during the experiments. The measured depth was ~193.5 µm, which was the distance to the lowest shear band formed during the experiment at the displacement of 75 µm. However, the presented material model was somehow limited, as there is no underlying mechanism to account for the material separation once the maximum shear stress was obtained and there was

no underlying mechanics to account for the shear-band evolution. Thus, the following step of our research was decided to be the development of strain-gradient-based constitutive material models, accounting for nucleation and evolution of shear-bands in a physically sound way. This would allow for shear band localisation (at the wedge tip) once shear bands are nucleated.

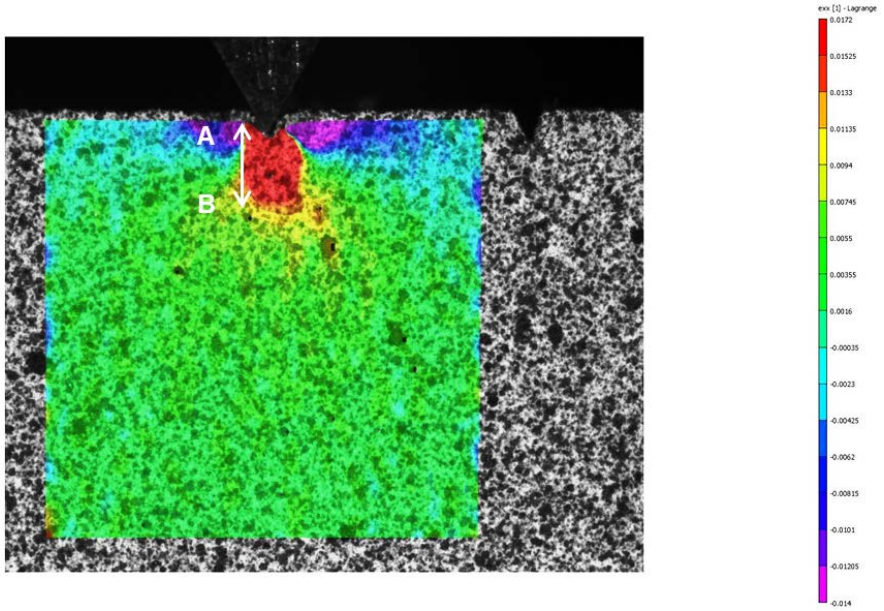

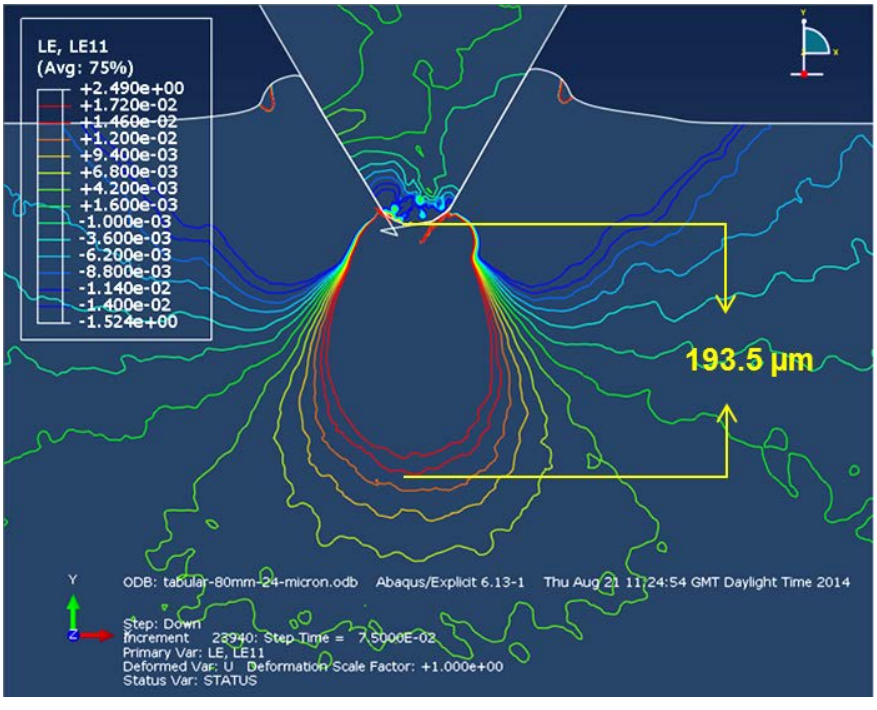

Figure 5-25 Plastic strain distribution (LE11) after 80µm displacement of the wedge

5.8 Conclusions

A relatively new technique – wedge indentation – was employed to calculate the stress level required for shear-band initiation in the metallic glass; it was estimated that this level was between 0.7-0.9 GPa. The wedge-indentation technique was also applied to compare fracture surfaces of the soda-lime-silica glass and the studied Zr-Cu-based metallic glass at microscale. Observation of fracture surfaces indicated that the propagating cracks did not result in any energy dissipation in the traditional glass; on the contrary, the shear-band evolution in the metallic glass showed branching mechanism contributing to the plastic deformation at microscale. The wedge- indentation technique was also used to study evolution of various sets of shear bands at the volume of the studied materials. The obtained results showed that wedge indentation was able to providing an incremental study of the shear band propagation. The difference in indentation depth for incremental and single loadings was less than 5%. At 1 kN, only semi-circular primary shear bands were observed. With increasing load, secondary shear bands were developed inside the plastic region. Shear behaviour strongly depended on the applied load that initiated shear bands at some “weak” sites, but it was not high enough to drive shear-band evolution to the surface, leading to their selective nucleation. The area underneath the force-displacement curve can be used to calculate the work-done for the total deformation including elastic, plastic and damage deformations. Finally, wedge indentation experiment was modelled with pressure dependent yield criteria, Drucker-Prager. A reasonable match between the spatial depth and the depth, at which the shear bands formed in the wedge indentation, was observed. This

indicated that other predicted variables could be used to describe the initiation of shear localisation in the material. These results of initial numerical simulations of deformation processes demonstrated that a maximum-shear-stress criterion can be used for developing of constitutive models of BMG to characterise the shear band localisation in BMGs.

6 Uniaxial Compression Experiments

6.1 Introduction

Due to lack of long-range order, BMGs show unique deformation mechanisms compared to dislocation-mediated flow in conventional crystalline materials. Previous studies of plastic flow in BMGs can be divided into three categories based on the specimen size: (i) millimetre range, (ii) micron range, and (iii) submicron range. It is well known that BMGs specimens in millimetre range in most monolithic glass systems have a tendency to fail along one dominant shear band under uniaxial compressive or tensile conditions with little global plasticity at room temperature. A large number of studies on different types of BMGs showed increased resistance to catastrophic failure, when the specimen sizes were in the micron range [51,137,138]. In micro scale level, as shown in Chapter 4, measurable plastic flow happens within multiple shear bands prior to eventual failure along the plane of maximum shear stress along the loading direction. In sub-micron range, some recent studies [23,50,139] have proposed that there is a transition in the deformation mode from inhomogeneous flow to non-localised or homogeneous flow as the test volumes approach the size of a shear band nucleus. Volkert *et al*. [139] argued that sub-microns pillar (below a certain size of 400 nm diameter) show homogeneous plasticity based on Griffith-like model due to the lack of a stored elastic strain energy for shear band formation. Schuster *et al* [138] investigated the effect of micropillar size (ranging from 2 to 20 µm in size) on yield strength of $Pd_{40}Ni_{40}P_{20}$, and concluded that yield strength was insensitive to the pillar size. Motivated by this work, the possible change in deformation mode from heterogeneous to homogeneous deformation was

examined as the specimen size was decreased in the current project. In addition, the influence of structural sate of BMGs on compressive stress-strain response of micropillars was studied in Zr-Cu-based BMG.

FIB milling is typically used to manufacture microsized pillars. Schuster *et al.* have suggested a strong dependence of yield strength of micro-pillars due to specimen taper. When the pillar diameter is not uniform along its height, stress field decreases toward its base, once its cross-section area gradually increases. This increasing gradient in stress considerably affects the deformation behaviour of the pillar, as shear band can propagate easier with decreasing stress. If the specimen taper is around 2º-3º, the ratio of maximum and minimum shear stresses on the shear-band plane is 1.07 leading to 7% stress gradient along the shear band plane. So, if the tapered angle is around zero, there no stress gradient to influence the shear band propagation during the compression experiments. Hence, this chapter summarises an investigation of different techniques to prepare micropillars of Zr-Cu-based BMGs in order to select the best technique to minimise the specimen taper. In addition, the specimen taper also influences the measured elastic modulus significantly. In current study, the size effect on strength, plasticity and deformation mode in the BMG was examined using microcompression specimens with cross sections of 10 μm × 10 μm to 230 nm × 230 nm. Additionally, micro-compression tests were conducted on as–cast and deformed specimens to understand the effect of multiple shear bands on the nominal elastic-plastic deformation of the material.

6.2 Cylindrical micro-compression specimens

The compression specimens were fabricated on the polished surface of the beam-shaped specimens using FIB (Nova 600 Nanolab Dual beam).The cylindrical compression samples were fabricated through top-down milling by sequentially reducing the inner and outer diameters of the annulus patterns at the final ion beam conditions of 30 kV and 1 nA to obtain a good surface finish and minimizing taper. The diameters of the produced pillars were 10 µm (Figure 6-1 (b)) and 5µm (Figure 6-1(b)), respectively. The aspect ratio (height/diameter) of the compression pillars was maintained at 2.5.

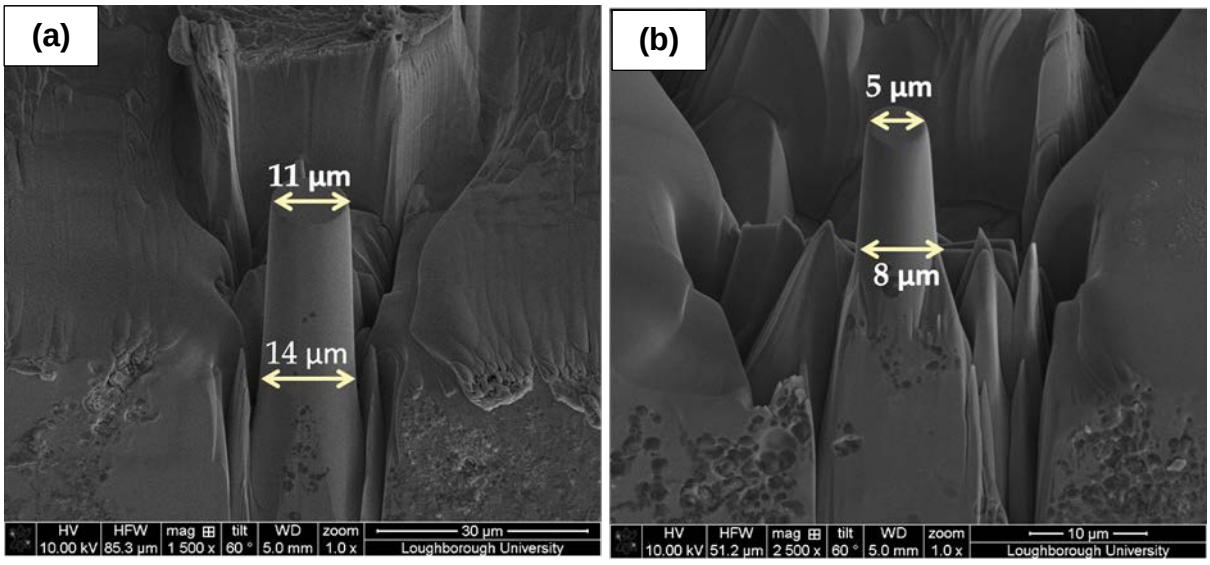

Figure 6-1 As-fabricated $Zr_{48}Cu_{36}Al_8Ag_8$ micropillars with 10 µm (a) and 5µm (b) initial diameter. The top surface is nearly perfectly flat; however, the tapered shaped resulting in the geometrical artefacts in microcompression test.

The dimensions and the degree of taper of the both pillars were measured using FEG-SEM. Based on the SEM measurements, the micropillar with 10 µm had the taper less than 7º, and that for the 5 µm pillar around 12º by considering through,

$$\tan\varphi = \frac{d_1 - d_0}{2.5 d_0}, \qquad 6\text{-}1$$

Where, d_0 is the initial diameter of the cylindrical pillar, d_1 is the final diameter and φ is the tapered angle. Since beam-spread effects were much noticeable for milling of smaller pillars, tapering angle increased significantly with decreasing the diameter. As yield stress and the elastic modulus are affected by the specimen taper, it was decided to prepare rectangle pillars to reduce or eliminate the tapering effect.

6.3 "Lift-out" technique for microcompression sample preparation

A "lift-out" technique is preferred when requiring TEM analysis in comparison to traditional FIB-TEM specimens as the total fabrication time for the "lift-out" technique are much shorter with improved dimensional stability [140]. Rectangle microcompression pillar of 8× 8 μm^2 cross section and aspect ratio of 2.8 were prepared, as shown in Figure 6-3. In this method, the location of an area of interest was found with an accuracy of microns using FEG-SEM attached to the FIB system. Two trenches were milled on either side of the area of interest using a large-beam current (20 nA) for fast ion milling (See Figure 6-2 (a)). The trenches were milled so as to just touch the tungsten on either side, leaving a wall of material in the centre. The trenches were approximately 50 μm wide, 30 μm long and 20 μm deep (see Figure 6-2(a)). A smaller beam current was applied to further thin the central membrane between the two trenches to the thickness of 10 μm and three cuts are made to the area of interest, framing it (Figure 6-2(b)). The next step involved milling away the attachment bonds on the top two corners of the membrane that were left by the frame cuts (Figure 6-2(c)).

The *in-situ* lift-out involved extracting and transferring the pillar with an internal nanomanipulator to the BMG substrate while it was still inside the FIB chamber. The *in situ* manipulation was enabled by the FIB deposition of Pt to first glue the manipulator needle to the pillar and then to glue it to the substrate (Figure 6-2(d-f)). The last FIB milling was performed to the desired cross section and length of the pillar; i.e. 8 µm × 8 µm and 22.5 µm, respectively (Figure 6-3).The SEM measurements showed that the tapering angle for the pillar from its top to the bottom was less than 1º.

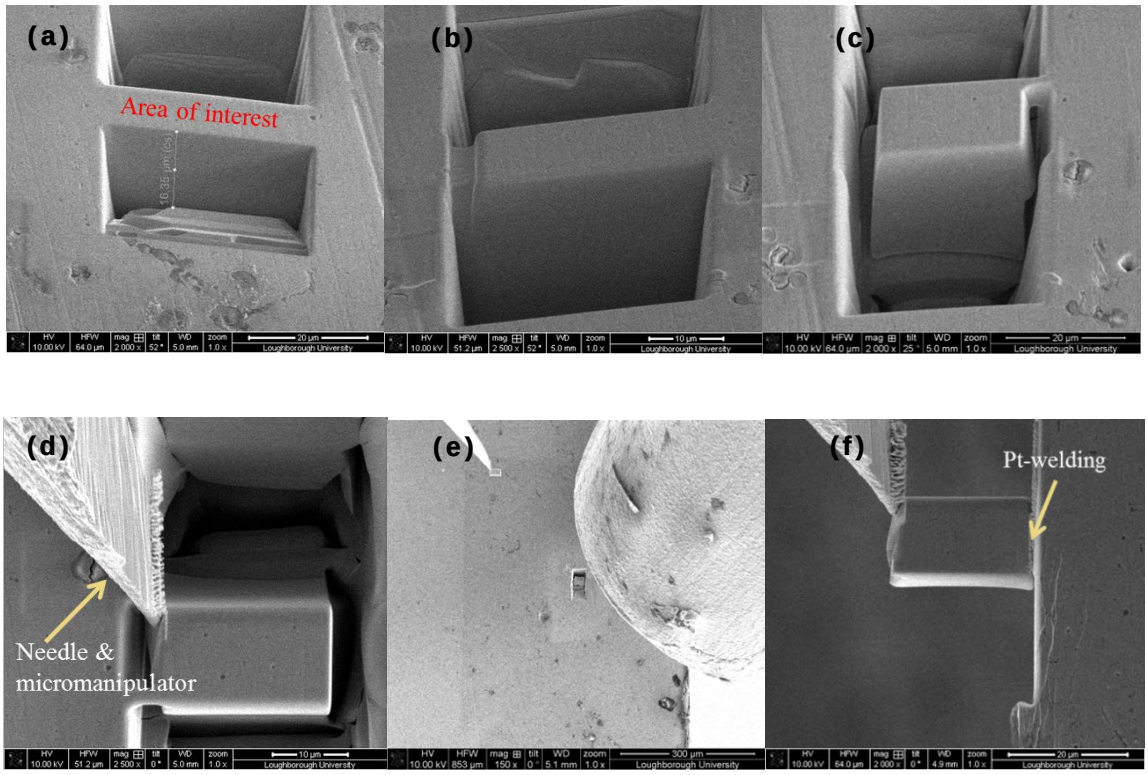

Figure 6-2 Milling sequence for microcompression specimens of Zr-Cu-based metallic glass using "lift-out method: (a) Iso view of rough cut on both sides of area of interest, (b) Iso-view of frame cuts, (c) Iso-view of free membrane from trench, (d) and (e) *In situ* lift-out of pillar by means of nanomanipulator needle mounted inside FIB chamber by Pt-deosition; (f) pillar mounted after transfer from the side on BMG substrate by Pt-welding.

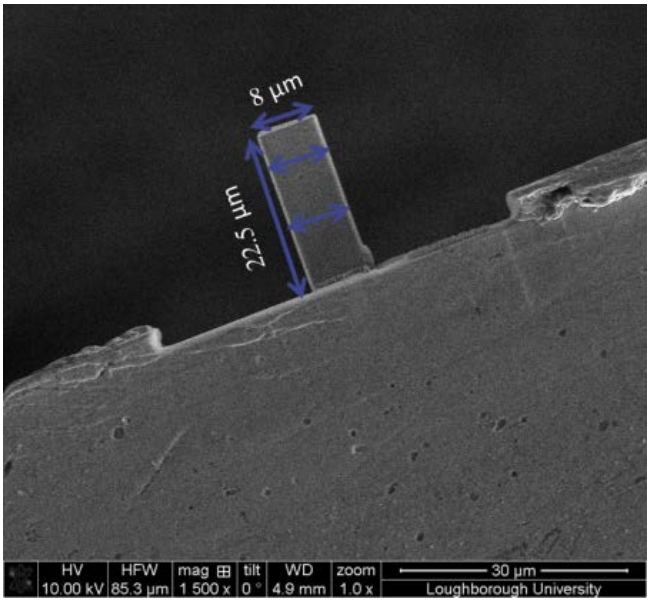

Figure 6-3 $Zr_{48}Cu_{36}Al_8Ag_8$ micropillar with 8 µm × 8 µm cross section and 22.5 µm length fabricated with lift-out method using FIB.

The microcompression test was performed on the nanoindentation system (Micromaterial Platform III) using a flat punch tip with an equilateral triangle cross-section measuring 50 µm inside length and a constant displacement rate of 8 nm/s. The corresponding load-displacement data is presented in Figure 6-4. The measured elastic modulus from the elastic region of stress-train curve was around 85 GPa. The curves showed an elastic loading followed by a plastic region without any serration with the load remaining constant. If the yield strength is assigned when the specimens undergoes plastic deformation in the stress-strain curve, the yield strength of the pillar was 250 MPa, which is much lower than the value of 1800 MPa for the $Zr_{48}Cu_{36}Al_8Ag_8$ bulk compression sample (see Figure 6-8). Morphology of the compressed pillar was examined by FEG-SEM. As can be seen in Figure 6-5, Pt-deposition used to glue the pillar to the substrate was not strong enough for preserving the pillar in position during microcompression tests, leading to failure of the pillar at the joint points.

Although the tapered angle the pillar was less than 1º for, it can be concluded that the "lift-out" technique is not suitable to provide micropillars as the Pt-deposition is much softer than the $Zr_{48}Cu_{36}Al_8Ag_8$ micropillars.

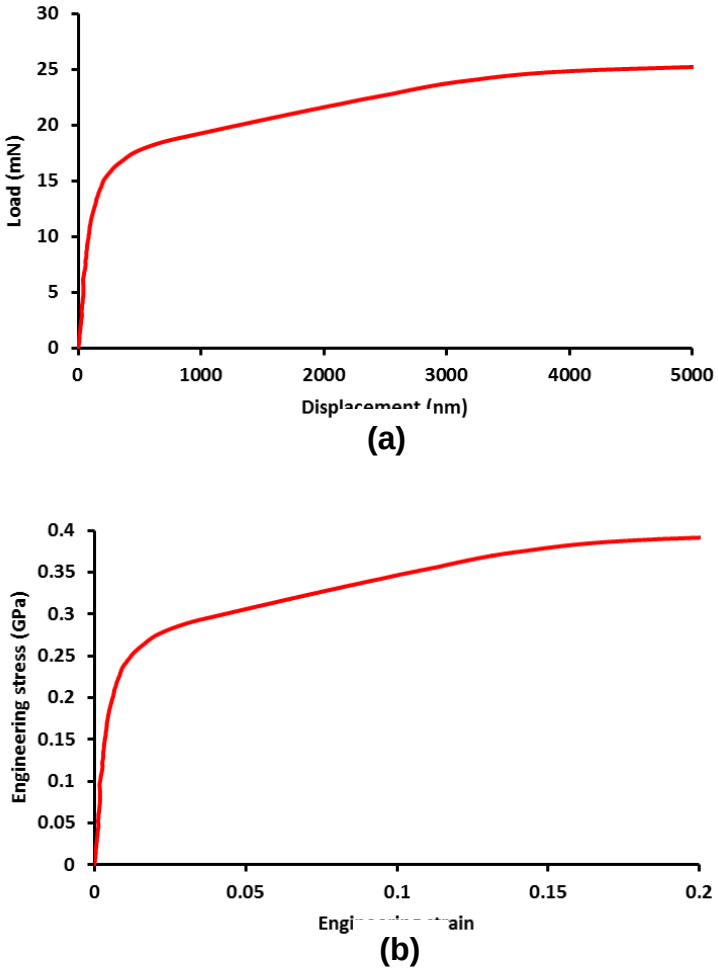

Figure 6-4 Compression load-displacement (a) and engineering stress-strain (b) curves of Zr-Cu based metallic glass with 8 μm × 8 μm cross section.

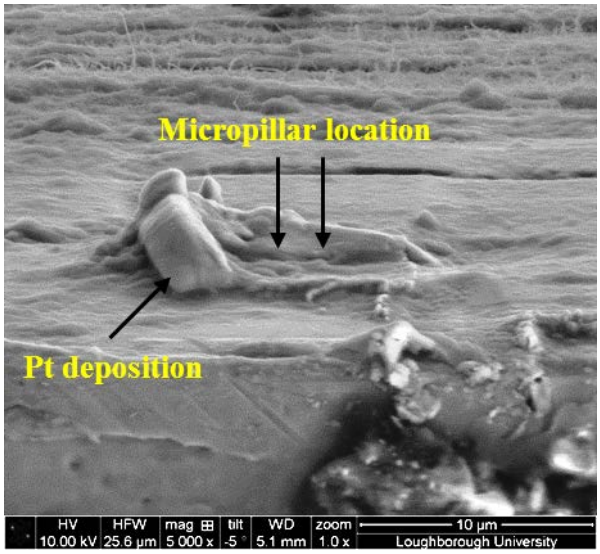

Figure 6-5 SEM micrograph showing that Pt-deposition used to glue the pillar to the substrate was not strong enough to preserve the pillar in position during the microcompression experiments.

6.4 Micompression test on rectangular $Zr_{48}Cu_{36}Al_8Ag_8$ pillars

6.4.1 Influence of structural state on micro-compression

The next set of microcompression specimens were prepared from beam-shaped samples of the as-cast BMG and its fracture surface area (sheared zone area) obtained from the three-point bending using the dual FIB to evaluate the deformation behaviour of a highly deformed region and as-cast specimens of the Zr-Cu-based BMG. To reduce the taper effect, rectangular micropillars (see Figure 6-6) with the cross-sectional area of around 10×10 μm^2 and the effective height of 25 µm were prepared by means of the top-down milling method by successively reducing the cross-section of the pillars at the final ion beam condition. A ion beam with a 30 kV accelerating voltage was used; an initial current of 20 nA was gradually reduced to 1 nA as the pillar cross section decreased. It was found that the tapered angle was less than 1º. Uniaxial

microcompression tests were performed on the micropillar samples with a nanoindentation system (Micromaterials Ltd. Platform III) using a flat punch tip with an equilateral triangle cross-section measuring inside length of 50 µm. To reduce the additional complexity of strain-rate effects, all tests were performed at a constant nominal displacement rate of 8 nm/s, resulting in the global strain rate of $1\times10^{-3}s^{-1}$. After the maximum length displacement was reached, the nanoindenter system had a short period of holding time, about 1 s. The pillars were examined prior and after the deformation using FEG-SEM.

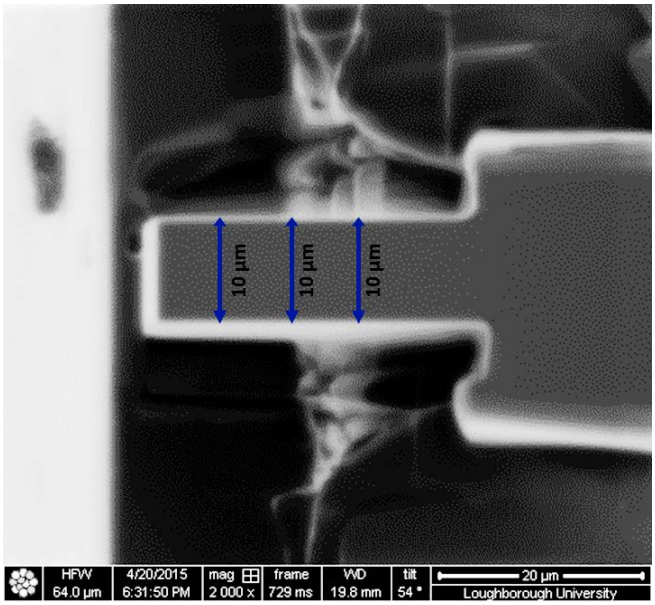

Figure 6-6 As fabricated $Zr_{48}Cu_{36}Al_8Ag_8$ rectangular micropillar with 10 µm ×10 µm. The top surface is nearly perfectly flat minimising geometrical artifacts in nano-compression tests

The morphologies of the representative micropillars after compression are shown in Figure 6-7. The deformation mode of these pillars was dominated by localised shear-banding in a manner of stress drops to release the energy, which is similar to that in crystalline solids [141]. As shown in Figure 6-7, the shear bands were

initiated from the corner of the contact surface between the specimens and the compression indenter punch at around 45º to the loading axis. This was because the pillars experienced maximum shear stress due to the large constraint caused by friction between the test specimens and the punch [137]. Furthermore, following yielding, the upper part of the specimens began to slide along a major shear plane. As a result, the effective load-bearing cross-section area did not remain constant, as the punch impressed into the bottom part of the micropillar. This explains the observation of “lips” on the top of the deformed samples (Figure 6-7(a)) and decreasing of load (Figure 6-8(a)). The latter was not indicative of any work hardening or softening and it is a measure of friction of sliding between two rigid bodies [137]. SEM images taken after deformation confirmed that plastic deformation proceeded via shear banding irrespective of the material condition, and no change in the deformation mode was observed. Qualitatively, there was also no difference in shear-band density between different conditions.

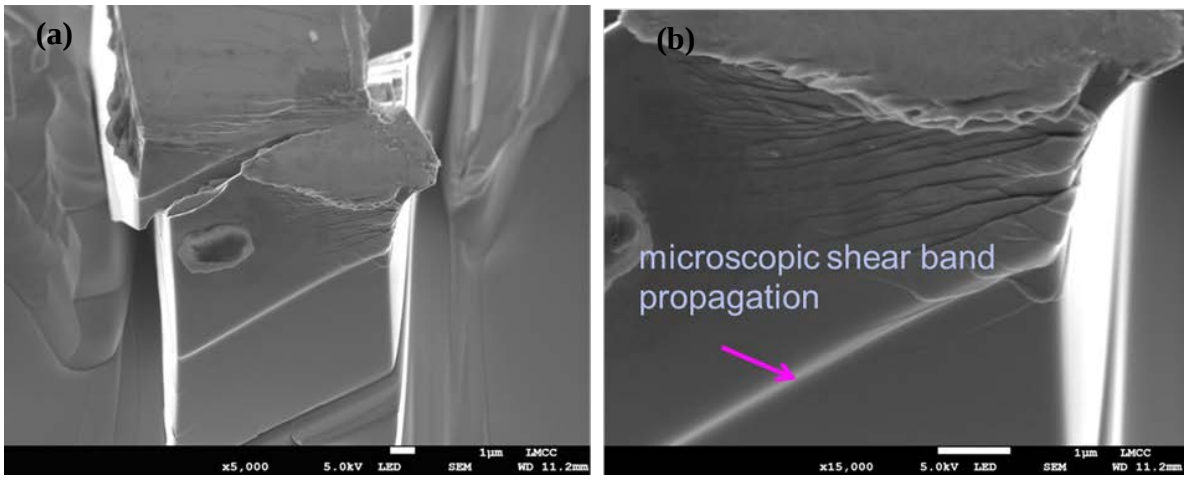

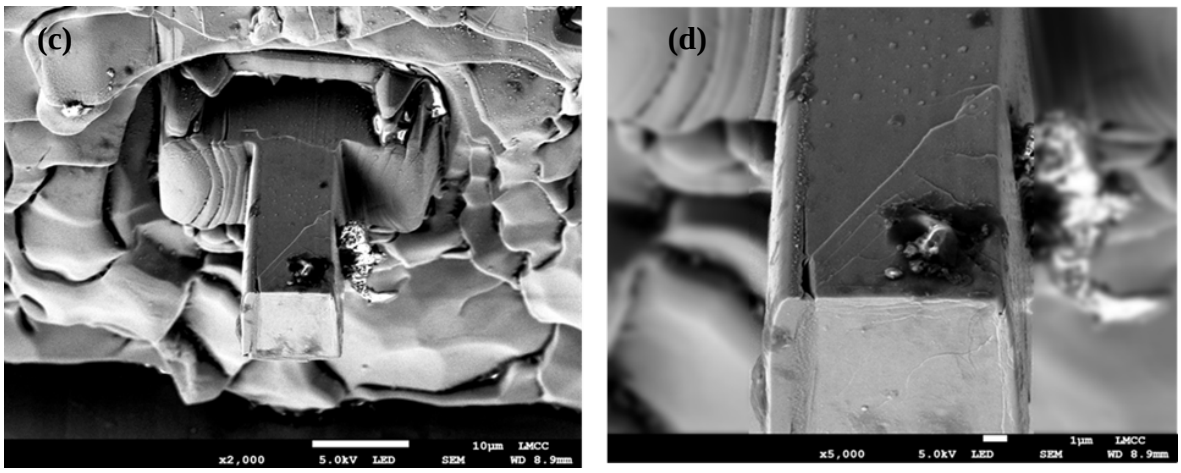

Figure 6-7 SEM micrographs of deformed micropillars rectangular: (a-c) as-cast micropillar; (b-d) micropillar from sheared zone area.

Figure 6-8 shows the representative engineering stress-strain response of the mocropillars in the as-cast and sheared zone states (fracture region). The engineering stress-strain curve is normally converted from the load-displacement data under assumption that the specimens were uniformly deformed. According to the engineering stress-strain curve (Figure 6-8), the mechanical behaviour of the BMG subjected to the external load can be classified into three different stages including a misalignment-effect region, an elastic region and a region with strain hardening followed by a steady-state plastic deformation. The misalignment region was a part of the initial deformation area deviated from linearity due to the imperfect contact between the punch and the pillar. As seen in Figure 6-8, the elastic-plastic transition in the pillars was abrupt, and deformation was characterised by discrete pop-in events throughout the plastic flow regime; there was a clear stress drop associated with each serration. The discrete pop-in events were triggered by the formation and propagation of one or multiple shear bands. The plastic-flow region shown in Figure 6-8 consists of a series of smaller stress drop followed by elastic loading, exhibiting increased

plasticity as the stress at the first stress drop was around 1.8 GPa; this is similar to the yield strength reported for Zr-Cu based metallic glass under compression. Strain hardening occurred immediately after yielding at around 4% of strain and declined when the steady-state plastic flow started. The steady-state part proceeded in a perfect-plastic manner without any sign of the strain softening or hardening. There were multiple stress drops observed and there seems to exist blocking resistance to evolution of shear bands. This appeared to induce initiation of subsequent shear bands operating at higher load (or stress), showing an extended ductility and intrinsic plasticity of the BMG. This suggested that initiation of shear bands was easier than their evolution and plasticity was mainly accomplished by formation of new shear bands. In Figure 6-9, the hardening effect observed is apparent in the true stress-true strain curves, in addition to the curves based on engineering stress. This indicated that the hardening effect is not an artifact resulting from the use of engineering stress-strain assumption.

In the deformed-region pillar, the stress required to initiate shear bands is significantly lower than that for the as-cast pillar (0.8 GPa). This demonstrated that the deformed area was twice softer compared to the as-cast material, which was also confirmed by indentation tests on the fracture surface area. The difference in the strength levels is associated with the flaw sensitivity [142] of defect population that helped shear-band initiation [49,139]. These defects include free volume, nano-voids and nanocrytallisation inside the shear bands. As there is no temperature inside shear bands based on the discussion on section 4.2.1, it would not be any crystallisation inside our shear bands.

The measured elastic modulus was estimated from the elastic region of engineering stress-strain curve. After applying the correction value of 1.25 for the extracted elastic modulus on the basis of the finite element simulation of microcompression [143], the elastic modulus of as-cast pillars was around 85 GPa, which was about 10 % less than the value of 95 GPa obtained in the three-point bending test. The possible reasons were the misalignment or imperfect contact between the top surface and the tip, as indicated in Figure 6-8. However, the results on the elastic modulus indirectly indicate that the misalignment artifact on the yield-stress measurement was minimised in this study. An additional effect can be potential damage caused by FIB to the pillar surface. The thickness of the damaged layer for a Zr-based BMG was estimated around 4 nm for 3.8 µm-diameter micropillars using Auger electron spectroscopy [51], and the damage thickness of 10-20 nm reported for 700 nm-diamtere micropillars. Therefore, an area of damage layer was less than 1 % for 10 µm micropillar, and FIB -induced damage of the pillar surface had no significant influence on strength and deformation behaviour of the studied micropillars. The magnitudes of the Young`s modulus of the sheared zone measured with the microcompression experiments were compared to those for the undeformed region: the former were considerably lower around 30 GPa. Hence, there was a significant decrease in excess of 50% in the values of the elastic modulus compared to those for the as-cast sample.

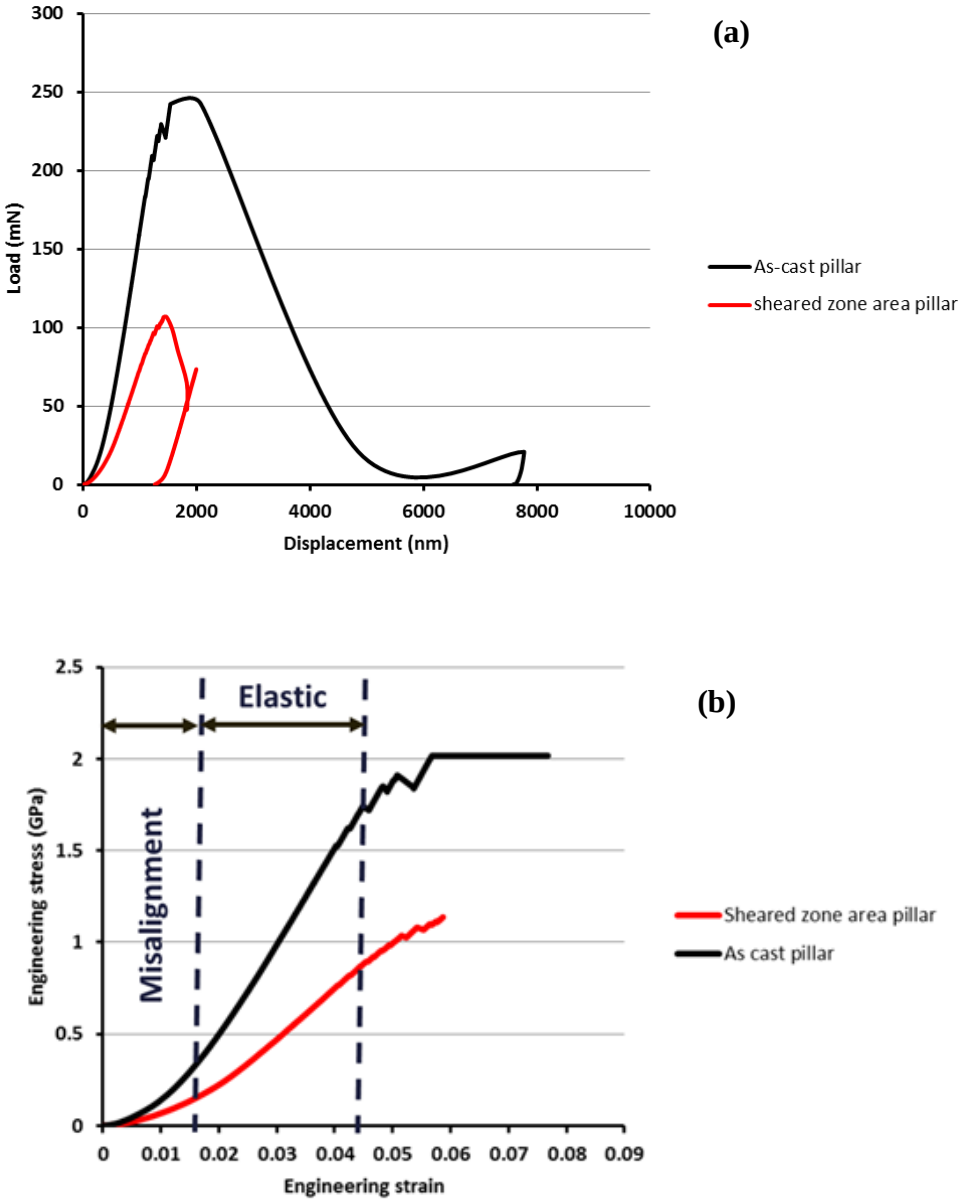

Figure 6-8 Characteristic engineering stress-strain curves of as cast and shear-zone micropillars of $Zr_{48}Cu_{36}Al_8Ag_8$ at constant displacement rate of 8 nm/s.

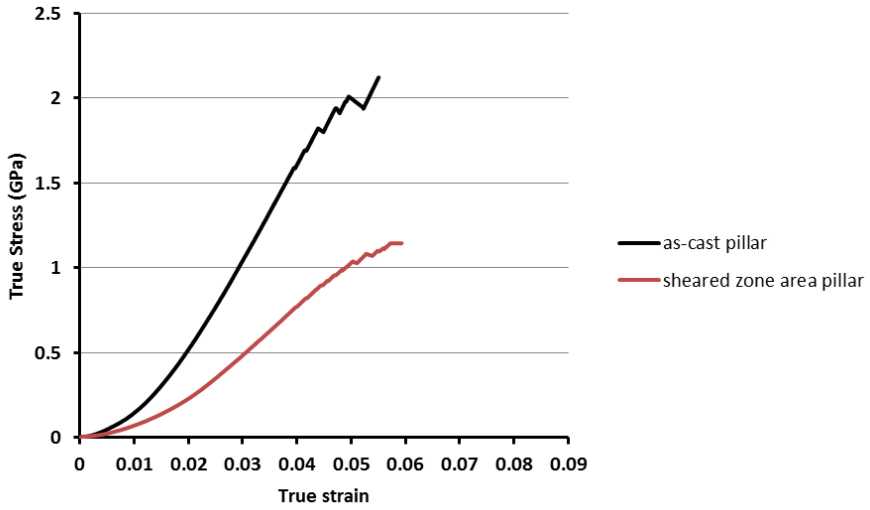

Figure 6-9 True stress-strain curves of as cast and sheared zone micropillars of $Zr_{48}Cu_{36}Al_8Ag_8$ at constant displacement rate of 8 nm/s.

6.4.2 Influence of sample size on micro-compression behaviour

Rectangular micropillars with cross-section of 230 nm × 230 nm and effective length of 580 nm (aspect ratio of 1:2.5) and the taper angle from the top to the bottom lower than 1 º were machined by FIB to perform *in-Situ* SEM micro-compression test. An ion beam with a 30 kV accelerating voltage was used; with an initial current of 12 nA gradually reduced to 100 pA as the pillar cross section decreased. Micro-compression tests were performed using a nanomanipulator system, Kleindiek nanotechnik, which has recently been set up at Loughborough Material Characterisation Centre (LMCC) inside the FEI Nova600 Nanolab DualBeam FIB-SEM. The flat tip (AFM tip) with an equilateral triangle cross-section measuring 1.5 µm in side length was also machined by FIB. The deformation characteristic of the nano-scale pillar was compared to 10 µm rectangle micro-pillar to investigate the effect of the sample size on inelastic

deformation. Quantitative Weibull analysis suggests that the increase in strength can be attributed to the lower probability of having weak flaws in a small sample.

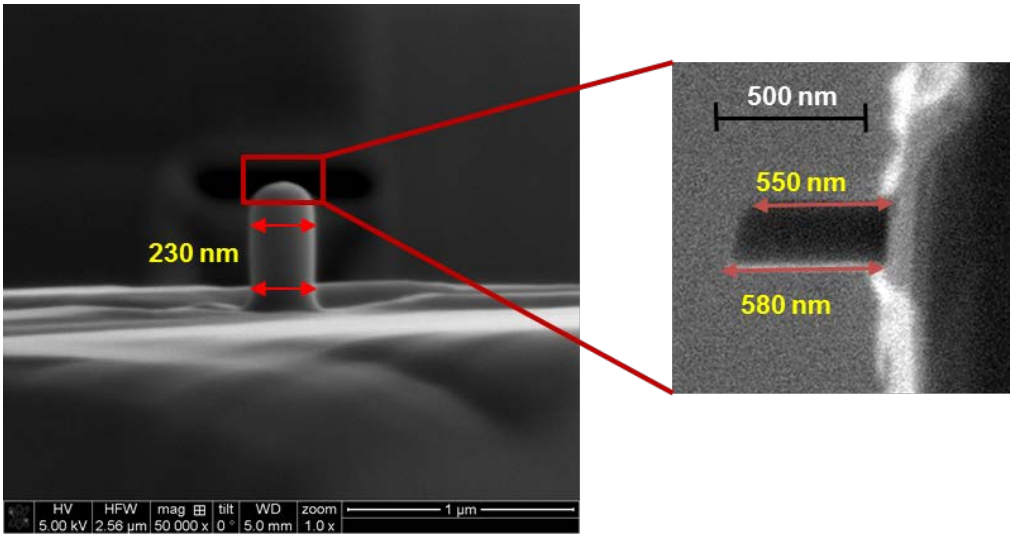

Figure 6-10 SEM image of the as-fabricated 230 nm nano-pillar. The tapering angle of the as-fabricated pillar is lower than 1 º and the pillar top is round. The height of the round region is ~ 30 nm, hence the inelastic deformation was rarely affected by the top pilar.

-Nanomanipulator Setup for micro-compression experiments

The setup is consisting nano robots with nanoelectronic controls, which can operate under SEM. These manipulators have joint configuration RRP (revolute–revolute–prismatic), which uses two rotational joints with 0.1 µrad resolution and one prismatic joint with 0.25 nm resolution. These nanomanipulators have well-behaved kinematic and backlash-free characteristics besides having nano-scale precision to guarantee accurate manipulation. The accuracy of a manipulator's tip control under SEM is in nanometers. It comprises a MM3A Manipulator attached with a microcantilever based force sensor at its gripper/tip position. There is a micro spring positioned next to it in order to generate force-deflection

experimental value. Using MM3A controls the manipulator can interact with objects in its work space at both micro- and nano- scale. When the manupulator tip made a contact with an object, it causes a feedback signal response proportional to the force applied because of a piezo-resistive layer on the surface of the force sensor. The force feedback signal is amplified and converted as audio output to sharply notice the first contact between the object and manipulator tip. The manipulator tip and cantilever spring interaction can be viewed on a computer screen in high resolution using SEM; these images show deflections in submicron range. The photographs of manipulator, complete setup, cantilever spring, and force are shown in Figure 6-11.

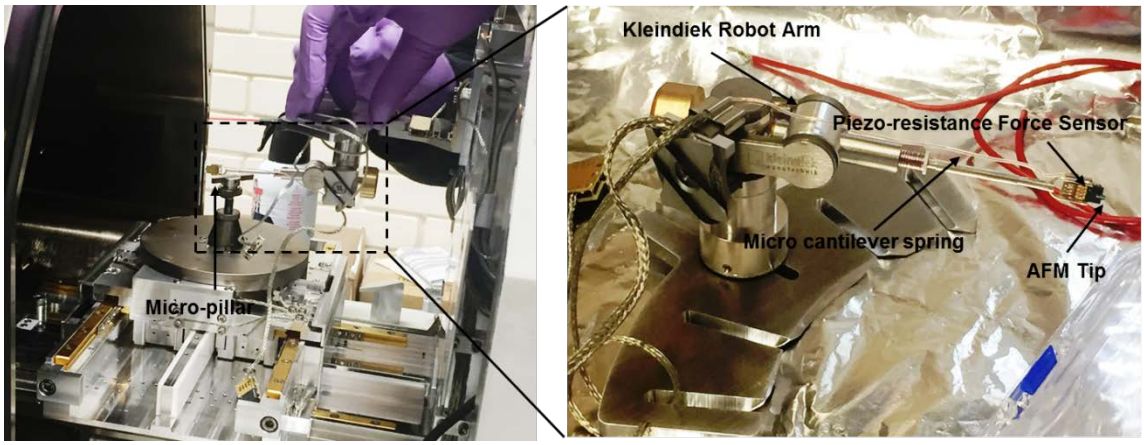

Figure 6-11 Experimental set-up of *in-Situ* microcompression study inside FIB (b) MM3A-LMP Micromanipulator and its component including AFM tip, Piezo-resistance force sensor and Micro cantilever spring.

Figure 6-12 shows a SEM image of the compressed the 230 nm pillar, where two shear offsets were observed. The shear band spacing was ~40 nm, which was easily measurable in the image. In contrast to the 10 µm pillar of the virgin state, the shear band did not form an intersect with the pillar top surface at the location of the indenter/pillar contact and the inelastic deformation was localised within shear bands (as shown by arrow in Figure 6-12). This indicated that the

deformation mode of the studied pillar was invariable with the localised shear banding, independent of sample size. There was no deformation change from localised-to-homogeneous deformation occurred up to 230 nano-pillar. Despite the fact that the micropillars were inhomogeneously deformed by localised shear bands, it was evident that the strength of these pillars was a function of the sample size. The yield strength of the 10 µm and 230 nm pillar are 1.8 GPa and 2.26 GPa, respectively.

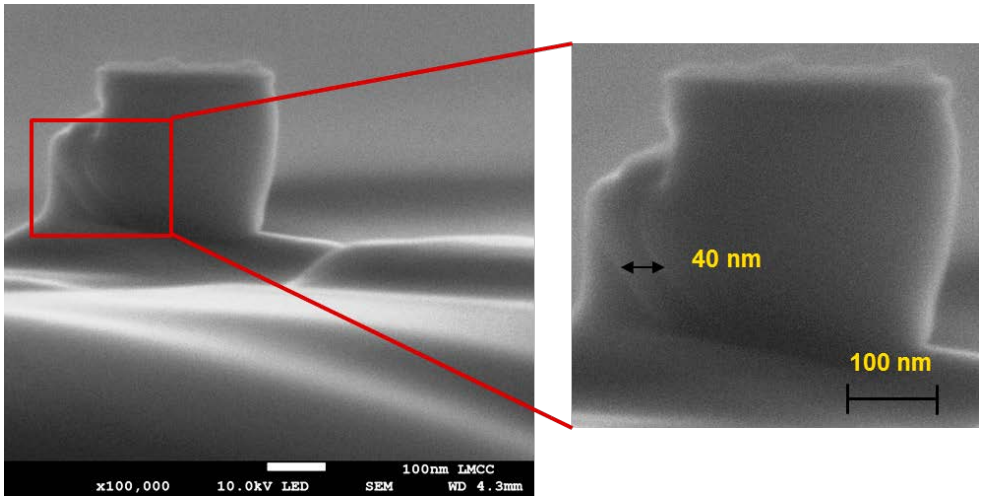

Figure 6-12 High resolution SEM micrographs of deformed 230 nm micropillars rectangular after compression test. Two shear bands were observed (highlighted with arrows)

The effect of possible geometrical artifacts such as tapering of the pillar and the pillar top roundedness was considered to interpret the plasticity and deformation mode of the 230 nm pillar. As shown in Figure 6-12, the taper in the 230 nm pillars in this study was less than 1º leading to very low stress gradient along the shear plan and it was unlikely to affect or suppress the shear band propagation as reported by Schuster *et al.* [138]. The non-planarity of the nano-pillar`s top resulted in non-uniaxial stress state directly underneath the contact with flat

punch. As the fabrication of the 230 nm pillar was very challenging, there was a possibility that the deformation mode of the pillar could be affected by this geometrical artifact of the non-flat top surface. However, the total plastic displacement of the pillar was larger than the height of the round region (around 30 nm). Thus, the round part of the pillar did not contribute to the plastic deformation and the deformation was accommodated by the lower section with constant cross section area, and the width of the pillar uniformly increased. SEM image of the compressed pillar presented in Figure 6-12 demonstrate the evidence of shear banding within the pillar in the section with constant cross-section area, that do not suffer from the geometrical artifacts.

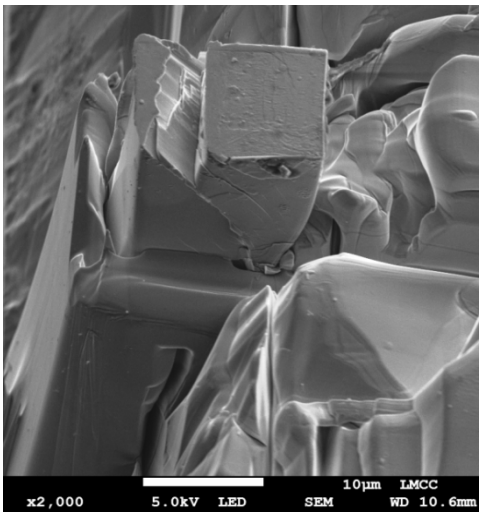

Figure 6-13 Fracture surface of a compressed 10 µm micropillar. The surface was smooth and shiny not showing any evidence of vein pattern or local melting. The top half of pillar was completely sheared off from the lower half.

Figure 6-13 shows the fracture surface of the 10 µm micro-pillar; its appearance was flat and shiny. The fracture surface of BMGs generally exhibit “vein” pattern with sub-micron dimension or evidence of molten droplets [144]. Hence, further investigation is required to discover a reason for flat fracture of the pillar.

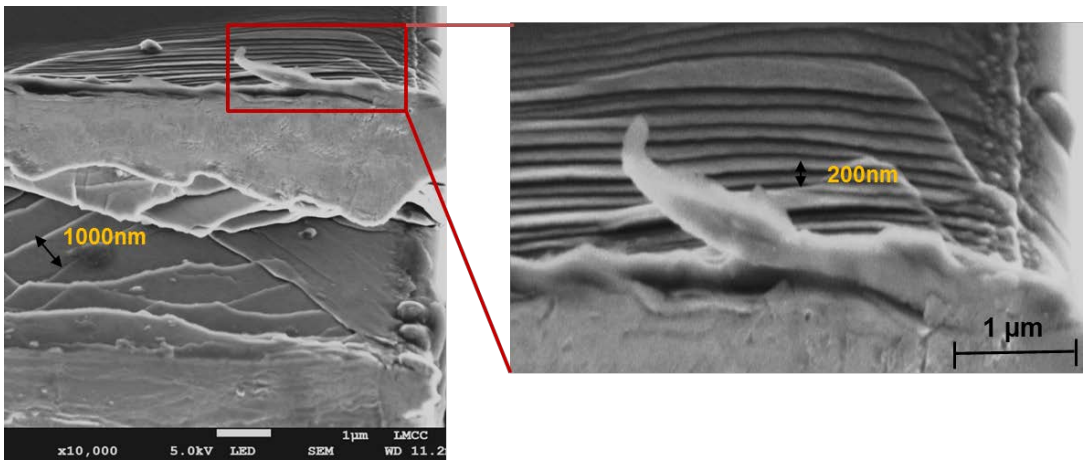

Figure 6-14 SEM micrographs of deformed 10 µm micropillars rectangular

As shown in Figure 6-12, there was a very limited number of shear bands in the 230nm pillar compared to the 10 µm pillar (see Figure 6-14). This suggests that smaller pillar was close to the size comparable with observed shear band spacing. Thus, the measured apparent yield strength of the 230 nm pillar (2.62 GPa) would represent the strength of the material without any volumetric defects. Figure 6-12 and Figure 6-14 illustrate the shear band spacing for the 230 nm and the 10 µm pillars. For micro-pillars of 10 µm, shear band spacing mainly ranged from 200 nm to 1000 nm. However, shear band spacing decreased from this range to 40 nm for 230 nm micro-pillar and finer shear bands were formed. Therefore, with decreasing the sample size, the average shear band spacing became narrower and the density of shear band decreased.

For brittle materials, flaw sensitivity can be used to describe the variability of their strength. Weibull statistics, as firstly discussed by Schuster [49], can describe the strength increase with decreasing sample size. The Weibull equation explains the fracture possibility of P_f as a function of a given uniaxial stress σ in forms of [145]:

$$P_f = 1 - exp\left[-V\left(\frac{\sigma - \sigma_u}{\sigma_0}\right)^m\right] \quad 6\text{-}2$$

where σ_0 is a scaling parameter, m is the Weibull modulus, and V is the volume of tested sample. The parameter σ_u represents the stress at which there is a zero failure probability, and is usually considered to be zero [51]. It was assumed that the characteristic flaw causing fracture in both micron and sub-micron micropillars were the same, then, at a fixed fracture probability, then $P_f = constant$, above equation can be simplified to:

$$\left[V\left(\frac{\sigma}{\sigma_0}\right)^m\right] = const. \quad 6\text{-}3$$

since $V = d^3$, where d is the diameter of the compression sample,

$$d^3\sigma^m = const. \quad 6\text{-}4$$

As mentioned previously, the apparent strength of 10 µm and 230 nm of the Zr-Cu-based BMG sample are 1.800 GPa and 2.26 GPa, respectively. Inserting these values to Eq.6-4, the Weibull module is calculated to be about 50, which is within range of the m values recently reported for the malleable (m=73.4) and brittle (m =25.5) Zr-Cu-based metallic glasses. The higher m -value indicated higher ductility of the specimens. The above analysis supported the observation that the compression stress increases with decreasing specimen size can be as result of reducing the defect populations in the specimens.

6.5 Conclusion

This chapter details an investigation on different techniques to prepare micropillars of the studied BMG with the lowest possible taper angle. As

described, the rectangular micropillars were milled by means of top-down milling method with specimen taper less than 1º.

The rectangular micropillar specimens with cross-sectional area of 10 µm × 10 µm were prepared from as-cast and the fracture surface area to study the deformation behaviour of a highly deformed region and as-cast specimens of the studied BMG. The deformation mode of these pillars was dominated by localised shear banding which manifest in stress drop to release the energy. The results also indicated that shear band initiation was easier than their evolution. In the deformed region, the stress required (0.8 GPa) to initiate shear bands is significantly lower than that for the as-cast pillar, which was ~ 1.8 GPa. The elastic modulus of as-cast pillar was ~ 85 GPa , which was 10 % lower than the value of 95 GPa obtained during three-point bending test due to the misalignment or imperfect contact between the top surface of the pillar and the flat punch.

Additionally, micro-pillars with cross section sizes of 10 µm × 10 µm and 230 nm × 230 nm were fabricated and then tested in homogenous loading condition to investigate the effect of sample size on deformation characteristics of the BMG. For all sizes, the plastic flow was localised in shear bands. The apparent yield strength of the pillar specimens was between 1.8 GPa and 2.26 GPa showing 25% variation in strength. The strength enhancement was successfully modelled using Weibull statistics for brittle materials. Therefore, the increase in strength can be as a result of the fact that a smaller sample has less defect population.

7 Characterisation of Shear Bands

7.1 Introduction

Shear-banding is one of the primary mechanisms of plastic deformation in BMGs [26,38]. It is a form of plastic instability that localises large shear strains in a relatively thin band (shear band), when a BMG is deformed. At room temperature, shear bands are particularly important, as they control the plastic deformation and failure behaviour in metallic glasses. To study mechanical behaviour of metallic glasses, the key is to fully understand shear bands, their initiation, propagation and overall mechanical properties. Hence, specific characteristics of shear bands were investigated, namely,

- initiation of shear bands: propagation, evolution and sliding;
- crystallinity / non-crystallinity of shear bands;
- geometric characteristics of shear bands;
- mechanical properties of shear bands.

A surface-decoration technique was adapted to investigate formation and evolution of shear bands during wedge indentation experiments (see chapter 5) at sub-micron length scales. Shear bands were microstructurally characterised using XRD and TEM. Mechanical properties of individual shear bands in the Zr-Cu-based metallic glass were investigated using an indentation technique in order to obtain a better understanding of how shear-band plasticity was influenced by non-crystalline defects.

7.2 Surface decoration

In experiments at microscale, surface features such as grains, inclusions, second-phase particles or surface scratches often lacks surface features of the appropriate size or optical contrast to study local displacements. Typical methods such as strain gauges or optical non-contact methods used for displacement measurements cannot be applied at nano- or micro-scale. Surface decoration is a process of applying an artificial surface pattern with the appropriate size or optical contrast as natural surface to evaluate local displacements by comparing corresponding area before and after deformation by using various techniques such as digital image correlation technique (DIC). Surface-decoration techniques such as spray painting, grinding or etching are used to provide patterns at the macro-scale [146]. These techniques can be used up to 1000X magnification with conventional optical microscopes. In the last few decades, research has led to the discovery and development of structures with features in the nanometre range [147]. Consequently, more specialized surface-decoration methods were required to visualise these nanometer features at higher magnifications. Scanning Electron Microscopy (SEM) can provide high- quality images over a broad range of magnifications from about 30x to greater than 100,000x. Furthermore, the decoration techniques such as microcontact printing, UV photolithography and gold coating are employed to create features less than 100 nm [148,149]. Surface decoration can be applied very locally using Focused Ion Beam (FIB) and a Focused Electron Beam (FEB) methods to create features on the specimens. FEB and FIB can also be used for sputtering of metallic films in the pattern of a randomly structured bitmap with resolution of features less than 5 nm in size [140,150]. In

addition, FEGSEM-FIB instruments can offer high quality imaging at high magnifications; those can image feature with resolution less than 5 nm in addition to allowing precise milling using as ion beam [151].

Surface-decoration techniques including etching and FIB were employed to create patterns on specimens in order to track formation and evolution of shear bands in the samples. The beam-shaped specimens of the studied BMG with a length of 40 mm, width of 10 mm and thickness of 2 mm were mechanically polished to a mirror finish (see chapter 4) to offer best conditions for observing shear bands. Polished specimens were etched using Nitro-Hydrochloric solution (Aqua Regia), by immersing them for duration times of 2 minutes and 10 seconds in the solution. Aqua regia is a mixture of two parts HCL, one part HNO3 and two parts of water. Morphology of the specimen`s surface after etching was characterised with FEG-SEM (Leo 1530VP FEGSEM). As shown in (Figure 7-1(a)), the 2 min immersion resulted in metal heavily reacted with etching solution, yielding no useful information. As can be seen in Figure 7-1(b), the 10s immersion of the sample revealed a few features; however, it led to formation of some holes with dimension of up to 3µm. This is a potential problem as shear bands have dimensions typically in tens of nanometre and the features generated after etching were significantly larger in size compared to size of shear bands. The formed holes can also lead to local compositional changes and structural changes due to dissolution of the valve-metal components, such as Zr, and partial re-decomposition of Cu [152]. In addition, the formed holes can act as favourable surface sites for initiation of bands and stress raiser since these holes, like sharp edges or tips, are mechanically weak points. These extended features can distort the overall conclusion of the study.

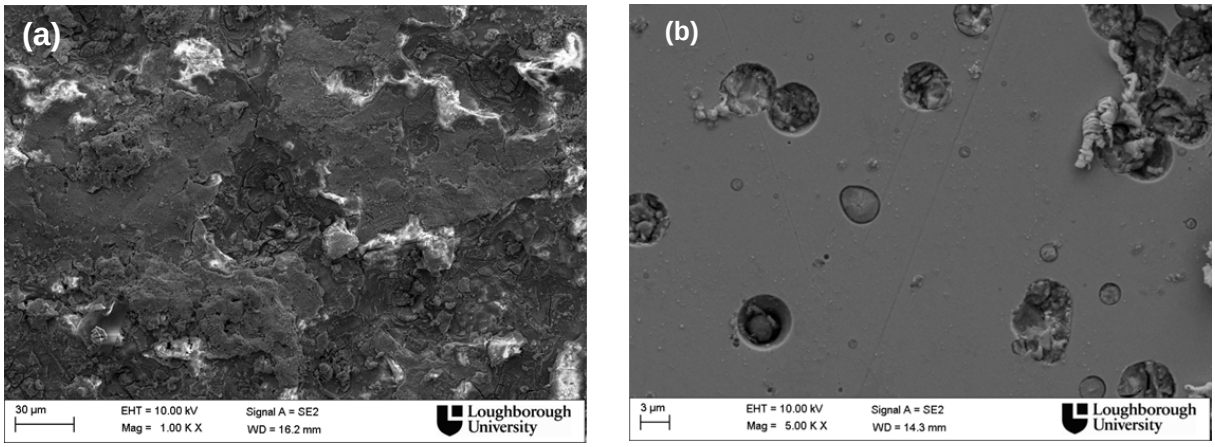

Figure 7-1 SEM images of $Zr_{48}Cu_{36}Al_8Ag_8$ surface after immersion in Nitro-Hydrochloric solution for 2 min (a) , which heavily reacted with etching solution and 10 s (b), which shows holes of 3 µm in diameter.

It can be concluded that specialized surface-decoration methods were needed to visualise nanometre-scale features at higher magnifications. To implement this approach, an initial indentation load of 500 N was applied using the wedge-indentation technique on a beam-shaped specimen with dimension of 80 mm × 5 mm× 2 mm. To create a fine local grid, microlines were milled using FIB with 30 kV acceleration voltage and 10 pA beam current; it took ~1 s to produce each microline. Milled lines had a length of 20 µm, width of 0.2 µm and spacing of 1 µm (Figure 7-2). Ten 6x6 sets of gridlines were milled on the front face of the indented sample. Next, wedge indentation was performed by applying subsequent load increments of 1 kN. SEM images of 5000x magnification with a 128 µm Horizontal Field Width (HFW) were taken before and after each incremental loading to evaluate surface deformation caused by wedge indentation into the tested material. The induced shear bands were characterised using a Zygo NEWVIEW 5000 system. Shear band morphology was examined at ten different locations as shown in Figure 7-4.

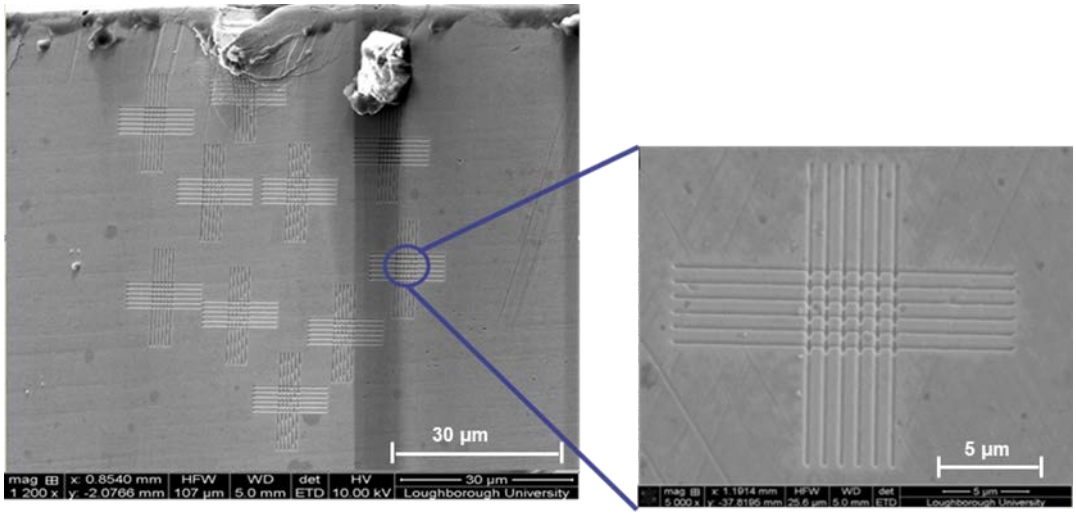

Figure 7-2 SEM images of FIB nano lines produced with surface-decoration process with detailed set of gridlines shown at higher magnification.

It is known that surface imperfections serve as preferable sites for initiation of shear bands [153]. In the present study, there were no obvious differences in shear band evolution in specimens with polished and decorated surfaces, suggesting that surface decoration had no influence on shear-band initiation and evolution (Figure 7-3).

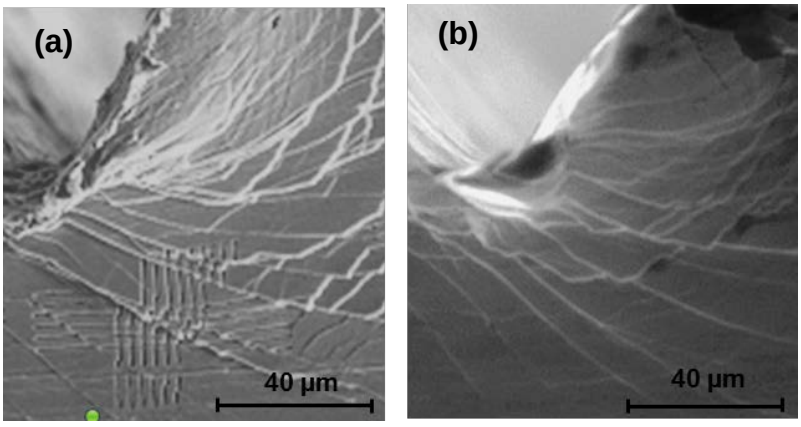

Figure 7-3 SEM image of shear band evolution with (a) and (b) without surface decoration.

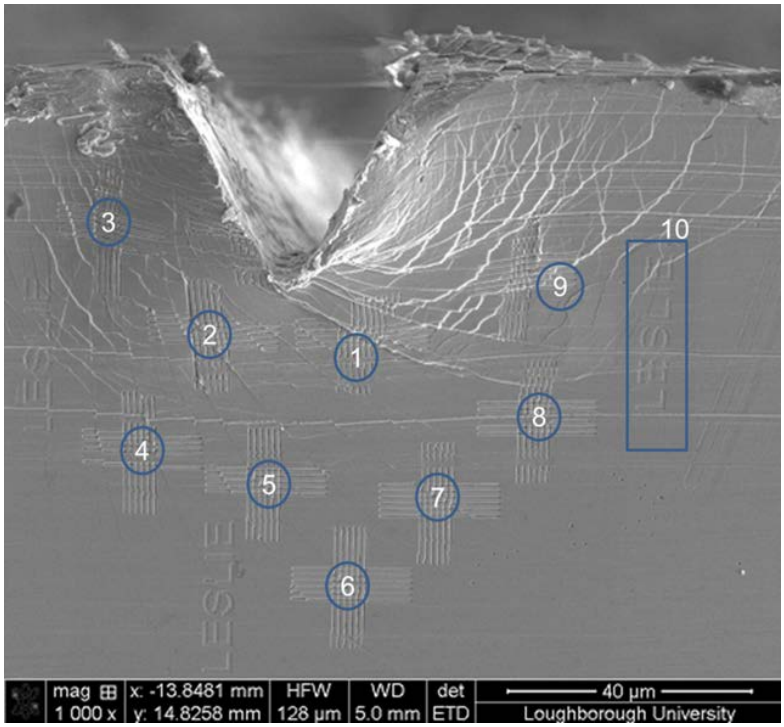

Figure 7-4 SEM image of surface decoration with numbered locations.

A new model of deformation behaviour of metallic glasses can be proposed based on the current observations in the surface-decoration experiments. Shear band did not operate simultaneously across the shear plane resulting in catastrophic behaviour with no plastic deformation in the BMG. As illustrated in Figure 7-5(b-e), shear bands formed a localised deformation zone and slip occurred across these bands as marked by black arrows in Figure 7-5. This indicates that once a shear band formed, it caused the material volume across it to slip (Figure 7-5 (c)). Thus, shear bands do not 'flow' in contrast to the motion of dislocations along a slip plane in conventional crystalline metals; they shear bands propagate discretely through the volume.

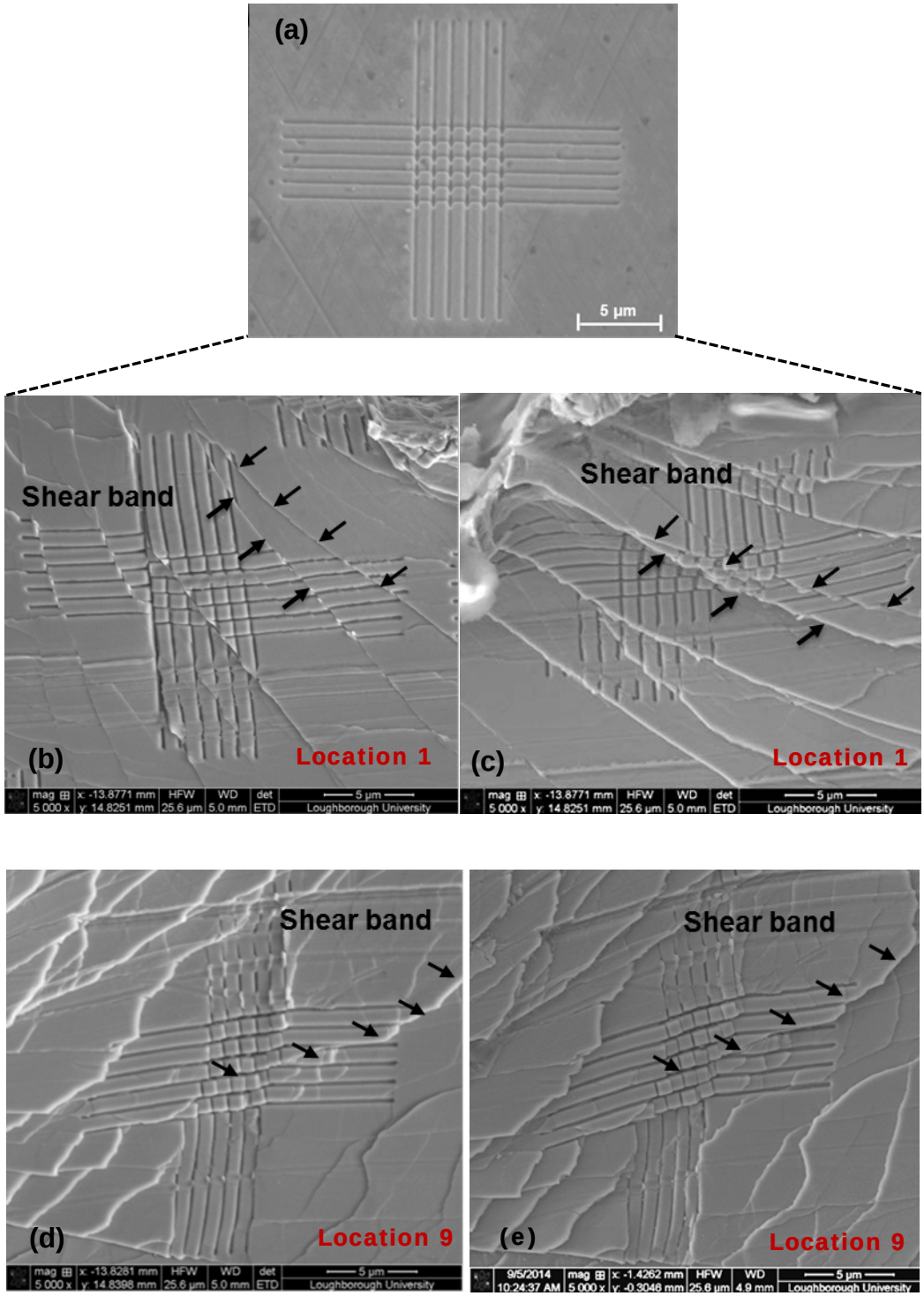

Figure 7-5 Evolution of shear bands with incremental loading in locations 1 and 9 shown in Figure 7-2 using surface-decoration technique: (a) undeformed gridline; (b) and (c) 1 kN; (d) and (e) 1-2 kN.

Next, morphology of the material surface showing shear bands was studied (front face in Figure 5-22(b)). A shear band was chosen for this as shown in Figure 7-6(a) and the variation of height across it was measured at three locations (designated by lines 1, 2 and 3 in Figure 7-6(a)). The measured profiles of the surface indicated that the variation of height across the shear band increased by moving further away from the indenter, indicating that shear bands caused an out-of-plane displacement. Interestingly, depending on location, a rotation of material volume was observed due to shear-band deformation (Figure 7-5 (c)).

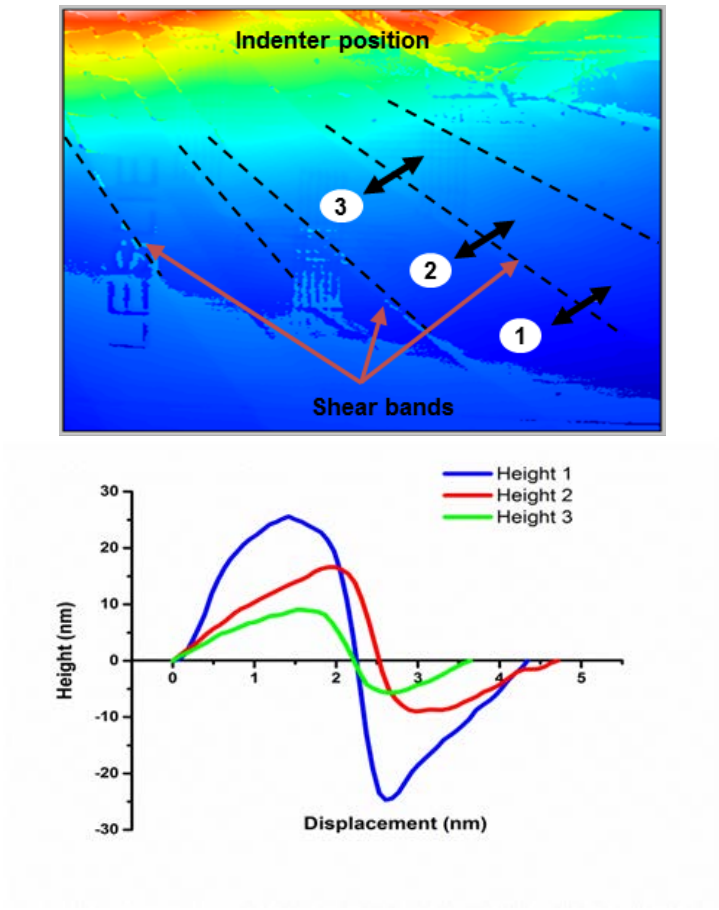

Figure 7-6 Measurement of material`s height along single shear bands: (a) overall appearance of shear bands; (b) sites variation of height along shear band for measurement shown in (a)

7.3 Microstructural characterisation

The amorphous nature of the deformed beam-shaped specimens under wedge indentation was examined via XRD; the X-ray diffraction patterns obtained from the top and front face of the wedge indented sample (Figure 5-22 (b)) are shown in Figure 7-7. A broad diffraction without any crystalline peak was observed in the XRD patterns of both deformed specimens under wedge-indentation and as-cast specimens, indicating fully amorphous structure, in both cases.

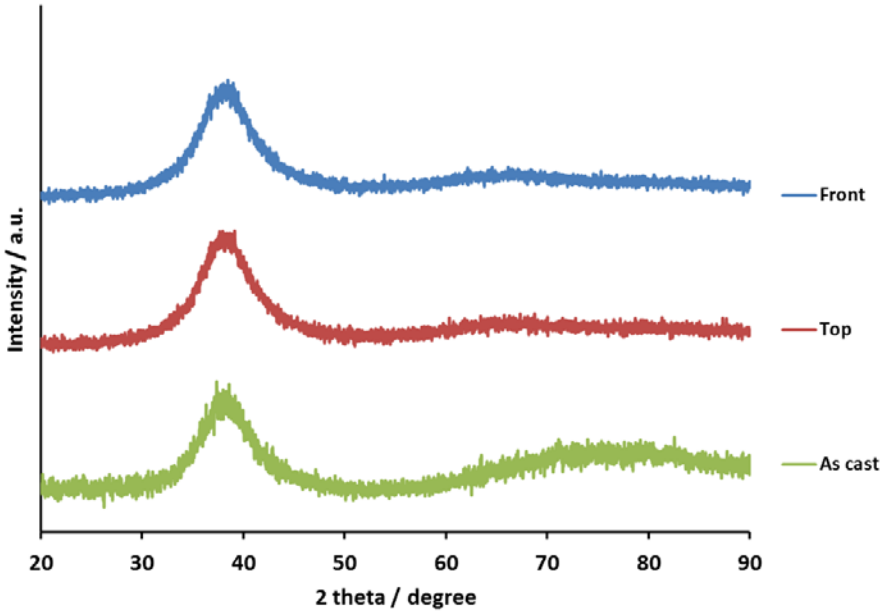

Figure 7-7 XRD patterns of as-cast $Zr_{48}Cu_{36}Al_8Ag_8$, top and front of wedge-indented sample. Note that the deformed sample did not have any detected crystal-diffraction peaks.

To understand the microstructural characteristics of the shear bands, TEM studies were performed to investigate a deformed region below the wedge indent, in particular the area with noticeable shear bands (See Figure 7-8). Thin-film foils for TEM were prepared using FIB providing locally uniform foil thickness; thin slices were cut along a plane parallel to the loading direction and

perpendicular to the visible shear planes identified from the traces of slip bands on the sample surfaces. The composition of the samples was locally studied using TEM-EDS.

In the bright-field image of specimen`s the cross-section (Figure 7-8(b)) extracted from a typical location shown in Figure 7-8(a), no dark contrast can be seen. For a TEM specimen with uniform thickness, lack of a noticeable contrast between shear bands and the surrounding undeformed matrix indicated that there was no significant change in the structure. The region within a shear band was studied by using a 200 nm × 200 nm square selected area aperture. As presented in Figure 7-8(b), there was no sharp diffraction pattern in this region demonstrating no formation of nano-crystalline structure in the shear bands, and a diffuse ring pattern indicated a fully amorphous structure. The combination of locations, where the SAED was obtained from, was tested in-situ with EDS. The measurements showed that the elemental concentrations were close to the nominal value of 47.2 at.% Zr, 37.1 at.% Cu, 7.8 at.% Al and 8.1 at.% Ag . Incidentally, similar compositions were observed during the study for the as-cast and the deformed BMG using the SAED technique. In summary, no compositional changes were found in the shear-band region.

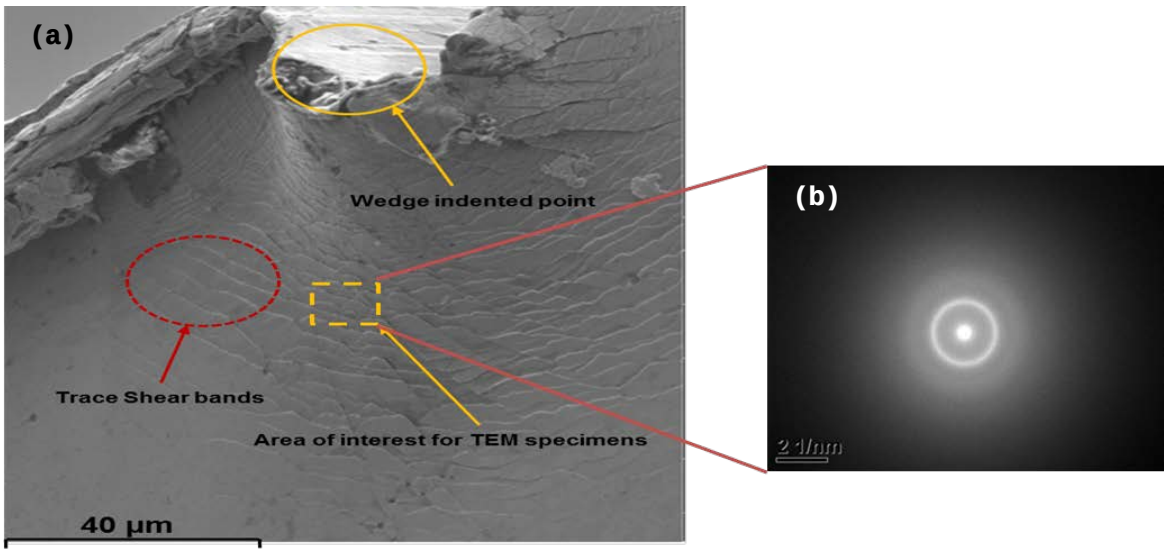

Figure 7-8 (a) SEM micrograph of wedge-indented $Zr_{48}Cu_{36}Al_8Ag_8$ sample with pre-polished surface showing traces of shear bands. (b) BF TEM image from regions within shear bands.

To further investigate the micromechanism of localised plastic deformation in the BMG, microstructure of the fracture surface obtained from three-point bending was characterised with XRD (Figure 7-9) and TEM (Figure 7-10(a)). The cross-sectional TEM foil was cut with FIB from an area with a typical vein pattern of the fracture surface (Figure 7-10(b)). Figure 7-11(a) shows a TEM image obtained from the fracture surface of the studied BMG and a representative crystalline material (Pt). For the crystalline structure, dark dots in the matrix illustrated in the image show ordered nano-domains of sizes less than several nanometers; the sharp diffraction spots demonstrating the formation of nanocrystals in the matrix. The bright-field (BF) image of the fracture specimen is shown in Figure 7-11(a), where the featureless contrast can be seen in the fracture-surface section. The featureless contrast in the BF image is associated with no significant structural changes in the fracture surface; hence, there is no structural ordering within the

fracture surface. The corresponding SAED pattern shows a diffuse ring without a sharp diffraction pattern confirming the amorphous structure. The composition measurements using TEM-EDS illustrated that the elemental concentrations were close to the nominal value of 46.8 at.% Zr, 37.00 at.% Cu, 8.1 at.% Al and 7.9 at.% Ag, which is similar to the as-cast materials. These results further confirmed that yielding of the BMG does not lead to crystallisation in the material.

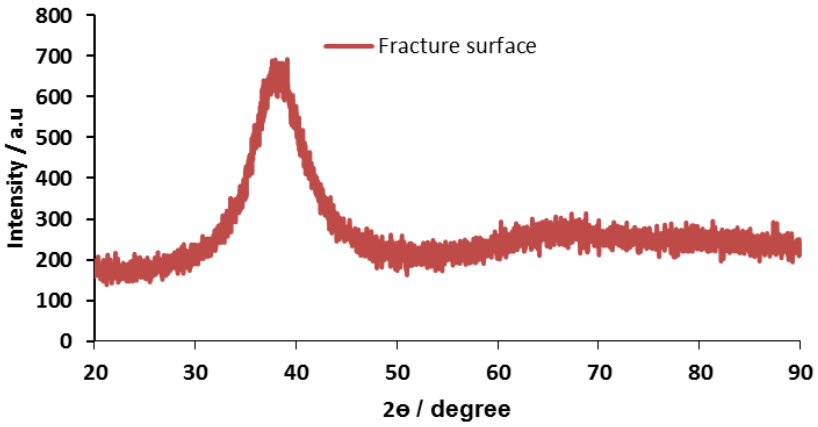

Figure 7-9 XRD pattern of $Zr_{48}Cu_{36}Al_8Ag_8$ for three-point bending.

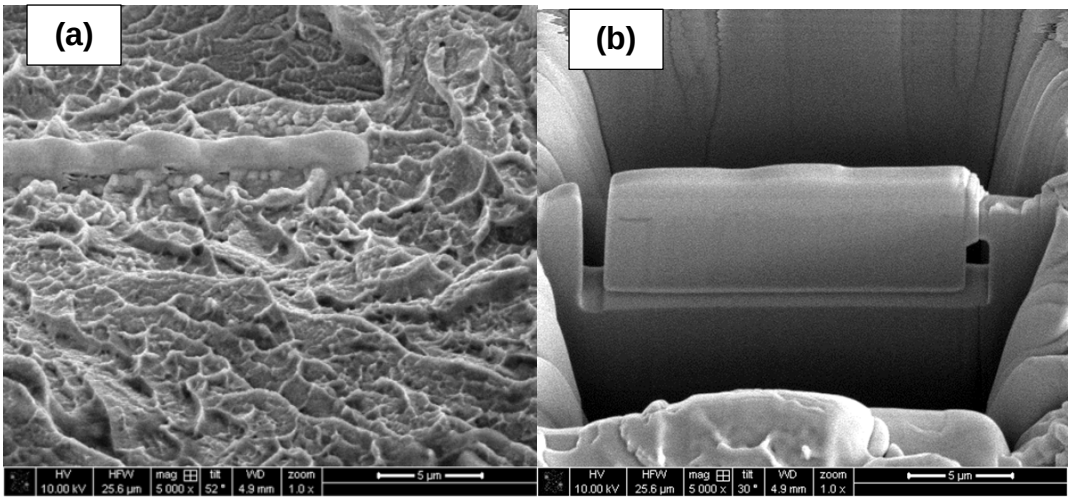

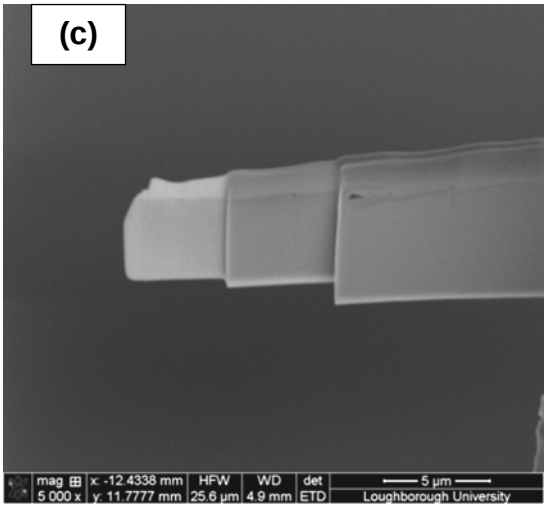

Figure 7-10 (a) Fracture surface of $Zr_{48}Cu_{36}Al_8Ag_8$ sample, showing typical vein morphology, under three-point bending used for TEM preparation: (b) initial stage of sample preparation for TEM; (c) TEM specimen mounted on TEM grid.

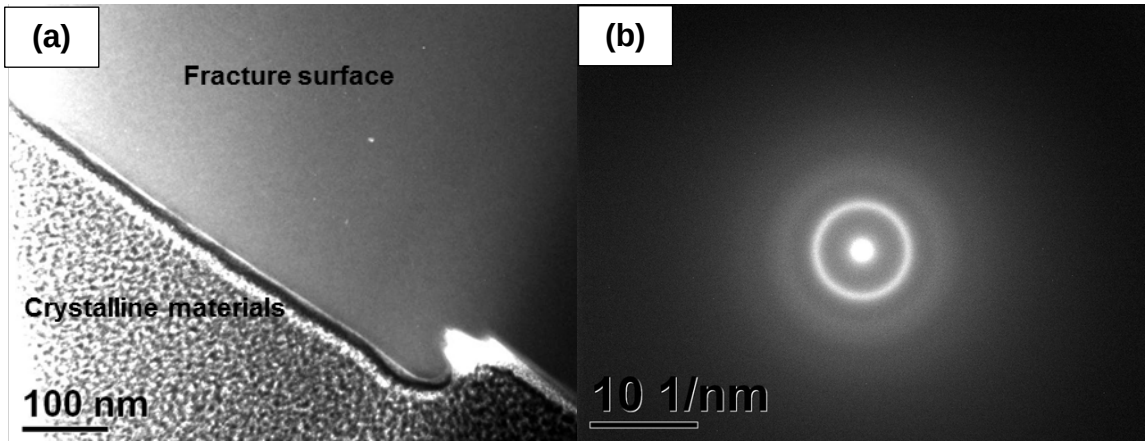

Figure 7-11 TEM micrograph and SAED pattern of fracture surface of $Zr_{48}Cu_{36}Al_8Ag_8$ sample under three-point bending: (a) dark field TEM micrograph image of the BMG vs. crystalline materials; (b) nanodiffraction patterns from fracture surface region with vein pattern on fracture surface.

7.4 Indentation of sheared zone

7.4.1 Indentation of individual shear bands

As shear band is a mechanism of plastic deformation in metallic glasses, mechanical properties of individual shear bands were investigated in order to obtain a better understanding of the effect of non-crystalline defects on shear-band plasticity. Thus, important questions arise are: (i) what actually are the mechanical properties of the shear bands; (ii) Are the inter-band mechanical properties similar to or higher than those of the shear band. The wedge indentation test was performed with a peak load of 2000 N to obtain well-developed shear bands on the front surface of the specimens (see Figure 7-12). Under this condition, it is easy to determine the location of shear bands or sheared regions in the specimens. A series of nano-indentation experiments were conducted near and on traces of the shear bands using a Vickers indenter with a maximum load of 100 mN and a loading rate of 2 mN/s (with a 30 s hold time at peak load). Since the indentations were spaced at an interval of 10 µm and their size was around 5 µm, the spatial resolution perpendicular to the shear band was within 3 µm. The values of hardness and modulus measured in the deformed region could be divided into two groups based on the location of nanoindentation imprints. Firstly, the indentations were made between the shear bands in the deformed region, as shown in Figure 7-12. Secondly, some indentation imprints were placed over the shear bands. The indentation made over shear bands exhibited a larger peak-load displacement than that in the inter-band area (Figure 7-13 (a)), indicating that shear bands were softer.

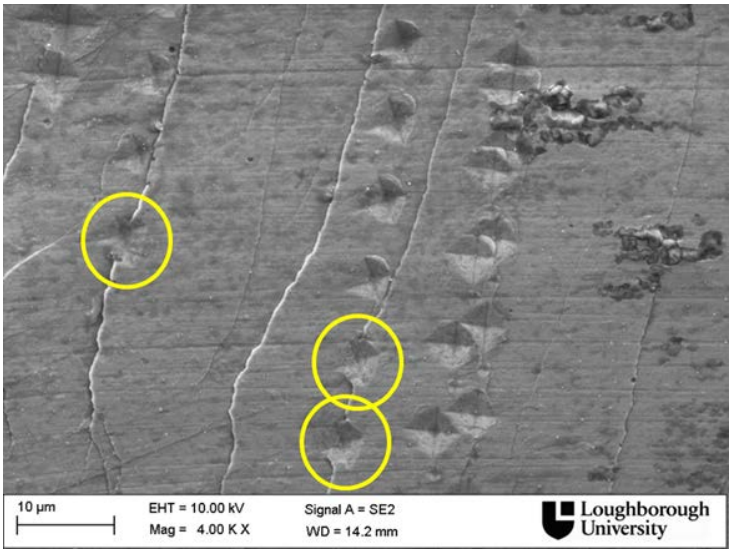

Figure 7-12 SEM image showing indentation made over shear bands and between them, i.e. in inter-band region.

The hardness values obtained for the bulk area were also higher than those for shear bands. It seems that the actual hardness of individual shear bands should be much lower than the measured value as the shear bands typically present only a small volume fraction of a deformed region, and the measured results average over both shear bands and an undeformed region. The initial part of the P-h diagram up to 10 mN still demonstrates a distinct difference in responses of the shear bands and bulk areas, indicating that the former are much softer. Obviously, at low indentation loads and, respectively depth, the material`s response is defined by the small volume localised around the shear band. In the subsequent stages of loading, contribution of parts outside the shear band would increase, moving towards the virgin-state behaviour. However, it is very challenging to perform indentations over the shear bands with very low loads and precise positioning is difficult to achieve.

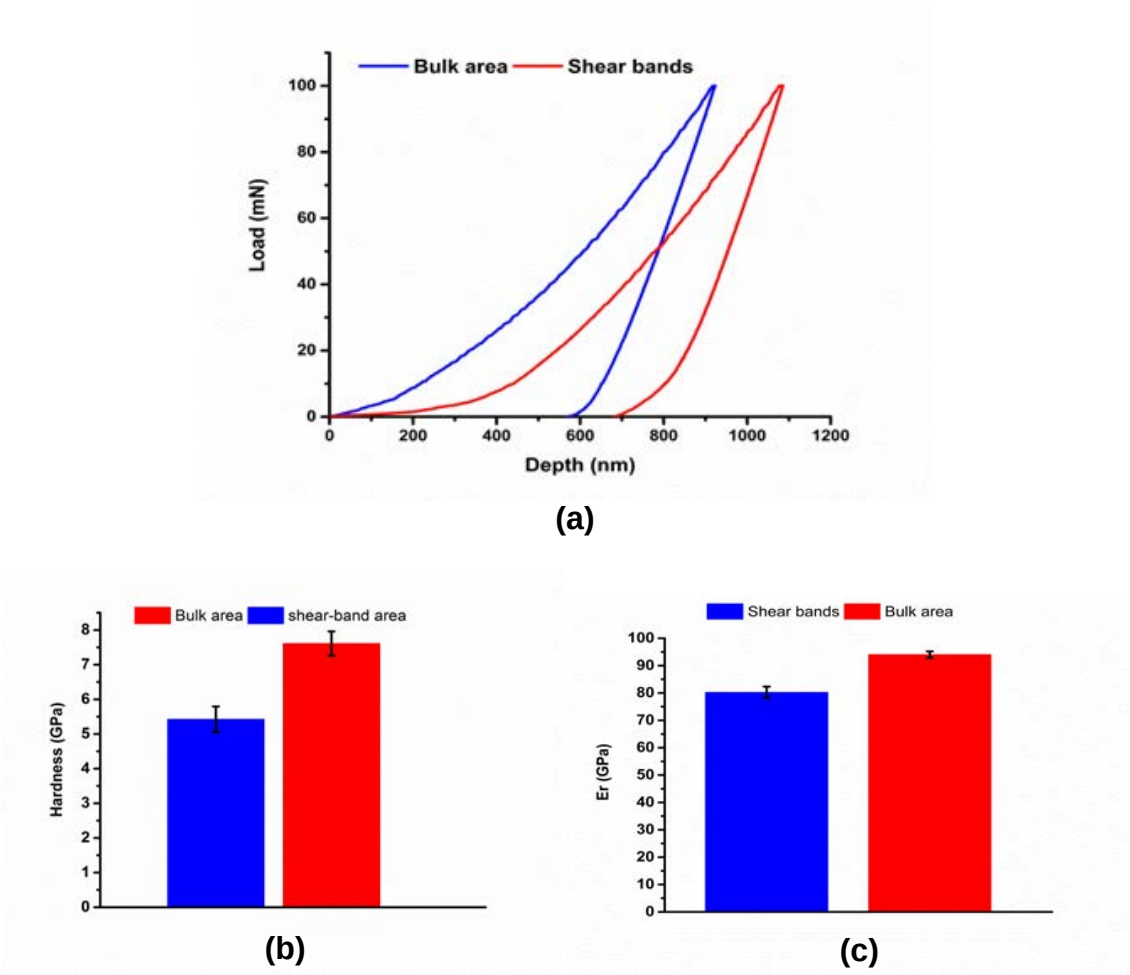

Figure 7-13 Shear bands vs. bulk area: (a) load-displacement; (b) hardness; (c) modulus.

Mechanical strength of the shear band can be estimated from the initial part of the P-h curve shown in Figure 7-13(a). The sheared zone can be about 500 µm wide based on the shear bands definition, at which deformation is localised and softening happens. The size of the sheared zone is similar to the shear-band width reported for crystalline materials [38]. The number of serrations is about 30 for the sheared zone in the indentation experiments. These results confirmed that the softening zone on the fracture surface was a sheared zone with the size of 400 µm. Hence, a large softening area was a result of concentration of

multiple thin shear bands in the deformed region. These shear bands were uniformly distributed in the sheared region, leading to formation of a composite comprising shear bands and undeformed region. SEM observations (Figure 7-12) showed much thinner shear bands compared to these results; it also indicated that a sheared zone was formed as a result of many serrations.

7.4.2 Indentation of fracture surface

Nano-indentation tests were carried out on the fracture surfaces of BMG specimens after three-point bending to investigate the effect of the dilatation process, which is considered as a mechanism of deformation-induced localisation, in a highly deformed region. The nano-indentation was performed at room temperature on Nanotest Platform III; equipped with a Vickers tip under a peak load of 100 mN and loading rate of 2 mN/s to determine mechanical properties of fracture surface during nano-indentation according to the theory by Oliver and Pharr. The obtained load-indentation depth (P-h) diagram for the indented fracture region is demonstrated in Figure 7-14 (a). Clearly, a distinct difference was observed between the fracture region and the undeformed material in indentation with 100 mN; the fracture region was much softer than the virgin material. In addition, the P-h curves exhibited increased serrated flow in the fracture region, indicating that a large number of shear bands were activated during the fracture process. The magnitudes of hardness and modulus of the fracture surface measured with nanoindentation were compared to those for of undeformed region: the former values were much lower, ranging from 0.5 to 1.5 GPa and 5 GPa to 30 GPa, respectively (Figure 7-14 (b-c)). There was a

significant decrease in excess of 80% in the values of hardness and modulus compared to those for the as-cast sample.

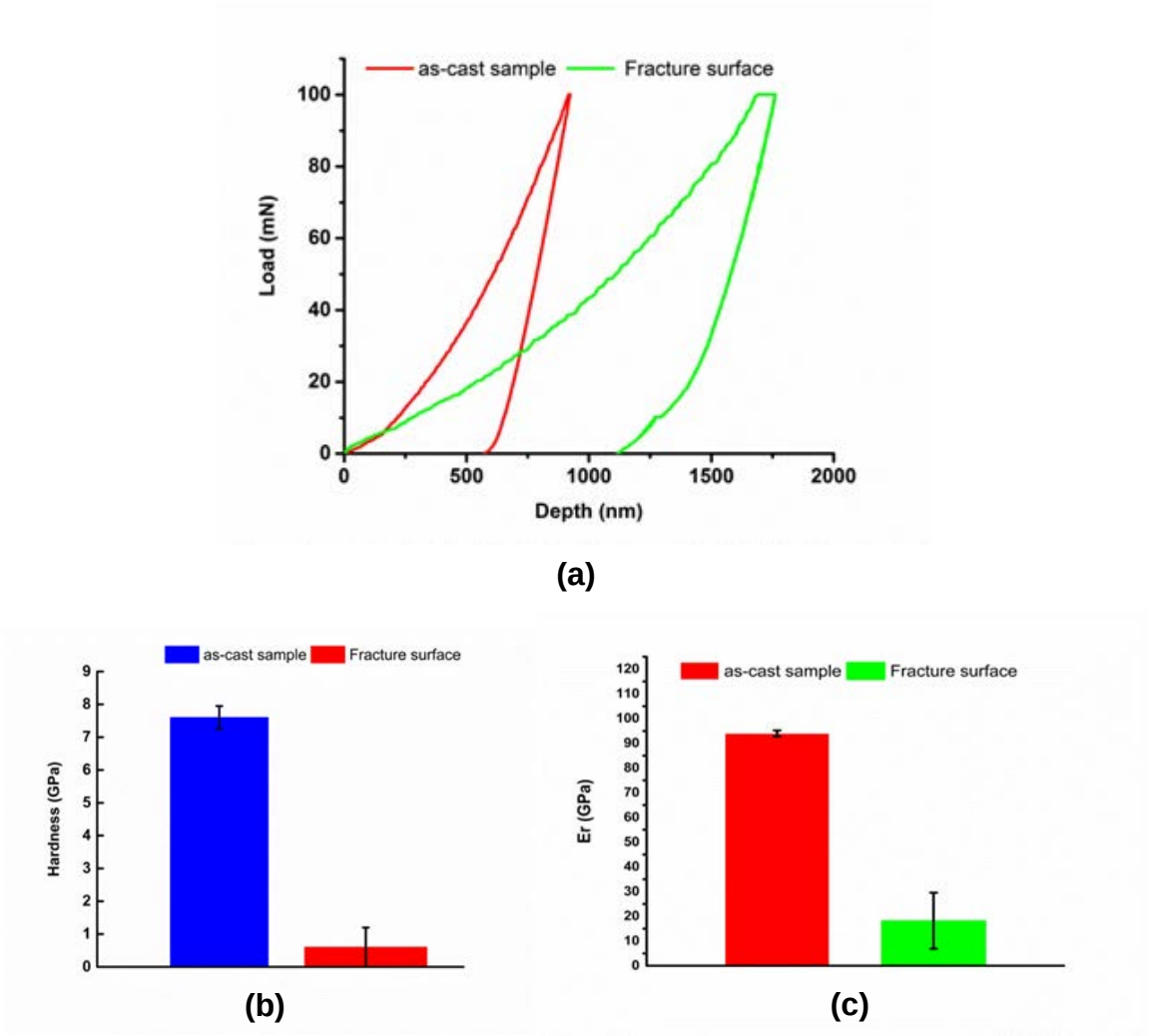

Figure 7-14 Fracture surface vs. as-cast sample: (a) load-displacement (P-h) curves; (b) hardness; (c) modulus under peak load of 100 mN.

The scatter presented in the experimental data may be due to the roughness of the fracture surface, affecting the contact area, or presence of softer shear bands close by. Hence, a series of nanoindentation experiments were performed on the fracture surface under peak load of 500 mN and loading rate of 2 mN/s with the Vickers indenter as the higher load to diminish the effect of surface

roughness. Figure 7-15 shows the representative nano-indentation load-displacement curve (P-h) curves, average hardness and reduced modulus (E_r) observed from two regions including fracture surface and as-cast sample. As shown in Figure 7-15(c), the indentation made in the undeformed area showed a much smaller displacement at the peak load than those in the fracture area, exhibiting that the fracture area was much softer than the as-cast materials. This trend implies that the undeformed BMG has less free volume, whereas the fracture region had a higher amount of statistically distributed free volume with random configuration of atoms [154]. The hardness and modulus of the fracture surface and undeformed region are shown in Figure 7-15 (a-b). As expected, the hardness and modulus of the deformed region are much smaller than those of the undeformed region, ranging from 0.25 to 0.5 GPa and 5 GPa to 30 GPa, respectively. Hence, it is also confirmed that there was a distinct decrease in excess of 80% in the values of hardness and modulus compared to those for the as-cast sample. To further confirm that the lower levels of hardness or modulus of the fracture surface were not experimental artefacts, nano-indentation experiments were conducted on the specimen's top surface close to the fracture surface area.

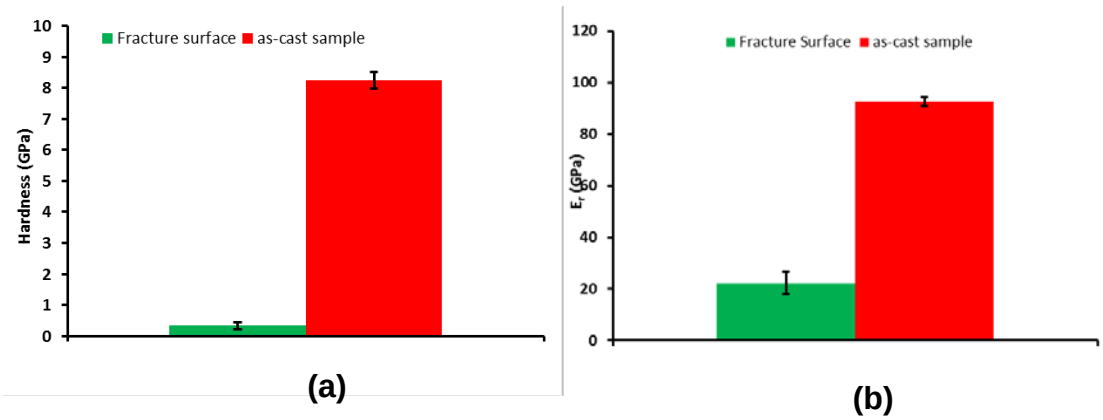

(a) (b)

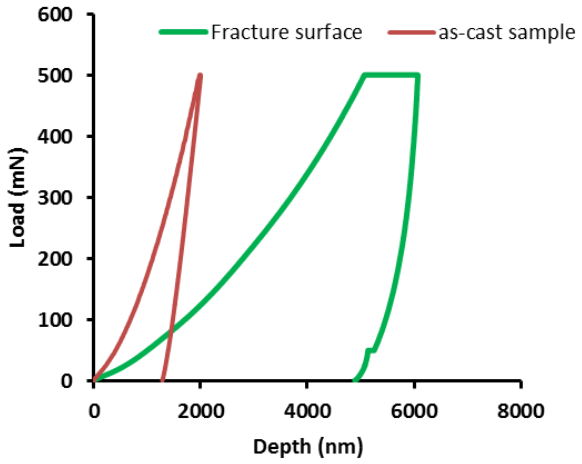

(c)

Figure 7-15 Fracture surface vs. as-cast sample: (a) hardness; (b) modulus; (c) load-displacement (P-h) curves under peak load of 500 mN.

Additional indents were made near the fracture surface under peak load of 100 mN and loading rate of 2 mN/s within the distance from ~16 µm to ~700 µm (Figure 7-16) to investigate variability of mechanical properties in the deformed region. This study demonstrated that the measured modulus varied from ~17 GPa to ~90 GPa with the latter corresponding to the respective value in the as-cast BMG, depending on the distance to the fracture surface (Figure 7-16(b)). The measured modulus gradually increased up to ~40 GPa in the region spanning around 400 µm from the fracture surface followed by a sharp increase to the as-cast level. These results also indicated that there was a weak zone or sheared zone, as discussed in the previous section, with the width of 400 µm followed by a distinct transition from the deformed region to the virgin-state area. The weaker zone can be as a result of STZs, which can operate everywhere within the plastic zone, Hence, it can be concluded that the extent of weaker zone gradually decreased in this zone from 81% to 55% of the modulus of the undeformed area with the distance to the fracture surface.

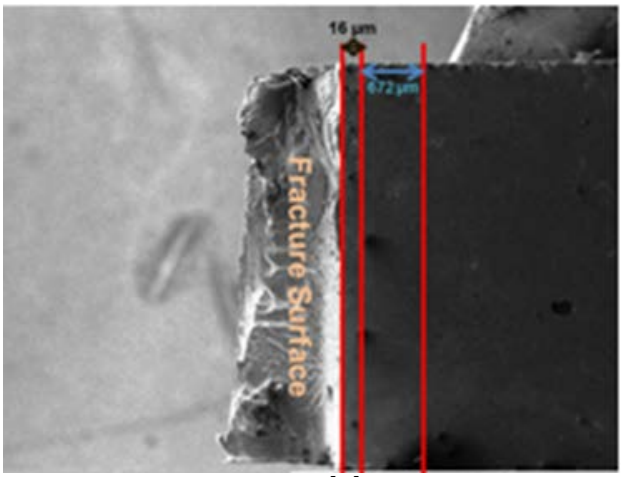

(a)

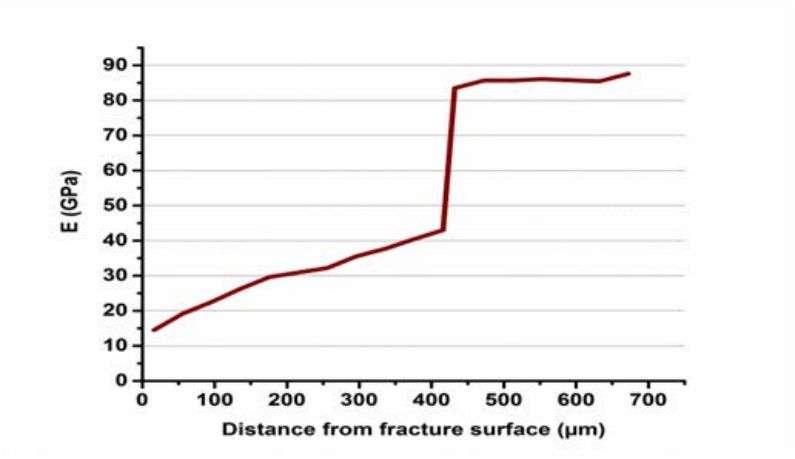

(b)

Figure 7-16 (a) Schematic of diagram illustrating indentation points on fracture surface and (b) variation in measured hardness with distance from fracture surface.

Some other factors may also cause the weak zone in BMGs such as excess free volume, nanovoid formation, nanocrystallisation and plastic deformation. The excess free volume leads to a situation, when the plastic zone is not limited to the fracture surface, and sheared zone could operate everywhere within this zone. It can also be indicated that the shear bands were evaluated through the materials volume [147]. Several researchers showed that temperature rises (from 0.1 K to ~1000 K) occurred inside shear bands, leading to strain softening. Such temperature rises are negligible at low strain rates as shown in Chapter 4;

therefore, it can be concluded that the onset of serration was controlled by the free-volume creation and annihilation leading to formation of shear bands. The pre-existing shear bands forming weak links are preferred sites for further deformation. As shown in Figure 7-5, old shear bands can act as artificial defects and promote the initiation of new shear bands and stabilize evolution of shear bands. This led to formation of a sheared zone contributing to plastic deformation. The sheared zone can be enlarged by nucleation of new shear bands, resulting in enhancing intrinsically ductility and free-volume creation. Yavari et al. [64] showed that the free volume in deformed metallic-glass ribbons was double that in the as-cast state.

The variation of the Young`s modulus and hardness can be also induced by damage evolution. In the last decade, much effort has gone to implement a continuum-damage- mechanics framework to predict failure behaviour of various types of materials such as metals [155], composites [156] and polymers [157]. In the pioneering work of Lemaitre and Dufailly [155], indentation approach was used to quantify deformation-induced damage through the degradation of indentation hardness and modulus. The hardness value is linearly proportional to the flow stress in the hardness-based damage quantification. Hence, this methodology investigated the hardness degradation with regard to the damage-induced changes in the flow stress. The damage parameter is considered as:

$$D_H = 1 - \frac{H_d}{H}, \qquad 7\text{-}1$$

where H_d is the measured damaged hardness and H is extrapolated from the hardness value in the undamaged area. In the similar way, the elastic-modulus-

based damage quantification assumes that the degradation due to the evolution of damage, and calculated by

$$D_E = 1 - \frac{E_d}{E} \qquad 7\text{-}2$$

where E_d and E are the elastic modulus in the damaged and undamaged area. If $D = 0$, the material is free of damage and if $D = 1$, the material is fully damaged. Although he microscopic damage morphology is not captured using this damage technique, the average flow response of the materials under the indenter is measured through the mean effects of all voids and discontinuities on the mechanical properties, which resulted in the direct damage measurements [158]. To achieve this, the nanoindentaion results obtained from the specimen's top surface close to the fracture surface area were studied carefully to assess the accuracy and overall applicability of the indentation-based damage quantification. As shown in Figure 7-16(b), there was a sharp increase in the measured modulus from the distance larger than 400 µm to fracture surface. The D parameter was calculated from the drop in the measured modulus, as shown in Figure 7-17. The results suggest that a major amount of damage was accumulated in the material, therefore it led to a sudden decrease in its modulus. For distances lower than 400 µm, the measured modulus reduces further, denoting an increasing damage, up to 80% (Figure 7-17). This is due to a higher shear-band density near to the fracture area. The damage in the studied BMG, as a result of three-point bending, was clearly observed with other experimental tools: Figure 4-6 shows SEM images of damage in the fracture surface of the material and the indentation studies on the fracture surface.

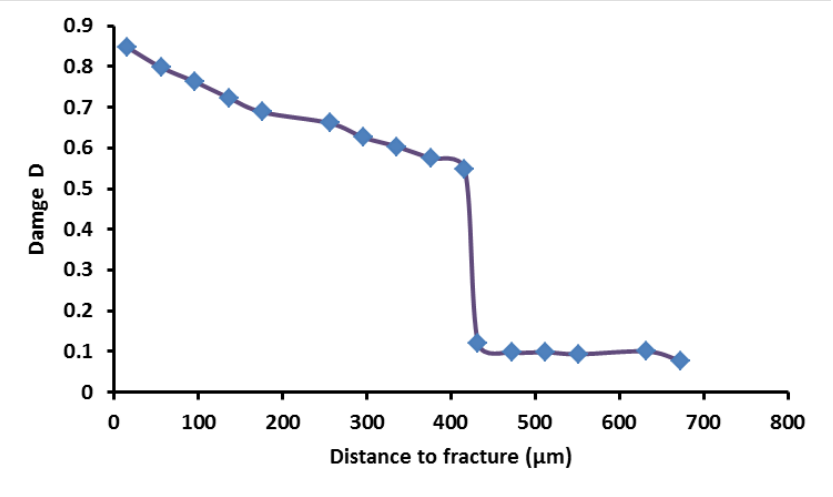

Figure 7-17 Damage versus distance to the fracture surface

7.5 Conclusion

A systematic study was carried out to investigate features of plastic deformation related to shear bands in $Zr_{48}Cu_{36}Al_8Ag_8$ using various techniques. This analysis provided a new insight into deformation behaviour of Zr-Cu-based BMGs, and its main conclusions are summarised as follows:

1. During plastic deformation, shear bands formed localised deformation zones, with deformation including discrete movement of the material`s volume along shear-band lines. Shear behaviour strongly depended on the applied load that initiated shear bands at some “weak” sites, but it was not high enough to drive shear-band evolution to the surface, leading to their selective nucleation.

2. Fracture surfaces of the studied BMGs, consisting of multiple localised shear bands, were 6 to 8 times weaker than the undeformed material.

3. TEM characterisation of individual shear bands revealed that there was no precipitation of nanocrystals inside the shear bands induced by wedge

indentation or three-point bending, and faces of the shear bands were amorphous.

4. The same compositions were observed in our study with SAED for the as-cast alloy and the deformed areas; hence, no compositional changes were found in the shear-band region. This shows that generation of shear bands is related rather to yielding behaviour of the BMG than crystallisation-induced changes in its microstructure.

8 Conclusions and Future works

8.1 Conclusions

The main purpose of this research was to bridge a gap in current knowledge on elastic and inelastic deformation of a Zr-Cu-based metallic glass under various loading conditions and at different length scales. This was achieved by conducting first an extensive literature review on deformation mechanism of BMGs, followed mostly by experimental studies. The experimental part of this research focused mainly on the analysis of deformation behaviour of the BMG and shear-band characterisation. The experiments were designed and conducted as part of continuation and extension of research into BMGs at Loughborough University except for DIC measurement performed at Sheffield University. To study deformation behaviour, a large number of experiments were performed at different length scale including nano-, micro- and macro-scales under inhomogeneous and homogeneous loading conditions. Additionally, shear bands were directly characterised to understand the nature of plastic deformation in the BMG. A preliminary numerical study was analysed to study local plastic deformation in the BMG. The results of this study made a valuable contribution to our existing understanding of deformation characteristics of the BMG under homogenous and inhomogeneous loading condition as well as mechanical behaviour of shear bands, which are responsible for an inelastic deformation mode in the BMG. Based on the above, the current research brought upon the following conclusions.

This thesis reviewed the theory behind the analysis techniques used for extracting magnitudes of the elastic modulus and hardness from nanoindentation

test data for metallic glasses using a spherical tip. The calibration measurements required to ensure correct performance of the instrument including frame compliance, cross-hair calibration and indenter area function were also discussed.

A standard macroscale three-point bending test was conducted to determine the bulk flexural modulus (E) of the BMG, which was evaluated to be 95 GPa with the Poisson's ratio (ν) of 0.35. Fracture morphology of specimen revealed a vein-like structure for both tension and compression sites as a result of shear-band sliding. This behaviour is distinctly different from the case of propagation of principal shear bands along a slip plane, widely reported in the literature. In this study, indentation techniques were extensively used to first study the elastic deformation of a Zr-Cu—based BMG alloy, followed by a systematic analysis of initiation and evolution of shear-band localisation in the indented materials. The initial stage of elastic deformation of the BMG was investigated via the nano-indentation test with a spherical indenter with 5 µm diameter. Below 4 mN, no appreciable plasticity was observed, and deformation was assumed to be purely elastic. However, in a subsequent loading case, a significant plastic event was observed at ~4 mN, which is considered to be the first 'pop-in'. The load at it was used to calculate the maximum shear stress underneath the indenter with the help of Hertz`s spherical contact mechanics. Additionally, the obtained experimental results showed hardening behaviour of the BMG with the load corresponding to the first pop-in increasing with each load increment. The incremental loading technique was also used to investigate the dependence of hardness on penetration depth, and this similarly indicated the work-hardening

phenomena in the metallic glass, especially at nanoscale. A discrete serrated flow was observed at low strain rates (0.02 s^{-1}); however, high rates suppressed this type of flow. As a result, the pop-in events for this metallic glass manifested as a stepped P-h curve with significantly strong rate sensitivity. The serration flow behaviour was analysed using the concept of free volume and localised heating. The temperature rise, calculated as 0.04 K for the low strain rate, was negligible to have an effect on the deformation mechanism. Shear bands appeared on the surface at load in excess of 100 mN, and shear steps were observed on the material`s surface at higher load magnitude.

The results obtained with the suggested wedge-indentation technique demonstrated the stress level required for initiation of shear bands in the BMG. It was estimated that the level of stress required to initiate shear bands was between 0.7-0.9 GPa in wedge indentation. Several serrated semi-circular slip steps formed by shear bands were observed on the front surface of the wedge-indented BMG. Apart from the serrated slip-steps, numerous smooth semi-circular slip steps of shear bands were seen, when the load was increased above 2 kN. These serrated and smooth semi-circular slip steps were named “primary shear bands” in order to discriminate them from other slip-steps of the shear bands formed at higher loads. The slip-steps of the semi-circular PSBs seemed to vanish as they approached the indentation surface. From the observations, few slip lines of the shear bands reached the top surface and they lined up along straight lines parallel to the imprint’s axis. This indicated that nucleation of shear bands occurred easier than their evolution. Above 1 kN, new types of shear bands were formed inside the zone of primary shear bands, originated radially from the indenter tip. The wedge-indentation technique was

also applied to compare fracture surfaces of the soda-lime-silica glass and the studied Zr-Cu-based metallic glass at microscale. Observations of the fracture surfaces indicated that the propagating cracks did not experience any energy dissipation in the traditional glass; on the contrary, the shear-band evolution in the metallic glass showed branching and healing mechanisms contributing to plastic deformation at micro-scale. There was a deviation from linear elastic deformation in the load-displacement curve due to shear-band operation for the single-load condition, and incremental loading resulted in no difference of the overall mechanical response of the BMG. The residual imprint depth for the first (22 µm) and the second (50 µm) incremental loads was equal to the initial displacement of the indenter engaged with the specimen. Consequently, the incremental load-displacement curve can be utilised to estimate the total work done for entire deformation. The wedge indentation is particularly useful for materials scientists for development of appropriate constitutive models that characterise plastic events in amorphous materials in the small-length scale. A systematic study was carried out to investigate the nature of shear bands by their direct characterisation around the fracture and the indented region using various techniques including XRD, SAED, EDS, surface decoration and nanoindentation. The surface-decoration results showed a localised deformation zone, which was formed as a result shear-banding, slipped across shear-band lines. This indicated that formation of shear bands resulted in slippage material volume. While dislocations move along specific slip planes in traditional metals, shear bands do not flow and propagate gradually across BMG specimens. The variation of height of the specimen`s surface along a chosen shear band showed rotation of a material volume due to shear-band formation. TEM studies of the

deformed and as-cast BMG demonstrated that deformation in the BMG did not lead to crystallisation inside the shear bands and no compositional change was found in the shear band region as well. This shows that generation of shear bands was a result of yielding behaviour of BMG. The indentation made on the individual shear bands exhibited that they were softer than the bulk materials based. However, the indentation results cannot be used as a shear-band property as the indentation inevitably deforms the harder surrounding bulk material. The sheared zone can be estimated from the initial part of the P-h curve; it was around 500 µm. The nano-indentation tests on the fracture surface showed that the fracture region was much weaker than the virgin material. It is hypothesized that the a dilatation process was a mechanism of deformation-induced localisation in a highly deformed region. Additional indents were made near to the fracture surface demonstrating that there was a softened zone with width of some 400 µm in addition to a sharp transition from the highly deformed region to the bulk area. The indentation approach was employed to quantify deformation-induced damage through the degradation of indentation hardness and modulus using continuum-damage-mechanics suggested by Lemaitre and Dufailly [155]. The results showed that a major amount of damage was accumulated in the BMG resulting in a significant decrease in the measured modulus due to a higher shear-band density near the fracture zone. Effects of size and structural states on deformation characteristics of the BMG under imposed homogeneous loading states were also studied. As a specimen`s taper has a significant effect on yield strength of micro-pillars, various pillar preparation techniques were examined to minimize the specimen`s taper. It was found that a rectangle pillar could reduce or eliminate the tapering effect. Although the

specimen`s taper can be eliminated by using a lift-out technique, the Pt-deposition that is much softer than the BMG to failure of the pillar at the joint point. So, compression tests were carried out on micropillars milled from the virgin BMG and its fracture surfaces. The deformation mode of these pillars was dominated by localised shear banding. The yield strength measured from the engineering stress-strain curve indicated that the fracture region (~1 GPa) was significantly softer that the virgin state (~1.8 GPa). There is a possibility that a higher amount of free volume resulted in a decrease in strength in the fracture region. However, a further investigation will be required to compare amounts of free volume in the fracture region and the bulk area. Rectangular pillars with cross-sections of 230 nm × 230 nm and 10 µm × 10 µm from the BMG were also fabricated using FIB and tested in compression to investigate the effect of sample size on deformation behaviour of the BMG in micro-scale. At all sizes, the plastic flow was localised in shear bands and there was limited number of shear bands in the smaller sample. The strength increase was successfully modelled using Weibull statistics for brittle materials. Thus, the increase in strength is a result of the fact that a smaller sample has fewer defects.

This study provided a new insight into the deformation behaviour related to shear bands of Z-Cu-based BMGs using various techniques. During plastic deformation, shear bands formed a localised deformation zone at various lengths (nano- and micro-scale) under homogenous (uniaxial compression) and inhomogeneous (wedge indentation) loading conditions. In the wedge-indentation experiment, it was shown that nucleation of new shear bands was easier than its evolution during inelastic deformation. The deformation comprised

discrete movements of the material`s volume along shear-band lines. For micro-compression experiments, the yield strength increased for smaller samples compared to the larger ones due to fewer defects. The fracture surface of the studied BMG was significantly weaker than the bulk materials based on nano-indentation and micro-compression results. There were no crystallisation and compositional changes inside the shear bands under inhomogeneous loading conditions. Hence, shear bands showed there an amorphous structure with composition similar to the bulk material.

8.2 Recommendation for future works

The results that were highlighted in this research project reflect a number of findings; still, some new topic arose during the course of the study which could benefit from a further research.

8.2.1 Experimentation

- Employing in-situ wedge-indentation experiments in addition to the surface decoration technique for BMGs to characterise deformation behaviour in terms of evolution of shear bands localised in the volume of materials. This will further information for deformation mechanism of BMGs.

- Studying a possible transition from heterogeneous deformation as the specimen`s size is decreased and the effect of a structural state on such a transition length scale using *in-situ* micro-compression experiments. It was shown by Greer *et al* [3] Zr-based glass micropillars with diameter of 100 nm or less exhibited homogeneous plastic deformation that preceded

shear-band propagation. This homogenous flow is different from high-temperature plasticity and it is worthy of a separate study to explore the specific mechanism responsible for homogenous deformation.

- Microstructural characterisation of microcompression specimens. The direct characterisation of shear bands around the compressed area using various techniques including SAED, EDS, surface decoration. The surface decoration can be employed to analyse multiple shear bands formed and propagated in compression studies.

- Investigating into the pressure sensitivity of the Zr-Cu-based metallic glass and its dependence on the structural state of the glass. Although plastic deformation in conventional crystalline metallic alloys is linked only to the motion of dislocations that is generally non-pressure-dependent, the plastic flow in BMGs is also sensitive to hydrostatic or normal stresses. This is due to the fact that shear in BMGs is accommodated through local atomic rearrangements leading to dilatation during deformation, so that pressure sensitivity can be expected.

8.2.2 Modelling

In Chapter 9, initial results for a numerical model of deformation process in the BMG were presented and used to characterise shear-band localisation. There are some additional directions for the future work.

- Development of 3-D finite-element (FE) models with a random distribution of weak elements in the bulk volume of BMGs; and incorporation of a strain - gradient formulation to implement inhomogeneous loading states –

e.g. wedge indentation, as well as homogeneous loading state as in the micro pillar compression technique to analyse the effect of strain gradients on shear band initiation and their propagation patterns.

- Development and implementation of a 3-D finite-element computational algorithm to incorporate local and non-local effects of strain gradients on initiation and propagation of shear bands under homogeneous and inhomogeneous loading states based on a non-local plasticity theory.
- A study of the effect of experimental conditions imposed on the analysis of homogeneous and inhomogeneous deformation modes, on the shear-band initiation and propagation and specific deformation behaviour observed in the force - displacement curves.

References

1. Jang J, Yoo B, Kim Y, Oh J, Choi I, Bei H. Indentation size effect in bulk metallic glass. Scr Mater 2011 ;64(8):753-756.

2. Greer AL, Cheng YQ, Ma E. Shear bands in metallic glasses. Mat Sci Eng R 2013 ;74(4):71-132.

3. Greer JR, De Hosson, Jeff Th M. Plasticity in small-sized metallic systems: Intrinsic versus extrinsic size effect. Prog Mater Sci 2011 ;56(6):654-724.

4. Wang WH. The elastic properties, elastic models and elastic perspectives of metallic glasses. Prog Mater Sci 2012 ;57(3):487-656.

5. Byrne CJ, Eldrup M. Bulk metallic glasses. Science 2008 ;321(5888):502-503.

6. Callister WD, Rethwisch DG. Fundamentals of materials science and engineering: an integrated approach. 4th ed. : Wiley; 2011.

7. Yavari AR, Moulec AL, Inoue A, Nishiyama N, Lupu N, Matsubara E, et al. Excess free volume in metallic glasses measured by X-ray diffraction. Acta Mater 2005 ;53(6):1611-1619.

8. Johnson WL. Thermodynamic and kinetic aspects of the crystal to glass transformation in metallic materials. Prog Mater Sci 1986 ;30(2):81-134.

9. Yeh X, Samwer K, Johnson W. Formation of an amorphous metallic hydride by reaction of hydrogen with crystalline intermetallic compounds-A new method of synthesizing metallic glasses. Appl Phys Lett 1983 ;42(3):242-243.

10. Van Diepen A, Buschow K. Hydrogen absorption in $CeFe_2$ and $ThFe_3$. Solid State Commun 1977 ;22(2):113-115.

11. Aning A, Wang Z, Courtney T. Tungsten solution kinetics and amorphization of nickel in mechanically alloyed Ni-W alloys. Acta Metall Mater 1993 ;41(1):165-174.

12. Schwarz R, Johnson W. Formation of an amorphous alloy by solid-state reaction of the pure polycrystalline metals. Phys Rev Lett 1983 ;51(5):415.

13. Klement W, Willens R, Duwez P. Non-crystalline structure in solidified gold–silicon alloys. Nature 1960 ; 869-870.

14. Inoue A, Shinohara Y, Gook JS. Thermal and magnetic properties of bulk Fe-based glassy alloys prepared by copper mold casting. Materials T JIM 1995 ;36(12):1427-1433.

15. Matthews D, Ocelik V, Bronsveld P, De Hosson, J Th M. An electron microscopy appraisal of tensile fracture in metallic glasses. Acta Mater 2008 ;56(8):1762-1773.

16. Liu Z, Wang R, Qu R, Zhang Z. Precisely predicting and designing the elasticity of metallic glasses. J Appl Phys 2014 ;115(20):203513.

17. Ma E. Tuning order in disorder. Nature Mater 2015 ;14(6):547-552.

18. Schroers J, Johnson WL. Ductile bulk metallic glass. Phys Rev Lett 2004 ;93(25):255506.

19. Wei Y, Lei X, Huo L, Wang W, Greer A. Towards more uniform deformation in metallic glasses: The role of Poisson's ratio. Mater Sci Eng: A 2013 ;560:510-517.

20. Madge S, Louzguine-Luzgin D, Lewandowski J, Greer A. Toughness, extrinsic effects and Poisson's ratio of bulk metallic glasses. Acta Mater 2012 ;60(12):4800-4809.

21. Ashby MF, Greer AL. Metallic glasses as structural materials. Scr Mater 2006 2;54(3):321-326.

22. Salimon AI, Ashby MF, Bréchet Y, Greer AL. Bulk metallic glasses: what are they good for? Mater Sci Eng: A 2004 7;375:385-388.

23. Jang D, Greer JR. Transition from a strong-yet-brittle to a stronger-and-ductile state by size reduction of metallic glasses. Nature Mater 2010 ;9(3):215-219.

24. Kumar G, Desai A, Schroers J. Bulk metallic glass: the smaller the better. Adv Mater 2011 ;23(4):461-476.

25. Gilman JJ. Mechanical behavior of metallic glasses. J Appl Phys 1975 ;46(4):1625-1633.

26. Argon A. Plastic deformation in metallic glasses. Acta Metall 1979 ;27(1):47-58.

27. Spaepen F. A microscopic mechanism for steady state inhomogeneous flow in metallic glasses. Acta Metall 1977 ;25(4):407-415.

28. Cohen MH, Turnbull D. Metastability of amorphous structures. 1964.

29. Elliott SR. Physics of amorphous materials.: Longman London; 1984.

30. Knauss WG, Emri I. Non-linear viscoelasticity based on free volume consideration. Comput Struct 1981 ;13(1):123-128.

31. Spaepen F. Homogeneous flow of metallic glasses: A free volume perspective. Scr Mater 2006 ;54(3):363-367.

32. Mayr S. Activation energy of shear transformation zones: A key for understanding rheology of glasses and liquids. Phys Rev Lett 2006 ;97(19):195501.

33. Yang B, Wadsworth J, Nieh T. Thermal activation in Au-based bulk metallic glass characterized by high-temperature nanoindentation. Appl Phys Lett 2007 ;90(6):061911.

34. Lund A, Schuh C. The Mohr–Coulomb criterion from unit shear processes in metallic glass. Intermetallics 2004 ;12(10):1159-1165.

35. Langer J. Shear-transformation-zone theory of deformation in metallic glasses. Scr Mater 2006 ;54(3):375-379.

36. Langer J. Dynamics of shear-transformation zones in amorphous plasticity: Formulation in terms of an effective disorder temperature. Phys Rev E 2004 ;70(4):041502.

37. Frost HJ, Ashby MF. Deformation mechanism maps: the plasticity and creep of metals and ceramics. th ed. : Pergamon press; 1982.

38. Schuh CA, Hufnagel TC, Ramamurty U. Mechanical behavior of amorphous alloys. Acta Materialia 2007 ;55(12):4067-4109.

39. Megusar J, Argon A, Grant N. Plastic flow and fracture in $Pd_{80}Si_{20}$ near T_g. Mater Sci Eng 1979 ;38(1):63-72.

40. Gouldstone A, Chollacoop N, Dao M, Li J, Minor AM, Shen Y. Indentation across size scales and disciplines: Recent developments in experimentation and modeling. Acta Mater 2007 ;55(12):4015-4039.

41. Guo W. On the influence of indenter tip geometry on the identification of material parameters in indentation testing. 2010.

42. Cheng Y, Cheng C. Scaling, dimensional analysis, and indentation measurements. Mat Sci Eng R 2004 ;44(4):91-149.

43. Fischer-Cripps A. Use of combined elastic modulus in the analysis of depth-sensing indentation data. Mat Res-Pittsburgh 2001 ;16(11):3050-3052.

44. Schuh C, Nieh T. A nanoindentation study of serrated flow in bulk metallic glasses. Acta Mater 2003 ;51(1):87-99.

45. Eswar Prasad K, Ramamurty U. Effect of temperature on the plastic zone size and the shear band density in a bulk metallic glass. Mater Sci Eng: A 2012 ;535:48-52.

46. Schuh C, Nieh T. A survey of instrumented indentation studies on metallic glasses. J Mater Res 2004 ;19(1):46-57.

47. Wei B, Zhang T, Li W, Xing D, Zhang L, Wang Y. Indentation creep behavior in Ce-based bulk metallic glasses at room temperature. Mater Trans 2005 ;46(12):2959-2962.

48. Zhang L, Wei B, Xing D, Zhang T, Li W, Liu Y. The characterization of plastic deformation in Ce-based bulk metallic glasses. Intermetallics 2007 ;15(5):791-795.

49. Schuster BE, Wei Q, Ervin MH, Hruszkewycz S, Miller MK, Hufnagel TC, et al. Bulk and microscale compressive properties of a Pd-based metallic glass. Scr Mater 2007 ;57(6):517-520.

50. Shan Z, Li J, Cheng Y, Minor A, Asif SS, Warren O, et al. Plastic flow and failure resistance of metallic glass: Insight from in situ compression of nanopillars. Phys Rev B 2008 ;77(15):155419.

51. Lai Y, Lee C, Cheng Y, Chou H, Chen H, Du X, et al. Bulk and microscale compressive behavior of a Zr-based metallic glass. Scr Mater 2008 ;58(10):890-893.

52. Abu Al-Rub RK. Prediction of micro and nanoindentation size effect from conical or pyramidal indentation. Mech Mater 2007 ;39(8):787-802.

53. Taljat B, Pharr G. Development of pile-up during spherical indentation of elastic–plastic solids. Int J Solids Struct 2004 ;41(14):3891-3904.

54. Alcala J, Barone A, Anglada M. The influence of plastic hardening on surface deformation modes around Vickers and spherical indents. Acta Mater 2000 ;48(13):3451-3464.

55. Martin M, Troyon M. Fundamental relations used in nanoindentation: Critical examination based on experimental measurements. J Mater Res 2002 ;17(09):2227-2234.

56. Keryvin V. Indentation of bulk metallic glasses: Relationships between shear bands observed around the prints and hardness. Acta Mater 2007 ;55(8):2565-2578.

57. Durst K, Göken M, Pharr GM. Finite element simulation of spherical indentation in the elastic-plastic transition. Zeitschrift für Metallkunde 2002 ;93(9):857-861.

58. Haag F, Beitelschmidt D, Eckert J, Durst K. Influences of residual stresses on the serrated flow in bulk metallic glass under elastostatic four-point bending–A nanoindentation and atomic force microscopy study. Acta Mater 2014 ;70:188-197.

59. Choi I, Zhao Y, Kim Y, Yoo B, Suh J, Ramamurty U, et al. Indentation size effect and shear transformation zone size in a bulk metallic glass in two different structural states. Acta Mater 2012 ;60(19):6862-6868.

60. Nix WD, Gao H. Indentation size effects in crystalline materials: a law for strain gradient plasticity. J Mech Phys Solids 1998 ;46(3):411-425.

61. Concustell A, Sort J, Alcalá G, Mato S, Gebert A, Eckert J, et al. Plastic deformation and mechanical softening of $Pd_{40}Cu_{30}Ni_{10}P_{20}$ bulk metallic glass during nanoindentation. J Mater Res 2005 ;20(10):2719-2725.

62. Van Steenberge N, Sort J, Concustell A, Das J, Scudino S, Suriñach S, et al. Dynamic softening and indentation size effect in a Zr-based bulk glass-forming alloy. Scr Mater 2007 ;56(7):605-608.

63. Lam DC, Chong AC. Model and experiments on strain gradient hardening in metallic glass. Mater Sci Eng: A 2001 ;318(1):313-319.

64. Bei H, Xie S, George EP. Softening caused by profuse shear banding in a bulk metallic glass. Phys Rev Lett 2006 ;96(10):105503.

65. Yoo B, Park K, Lee J, Ramamurty U, Jang J. Role of free volume in strain softening of as-cast and annealed bulk metallic glass. J Mater Res 2009 ;24(04):1405-1416.

66. Vincent S, Murty B, Kramer M, Bhatt J. Micro and nano indentation studies on Zr 60 Cu 10 Al 15 Ni 15 bulk metallic glass. Mater Des 2015 ;65:98-103.

67. Nachum S, Greer A. Indentation size effect in metallic glasses: Mean pressure at the initiation of plastic flow. J Alloys Compounds 2014 ;615:S98-S101.

68. Huang Y, Sun Y, Shen J. Tuning the mechanical performance of a Ti-based bulk metallic glass by pre-deformation. Intermetallics 2010 ;18(11):2044-2050.

69. Vincent S, Basu J, Murty B, Bhatt J. Micro indentation study on $Cu_{60}Zr_{20}Ti_{20}$ metallic glass. Mater Sci Eng: A 2012 ;550( ):160-166.

70. Chen H. Metallic glasses. Mater Sci Eng 1976 ;25:59-69.

71. Vianco P, Li J. Annealing of shear bands in metallic glasses. J Mater Sci 1987 ;22(9):3129-3138.

72. Pampillo C, Chen H. Comprehensive plastic deformation of a bulk metallic glass. Mater Sci Engineering 1974 ;13(2):181-188.

73. Guoan W, Cowlam N, Gibbs M. An investigation of the influence of cold-rolling on the structure factor of a metallic glass. J Mater Sci 1984 ;19(4):1374-1384.

74. Reynolds O. British Association Report: On the dilatancy of media composed of rigid particles in contact. With experimental illustrations. Phil Mag 1885 ;20(223):8.

75. Free volume changes and crack tip deformation in bulk metallic glass alloys and their composites. MRS Proceed; Cambridge Univ Press; 2003.

76. Koba E, Milman YV, Rachek A. Effect of plastic deformation and high pressure working on the structure and microhardness of metallic glasses. Acta Metall Mater 1994 ;42(4):1383-1388.

77. Suh D, Dauskardt RH, Asoka-Kumar P, Sterne PA, Howell RH. Temperature dependence of positron annihilation in a Zr–Ti–Ni–Cu–Be bulk metallic glass. J Mater Res 2003 ;18(09):2021-2024.

78. Vincent S, Murty B, Kramer M, Bhatt J. Micro and nano indentation studies on $Zr_{60}Cu_{10}Al_{15}Ni_{15}$ bulk metallic glass. Mater Des 2014 ; 65:98-103.

79. Chen M, Inoue A, Zhang W, Sakurai T. Extraordinary plasticity of ductile bulk metallic glasses. Phys Rev Lett 2006 ;96(24):245502.

80. Kumar G, Ohkubo T, Mukai T, Hono K. Plasticity and microstructure of Zr–Cu–Al bulk metallic glasses. Scr Mater 2007 ;57(2):173-176.

81. Yu HB, Wang WH, Zhang JL, Shek CH, Bai HY. Statistic analysis of the mechanical behavior of bulk metallic glasses. Adv Eng Mater 2009 ;11(5):370-373.

82. Jiang W, Atzmon M. Mechanically-assisted nanocrystallization and defects in amorphous alloys: A high-resolution transmission electron microscopy study. Scr Mater 2006 ;54(3):333-336.

83. Kim JJ, Choi Y, Suresh S, Argon AS. Nanocrystallization during nanoindentation of a bulk amorphous metal alloy at room temperature. Science 2002 Jan 25;295(5555):654-657.

84. Wesseling P, Ko B, Vatamanu L, Caris J, Lewandowski J. Effects of annealing and annealing with pressure on devitrification of $Al_{87}Ni_7Gd_6$. MRS

Proceed: Supercooled Liquids, Glass Transition and Bulk Metallic Glasses 2003 ;365-370.

85. El-Eskandarany MS, Saida J, Inoue A. Room-temperature mechanically induced solid-state devitrifications of glassy $Zr_{65}Al_{7.5}Ni_{10}Cu_{12.5}Pd_5$ alloy powders. Acta Mater 2003 ;51(15):4519-4532.

86. Perepezko J, Hebert R, Wilde G. Synthesis of nanostructures from amorphous and crystalline phases. Mater Sci Eng: A 2004 ;375:171-177.

87. Wang K, Fujita T, Zeng Y, Nishiyama N, Inoue A, Chen M. Micromechanisms of serrated flow in a $Ni_{50}Pd_{30}P_{20}$ bulk metallic glass with a large compression plasticity. Acta Mater 2008 ;56(12):2834-2842.

88. Lewandowski J, Greer A. Temperature rise at shear bands in metallic glasses. Nature Mater 2006 ;5(1):15-18.

89. Lund AC, Schuh CA. Driven alloys in the athermal limit. Phys Rev Lett 2003 ;91(23):235505.

90. Kawamura Y, Nakamura T, Inoue A. Superplasticity in $Pd_{40}Ni_{40}P_{20}$ metallic glass. Scr Mater 1998 ;39(3):301-306.

91. Rösner H, Peterlechner M, Kübel C, Schmidt V, Wilde G. Density changes in shear bands of a metallic glass determined by correlative analytical transmission electron microscopy. Ultramicroscopy 2014 ;142:1-9.

92. Nemat-Nasser S, Li JY. Electromechanical response of ionic polymer-metal composites. J Appl Phys 2000 ;87(7):3321-3331.

93. Wang WH. The elastic properties, elastic models and elastic perspectives of metallic glasses. Prog Mater Sci 2012 ;57(3):487-656.

94. Glucklich J. Fracture of plain concrete. J Eng Mech-ASCE 1963 ;89(EM-6):127-138.

95. Brace Wd, Bombolakis E. A note on brittle crack growth in compression. J Geophys Res 1963 ;68(12):3709-3713.

96. Brandtzaeg A. Failure of a Material Composed of Non-iostropic Elements: An Analytical Study with Special Application to Concrete.: F. Brun; 1927.

97. Steif P, Spaepen F, Hutchinson J. Strain localization in amorphous metals. Acta Metall 1982 ;30(2):447-455.

98. Huang R, Suo Z, Prevost J, Nix W. Inhomogeneous deformation in metallic glasses. J Mech Phys Solids 2002 ;50(5):1011-1027.

99. Jiang M, Ling Z, Meng J, Dai L. Energy dissipation in fracture of bulk metallic glasses via inherent competition between local softening and quasi-cleavage. Philos Mag 2008 ;88(3):407-426.

100. Ruan H, Zhang L, Lu J. A new constitutive model for shear banding instability in metallic glass. Int J Solids Structures 2011 ;48(21):3112-3127.

101. Cheng J, Ghosh S. Computational modeling of plastic deformation and shear banding in bulk metallic glasses. Comp Mater Sci 2013 ;69:494-504.

102. Chu JP, Jang JSC, Huang JC, Chou HS, Yang Y, Ye JC, et al. Thin film metallic glasses: Unique properties and potential applications. Thin Solid Films 2012 6/1;520(16):5097-5122.

103. Shi Y, Falk ML. Stress-induced structural transformation and shear banding during simulated nanoindentation of a metallic glass. Acta Mater 2007 8;55(13):4317-4324.

104. Qiu C, Zhu P, Fang F, Yuan D, Shen X. Study of nanoindentation behavior of amorphous alloy using molecular dynamics. Appl Surf Sci 2014 ;305:101-110.

105. Thamburaja P. Length scale effects on the shear localization process in metallic glasses: A theoretical and computational study. J Mech Phys Solids 2011 ;59(8):1552-1575.

106. Gao Y. An implicit finite element method for simulating inhomogeneous deformation and shear bands of amorphous alloys based on the free-volume model. Modell Simul Mater Sci Eng 2006 ;14(8):1329.

107. Chen Y, Jiang M, Dai L. How does the initial free volume distribution affect shear band formation in metallic glass? Sci China Phys Mech Astron 2011 ;54(8):1488-1494.

108. Li JC, Wei Q, Chen XW, Huang FL. On the mechanism of deformation and failure in bulk metallic glasses. Mater Sci Eng: A 2014 7/29;610(0):91-105.

109. Cullity B. Elements of XRD 1978 ;102.

110. White S, Mather P, Smith M. Characterization of the cure-state of DGEBA-DDS epoxy using ultrasonic, dynamic mechanical, and thermal probes. Polym Eng Sci 2002 ;42(1):51-67.

111. Zhao Z, Wen P, Shek C, Wang W. Measurements of slow β-relaxations in metallic glasses and supercooled liquids. Phys Rev B 2007 ;75(17):174201.

112. Fischer-Cripps A. Elastic–plastic behaviour in materials loaded with a spherical indenter. J Mater Sci 1997 ;32(3):727-736.

113. Chen M, Zhang T, Inoue A, Sakai A, Sakurai T. Quasicrystals in a partially devitrified ZrAlNiCuAg bulk metallic glass. Appl Phys Lett 1999 ;75( ):1697.

114. Jiang M, Ling Z, Meng J, Dai L. Energy dissipation in fracture of bulk metallic glasses via inherent competition between local softening and quasi-cleavage. Philos Mag 2008 ;88(3):407-426.

115. Lee J, Han K, Park J, Chattopadhyay K, Kim W, Kim D. Deformation and evolution of shear bands under compressive loading in bulk metallic glasses. Acta Mater 2006 ;54(19):5271-5279.

116. Hufnagel T, El-Deiry P, Vinci R. Development of shear band structure during deformation of a $Zr_{57}Ti_5Cu_{20}Ni_8Al_{10}$ bulk metallic glass. Scr Mater 2000 ;43(12):1071-1075.

117. Liu YH, Liu CT, Gali A, Inoue A, Chen MW. Evolution of shear bands and its correlation with mechanical response of a ductile $Zr_{55}Pd_{10}Cu_{20}Ni_5Al_{10}$ bulk metallic glass. Intermetallics 2010 8;18(8):1455-1464.

118. Packard C, Schuh C. Initiation of shear bands near a stress concentration in metallic glass. Acta Mater 2007 ;55(16):5348-5358.

119. Tang C, Li Y, Zeng K. Characterization of mechanical properties of a Zr-based metallic glass by indentation techniques. Mater Sci Eng: A 2004 ;384(1):215-223.

120. Yang B, Riester L, Nieh T. Strain hardening and recovery in a bulk metallic glass under nanoindentation. Scr Mater 2006 ;54(7):1277-1280.

121. Yang B, Morrison ML, Liaw PK, Buchanan RA, Wang G, Liu CT, et al. Dynamic evolution of nanoscale shear bands in a bulk-metallic glass. Appl Phys Lett 2005 ;86(14):141904.

122. Cheng L, Jiao Z, Ma S, Qiao J, Wang Z. Serrated flow behaviors of a Zr-based bulk metallic glass by nanoindentation. J Appl Phys 2014 ;115(8):084907.

123. Eshelby J, Pratt P. Note on the heating effect of moving dislocations. Acta Metall 1956 ;4(5):560-562.

124. Flores KM, Dauskardt RH. Enhanced toughness due to stable crack tip damage zones in bulk metallic glass. Scr Mater 1999 ;41(9):937-943.

125. Constantinides G, Tweedie CA, Holbrook DM, Barragan P, Smith JF, Van Vliet KJ. Quantifying deformation and energy dissipation of polymeric surfaces under localized impact. Mater Sci Eng: A 2008 ;489(1):403-412.

126. Donovan P. A yield criterion for $Pd_{40}Ni_{40}P_{20}$ metallic glass. Acta Metall 1989 ;37(2):445-456.

127. Donovan P. Plastic flow and fracture of $Pd_{40}Ni_{40}P_{20}$ metallic glass under an indentor. J Mater Sci 1989 ;24(2):523-535.

128. Bhowmick R, Raghavan R, Chattopadhyay K, Ramamurty U. Plastic flow softening in a bulk metallic glass. Acta Mater 2006 ;54(16):4221-4228.

129. Ramamurty U, Jana S, Kawamura Y, Chattopadhyay K. Hardness and plastic deformation in a bulk metallic glass. Acta Mater 2005 ;53(3):705-717.

130. Cai H, Kalceff SMA, Lawn BR. Deformation and fracture of mica-containing glass-ceramics in Hertzian contacts. J Mater Res 1994 ;9(03):762-770.

131. Zhang H, Jing X, Subhash G, Kecskes LJ, Dowding RJ. Investigation of shear band evolution in amorphous alloys beneath a Vickers indentation. Acta Mater 2005 ;53(14):3849-3859.

132. Jana S, Bhowmick R, Kawamura Y, Chattopadhyay K, Ramamurty U. Deformation morphology underneath the Vickers indent in a Zr-based bulk metallic glass. Intermetallics 2004 ;12(10):1097-1102.

133. Mulhern J, Rogers T, Spencer A. A continuum theory of a plastic-elastic fibre-reinforced material. Int J Eng Sci 1969 ;7(2):129-152.

134. Nekouie V, Abeygunawardane-Arachchige G, Kühn U, Roy A, Silberschmidt VV. Indentation-induced deformation localisation in Zr–Cu-based metallic glass. J Alloys Compounds 2014 12/5;615, Supplement 1(0):S93-S97.

135. Jana S, Ramamurty U, Chattopadhyay K, Kawamura Y. Subsurface deformation during Vickers indentation of bulk metallic glasses. Materials Science and Engineering: A 2004 ;375( ):1191-1195.

136. Lee JY, Han KH, Park JM, Chattopadhyay K, Kim WT, Kim DH. Deformation and evolution of shear bands under compressive loading in bulk metallic glasses. Acta Mater 2006 11;54(19):5271-5279.

137. Lee C, Huang J, Nieh T. Sample size effect and microcompression of Mg65Cu25Gd10 metallic glass. Appl Phys Lett 2007 ;91(16):161913-162100.

138. Schuster B, Wei Q, Hufnagel T, Ramesh K. Size-independent strength and deformation mode in compression of a Pd-based metallic glass. Acta Mater 2008 ;56(18):5091-5100.

139. Volkert C, Donohue A, Spaepen F. Effect of sample size on deformation in amorphous metals. J Appl Phys 2008 ;103(8):3539.

140. Giannuzzi LA. Introduction to focused ion beams: instrumentation, theory, techniques and practice.: Springer Science & Business Media; 2006.

141. Uchic MD, Dimiduk DM, Florando JN, Nix WD. Sample dimensions influence strength and crystal plasticity. Science 2004 ;305(5686):986-989.

142. Wu W, Li Y, Schuh C. Strength, plasticity and brittleness of bulk metallic glasses under compression: statistical and geometric effects. Philos Mag 2008 ;88(1):71-89.

143. Zhang H, Schuster BE, Wei Q, Ramesh KT. The design of accurate micro-compression experiments. Scr Mater 2006 ;54(2):181-186.

144. Nagendra N, Ramamurty U, Goh T, Li Y. Effect of crystallinity on the impact toughness of a La-based bulk metallic glass. Acta Mater 2000 ;48(10):2603-2615.

145. Weibull W. Wide applicability. J Appl Mech 1951 ;103:33.

146. Sun Z, Lyons JS, McNeill SR. Measuring microscopic deformations with digital image correlation. Opt Laser Eng 1997 ;27(4):409-428.

147. Winiarski B, Schajer G, Withers P. Surface decoration for improving the accuracy of displacement measurements by digital image correlation in SEM. Exp Mech 2012 ;52(7):793-804.

148. Berfield T, Patel J, Shimmin R, Braun P, Lambros J, Sottos N. Micro-and nanoscale deformation measurement of surface and internal planes via digital image correlation. Exp Mech 2007 ;47(1):51-62.

149. Collette S, Sutton M, Miney P, Reynolds A, Li X, Colavita P, et al. Development of patterns for nanoscale strain measurements: I. Fabrication of imprinted Au webs for polymeric materials. Nanotechnology 2004 ;15(12):1812.

150. Utke I, Hoffmann P, Melngailis J. Gas-assisted focused electron beam and ion beam processing and fabrication. J Vac Sci Technol B 2008 ;26(4):1197-1276.

151. Tellez H, Vadillo JM, Chater RJ, Laserna JJ, McPhail DS. Focused ion beam imaging of laser ablation sub-surface effects on layered materials. Appl Surf Sci 2008 ;255(5):2265-2269.

152. Gebert A, Gostin PF, Uhlemann M, Eckert J, Schultz L. Interactions between mechanically generated defects and corrosion phenomena of Zr-based bulk metallic glasses. Acta Mater 2012 3;60(5):2300-2309.

153. Li H, Ghosh A, Han Y, Bradt R. The frictional component of the indentation size effect in low load microhardness testing. J Mater Res 1993 ;8(05):1028-1032.

154. Yoo B, Kim Y, Oh J, Ramamurty U, Jang J. On the hardness of shear bands in amorphous alloys. Scr Mater 2009 ;61(10):951-954.

155. Lemaitre J. A continuous damage mechanics model for ductile fracture. J Eng Mater Technol 1985 ;107(1):83-89.

156. Tasan C, Hoefnagels J, Geers M. Indentation-based damage quantification revisited. Scr Mater 2010 ;63(3):316-319.

157. Govindjee S, Simo J. A micro-mechanically based continuum damage model for carbon black-filled rubbers incorporating Mullins' effect. J Mech Phys Solids 1991 ;39(1):87-112.

158. Tasan C, Hoefnagels J, Geers M. A critical assessment of indentation-based ductile damage quantification. Acta Mater 2009 ;57(17):4957-4966.

159. Vaidyanathan R, Dao M, Ravichandran G, Suresh S. Study of mechanical deformation in bulk metallic glass through instrumented indentation. Acta Mater 2001 ;49(18):3781-3789.

160. Johnson GR, Holmquist TJ. Response of boron carbide subjected to large strains, high strain rates, and high pressures. J Appl Phys 1999 ;85(12):8060-8073.

161. Holmquist TJ, Johnson GR. Characterization and evaluation of silicon carbide for high-velocity impact. J Appl Phys 2005 ;97(9):093502.

162. Yu T, Teng J, Wong Y, Dong S. Finite element modeling of confined concrete-I: Drucker–Prager type plasticity model. Eng Struct 2010 ;32(3):665-679.

163. Ghadbeigi H, Pinna C, Celotto S, Yates J. Local plastic strain evolution in a high strength dual-phase steel. Mater Sci Eng: A 2010 ;527(18):5026-5032.

164. Winiarski B, Withers PJ. Mapping residual stress profiles at the micron scale using FIB micro-hole drilling. Appl Mech Mater 2010; 24:267-272.

165. Sabaté N, Vogel D, Keller J, Gollhardt A, Marcos J, Gràcia I. FIB-based technique for stress characterization on thin films for reliability purposes. Microelectron Eng 2007 ;84(5):1783-1787.

166. Baker T. The fracture resistance of flake graphite cast iron. International J Mater Eng Appl 1978 ;1(1):13-18.

167. De Vree J, Brekelman W, Van Gils M. Comparison of nonlocal approaches in continuum damage mechanics. Comput Struc 1995 ;55(4): 581-588.

168. Leamy HJ, Wang TT, Chen HS. Plastic flow and fracture of metallic glass. Matell Trans 1972 ;3(3): 699-408